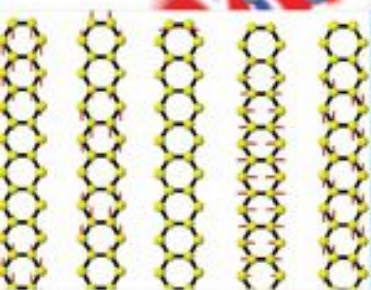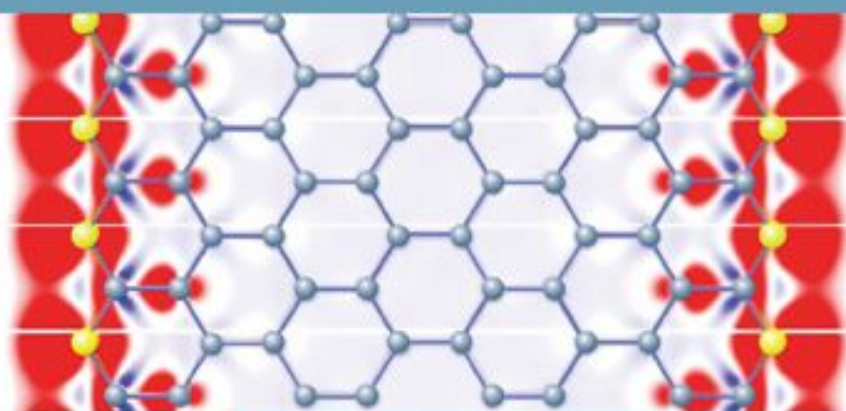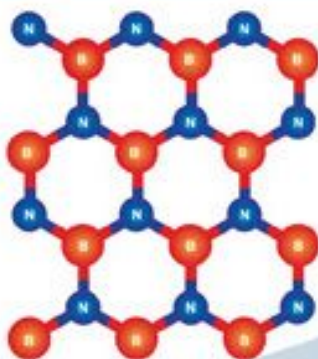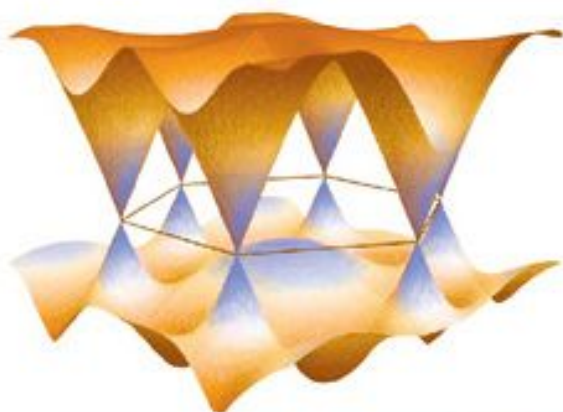# GRAPHENE
AND ITS FASCINATING ATTRIBUTES

Editors

Swapan K. Pati
Toshiaki Enoki
C. N. R. Rao

World Scientific

Graphene and Its Fascinating Attributes

This page intentionally left blank

Graphene and Its Fascinating Attributes

Editors

Swapan K. Pati

Jawarharlal Nehru Centre for Advanced Scientific Research, India

Toshiaki Enoki

Tokyo Institute of Technology, Japan

C. N. R. Rao

Jawarharlal Nehru Centre for Advanced Scientific Research, India

British Library Cataloguing-in-Publication Data
A catalogue record for this book is available from the British Library.

GRAPHENE AND ITS FASCINATING ATTRIBUTES

Printed in Singapore.

Preface

Carbon is the fourth most abundant element on earth. The diversity in bonding makes carbon the most important element in a variety of disciplines. The catenation property, i.e. the ability to form large stable frameworks of interconnecting bonds with different hybridization allows carbon to form innumerable compounds with varying dimensionalities. A recent addition to this large family of carbon allotropes is Graphene, a two-dimensional monolayer of sp^2 carbon atoms arranged in a honeycomb lattice. Graphene can be considered as the parental compound for the carbon allotropes of other dimensionalities. The wrapping of graphene, introducing curvature in terms of intervening five membered rings leads to fullerene. Rolling of graphene segments with different boundaries results in carbon nanotubes of varying chiralities. Three-dimensional graphite can be obtained by the stacking of graphene layers, stabilized by weak interlayer interactions. Graphene has also made it possible to understand properties in low-dimension. It has opened huge possibilities in electronic device fabrication and has also shown much promise in replacing silicon-based electronics. A number of fascinating properties including the observation of integer quantum Hall effect even at room temperature, breakdown of adiabatic Born–Oppenheimer approximation, realization of Klein paradox, possibilities of high T_c superconductivity, metal-free magnetism, ballistic electronic propagation, charge-carrier doping, chemical activities and high surface area, have made graphene the material of the 21st century. The diverse structural and electronic features as well as exciting applications have attracted theoretical and experimental scientists all over the world to explore this low dimensional material.

In November 2009, we had a successful India–Japan bilateral meeting on graphene at the JNCASR, Bangalore, India. The meeting covered all

the fast developing facets of graphene presented by leading experts in the subject. We, therefore, considered it to be of value to present the proceedings of the meeting in the form of a book to the scientific community. While the subject is in a highly active phase of development, we present in this volume the physics, chemistry and engineering of this 21st century material.

There are 15 chapters in the book. In the first chapter, Rao *et al.* have presented a number of experimental routes to synthesize and characterize one to few layers graphene. They have also presented functionalization of graphene by employing both covalent and non-covalent modifications and have studied in detail a number of properties including surface and magnetic properties and doping of graphene by electron donor and acceptor molecules. In the second chapter, Sampath *et al*. report the synthesis and characterization of graphene-bimetallic alloy composites which show good elctro-catalytic, electro-sensing and electrochemical capacitors properties. Kubo *et al*. have analyzed theoretically the singlet open-shell character of polyperiacenes based on Clar's rule and quantum chemical calculations in Chapter 3. They have also isolated a few polyperiacenes experimentally.

The fourth chapter describes the work of Pati *et al*. on the effect of charge transfer on the low-energy characteristics of graphene when it is decorated with donor acceptor organic molecules and metal nanoparticles using *ab-initio* methods. In the fifth chapter, Waghmare *et al*. have studied the uni-axial strain in graphene and its BN analogue theoretically and have explored the reason for the buckling of the two-dimensional layer using *ab-initio* modeling.

R. Saito presents the Raman spectroscopy of graphene edge from the theoretical point of view in Chapter 6. He shows that the LO and TO phonon modes show an opposite polarization dependence in the intensities because of the symmetry of the graphene nanoribbon edges. In the seventh chapter, Sood *et al*. have discussed the Raman spectroscopy of single and bilayer graphene as a function of Fermi level shift achieved by electrochemical top gating. Combining the transport and *in-situ* Raman studies of the field effect devices, they have shown a quantitative understanding of the phonon renormalization due to the doping. T. Ando has reviewed the long-wave length acoustic and optical phonon and

zone-boundary phonons in graphene and carbon-nanotubes and their interaction with electron from a theoretical point of view in Chapter 8. The author has discussed at length the resistivity and conductivity limits and the frequency shift and broadening properties related to various phonon modes in graphene and carbon nanotubes.

In the nineth chapter, Enoki *et al.* investigate edge states of graphene using UHV-STM/STS techniques. They have shown the unconventional magnetic properties of the edge state in the zigzag edges using activated carbon fibers consisting of 3D network of nanographene sheets. In the subsequent chapter, K. Wakabayashi discusses theoretically the transport properties of graphene nanoribbons. He has shown that the graphene nanoribons with zigzag edges subjected to long-ranged impurities could provide a perfectly conducting channel.

Tsukagoshi *et al.* have reviewed the experiments on graphene transistor for its potential use as an atomic film switching device in Chapter 11. They have discussed the preparation and characterization of layered graphene structures and their novel fabrication technique of gate electrodes specialized for the graphene system which is useful for passing of high electric field in the transistor geometry. In Chapter 12, K. Sengupta has theoretically analyzed the Kondo effect in graphene which can be tuned by gate voltage. He argues that graphene might provide the first example of experimental realization of non-Fermi liquid ground states via multichannel Kondo effect. Chapter 13 contains the work of Ghosh *et al.* on experimental studies of low frequency fluctuations in electrical resistance of graphene based field-effect devices with varying layer thickness. They have carried out measurements on the low frequency resistance noise in bilayer graphene flakes as a function of charge density and inter-electrode electric field, and analyzed their results with an analytical model.

In Chapter 14, Shiraishi *et al.* have studied the spin transport properties of single and multilayer graphene experimentally. They have described in detail the generation of pure spin current in graphene and the non-local spin transport. The book finishes with an overview by Baskaran, who has discussed at length various unanticipated and emergent properties of graphene because of complexity, theoretically. In particular, he has reviewed the possibility and realization of spin-1

collective mode, room temperature superconductivity, composite Fermi sea, two-channel Kondo effect in graphene with doping and with external fields.

We believe that the 15 chapters in the book bring out the flavor of the subject nicely and show that research on graphene is emerging to be of major interest. We earnestly hope that the book will be found beneficial by students, teachers and practitioners.

S. K. Pati, T. Enoki and C. N. R. Rao

Contents

Chapter 1

Graphene: Synthesis, Functionalization and Properties

C. N. R. Rao, K. S. Subrahmanyam, H. S. S. Ramakrishna Matte
and A. Govindaraj

Chemistry and Physics of Materials Unit,
International Centre for Materials Science,
New Chemistry Unit and CSIR Centre of Excellence in Chemistry,
Jawaharlal Nehru Centre for Advanced Scientific Research,
Jakkur P.O., Bangalore – 560 064, India

Graphenes with varying number of layers can be synthesized by different strategies. Thus, single-layer graphene is obtained by the reduction of single layer graphene oxide, CVD and other methods besides micromechanical cleavage. Few-layer graphenes are prepared by the conversion of nanodiamond, arc-discharge of graphite and other means. We briefly present the various methods of synthesis and the nature of graphenes obtained. We then discuss the various properties of graphenes. The remarkable property of graphene of quenching fluorescence of aromatic molecules is shown to be associated with photo-induced electron transfer, on the basis of fluorescence decay and time-resolved transient absorption spectroscopic measurements. The interaction of electron donor and acceptor molecules with few-layer graphene samples has been discussed. Decoration of metal nano-particles on graphene sheets and the resulting changes in electronic structure are examined. Few-layer graphenes exhibit ferromagnetic features along with antiferromagnetic properties, independent of the method of preparation. Graphene-like MoS_2 and WS_2 have been prepared by chemical methods, and the materials are characterized by electron microscopy, atomic force microscopy (AFM) and other methods. Boron nitride analogues of graphene have been obtained by a simple chemical procedure starting with boric acid and urea and have been characterized by various techniques.

1. Introduction

Graphene, the mother of all graphitic forms (Fig. 1), has become one of the most exciting topics of research in the last 4 to 5 years [1-6]. This

two-dimensional material constitutes a new nanocarbon comprising layers of carbon atoms forming six-membered rings.
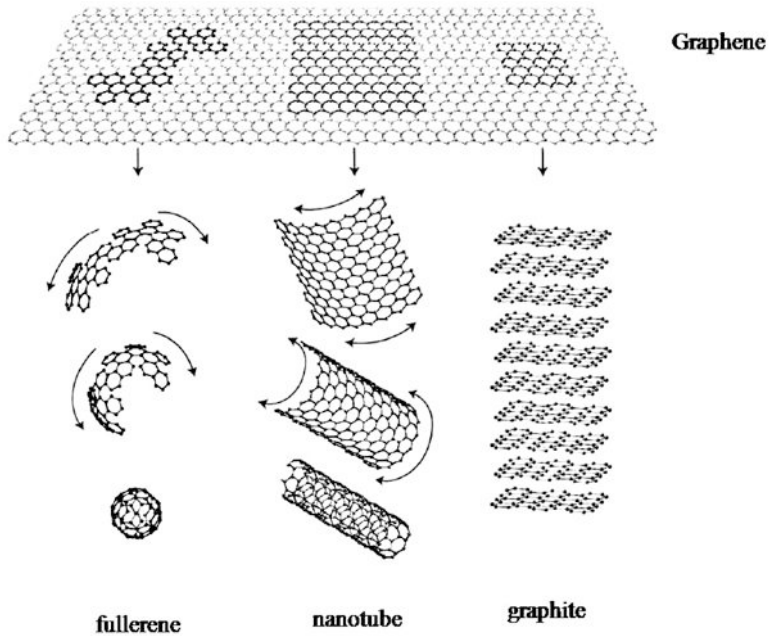
Fig. 1. Graphene: mother of all graphitic forms (From reference 1).

It is distinctly different from carbon nanotubes and fullerenes, exhibiting unique properties which have fascinated the scientific community. Typically important properties of graphene are fractional quantum Hall effect at room temperature [7-9], an ambipolar electric field effect along with ballistic conduction of charge carriers [10], tunable band gap [11] and high elasticity [12]. Although graphene is expected to be perfectly flat, ripples occur because of thermal fluctuations [1]. Ideally graphene is a single-layer material, but graphene samples with two or more layers are being investigated with equal interest. One can define three different types of graphenes: single-layer graphene (SG), bi-layer graphene (BG) and few-layer graphene (number of layers ≤ 10). Although SG and BG were first obtained by micro-mechanical cleavage [10], since then, graphenes containing different

numbers of layers have been prepared using diverse strategies [4,5,13]. There are a few reports on some of the properties of few-layer graphenes, but there are not many studies reporting changes in properties brought about by the number of layers. Furthermore, we do not have well-defined procedures for the synthesis of graphenes with the desired number of layers.
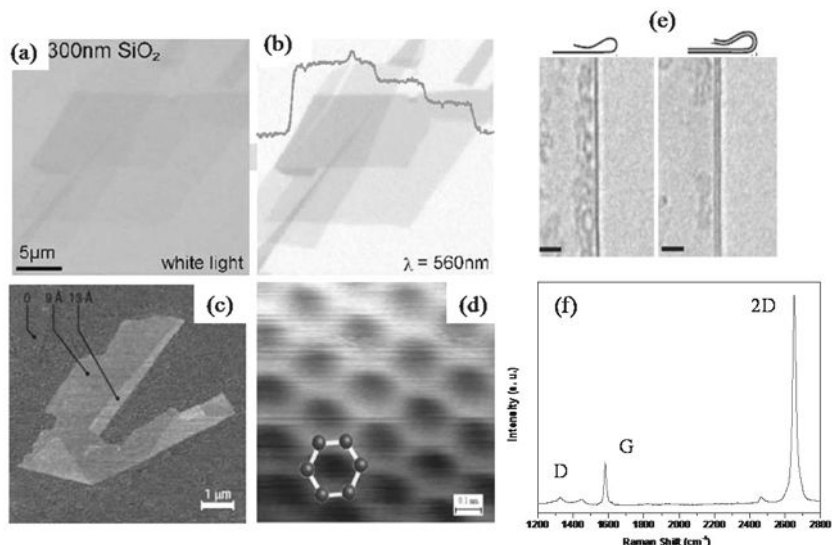
Fig. 2. Optical microscope images of grapheme crystallites on 300 nm SiO_2 imaged with (a) white and (d) green light. (b) Shows step-like changes in the contrast for single, bi- and tri-layer graphenes. (c) AFM image of single-layer graphene. The folded edge exhibits a relative height of ≈4 Å indicating that it is single-layer. (d) High-resolution STM image. (e) TEM images of folded edges of single and bi-layer graphenes (From references 14, 15, 17 and 19). (f) Raman spectrum of single-layer graphene prepared by micromechanical clevage.

Graphene has been characterized by a variety of microscopic and other physical techniques including atomic force microscopy (AFM), transmission electron microscopy (TEM), scanning tunneling microscopy (STM) and Raman spectroscopy [1-5]. It is interesting that SG placed on a Si wafer with a 300 nm thick layer of SiO_2, becomes visible in an optical microscope (Figs. 2(a) and 2(b)) [14-16]. While AFM directly gives the number of layers (Fig. 2(c)) [14-15], STM (Fig. 2(d)) [17]

and TEM images (Fig. 2(e)) [18-19] are useful in determining the morphology and structure of graphene. Raman spectroscopy is an important tool to characterize graphene and provides information about the quality and number of layers in a given sample (Fig. 2(f)) [20-24]. Single-layer graphene shows the well-known G-band around 1580 cm^{-1}. The D-band around 1350 cm^{-1} arising from disorder is very weak or absent. The 2D-band (2600 cm^{-1}) which appears in both single-layer and few-layer graphenes is sensitive to the number of layers, as well as doping. The 2D band is intense in single layer graphene.

2. Synthesis

A large majority of the studies of graphene have been directed towards synthesis. Single-layer graphene (SG) was first prepared by micromechanical cleavage from highly ordered pyrolyitc graphite (HOPG) [10]. In this procedure, a layer is peeled off the HOPG crystal by using scotch tape and then transferred on to a silicon substrate. A chemical method to prepare single-layer graphene involves reduction of single-layer graphene oxide (SGO) dispersion in dimethlyformamide with hydrazine hydrate [25]. The procedure is as follows. Graphite oxide (GO) is first prepared by oxidative treatment of graphite by employing Hummers procedure, [26] by the reaction of graphite powder (500 mg) with a mixture of concentrated H_2SO_4 (12 ml) and $NaNO_3$ (250 mg) in a 500 ml flask kept in an ice bath. While stirring the mixture, 1.5 g of $KMnO_4$ is added slowly and the temperature brought up to 35°C. After stirring the mixture for 30 minutes, 22 ml of water is slowly added and the temperature raised to 98°C. After 15 minutes, the reaction mixture is diluted to 66 ml with warm water and treated with 3% of H_2O_2. Then suspension so obtained is filtered to obtain a yellow-brown powder. This is washed with warm water. GO readily forms a stable colloidal suspension in water and the suspension is subjected to ultrasonic treatment (300 W, 35 kHZ) to produce single-layer graphene oxide (SGO). The SGO (0.3 mg/ml) suspension in a H_2O+ N,N-dimethylformamide (DMF) mixture (50 ml) is treated with hydrazine hydrate at 80°C for 12 h [25]. This yields a black suspension of reduced graphene oxide

(RGO) in DMF/H_2O. To make a stable dispersion of RGO, a further amount of DMF is added to the suspension. It is useful to distinguish this single-layer material (RGO) from the SG obtained by micromechanical cleavage of graphite or other means since RGO may yet contain some residual oxygen functionalities. Gram quantities of single-layer graphene have been obtained by a solvothermal procedure using sodium and ethanol [27]. Exfoliation of graphite in N-methylpyrrolidone or a surfactant/water solution employing ultrasonication yields stable SG dispersions [28-29].

SG films are produced on the Si- terminated (0001) face of single-crystal 6H-SiC by thermal desorption of Si [30-32]. In this procedure, the substrates are subjected to electron bombardment in ultrahigh vacuum to 1000°C to remove oxide contaminants and then heated to temperatures ranging from 1250 to 1450°C for 1-20 min. SG is prepared more conveniently using chemical vapor deposition (CVD) by decomposing hydrocarbons on films or sheets of transition metal such as Ni, Cu, Co and Ru [33]. We have grown graphene layers on different transition metal substrates by decomposing a variety of hydrocarbons such as methane, ethylene, acetylene and benzene, the number of layers varying with the hydrocarbon and reaction parameters. In our experiments, nickel (Ni) and cobalt (Co) foils with thickness of 0.5 mm and 2 mm respectively were used as catalysts. These foils were cut into 5×5 mm^2 pieces and polished mechanically and the CVD process carried out by decomposing hydrocarbons around 800-1000°C. By employing a nickel foil, CVD was carried out by passing methane (60-70 sccm) or ethylene (4-8 sccm) along with a high flow of hydrogen around 500 sccm at 1000°C for 5-10 minutes. With benzene as the hydrocarbon source, benzene vapor diluted with argon and hydrogen was decomposed at 1000°C for 5 minutes. On a cobalt foil, acetylene (4 sccm) and methane (65 sccm) were decomposed at 800 and 1000°C respectively. In all these experiments, the metal foils were cooled gradually after the decomposition. Figure 3 shows high resolution TEM images of graphene sheets obtained by CVD on a nickel foil. Figure 3(a) shows graphenes obtained by the thermal decomposition of methane on the nickel foil where as 3(b) shows graphene obtained by thermal decomposition of benzene. The insets in Figs. 3(a) and 3(b) show selected area electron

diffraction (SAED) patterns. Figure 3(c) shows the Raman spectrum of graphene obtained on a nickel sheet by the thermal decomposition of methane.
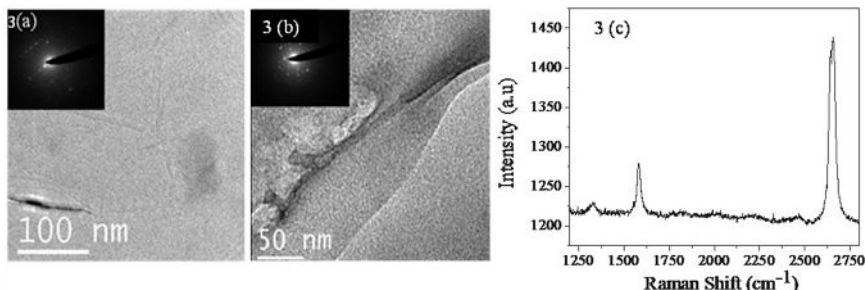
Fig. 3. TEM images of graphene prepared by the thermal decomposition of (a) methane (70 sccm) at 1000°C and (b) benzene (Ar passed through benzene with flow rate of 200 sccm) at 1000°C on a nickel sheet. (c) Raman spectra of graphene prepared by the thermal decomposition of methane (70 sccm) at 1000°C on a nickel sheet.

An important method to prepare few-layer graphene (EG) is by thermal exfoliation of GO at high temperatures [34-35]. In this method, graphitic oxide (GO) is first prepared by the Staudenmaier method which is as follows. A mixture of, sulfuric acid (10 ml) and nitric acid (5 ml) is taken in a 250 ml reaction flask cooled in an ice bath and graphite (0.5 g) is added under vigorous stirring to the acid mixture. After the graphite powder is fully dispersed, potassium chlorate (5.5 g) is added slowly over 15 min. The reaction mixture is stirred for 96 h at room temperature. On completion of the reaction, the mixture is filtered and the residue (GO) is washed in a 5% solution of HCl. GO is then washed repeatedly with deionized water until the pH of the filtrate is neutral and then dried in vacuum at 60°C. GO so prepared (0.2 g) is placed in an alumina boat and inserted into a long quartz tube sealed at one end. The sample is purged with Ar for 10 min, and then quartz tube is quickly inserted into a tube furnace preheated to 1050°C and held in the furnace for 10 minutes. The sample obtained after this procedure corresponds to the few-layer graphene (EG). Another method of preparing few-layer graphene is by reacting SGO in water with hydrazine hydrate at the refluxing temperature or by microwave treatment (EG-H) [5,36]. In this

method hydrazine hydrate (1 ml) is added to 100 ml of stable aqueous exfoliated graphene oxide solution (1 mg/1 ml) and refluxed for 24 h. The reduced GO turns black and precipitates at the bottom of the flask. The resulting precipitate is filtered and washed with water and methanol. Instead of using hydrazine hydrate one can also use ethylene glycol as a reducing agent to prepare few-layer graphene (EG-H(G)). In this procedure, the homogeneous mixture of 25 ml of exfoliated graphene oxide and 2 ml of ethylene glycol is taken in a 50 mL PTFE-lined bomb. The sealed autoclave is kept in an oven at 170°C for 24 h under autogenous pressure and allowed to cool room temperature gradually. The product is washed with water and ethanol.

Graphene can be prepared by heating nanodiamond in an inert or a reducing atmosphere. The effect of heating nanodiamond at different temperatures has been studied by Enoki *et al.*, [37-38]. Annealing of nanodiamond at high temperatures in an inert atmosphere produces few-layer graphenes (DG) [35,37]. We have examined this procedure in detail. In this preparation, we treated nanodiamond particles by soaking in concentrated HCl before use in order to avoid contamination with magnetic impurities. We heated 100 mg of pristine nanodiamond powder (particle size 4-6 nm, Tokyo Diamond Tools, Tokyo, Japan) placed in a graphite container was heated in a graphite furnace in a helium atmosphere at different temperatures (1650, 1850, 2050 and 2200°C) for 1 hr. These samples are designated as DG-1650, DG-1850, DG-2050 and DG-2200°C respectively. In Fig. 4 we show the TEM images of the graphenes obtained by conversion of nanodiamond at different temperatures. From an AFM study, we find that there is a slight increase in the number of layers and a decrease in lateral dimensions in the samples heated at 2200°C in comparison to 1650°C.

We have discovered that arc evaporation of graphite in the presence of hydrogen yields graphene (HG) with exclusively 2-3 layers although flake size is smaller having 100-200 nm [39]. This makes use of the knowledge that the presence of H_2 during arc-discharge process terminates the dangling carbon bonds with hydrogen and prevents the formation of closed structures. To prepare HG direct current arc discharge of graphite evaporation was carried out in a water-cooled stainless steel chamber filled with a mixture of hydrogen and helium in

different proportions without using any catalyst. The proportions of H_2 and He used in our experiments are, H_2 (70 torr)-He (500 torr), H_2 (100 torr)-He (500 torr), H_2 (200 torr)- He (500 torr) and H_2 (400 torr)-He (300 torr).
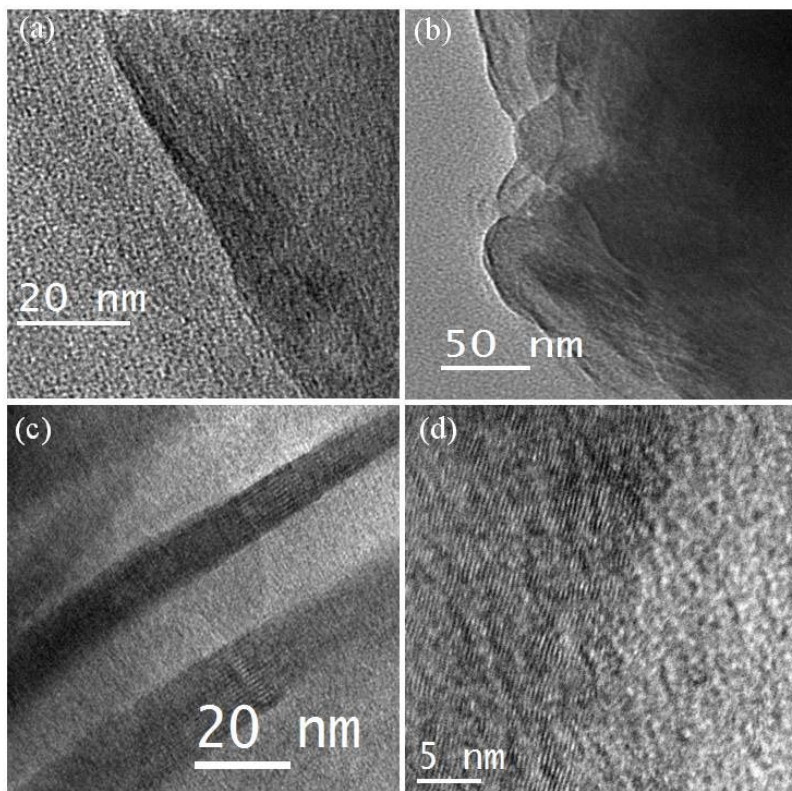
Fig. 4. TEM images of (a) DG-1650, (b) DG-1850, (c) DG-2050 and (d) DG-2200. The numbers correspond to the temperature of transformation in °C.

In a typical experiment, a graphite rod (Alfa Aesar with 99.999% purity, 6 mm in diameter and 50 mm long) was used as the anode and another graphite rod (13 mm in diameter and 60 mm in length) was used as the cathode. The discharge current was in the 100-150 A range, with a maximum open circuit voltage of 60 V [40]. In Fig. 5 we show typical TEM and AFM images of the sample. An important aspect of the

arc-discharge method is its use in doping graphene with boron and nitrogen [41]. Boron and nitrogen doped graphene (B-HG and N-HG) have been obtained by carrying out the discharge in the presence of H_2+diborane and H_2+ (pyridine or ammonia) respectively. In spite of the many advances made in the last four years, controlled synthesis with desired number of layers remains a challenge.
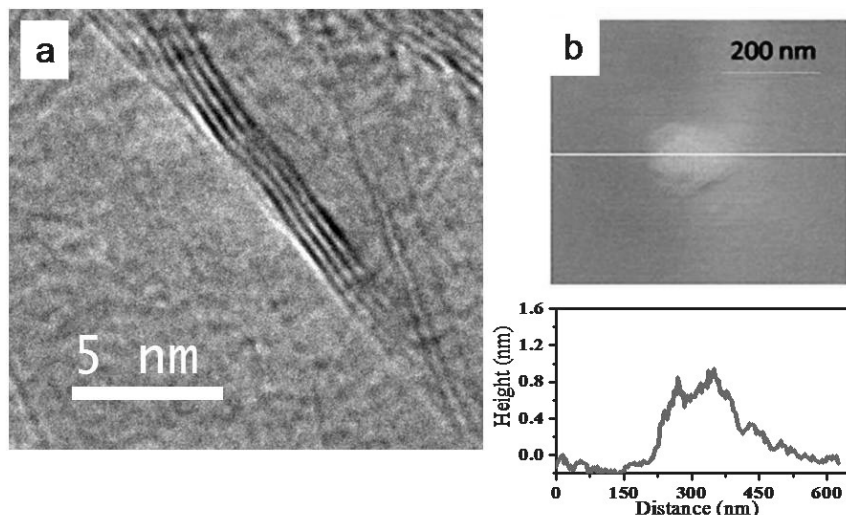
Fig. 5. (a) TEM and (b) AFM images of HG, prepared by arc discharge of graphite in Hydrogen (From reference 6).

3. Functionalization and Solubilization

Carbon nanotubes (CNTs) have been functionalized by both covalent and non-covalent means in order to disperse or solubilize them in different solvents [42-43]. Functionalization of graphene has been carried out by employing similar strategies [4-5]. For example, by employing covalent modification, Haddon and co-workers have achieved functionalization of graphene by several methods. Acid-treated graphene containing surface –OH and –COOH groups was first reacted with $SOCl_2$ to create -COCl groups, followed by reaction with a long chain aliphatic amine to obtain the amide derivative soluble in nonpolar solvents [44]. Another method

employed by these workers is by grafting aryl groups through diazotization reaction [45]. Soluble graphene layers in THF can be generated by the covalent attachment of alkyl chains to graphene layers via reduction of graphite fluoride with alkyl lithium reagents [46]. Such covalent functionalization enables solubilization in organic solvents such as CCl_4, CH_2Cl_2 and THF (Fig. 6(a)) [35]. Similar procedures have been employed by Subrahmanyam *et al.* as well [4,47].
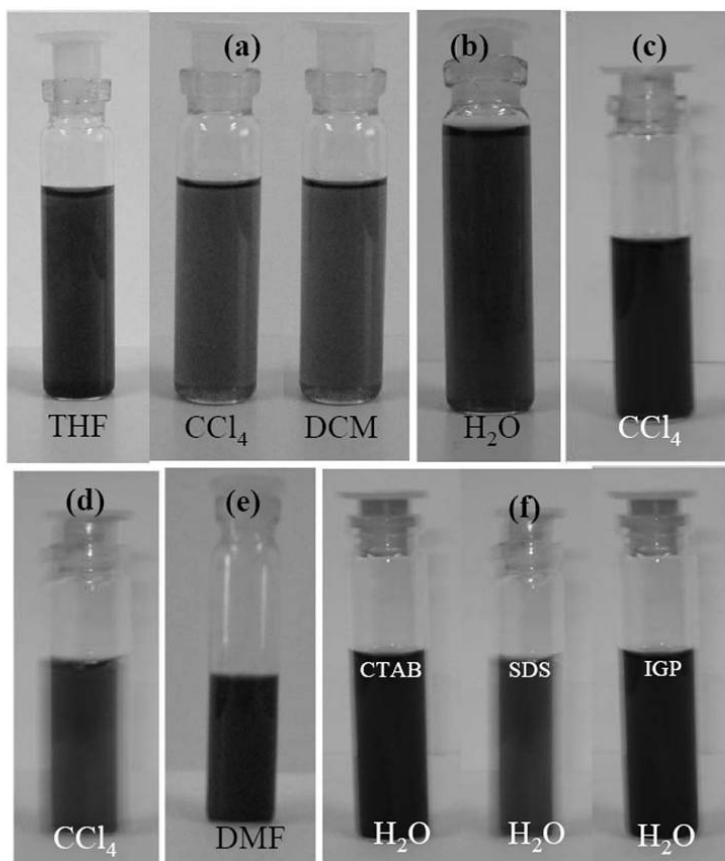
Fig. 6. Photographs of (a) dispersions of the amide-functionalized EG in THF, CCl_4 and dichloromethane, (b) water soluble EG, (c) dispersion of HDTMS treated EG in CCl_4, (d) dispersion of DBDT treated EG in CCl_4, (e) dispersion of PYBS treated EG in DMF and (f) water dispersions of EG treated with CTAB, SDS and IGP (From references 35, 47, 48).

Figure 6(a) shows photographs of dispersions of few-layer graphene in nonpolar solvents. The reaction of graphene with a mixture of concentrated H_2SO_4 and HNO_3 gives water-soluble graphene which is stable for several months (see Fig. 6(b)). Graphene is solubilized in CCl_4 by interaction with organosilane and organotin reagents such as hexadecyltrimethoxysilane (HDTMS) and dibutyldimethoxytin (DBDT) as can be seen from Figs. 6(c) and 6(d) respectively [47].

Graphene can be functionalized through non-covalent modification without affecting its electronic structure by wrapping with surfactants or through π-π interaction with aromatic molecules such as 1-pyrenebutanoic acid succinimidyl ester (PyBS) (I) (Fig. 6(e)) and the potassium salt of coronene tetracarboxylic acid (CS) (II).

I   **II**
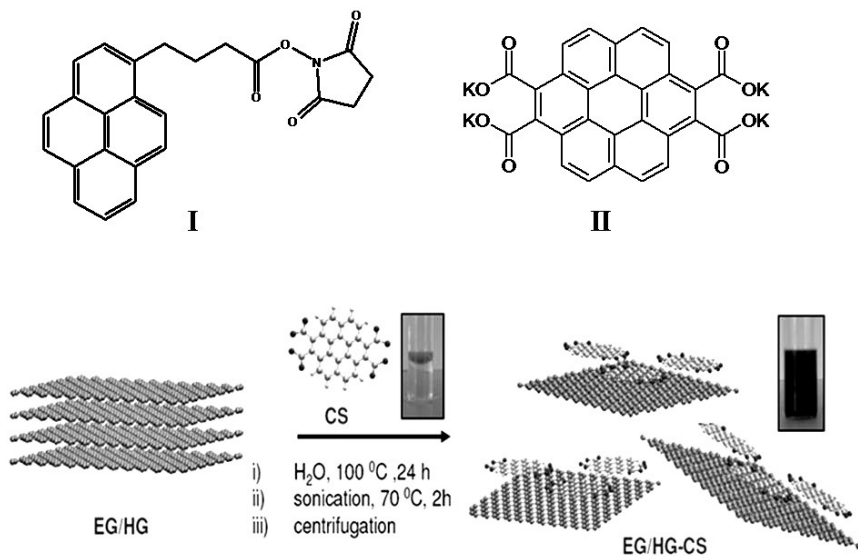
Scheme 1. Exfoliation of few-layer graphene with CS to yield monolayer graphene–CS composites (From reference 48).

Interaction of **II** with few-layer graphene causes exfoliation and selectively solubilizing single-and double-layer graphenes in water through molecular charge-transfer interaction [48]. Non-covalent interaction of graphene with surfactants such as Igepal CO-890

(polyoxyethylene (40) nonylphenylether, IGP), sodium dodecylsulfate (SDS) and cetyltrimethylammoniumbromide (CTAB) gives water-soluble graphene. Figure 6(f) shows and IGP photographs of water-soluble graphene obtained with CTAB, SDS [47]. Water-soluble graphene can also be prepared by PEGylation method in which, acidified graphene is treated with excess of polyethylene glycol (PEG) and conc. HCl under solvothermal conditions [35].

4. Surface Properties

Single-layer graphene is theoretically predicted to have large surface area of 2600 m^2/g [49]. We have measured the surface properties of few-layer graphene samples prepared by different methods. The BET surface area of these samples are found to be in the range of 270-1550 m^2/g, some of them approaching the value of single-layer graphene (Fig. 7(a)) [50].
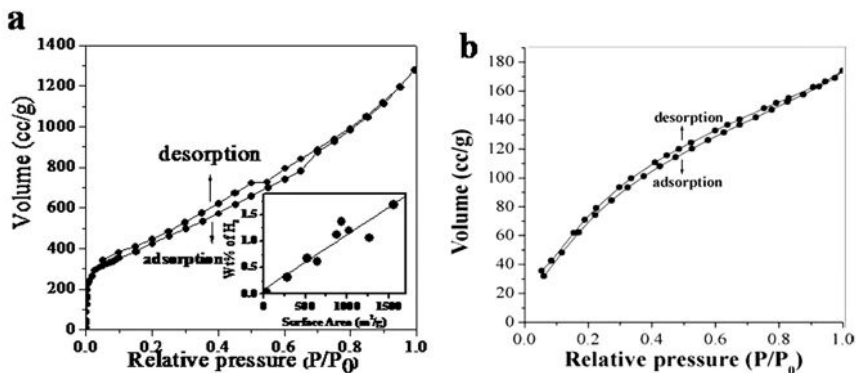
Fig. 7. (a) Nitrogen adsorption and desorption isotherms of graphene at 1 atm and 77 K and (b) Adsorption and desorption isotherms of CO_2 at 1 atm and 195 K. Inset in Fig. 7(a) shows the linear relation between the BET surface area and the weight percentage of hydrogen uptake at 1 atm and 77 K (From reference 50).

The surface area varies as EG > DG > EG-H > HG. We considered that these high surface area samples might enable storage of hydrogen. Hydrogen storage reaches 3 wt% at 100 bar and 300 K and the uptake

varies linearly with the surface area (see inset of Fig. 7(a)) [50]. Theoretical calculations show that SLG can accommodate up to 7.7 wt% of hydrogen, while bi- and tri layer graphene can have an uptake of ~2.7%. The H_2 molecule sits on the graphene surface in end- on and side- on fashion alternatively. CO_2 uptake of few-layer graphenes at 1 atm and 195 K is around 35 wt%. Theoretical calculations show SLG can have a maximum uptake of 37.9 wt% of CO_2 (Fig. 7(b)). The CO_2 molecule sits alternatively in a parallel fashion on the rings.

5. Interaction with Electron Donor and Acceptor Molecules

Raman bands of graphene are affected strongly by electron-phonon interactions and hence by doping with holes and electrons. It has been found recently that a top-gated single graphene layer transistor is able to reach doping levels of up to 5×10^{13} cm^{-1} by in-situ Raman measurements [51]. The G- and 2D- bands show changes on doping. Electron-donor and –acceptor molecules have been found to affect the Raman spectrum of few-layer graphene giving rise to rather large shifts in the Raman bands positions and band widths. In particular, the changes in the Raman spectrum caused by the interaction of tetrathiafulavalene (TTF) and tetracyanoethylene (TCNE) with few-layer exfoliated graphene are quite large [52], the shifts in the G-band going up to 25 cm^{-1}. A possible reason for such large changes in the Raman spectrum is considered to be surface effects. We have, therefore, investigated the effects of TTF and TCNE on the Raman bands with few-layer graphenes prepared by three different methods and hence associated with differences in the nature of the surface [53].

In Fig. 8, we show the Raman G-bands of the EG, DG and HG samples and the changes brought about by interaction with TTF and TCNE. The band on the right-side of G-band is due to the defect-related G'-band (also referred to as D' band by some workers). The G'-band is more prominent in HG than in DG and EG. The full-width at half maximum (FWHM) of the G-band is lowest in HG and highest in EG.
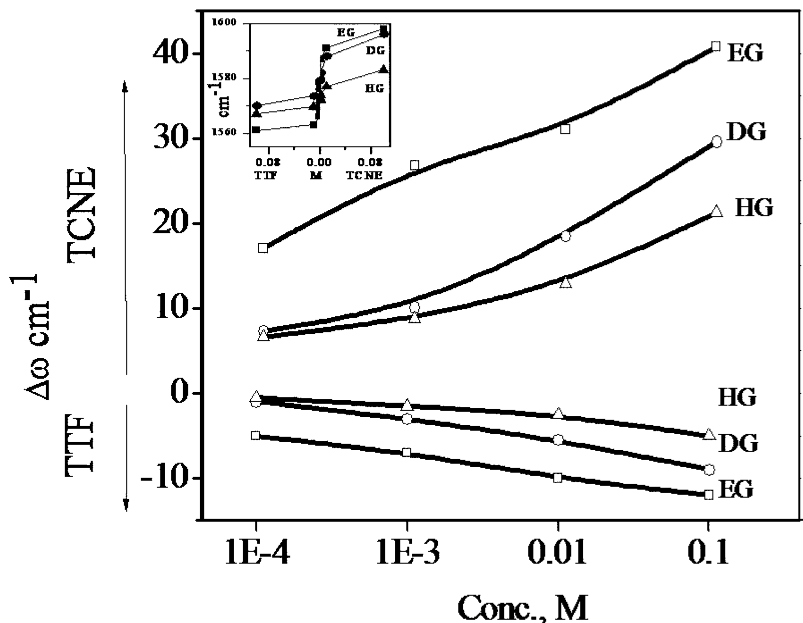
Fig. 8. Changes in the position of G-band plotted against the logarithm of concentration of TTF and TCNE. Inset shows the data plotted against the concentration (From reference 52).

We have followed the variation in the G-bands of EG, DG and HG on interaction with different of concentrations TTF and TCNE. All the samples show an increase in the G-band frequency on interaction with TCNE and a decrease in the G-band frequency on interaction with TTF. Figure 9 shows the changes in the G-band position of the three graphene samples with varying concentrations of TTF and TCNE. The change in the G-band frequency is maximum in the case of EG and least in the case of HG. Thus, the shifts in the G-band in the EG, DG and HG samples are 25,17 and 11 cm^{-1} respectively on interaction with 0.1M TCNE. The full-width-at-half-maxima (FWHM) of the G-bands of the three graphene samples also vary with the concentration of TTF and TCNE. The FWHM of the G-band generally increases on interaction with TTF and TCNE, the magnitude of increase being highest in the case of EG. We also notice that the initial increase is generally sharp. We could obtain reliable

data on the changes in the G' band in the case of HG. The FWHM of the G' band also increases with the increase in concentration of TTF or TCNE.
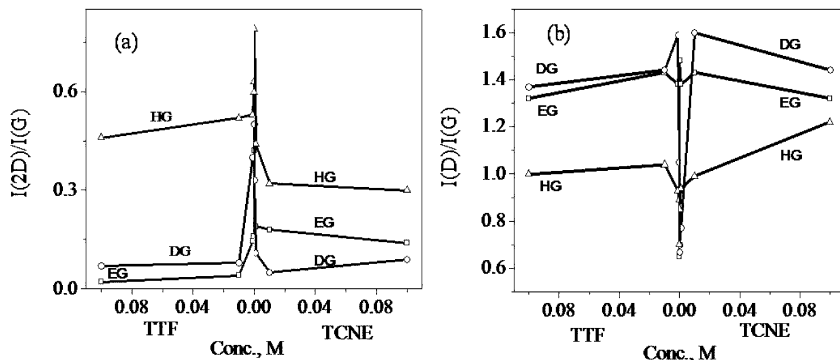
Fig. 9. Variation in (a) 2D/G and (b) D/G intensity ratios with the concentration of TTF and TCNE (From reference 42).

In Fig. 9(a), we have plotted the ratio of intensities of the of 2D and G bands, $I_{(2D)}/I_{(G)}$ against the concentrations of TTF and TCNE. The 2D-band intensity decreases with the increase in concentration of both TTF and TCNE, the initial decrease being sharp. The decrease in intensity is higher with EG and DG when compared to HG. The intensity of the defect-related D band also varies with the TTF/TCNE concentration, but in a direction opposite to that of the 2D-band as shown in Fig. 9(b). This is because the origin of the 2D and D bands is different. The D-band, unlike the 2D-band couples preferentially to electronic states with the wave vector k such that 2q = k [54]. Two scattering events of which one is an elastic process involving defects and another is inelastic involving a phonon occur in the case of the D-band. In the case of the 2D-band both processes are inelastic involving phonons. The intensity ratio of $I_{(D)}/I_{(G)}$ increases more markedly in the case of EG and DG compared to HG, the initial increase being sharp in all the cases.

Changes in the Raman spectra and hence the magnitude of the charge-transfer interaction are found to be highest in the case of EG and least in the case of HG. The changes in band widths, intensities and

frequencies caused by electron donor and acceptor molecules occur sharply, with large changes at low concentrations. This is probably because the very first layer of the donor and acceptor molecules interact strongly, causing large changes in the electronic structure. The present study shows the importance of the graphene surface in determining doping effects through molecular charge-transfer.

Interaction of electron donor and acceptor molecules with graphene samples prepared by different methods has been investigated by isothermal titration calorimetry (ITC) [55]. The ITC interaction energies of the graphene samples with electron acceptor molecules are higher than those with electron donor molecules. Thus, tetracyanoethylene (TCNE) shows the highest interaction energy. The interaction energy with acceptor molecules varies with the electron affinity as well as with the charge-transfer transition energy with aromatics.

Fluorescence quenching property of graphene has been made use for the selective detection of biomolecules [56] and other purposes [57,58]. Graphene is reported to quench the fluorescence of porphyrin [59], but the mechanism of fluorescence quenching by graphene has not been examined although the electron transfer or energy transfer is suspected to occur. We have investigated the quenching of fluorescence of aromatic molecules by non-covalent interaction with graphene and provided definitive proof for the occurrence of intermolecular photoinduced electron transfer.

Absorption spectra of a mixture of the PyBS or OPV ester (10^{-5} M solution in DMF and chloroform respectively) and amide functionalized graphene (EGA), do not show a new band due to charge-transfer between the aromatic molecules and EGA suggesting the absence of any ground-state charge-transfer interaction. Instead, there is increase in the absorbance with increase in EGA concentration due to the absorption of graphene [60]. It appears that there is only π-π type interaction between EGA and PyBS or OPV ester. Unlike the absorption spectra, fluorescence spectra of PyBS and OPV ester show remarkable changes on the addition of EGA. The intensity of the fluorescence bands decrease markedly with the increase in EGA concentration as illustrated in the Fig. 10. (From reference 63)
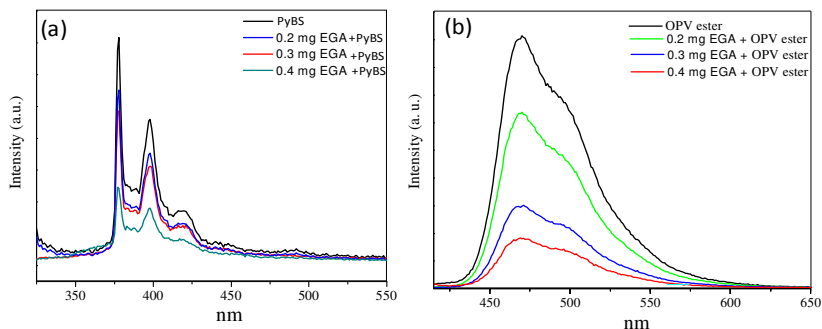
Fig. 10. Fluorescence spectra of (a) PyBS (10^{-5} M in DMF, λexc = 275 nm) and (b) OPV ester, (10^{-5} M in Chloroform, λexc = 400 nm) with increasing concentration of graphene (From reference 63).
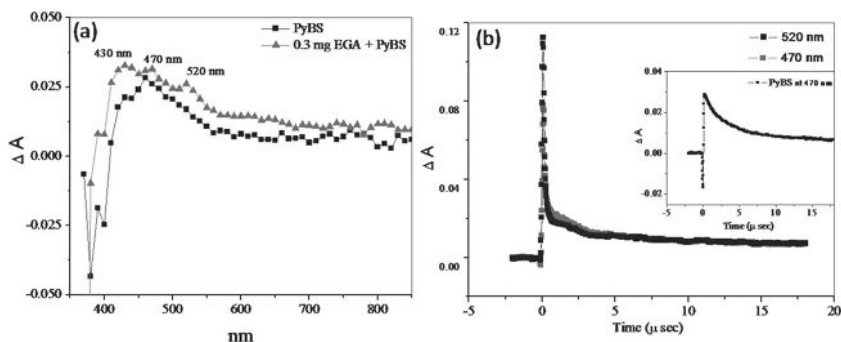
Fig. 11. (a) Effect of addition of EGA on the transient absorption spectrum of PyBS, I, (λexc = 355 nm) after 500 ns. (b) Life time decay of transient species of PyBS + EGA recorded at 470 and 520 nm. Inset shows the decay of pure PyBS at 470 nm (From reference 63).

We have carried out laser flash photolysis studies to explore the transient species. In Fig. 11(a), we compare the transient absorption spectrum of the pure PyBS with that of PyBS on addition of 0.3 mg of graphene. The spectrum of PyBS shows an absorption maximum around 430 nm together with a broad band in the 450-530 nm range due to the triplet state [61]. Upon the addition of EGA new bands emerge around 470 and 520 nm in the transient absorption spectrum at 500 nanoseconds. The 470 nm band can be assigned to the pyrenyl radical cation as reported in the literature [62], suggesting the occurrence of photo-induced

electron transfer from the PyBS to the graphene. Accordingly, we also observe the transient absorption around 520 nm which we assign to the graphene radical anion. The decay of the radical cation formed in the presence of graphene was fast as evidenced from the appearance of a short-lived component (900 ns) in the decay profile (Fig. 11(b)). However, the decay of the transient absorption of pure PyBS monitored at 470 nm (see inset of Fig. 11(b)) shows a long-lived triplet with a lifetime of 6.17 microseconds. The transient absorption at 520 nm decays simultaneously with that of the pyrene radical cation indicating that it is due to the graphene radical anion.

6. Decoration of Graphene with Metal Nanoparticles

Graphene can be decorated with nanoparticles of metals such as Au and Pt [4,5]. Decoration can be carried out in a single step by the simple polyol reduction method using chloroplatinic acid (H_2PtCl_6), silver nitrate ($AgNO_3$), chloroauric acid ($HAuCl_4$) and tetra-chloropalladic acid (H_2PdCl_4) as the metal precursors. On coating with the metal nanoparticles, there are significant changes in the Raman spectrum of graphene, exhibiting shifts in the G-band as well as the other bands (Fig. 12) with variation in the relative intensities of D and 2D bands [4].
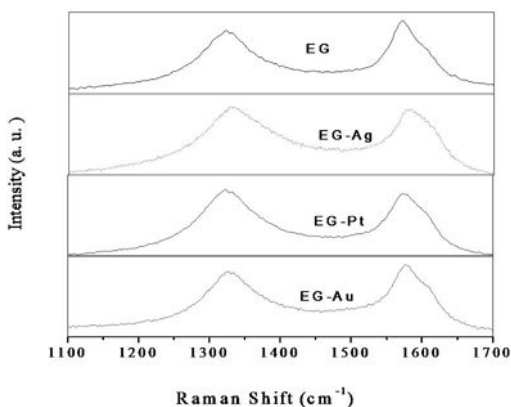
Fig. 12. Raman spectra of EG, EG-Ag (Diameter of silver nanoparticles ~4 nm), EG-Pt (Diameter of platinum nanoparticles ~10 nm) and EG-Au (Diameter of gold nanoparticles ~14 nm).

Interestingly, the magnitude of the band shifts decreases with increase in ionization energy of the metal. As silver has the lowest ionization energy has the maximum effect on the Raman spectrum while gold with the highest ionization energy has the least effect. This might be related to magnitude of Columbic charge transfer between the metal nanoparticles and graphene.

7. Magnetic Properties

There has been considerable interest on the magnetism of nanographite particles for some time. Enoki *et al.* [64]. pointed out that edge states as well as of adsorbed or intercalated species play an important role in determining magnetic properties of these nanographite particles. Recently magnetic properties of graphene samples prepared by exfoliation of graphite oxide, conversion of nanodiamond, arc evaporation of graphite and partial chemical reduction of graphene oxide have been studied [65,66]. All these samples show the divergence between field-cooled (FC) and zero-field-cooled (ZFC) data at 500 Oe (Fig. 13(a)) and the divergence nearly disappears on the application of 1T as can be seen from the inset of Fig. 13(a). All the samples show magnetic hysteresis at room temperature (Fig. 13(b)) [65]. Magnetic properties of graphene reveal that dominant ferromagnetic interactions coexist along with antiferromagnetic interactions in all of the samples, somewhat like in frustrated or phase-separated systems. It is not possible to exactly pin down the origin of magnetism in the graphene samples although defects, and edge effects, are likely to play a major role. Adsorption of benzene solutions of TTF and TCNE has a profound effect on the magnetic properties of graphene. In Fig. 14, we show typical results on the effect of adsorbing 0.01 M and 0.05 M solutions of TTF on the magnetic properties of HG. The value of the magnetization drastically decreases on adsorption of TTF and TCNE, although the basic trend in the temperature-variation of magnetization remains the same.

Thus, the graphene sample continues to show room-temperature hysteresis. On increasing the concentration of TTF or TCNE, the magnetization value decreases progressively. Interestingly, TTF has a greater effect than TCNE, even though the magnitude of adsorption of

TCNE on HG is greater. Magnetic hysteresis of HG persists even after adsorption of TTF and TCNE.
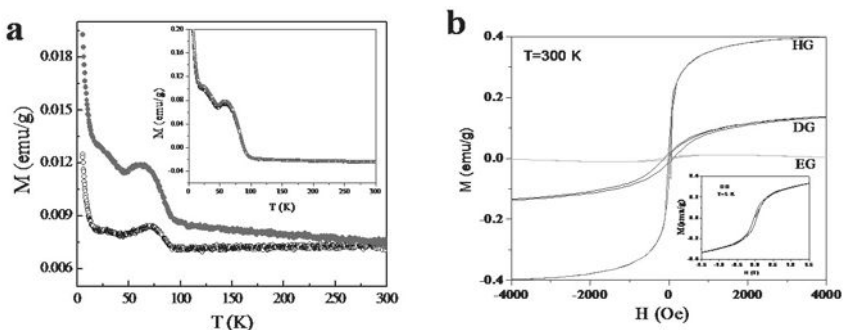
Fig. 13. (a) Temperature variation of magnetization of exfoliated graphene at 500 Oe showing the ZFC and FC data. The inset shows the magnetization data at 1 T. (b) Magnetic hysteresis in different samples at 300 K. Inset shows magnetic hysteresis in DG at 5 K. (From reference 65) (EG: by exfoliation of graphite oxide, DG: by conversion of nanodiamond, HG: by arc evaporation of graphite rod in the presence of H_2)
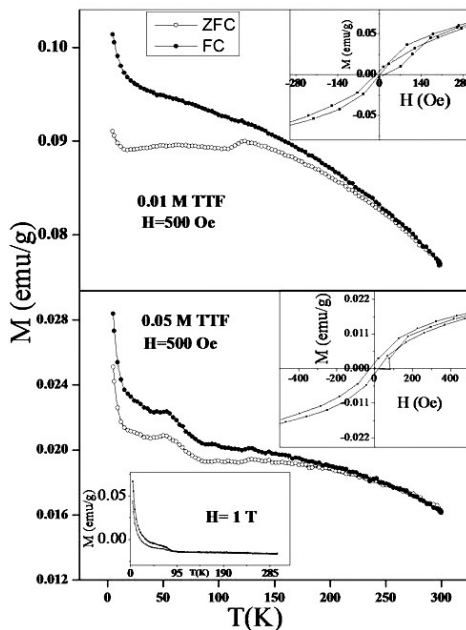
Fig. 14. Temperature-variation of the magnetization of HG samples (500 Oe) after adsorption of 0.01 M and 0.05 M TTF solutions (From reference 65).

The magnetization data given in the Fig. 14 are corrected for the weight of adsorbed TTF. Magnetic hysteresis data at 300 K are shown as insets. In the case of 0.05 M TTF-HG, magnetization data are shown at 1 T as an inset. Magnetization data of HG with adsorbed TCNE are similar to those with TTF, except that the decrease in magnetization relative to pure HG is smaller.

The value of M_S at 300 K decreases on adsorption of TTF and TCNE, the decrease being larger in the case of former. The Curie-Weiss temperature, θp, also decreases markedly on adsorption of these molecules. Clearly, charge-transfer interaction between graphene and TTF (TCNE) is responsible for affecting the magnetic properties.

8. Inorganic Graphene Analogues

Following the discovery of fullerenes [67] in 1985, it was soon recognized that inorganic layered materials such as MoS_2 and WS_2 can also form fullerene-like structures [68-70]. After the discovery of carbon nanotubes [71], inorganic nanotubes analogous to carbon nanotubes were prepared and characterized, nanotubes of MoS_2 and WS_2 being archetypal examples [72-75]. With the discovery and characterization of graphene, the two dimensional nanocarbon, which has created great sensation in last three to four years, it would seem natural to explore the synthesis of graphene analogues of inorganic materials such as dichalcogenides of molybdenum and tungsten which posses layered structures [76]. We have been making efforts to prepare graphene-like analogues of MoS_2 and WS_2. There is an early report [77] on graphene-like MoS_2 prepared by lithium intercalation and exfoliation, but the material was characterized only by X-ray diffraction which is not sufficient to determine the exact nature and number of layers. There have been attempts to prepare single layers of WS_2 by lithium intercalation and exfoliation as well [78-79] and here again the product was only characterized on the basis of (002) reflection in the X-ray diffraction pattern Since even few-layer MoS_2 and WS_2 containing five layers do not exhibit the (002) reflection prominently, it is necessary that layered MoS_2 and WS_2 produced by lithium intercalation and exfoliation are

investigated by transmission electron microscopy and other techniques. Furthermore it seems desirable to explore alternative synthesis of these graphene-like materials. For this purpose, we have employed three different methods to synthesize graphene-like MoS_2 and WS_2. In Method 1, bulk MoS_2 and WS_2 was intercalated with lithium and exfoliated in water. Reaction between lithium-intercalated MoS_2 and WS_2 and water results in the formation of lithium hydroxide and hydrogen gas giving rise to the separation of the layers of the sulfide and the loss of periodicity along the c-axis. In Method 2, molybdic acid and tungstic acid were reacted with excess of thiourea in a N_2 atmosphere at 773 K. Method 3 involved the reaction between MoO_3 and KSCN under hydrothermal conditions [80].
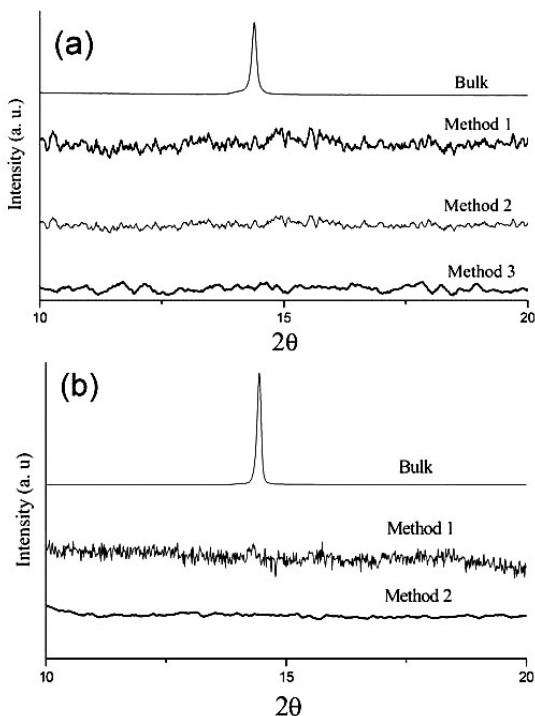
Fig. 15. Comparison of XRD patterns of (a) bulk MoS_2 and MoS_2 layers obtained by Methods 1, 2 and 3 and (b) bulk WS_2 and WS_2 layers obtained by Methods 1 and 2 (From reference 81).

The products of these reactions were characterized by transmission electron microscopy (TEM), atomic force microscopy (AFM), field emission scanning electron microscopy (FESEM) and Raman spectroscopy in addition to X-ray Diffraction (XRD).

XRD patterns of the molybdenum sulphide samples obtained by the three methods do not exhibit the (002) reflection as shown in Fig. 12(a). Energy dispersive x-ray analysis (EDAX) shows the products to be stoichiometric MoS_2. TEM images of the products obtained from these three procedures show the presence of one or few layers of MoS_2 as can be seen from Fig. 13.
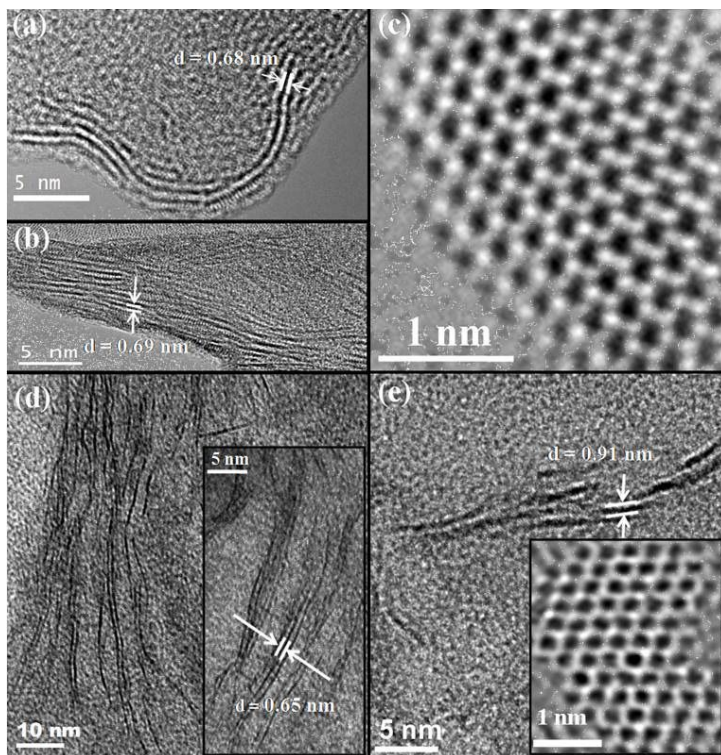
Fig. 16. (a) and (b) the TEM images of MoS_2 layers obtained by Methods 2 and 3, (c) is the high resolution TEM image of layered MoS_2 from Method 3, (d) and (e) images of WS_2 layers from Methods 1 and 2 respectively. The bends in the layers can arise from defects (From reference 81).

Figures 16(a) and 16(b) show the graphene-like MoS_2 layers obtained from methods 2 and 3 with a layer separation in the range of 0.65-0.7 nm. The high resolution image in the Fig. 16(c) shows the hexagonal structure formed by Mo and S atoms with a Mo-S distance of 2.30 Å. AFM images and the height profiles of the products also confirm the formation of few-layer MoS_2. In Fig. 17(a), we compare the Raman spectra of graphene-like MoS_2 samples prepared by us with the spectrum of bulk MoS_2 [81].
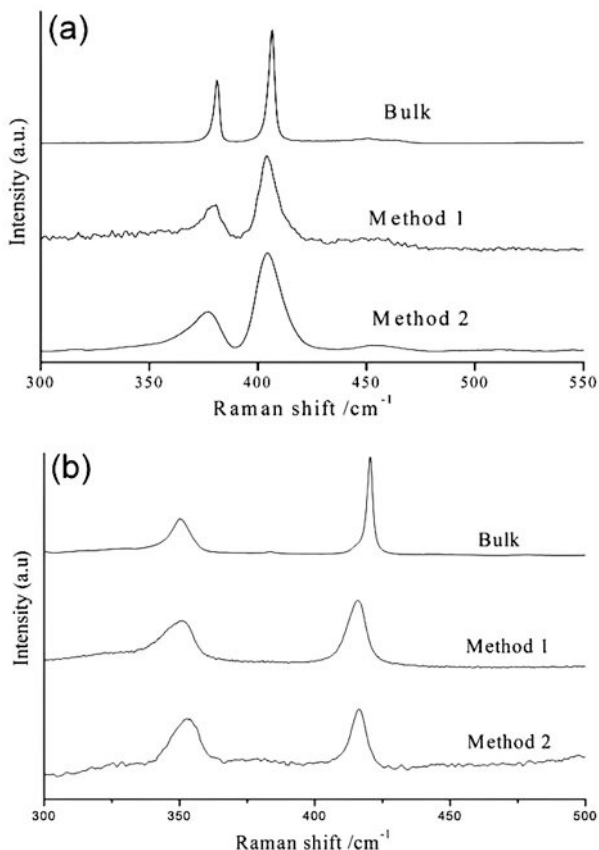
Fig. 17. Raman spectra of (a) bulk MoS_2 and MoS_2 layers obtained by Methods 1 and 2 and (b) bulk WS_2 and WS_2 layers obtained by Methods 1 and 2 (From reference 81).

The bulk sample gives bands at 406.5 and 381.2 cm^{-1} due to the A_{1g} and E_{2g} modes with the full-width half maximum (FWHM) of 2.7 and 3.1 cm^{-1} respectively. Interestingly, few-layered MoS$_2$ prepared by lithium intercalation exhibits the corresponding bands at 404.7 and 379.7 cm^{-1}. The sample obtained by Method 2 show these bands at 404.7 and 377.4 cm^{-1}. There is a clear softening of the A_{1g} and E_{2g} modes in the graphene analogues of MoS$_2$. Furthermore, the FWHM values are larger in the graphene-like samples, the values varying from 10 to 16 cm^{-1} compared to ~3 cm^{-1} in the bulk sample. The broadening of the Raman bands is considered to be due to the phonon confinement. The broadening also suggests that the lateral dimensions of these layers are in the nano regime.

Graphene analogues of WS$_2$ have been prepared by two methods as mentioned earlier. XRD patterns of these samples show the absence of the (002) reflection as shown in the Fig. 15(b). EDAX analysis confirms the stoichiometry of the products to be WS$_2$. The TEM images in Figs. 16(d) and 16(e) reveal that WS$_2$ obtained from both methods 1 and 2 mostly consists of bilayers and single layers. The separation between the WS$_2$ layers in the bilayers sample is in the 0.65-0.70 nm range. WS$_2$ layers obtained by the thiourea method show an interlayer spacing of ~0.9 nm.

AFM images and height profiles of the WS$_2$ obtained by method 1 confirms the existence of 2-3 layers of WS$_2$ with an average thickness of ~1.3 nm. Presence of bilayers of WS$_2$ in the sample obtained by the thiourea method is also confirmed by AFM studies. Raman spectra of WS$_2$ obtained by both the methods show softening of the bands due to the A1g mode (see Fig. 17(b)). Compared to the narrow bands at 351 (E_{2g}) and 420 cm^{-1} (A_{1g}) of bulk WS$_2$ with FWHM values around 7.8 and 2.4 cm^{-1} respectively, the spectrum of WS$_2$ obtained from lithium intercalation shows bands at 350 and 415 cm^{-1} with FWHM values of 13.7 and 8.4 cm^{-1}. The Raman spectrum of WS$_2$ layers synthesized by Method 2 also shows similar softening of the Raman bands and increase in the FWHM [81].

Single- and few-layer graphene analogues of BN flakes were prepared by reacting boric acid with different proportions of urea at 900°C [82]. The number of BN layers decreases with the increase in urea content in

the reaction mixture, allowing a control on the number of BN layers (Fig. 18). We believe that this is the first report of a bottom-up chemical synthesis of few-layer BN, enabling large-scale production. The surface area of the BN layers increases with the decrease in layer thickness as expected, the sample with lowest layer thickness exhibiting a surface area of 927 m^2/g and high CO_2 uptake. Few-layer BN can be functionalized and solubilized by employing Lewis bases. First-principles simulations show that it is energetically easy for few-layer BN to form stacking faults that involve slips and twists of adjacent planes resulting in inhomogeneity in the interplanar distances and deform through forming ripples. It has a smaller buckling strength and elastic stiffness than graphene. Long-range Coulomb interactions are found to be important to the stability of the different structures of BN. Our calculations demonstrate only weak interaction of hydrogen with BN sheets. Graphene analogues of BN may find several interesting applications. They can be used to form composites with polymers, with desirable applications.
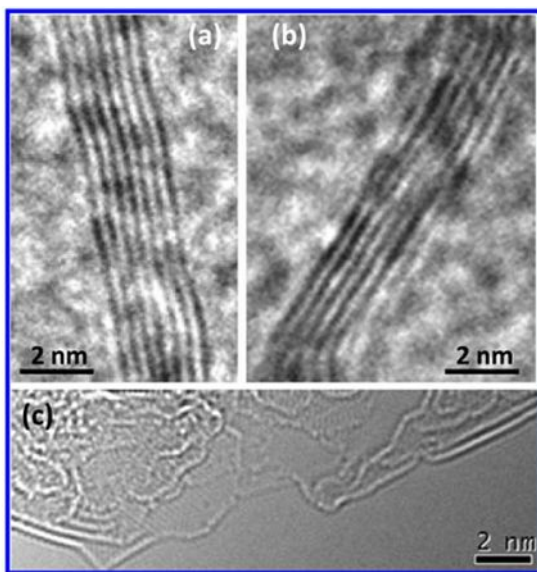
Fig. 18. TEM images of few-layer BN prepared with (a) 1:12, (b) 1:24, and (c) 1:48 boric acid/urea mixture (From reference 82).

References

1. Geim, A. K. and Novoselov, K. S. (2007). The rise of graphene, Nat. Mater, 6, pp. 183-191.
2. Li, D. and Kaner, R. B. (2008). Graphene-Based Materials, Science, 320, pp. 1170-1171.
3. Katsnelson, M. I. (2007). Graphene: carbon in two dimensions, Materials Today, 10, pp. 20-27.
4. Rao, C. N. R., Biswas, K., Subrahmanyam, K. S. and Govindaraj, A. (2009). Graphene, the new nanocarbon, J. Mater. Chem., 19, pp. 2457-2469.
5. Rao, C. N. R., Sood, A. K., Subrahmanyam, K. S. and Govindaraj, A. (2009). Graphene: The New Two-Dimensional Nanomaterial, Angew. Chem. Int. Ed, 48, pp. 7752-7777.
6. Rao, C. N. R., Sood, A. K., Voggu, R. and Subrahmanyam, K. S. (2010). Some Novel Attributes of Graphene, J. Phys. Chem. Lett., 1, 572-580.
7. Novoselov, K. S., Geim, A. K., Morozov, S. V., Jiang, D., Katsnelson, M. I., Grigorieva, I. V., Dubonos, S. V. and Firsov, A. A. (2005). Two-dimensional gas of massless Dirac fermions in graphene, Nature, 438, pp. 197-200.
8. Zhang, Y., Tan, J. W., Stormer, H. L. and Kim, P. (2005). Experimental observation of the quantum Hall effect and Berry's phase in graphene, Nature 438, pp. 201-204.
9. Novoselov, K. S., Jiang, Z., Zhang, Y., Morozov, S. V., Stormer, H. L., Zeitler, U., Maan, J. C., Boebinger, G. S., Kim, P. and Geim, A. K. (2007). Room-Temperature Quantum Hall Effect in Graphene, Science, 315, pp. 1379.
10. Novoselov, K. S., Geim, A. K., Morozov, S. V., Jiang, D., Zhang, Y., Dubonos, S. V., Grigorieva, I. V. and Firsov, A. A. (2004). Electric Field Effect in Atomically Thin Carbon Films, Science, 306, pp. 666-669.
11. Han, M. Y., Oezyilmaz, B., Zhang, Y. and Kim, P. (2007). Energy Band-Gap Engineering of Graphene Nanoribbons, Phys. Rev. Lett., 98, pp. 206805.
12. Lee, C., Wei, X., Kysar, J. W. and Hone, J. (2008). Measurement of the Elastic Properties and Intrinsic Strength of Monolayer Graphene, Science 321, pp. 385-388.
13. Park, S. and Ruoff, R. S. (2009). Chemical methods for the production of graphenes, Nature Nanotech., 4, pp. 217-224.
14. Novoselov, K. S., Jiang, D., Schedin, F., Booth, T. J., Khotkevich, V. V., Morozov, S. V. and Geim, A. K. (2005). Two-dimensional atomic crystals, Proc. Natl. Acad. Sci. USA, 102, pp. 10451-10453.
15. Blake, P., Hill, E. W., Neto, A. H. C., Novoselov, K. S., Jiang, D., Yang, R., Booth, T. J. and Geim, A. K. (2007). Making graphene visible Appl. Phys. Lett., 91, pp. 63124.
16. Roddaro, S., Pingue, P., Piazza, V., Pellegrini, V. and Beltram, F. (2007). The Optical Visibility of Graphene: Interference Colors of Ultrathin Graphite on SiO$_2$, Nano Lett., 7, pp. 2707-2710.

17. Stolyarova, E., Taeg, R. K., Ryu, S., Maultzsch, J., Kim, P., Brus, L. E., Heinz, T. F., Hybertsen, M. S., Flynn and G. W. (2007). High-resolution scanning tunneling microscopy imaging of mesoscopic graphene sheets on an insulating surface, Proc. Natl. Acad. Sci., USA, 104, pp. 9209-9212.

18. Meyer, J. C., Geim, A. K., Katsnelson, M. I., Novoselov, K. S., Booth, T. J. and Roth, S. (2007). The structure of suspended graphene sheets, Nature 446, pp. 60-63.

19. Meyer, J. C., Kisielowski, C., Erni, R., Rossell, M. D., Crommie, M. F. and Zettl, A. (2008). Direct Imaging of Lattice Atoms and Topological Defects in Graphene Membranes, Nano Lett., 8, pp. 3582-3586.

20. Gupta, A., Chen, G., Joshi, P., Tadigadapa, S. and Eklund, P. C. (2006). Raman Scattering from High-Frequency Phonons in Supported n-Graphene Layer Films, Nano Lett., 6, 2667-2673.

21. Ferrari, A. C. (2007). Raman spectroscopy of graphene and graphite: Disorder, electron–phonon coupling, doping and nonadiabatic effects, Solidstate Commun., 143, pp. 47-57.

22. Ferrari, A. C., Meyer, J. C., Scardaci, V., Casiraghi, C., Lazzeri, M., Mauri, F., Piscanec, S., Jiang, D., Novoselov, K. S., Roth, S. and Geim, A. K. (2006). Raman Spectrum of Graphene and Graphene Layers, Phys. Rev. Lett., 97, pp. 187401.

23. Pimenta, M. A., Dresselhaus, G., Dresselhaus, M. S., Cancado, L. A., Jorio, A. and Sato, R. (2007). Studying disorder in graphite-based systems by Raman spectroscopy, Phys. Chem. Chem. Phys., 9, pp. 1276-1290.

24. Graf, D., Molitor, F., Ensslin, K., Stampfer, C., Jungen, A., Hierold, C. and Wirtz, L. (2007). Spatially Resolved Raman Spectroscopy of Single- and Few-Layer Graphene, Nano Lett., 7, pp. 238-242.

25. Park, S., An, J., Jung, I., Piner, R. D, An, S. J., Li, X., Velamakanni, A. and Ruoff, R. S. (2009). Colloidal Suspensions of Highly Reduced Graphene Oxide in a Wide Variety of Organic Solvents, Nano Lett., 9, pp. 1593-1597.

26. Hummers, W. and Offeman, R. E. (1958). Preparation of Graphite oxide, J. Am. Chem. Soc. 80, pp. 1339.

27. Choucair, M., Thordarson, P. and Stride, J. A. (2009). Gram-scale production of graphene based on solvothermal synthesis and sonication, Nature Nanotech., 4, pp. 30-33.

28. Hernandez, Y., Nicolosi, V., Lotya, M., Blighe, F. M., Sun, Z., De. S., Mcgovern, I. T., Holland, B., Byrne, M., Gun'ko, Y. K., Boland, J. J., Niraj, P., Duesberg, G., Krishnamurthy, S., Goodhue, R., Hutchison, J., Scardaci, V., Ferrari, A. C. and Coleman, J. N. (2008). High-yield production of graphene by liquid-phase exfoliation of graphite, Nat. Nanotech., 3, pp. 563-568.

29. Lotya, M., Hernandez, Y., King, P. J., Smith, R. J., Nicolosi, V., Karlsson, L. S., Blighe, F. M., De, S., Wang, Z., McGovern, I. T., Duesberg, G. S. and Coleman, J. N. (2009). Liquid Phase Production of Graphene by Exfoliation of Graphite in Surfactant/Water Solutions J. Am. Chem. Soc., 131, 3611-3620.

30. Berger, C., Song, Z., Li, T., Li, X., Ogbazghi, A. Y., Feng, R., Dai, Z., Marchenkov, A. N., Conrad, E. H., First, P. N. and de Heer, W. A. (2004). Ultrathin Epitaxial Graphite: 2D Electron Gas Properties and a Route toward Graphene-based Nanoelectronics, J. Phys. Chem. B, 108 (2004) 19912-19916.

31. Rollings, E., Gweon, G.-H., Zhou, S. Y., Mun, B. S., McChesney, J. L., Hussain, B. S., Fedorov, A. V., First, P. N., de Heer, W.A. and Lanzara, A. (2006). Synthesis and characterization of atomically thin graphite films on a silicon carbide substrate, J. Phys. Chem. Solids, 67, 2172.

32. Emtsev, K. V., Bostwick, A., Horn, K., Jobst, J., Kellogg, G. L., Ley, L., McChesney, J. L., Ohta, T., Reshanov, S. A., Rohrl, J., Rotenberg, E., Schmid, A. K., Waldmann, D., Weber, H. B. and Seyller, T. (2009). Towards wafer-size graphene layers by atmospheric pressure graphitization of silicon carbide, Nature Mater., 8, 203-207.

33. Reina, A., Jia, X., Ho, J., Nezich, D., Son, H., Bulovic, V., Dresselhaus, M. S. and Kong, J. (2009). Large Area, Few-Layer Graphene Films on Arbitrary Substrates by Chemical Vapor Deposition, Nano Lett., 9, 30-35.

34. Schniepp, H. C., Li, J. L., McAllister, M. J., Sai, H., Herrera-Alonso, M., Adamson, D. H., Prud'homme, R. K., Car, R., Saville, D. A. and Aksay, I. A. (2006). Functionalized Single Graphene Sheets Derived from Splitting Graphite Oxide, J. Phys. Chem. B, 110, 8535-8539.

35. Subrahmanyam, K. S., Vivekchand, S. R. C., Govindaraj, A. and Rao, C. N. R. (2008). A study of graphenes prepared by different methods: characterization, properties and solubilization, J. Mater. Chem. 18, 1517-1523.

36. Stankovich, S., Dikin, D. A., Piner, R. D., Kohlhaas, K. A., Kleinhammes, A., Jia, Y., Wu, Y., Nguyen, S. T. and Ruoff, R. S. (2007). Synthesis of graphene-based nanosheets via chemical reduction of exfoliated graphite oxide Carbon, 45 pp. 1558.

37. Andersson, O. E., Prasad, B. L. V., Sato, H., Enoki, T., Hishiyama, Y., Kaburagi, Y., Yoshikawa, M. and Bandow, S. (1998). Structure and electronic properties of graphite nanoparticles, Phys. Rev. B, 58, pp. 16387-16395.

38. Prasad, B. L. V., Sato, H., Enoki, T., Hishiyama, Y., Kaburagi, Y., Rao, A. M., Eklund, P. C., Oshida, K. and Endo, M. (2000). Heat-treatment effect on the nanosized graphite π-electron system during diamond to graphite conversion, Phys. Rev. B, 62, pp. 11209-11218.

39. Subrahmanyam, K. S., Panchakarla, L. S., Govindaraj, A., Rao, C. N. R. (2009). Simple Method of Preparing Graphene Flakes by an Arc-Discharge Method, J. Phys. Chem. C, 113, pp. 4257-4259.

40. Seshadri, R., Govindaraj, A., Aiyer, H. N., Sen, R., Subbanna, G. N., Raju, A. R., and Rao, C. N. R. (1994). Investigations of carbon nanotubes, Curr. Sci., 66, pp. 839-847.

41. Panchakarla, L. S., Subrahmanyam, K. S., Saha, S. K., Govindaraj, A., Krishnamurthy, H. R., Waghmare, U. V., Rao, C. N. R. (2009). Synthesis, Structure, and Properties of Boron- and Nitrogen-Doped Graphene, Adv. Mater., 21, pp. 4726.

42. Rao, C. N. R. and Govindaraj, A., *Nanotubes and Nanowires, RSC series on Nanoscience*, Royal Society of Chemistry, London, 2006.

43. *Nanomaterials Chemistry: Recent Devolopments*, eds. C. N. R. Rao, A. K. Cheetham, A. Muller, Wiley-VCH, Weinheim, 2007.

44. Niyogi, S., Bekyarova, E., Itkis, M. I., McWilliams, J. L., Hamon, M. A. and Haddon, R. C. (2006). Solution Properties of Graphite and Graphene, J. Am. Chem. Soc., 128, pp. 7720-7721.

45. Bekyarova, E., Itkis, M. E., Ramesh, P., Berger, C., Sprinkle, M., de Heer, W. A. and Haddon, R. C. (2009). Chemical Modification of Epitaxial Graphene: Spontaneous Grafting of Aryl Groups, J. Am. Chem. Soc., 131, pp. 1336-1337.

46. Worsley, K. A., Ramesh, P., Mandal, S. K., Niyogi, S., Itkis, M. E. and Haddon, R. C. (2007). Soluble graphene derived from graphite fluoride, Chem. Phys. Lett., 445, pp. 51-56.

47. Subrahmanyam, K. S., Ghosh, A., Gomathi, A., Govindaraj, A. and Rao, C. N. R. (2009). Covalent and Noncovalent Functionalization and Solubilization of Graphene Nanosci., Nanotechnol. Lett., 1, pp. 28.

48. Ghosh, A., Rao, K. V., George, S. J. and Rao, C. N. R. (2010). Non-Covalent Functionalization, Exfoliation and Solubilization of Graphene in Water Employing a Fluorescent Coronene Carboxylate., Chem. Eur. J., 16, 2700.

49. Peigney, A., Laurent, Ch., Flahaut, E., Bacsa, R. R., Rousset, A. (2001). Specific surface area of carbon nanotubes and bundles of carbon nanotubes, Carbon, 39, pp. 507.

50. Ghosh, A., Subrahmanyam, K. S., Krishna, K. S., Datta, S., Govindaraj, A., Pati, S. K. and Rao, C. N. R. (2008). Uptake of H_2 and CO_2 by Graphene, J. Phys. Chem. C, 112, pp. 15704-15707.

51. Das, A., Pisana, S., Chakraborty, B., Piscanec, S., Saha, S. K., Waghmare, U. V., Novoselov, K. S., Krishnamurthy, H. R., Geim, A. K., Ferrari, A. C. and Sood, A. K. (2008). Monitoring dopants by Raman scattering in an electrochemically top-gated graphene transistor, Nature Nanotech., 3, pp. 210.

52. Voggu, R., Das, B., Rout, C. S. and Rao, C. N. R., J. Phys.: Condens. Matter, (2008). Effects of charge transfer interaction of graphene with electron donor and acceptor molecules examined using Raman spectroscopy and cognate techniques, 20 pp. 472204.

53. Subrahmanyam, K. S., Voggu, R., Govindaraj, A. and Rao, C. N. R. (2009). A comparative Raman study of the interaction of electron donor and acceptor molecules with graphene prepared by different methods, Chem. Phys. Lett., 472, pp. 96-98.

54. Saito, R., Jorio, A., SouzaFilho, A. G., Dresselhaus, G., Dresselhaus, M. S. and Pimenta, M. A. (2002). Phys. Rev. Lett., 88, pp. 02740.

55. Varghese, N., Ghosh, A., Voggu, R., Ghosh, S. and Rao, C. N. R. (2009). Selectivity in the interaction of electron donor and acceptor molecules with graphene and singled wall carbon nanotubes, J. Phys. Chem. Lett., 113, pp. 16855-16859.

56. Lu, C-H., Yang, H-H., Zhu, C-L., Chen, X. and Chen, G-N. (2009). A platform for sensing biomolecules, Angew. Chem. Int. Ed., 48, pp. 4785-4787.

57. Treossi, E., Melucci, M., Liscio, A., Gazzano, M., Samori, P. and Palermo, V. (2009). High-Contrast Visualization of Graphene Oxide on Dye-Sensitized Glass, Quartz, and Silicon by Fluorescence Quenching, J. Am. Chem. Soc., 131, pp. 15576-15577.

58. Xie, L., Ling, X., Fang, Y., Zhang, J. and Liu, Z. (2009). Graphene as a Substrate To Suppress Fluorescence in Resonance Raman Spectroscopy, J. Am. Chem. Soc., 131, pp. 9980-9981.

59. (a) Xu, Y., Liu, Z., Zhang, X., Wang, Y., Tian, J., Huang, Y., Ma, Y., Zhang, X. and Chen, Y. (2009). A Graphene Hybrid Material Covalently Functionalized with Porphyrin: Synthesis and Optical Limiting Property, Adv. Mater., 21, pp. 1275-1279. (b) Xu, Y., Zhao, L., Hong, W., Li, C. and Shi, G. (2009). J. Am. Chem. Soc., 131, pp. 13490.

60. Englert, J. M., Rohrl, J., Schmidt, C. D., Graupner, R., Hundhausen, M., Hauke, F. and Hirsch, A. (2009). Soluble Graphene: Generation of Aqueous Graphene Solutions Aided by a Perylenebisimide-Based Bolaamphiphile, Adv. Mater., 21, pp. 4265-4269.

61. Shafirovicl, V. Ya., Levin, P. P., Kuzmin, V. A., Thorgeirsson, T. E., Kliger, D. S. and Geacintov, N. E. (1994). Photoinduced Electron Transfer and Enhanced Triplet Yields in Benzo pyrene Derivative-Nucleic Acid Complexes and Covalent Adducts, J. Am. Chem. Soc., 116, pp. 63-72.

62. Alvaro, M., Atienzar, P., Bourdelande, J. L. and Garcıa, H. (2004). An organically modified single wall carbon nanotube containing a pyrene chromophore: fluorescence and diffuse reflectance laser flash photolysis study, Chem. Phys. Lett., 384, pp. 119-123.

63. Matte, H. S. S. R., Subrahmanyam, K. S., Rao, K. V., Georje, S. J. and Rao, C. N. R. (2010). Quenching of fluorescence of aromatics by graphene, Submitted.

64. Enoki, T. and Kobayashi, Y. (2005). Magnetic nanographite: an approach to molecular magnetism, J. Mater. Chem., 15, pp. 3999-4002.

65. Matte, H. S. S. R., Subrahmanyam, K. S. and Rao, C. N. R. (2009). Novel Magnetic Properties of Graphene: Presence of Both Ferromagnetic and Antiferromagnetic Features and Other Aspects, J. Phys. Chem. C, 113, pp. 9982-9985.

66. Wang, Y., Huang, Y., Song, Y., Zhang, X., Ma, Y., Liang, J. and Chen, Y. (2009). Room-Temperature Ferromagnetism of Graphene, Nano Lett., 9, pp. 220-224.

67. Kroto, H. W., Heath, J. R., Brien, S. C. O., Curl, R. F. and Smalley, R. E. (1985). C_{60}: Buckminsterfullerene, Nature, 318, pp. 162-163.

68. Tenne, R., Margulis, L., Genut, M. and Hodes, G. (1992). Polyhedral and cylindrical structures of tungsten Disulphide, Nature, 360, pp. 444-446.

69. Margulis, L., Salitra, G., Tenne, R. and Talianker, M. (1993). Nested fullerene-like structures, Nature, 365, pp. 113-114.

70. Rosentsveig, R., Margolin, A., Gorodnev, A., Biro, R. P., Rapaport, L., Novema, Y., Naveh, G. and Tenne, R. (2009). Synthesis of fullerene-like MoS_2 nanoparticles and their tribological behaviour, J. Mater. Chem., 19, pp. 4368-4374.

71. Iijima, S. (1991). Helical microtubules of graphitic carbon, Nature, 354, pp. 56-58.

72. Rothschild, A., Sloan, J. and Tenne, R. (2000). Growth of WS_2 Nanotubes Phases, J. Am. Chem. Soc., 122, pp. 5169-5179.

73. Nath, M. and Rao, C. N. R. (2003). Inorganic nanotubes, Dalton Trans., pp. 1-24.

74. Tenne, R. and Rao, C. N. R. (2004). Inorganic nanotubes, Phil. Trans. R. Soc. Lond. A., 362, pp. 2099-2125.

75. Rao, C. N. R. and Govindaraj, A. (2009). Synthesis of Inorganic Nanotubes, Adv. Mater. 21, pp. 4208-4233.

76. Novoselov, K. S., Jiang, D., Schedin, F., Booth, T. J., Khotkevich, V. V., Morozov, S. V. and Geim, A. K. (2005). Two-dimensional atomic crystals, Proc. Natl. Acad. Sci. USA, 102, pp. 10451-10453.

77. Joensen, P., Frindt, R. F. and Morrison, S. R. (1986). Single-Layer MoS_2, Mater. Res. Bull., 21, pp. 457-461.

78. Miremadi, B. K. and Morrison, S. R. (1988). The intercalation and exfoliation of tungsten disulfide, J. Appl. Phys., 63, pp. 4970-4974.

79. Yang, D. and Frindt, R. F. (1996). Li-intercalation and exfoliation of WS_2, J. Phys. Chem. Solids, 57, pp. 1113-1116.

80. Tian, Y., He, Y. and Zhu, Y. (2004). Low temperature synthesis and characterization of molybdeniumdisulfide nanotubes and nanorods, Mater. Chem. Phys, 87, pp. 87-90.

81. Matte, H. S. S. R., Gomathi, A., Manna, A. K., Late, D. J., Datta, R., Pati, S. K. and Rao, C. N. R. (2010). MoS_2 and WS_2 analogues of Graphene, Angew. Chem. Int. Ed, 49, 4059-4062.

82. Nag, A., Raidongia, K., Hembram, K. P. S. S., Datta, R., Waghmare, U. V. and Rao, C. N. R. (2010). Graphene Analogues of BN: Novel Synthesis and Properties, ACS Nano, 4, 1539-1544.

Chapter 2

Synthesis and Characterization of Exfoliated Graphene- and Graphene Oxide-Based Composites

K. R. Rasmi, K. Chakrapani and S. Sampath*

Department of Inorganic and Physical Chemistry, Indian Institute of Science, Bangalore-560012, India
*sampath@ipc.iisc.ernet.in

Graphene- and graphene oxide-based composites have attracted significant research interest in recent years, owing to their important applications in various technological fields. In the present study, we report the synthesis and characterization of graphene-bimetallic alloy composite and its use in sensing of a neurotransmitter, dopamine. The preparation and characterization of graphene oxide with metal oxides such as RuO_x and Co_3O_4 are also presented.

1. Introduction

Graphene, one atom thick with two dimensional honeycomb sp^2 network has attracted enormous attention in recent years owing to its large specific surface area and unique electrical, mechanical and thermal properties.[1-5] It exhibits excellent physical and chemical properties, which makes it promising for variety of applications in the areas such as solar-cells,[6] energy storage,[7] field effect transistors,[8] catalyst support,[9] sensors,[10] and nanocomposites.[11] The production of graphene by chemical reduction of graphene-oxide (GO) in solution[12-14] has been achieved using a variety of reducing agents. The presence of abundant functional groups on the surface of GO makes it possible to be used as anchoring sites for nanocomposites with polymers[15-16] and polar molecules.[17-19] The dispersion of metal and metal oxide nanoparticles on graphene sheets provides a new way to develop potentially interesting materials with novel catalytic, energy storage and optoelectronic properties.

Carbon nanomaterials such as carbon nanotubes and graphite nanoplatelets have been explored as supporting materials for immobilizing and stabilizing metal and metal oxide nanoparticles.[20-23] Hybrid structures of graphene with metal and metal oxide nanoparticles have been developed.[24-26] Efforts have also been made to synthesize silver nanoparticles by protecting with GO and assembled as thin films using layer by layer self assembly technique.[27] In this section, we report the synthesis of bimetal (Au-Ag alloy) and metal oxide (Co_3O_4, RuO_2) nanoparticles supported on chemically modified graphene sheets.

2. Experimental Section

2.1. *Materials*

Graphite flakes were obtained from Stratmin graphite co., USA. Cobaltous chloride was from Qualigens fine chemicals and Ruthenium chloride was purchased from Arora Matthey ltd, India. Silver nitrate and auric chloride were bought from Aldrich, USA.

2.2. *Synthesis of exfoliated graphene oxide*

Graphene oxide was synthesized from exfoliated graphite using modified Hummers method as reported earlier[28] from our group. Briefly, the process involved the treatment of cleaned graphite flakes of certain size (~300 µm) with sulphuric acid/nitric acid mixture to obtain intercalated graphite. The intercalated graphite was given a thermal shock at 800°C for about a minute that resulted in the exfoliation of graphite. The low density exfoliated graphite was further oxidized using $KMnO_4$ and H_2O_2 to obtain brown coloured exfoliated graphene oxide (EGO) powder.

2.3. *Synthesis of EGO- Au-Ag alloy composites*

The alloy nanoparticle – EGO composites were prepared by chemical reduction of $AuCl_3$ and $AgNO_3$ using $NaBH_4$ as reducing agent in presence of EGO. In a typical procedure, EGO (22.0 mg) was dispersed in water by ultrasonication and the pH of the colloid was adjusted to 10

using NaOH. To the above solution, 2.0 mL each of 10.0 mM $AuCl_3$ and $AgNO_3$ solutions (depending on the alloy composition) were added and stirred for 20 minutes at 25°C. Subsequently, 4.0 mL of ice cold $NaBH_4$ (50 mM) was added and vigorously stirred for 1 hour. Instantaneous colour change from dark brown to black was observed. The black colour is due to the reduction of EGO to reduced EGO. The as-synthesized nanocomposite was washed with ethanol to remove any by-product and the material thus obtained was dried and used for subsequent characterization. Au-Ag alloy nanocomposites with different molar ratios such as 0.6:0.4, 1:2, 1:3, 1:4, 1:5, 1:6, 1:7, 1:8 and 1:9 were prepared by similar procedure. Monometallic graphene-Au nanocomposite and graphene-Ag nanocomposite were also prepared using a similar protocol for comparative purposes.

2.3. *Synthesis of GO-Co₃O₄ composite*

500.0 mg of $Co(NO_3)_2$ was dissolved in 40.0 mL of hexanol which formed a red colour solution. To this, 100 mg of EGO was added and dispersed by ultrasonication for 3 hours. The solution was then refluxed at 120°C for about 10 hours.[29] After cooling down to room temperature, the as-synthesized product was washed with ethanol repeatedly to remove any by-product and dried.

2.4. *Synthesis of EGO-RuOx composite*

The preparation of EGO and ruthenium oxide composite was based on the method proposed for the preparation of sol-gel derived $RuO_x.xH_2O$.[30] 500 mg of EGO was suspended in a mixture of 1:1 (by volume) methanol: water (100 mL) containing 60 mg of $RuCl_3$. The mixture was stirred for 2 hours and the pH of the solution was adjusted to 7 by using 1 M NaOH. During the process ruthenium hydroxide particles precipitated out and got dispersed on EGO. It was centrifuged and washed several times with distilled water to remove NaCl completely. The material was subsequently dried in vacuum at room temperature and subsequently at 300°C for 2 hours.

2.5. *Materials characterization*

The crystallographic information of as-synthesized materials was investigated using powder X-ray diffraction technique (PAN analytical X-ray BV diffractometer, Cu Kα radiation λ = 1.506 Å at a scan rate of 2° per minute). Scanning electron microscopy (ESEM, Quanta) was employed to examine the morphology of the nanocomposites. Electrochemical studies were carried out using a potentiostat (CH Instruments, USA, Model CH 660A) in aqueous phosphate buffer with saturated calomel reference electrode (SCE) and a large area Pt foil counter electrode.

3. Results and Discussion

Bimetallic and alloy surfaces, both in the planar and nanoparticulate form, attract wide interest because of their distinctive properties that distinguish them from their monometallic counter parts. Alloys containing Au as one of their components are particularly interesting, since Au, which is a very inert metal behaves quite differently when it is in conjunction with another metal. The structure of Au-Ag bimetallic nanoparticle has generated a lot of interest since both Au and Ag have very similar lattice constants and are completely miscible over entire composition range, forming homogeneous alloys in bulk phase. Graphene and Au-Ag alloy composites are expected to possess properties of both the components (graphene as well as alloy counterparts) and hence these hybrid materials may have good features for (electro)catalysis.

The absorption spectra (not shown) of graphene – Au-Ag alloys of different compositions reveal only one surface plasmon band corresponding to the particular alloy composition. The change in position of the λ_{max} depends on the composition and falls in between the surface plasmon band positions of gold and silver. The reduced graphene oxide shows an absorption band near 266 nm. However, a physical mixture of individual colloids shows two surface plasmon bands corresponding to the monometallic counter parts. Powder X-ray diffractommograms (Fig. 1) of graphene-Au-Ag alloy nanocomposites show a peak around

38° (2θ) that corresponds to the {111} plane while another peak observed near 44° (2θ) corresponds to the {200} crystallographic plane. Two other peaks observed near 64° and 77° (2θ) correspond to the {220} and {311} planes. A slight shift is observed for the alloy phase. The SEM and the EDX spectrum of the graphene-metal nanocomposites (Figs. 2 and 3) reveal that metal alloy nanoparticles are spread fairly uniformly on the surface of graphene. Elemental mapping and spot EDAX confirm the formation of alloy phase. The particles are finely dispersed and the average particle size is of few tens of nm.
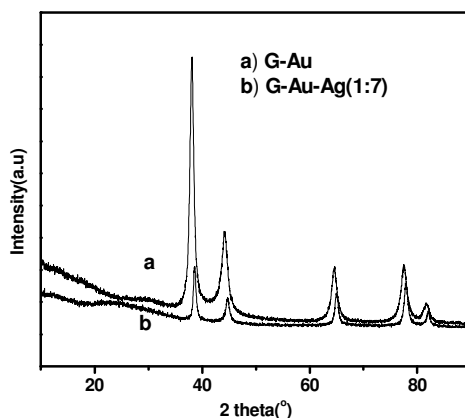
Fig. 1. XRD patterns of graphene-Au (a) and graphene- Au-Ag alloy (b) (1:7 molar ratio) nanocomposites.
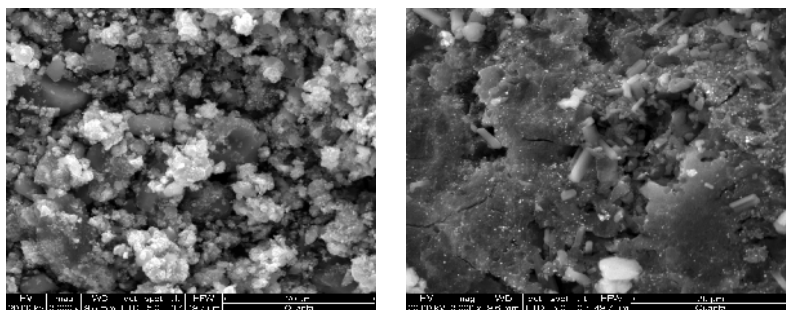
Fig. 2. SEM images of graphene-Au (left) and graphene-Ag (right) nanocomposites. The scale bars correspond to 20 µm.
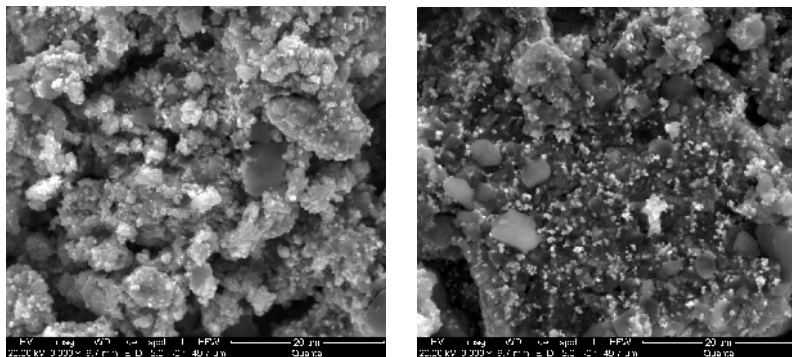
Fig. 3. SEM images of graphene-Au-Ag alloy nanocomposites with compositions 1:1 (left), 1:8 (right) respectively. The scale bars correspond to 20 µm.

3.1. *Electrochemical detection of dopamine using graphene-alloy nanocomposites*

The need to detect neurotransmitters such as dopamine and ascorbic acid is over emphasized in the literature. However, preparation of an electrode that requires minimum surface treatment with good response is still a challenge. The response of dopamine (DA) on bare glassy carbon electrode (GCE) and on graphene-Au-Ag alloy composite modified GCE is followed by cyclic voltammetry. The composite colloid is drop coated (50 µL) on the surface of GCE (0.2 cm^2 area) and the solvent is subsequently evaporated to result in a stable alloy colloidal film on the surface. Typical cyclic voltammograms of DA are recorded in phosphate buffer, pH = 7.0 (Fig. 4). It is clear that well-defined and resolved voltammetric peak is observed for DA oxidation on alloy composite modified electrode in comparison to bare GCE. DA shows an irreversible redox reaction on bare GCE while well-defined, sharp redox pair with obviously increased current response is obtained for DA on the alloy composite modified GCE. For example, the negatively shifted anodic peak potential (Epa = 184 mV) and the positively shifted cathodic peak potential (Epc = 97 mV) results in small ΔE_p value (67 mV) for a concentration of 1 mM DA in the buffer. The negative shifts of the oxidation potentials together with the formation of well-defined redox peaks clearly indicate the favorable electrocatalysis for the oxidation of

DA on the alloy-based composite modified electrode. DA is also found to adsorb strongly on the electrode surface. Oxidized form of DA is known to give a cyclized product by a follow-up chemical reaction. The cyclization is reported to occur through the nitrogen of the amino group to the ring. This product is also electrochemically active and the redox peaks are observed around -0.311 V in the present study. The pKa of DA is 8.87 and at pH 7, DA would mostly exist in the unionized form. Hence, cyclization is favored at neutral pH while acidic conditions do not favor cyclization due to charge associated with the amino group. The cyclized product is also found to adsorb on the electrode surface. This is confirmed by checking the used electrodes in fresh buffer after performing DA oxidation. The first cycle from -0.40 V does not show any peak for the cyclized product at -0.10 V since the chemical reaction takes place only after the electrochemical oxidation of DA. Hence, from II cycles onwards, the cyclized product is observed as a reversible redox couple.
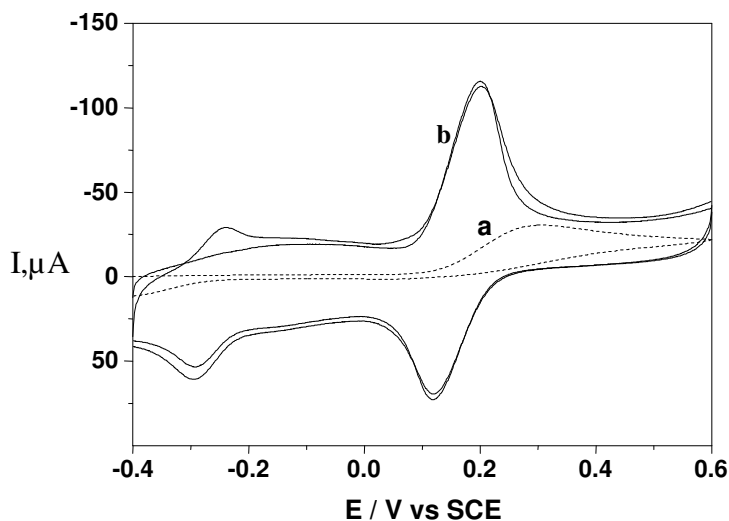
Fig. 4. Cyclic voltammograms of (a) bare GCE and (b) GCE modified with graphene-Au-Ag nanocomposite for the detection of DA (1 mM) in phosphate buffer of pH 7. Reference electrode used is SCE and counter electrode used is Pt foil. Scan rate used is 5 mV/sec.

3.2. *Composites of exfoliated graphene oxide- and Co₃O₄ or RuOₓ*

The XRD pattern of EGO-Co$_3$O$_4$ is shown in Fig. 5. The diffraction peaks of as-synthesized composites belong to characteristic peaks of Co$_3$O$_4$, which are close to the reported values (JCPDS file no.43-1003) with lattice constant of a = 8.083 Å. The broad peaks of Co$_3$O$_4$ in the X-ray pattern indicate that the nanoparticles are small and the average size is about 15 nm as determined using Scherrer equation. Figure 6 shows the SEM images of EGO-Co$_3$O$_4$ and it is observed that the surface of EGO is randomly decorated with Co$_3$O$_4$. The XRD pattern of EGO-RuO$_x$ composite shows an amorphous ruthenium oxide phase for the as-prepared material. Annealing the composite at 300°C makes the material crystalline typical of rutile type structure of RuO$_2$ (Fig. 7).
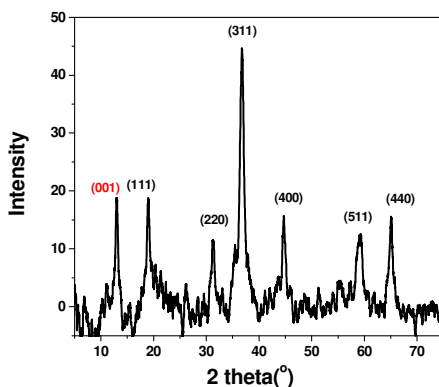
Fig. 5. XRD pattern of EGO-Co$_3$O$_4$ composite.
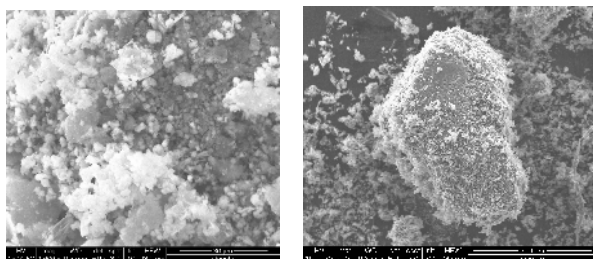
Fig. 6. SEM images of EGO-Co$_3$O$_4$ composite. The scale bars correspond to 30 µm (left) and 300 µm (right).

The SEM images of EGO-RuO$_2$ (Fig. 8) composite reveal that the ruthenium oxide particles are well distributed on the surface of EGO.
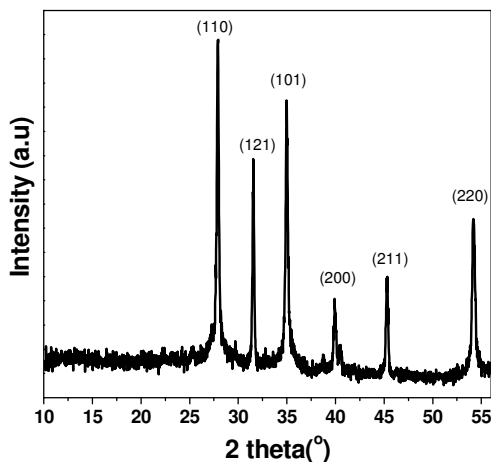
Fig. 7. XRD pattern of EGO-RuO$_2$ composite annealed at 300°C.
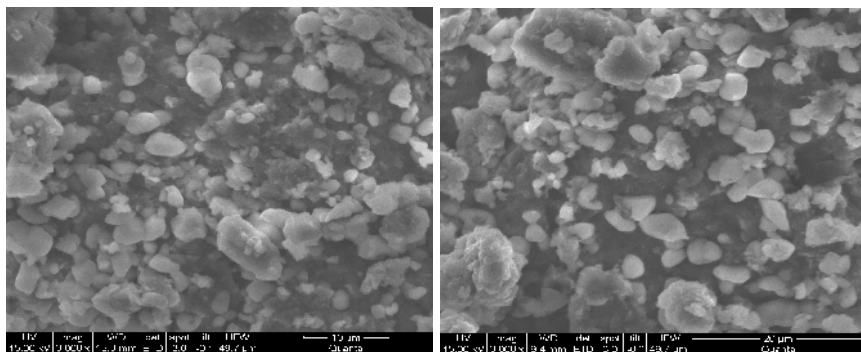
Fig. 8. SEM images of EGO-RuO$_2$ composite. The scale bars correspond to 10 µm (left) and 20 µm (right).

4. Summary

Exfoliated graphene oxide and its reduced form are amenable for composite formation. The alloy-based composite shows good

electrocatalytic properties and will be very useful for the development of electrochemical sensors. The metal oxide - based composites with EGO may be good candidates for electrochemical capacitors since the combination of EGO functional groups with the metal oxide pseuodoredox properties are expected to yield high capacitance.

Acknowledgments

References

1. A.K. Geim, *Science* **324**, 1530 (2009).
2. C.N.R. Rao, A.K. Sood, K.S. Subrahmanyam, A. Govindaraj, *Angew. Chem. Int. Ed.* **48**, 7752 (2009).
3. A.K. Geim, K.S. Novoselov, *Nat. Mater.* **6**, 183 (2007).
4. M. Segal, *Nat. Nanotechnol.* **4**, 612 (2009).
5. K.S. Novoselov, A.K. Geim, S.V. Morozov, D. Jiang, S.V. Dubonos, I.V. Grigorevia, A.A. Firsov, *Science* **306**, 666 (2004).
6. X. Wang, L. Zhi, K. Mullen, *Nano. Lett.* **8**, 3498 (2008).
7. M.D. Stoller, S. Park, Y. Zhu, J. An, R.S. Ruoff, *Nano. Lett.* **8**, 323 (2008).
8. L.A. Ponomarenko, F. Schedin, M.I. Katnelson, R. Yang, E.W. Hill, K.S. Novoselov, A.K. Geim, *Science* **320**, 356 (2008).
9. Y. Si, E.T. Samulski, *Chem. Mater.* **20**, 6792 (2008).
10. F. Schedin, A.K. Geim, S.V. Morozov, E.W. Hill, P. Blake, M.I. Katnelson, K.S. Novoselov, *Nat. Mater.* **6**, 652 (2007).
11. S. Stankovich, D.A. Dikin, H.B. Geoffrey Dommett, K.M. Kohlhaas, E.J. Zimney, E.A. Stach, R.D. Piner, S.T. Nguyen, R.S. Ruoff, *Nature* **442**, 282 (2006).
12. S. Stankovich, D.A. Dikin, R.D. Piner, K.M. Kohlhaas, Y. Jia, Y. Wu, A. Kleinhammes, R.S. Ruoff, *Carbon* **45**, 1558 (2007).
13. D. Li, M.B. Muller, S. Gilje, R.B. Kaner, G.G. Wallace, *Nat. Nanotechol.* **3**, 101 (2008).
14. Y. Si, E.T. Samulski, *Nano.Lett.* **8**, 1679 (2008).
15. R. Bissessur, P.K. Liu, W. White, S.F. Scully, *Langmuir* **22**, 1729 (2006).
16. G.C. Wang, Z.Y. Yang, X.W. Li, C.Z. Li, *Carbon* **43**, 2564 (2005).
17. D. Cai, M. Song, *J. Mater. Chem.* **17**, 3678 (2007).

18. M. Herrera-Alonso, A.A. Abdala, M.J. McAllister, I.A. Aksay, R.K. Proudhomme, *Langmuir* **23**, 10644 (2007).
19. Z. Liu, Z.M. Wang, X. Wang, K. Ooi, *Langmuir* **18**, 4926 (2002).
20. J. Lu, I. Do, L.T. Drzal, R.M. Worden, I. Lee, *ACSNano* **2**, 1825 (2008).
21. K.A. Mahmoud, S. Hrapovic, J.H.T. Luong, *ACSNano* **2**, 1051 (2008).
22. L. Jiang, L. Gao, *Carbon* **41**, 2923 (2003).
23. W. Chen, Y. Tang, J. Bao, Y. Gao, C. Liu, W. Xing, T. Lu, *J. Power Sources* **167**, 315 (2007).
24. Y. Si, E.T. Samulski, *Chem. Mater.* **20**, 6792 (2008).
25. R. Muszynski, B. Seger, P.V. Kamat, *J. Phy. Chem C* **112**, 5263 (2008).
26. A. Mastalir, Z. Kiraly, A. Patzko, I. Dekany, P. L'Argentiere, *Carbon* **46**, 1631 (2008).
27. T. Cassagneau, J.H. Fendler, *J. Phy. Chem. B* **103**, 1789 (1999).
28. P. Ramesh, S. Sampath, *J. Colloid Interface. Sci*. **274**, 95 (2004).
29. C. Xiu, X. Wang, J. Zhu, X. Yang, L. Lu, *J. Mater. Chem.* **18**, 5625 (2008).
30. J.P. Zheng, T.R. Jow, *J. Electrochem. Soc* **142**, L6 (1995).

Chapter 3

Singlet Open-Shell Character of Polyperiacenes

Akihiro Shimizu, Akihito Konishi, Yasukazu Hirao* and Takashi Kubo[†]

Department of Chemistry, Graduate School of Science, Osaka University, Machikaneyama 1-1, Toyonaka, Osaka 560-0043, Japan
**y-hirao@chem.sci.osaka-u.ac.jp;* [†]*kubo@chem.sci.osaka-u.ac.jp*

Singlet open-shell character of polyperiacenes has been elucidated by theoretical analysis based on the Clar's aromatic sextet valence bond model and quantum chemical calculations. Anti-ferromagnetic ground state of large polyperiacenes was relevant to the sufficient stabilization energy derived from aromatic sextet formation to overcome the energetic penalty associated with π-bond cleavages. Experimental study on the smallest potential biradicaloid, 2,5,9,12-tetra-*tert*-butylbisanthene **1**, demonstrated no appreciable biradical character in physical measurements, whereas **1** showed biradicaloid behavior toward oxygen.

1. Introduction

Graphene, which is a two dimensional sheet consisting of fused six membered rings of carbon atoms, has zigzag and armchair edges. STM/STS measurements have revealed the edge-localized electrons at the zigzag edge,[1] where a large magnetic moment is suggested by the tight binding band calculations.[2] Magnetic and related electronic properties originating the edge spins are extensively studied theoretically and experimentally for realization of carbon-based nanoelectronics.[3] In this context, nanographenes as small components of the graphene sheet have attracted considerable attention recently from synthetic[4] and theoretical points of view,[5] and the theoretical studies using symmetry-broken DFT calculations on nanographene molecules with zigzag edges figure out anti-parallel spin orientation between the two edges in the

ground state instead of the non-magnetic (that is, closed-shell singlet) ground state predicted simply from their Kekulé structures.[5c,e,i,l] Although the anti-ferromagnetic (that is, open-shell singlet) ground state would be derived from degeneracy of π and π^* bands at the Fermi level,[2] easy-understandable guidance for structure–property relationship is required to simply predict the electronic structures of zigzag-edged nanographenes including polyperiacenes as well as polyacenes. In this chapter, we present theoretical consideration on polyperiacenes based on Clar sextet valence bond model in combination with natural population and NICS analyses using DFT calculations, and demonstrate that the anti-ferromagnetic ground state in polyperiacenes **a-b** is closely related to formation of the Clar sextets,[6a,b] that is, aromatic stabilization. Additionally, we describe preparation of the smallest polyperiacenes, a derivative of bisanthene **3-3**, and experimental elucidation of its singlet open-shell character.
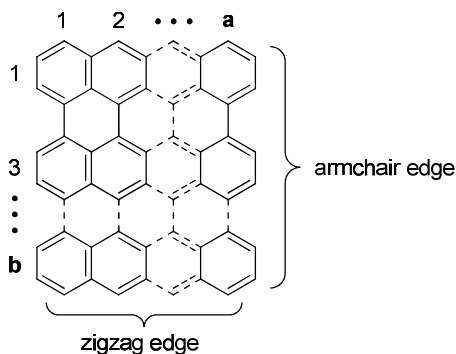
Fig. 1. Structure of polyperiacenes **a**-**b**.

2. Theoretical Consideration on Open-Shell Character

2.1. *Clar's aromatic sextet valence bond model*

Open-shell character in seemingly intrinsic closed-shell (Kekulé) molecules would originate from some kind of extra stabilizations to compensate the destabilization by π-bond cleavage. In order to consider

the relation between the magnetic state and the stabilization balance, we focus on anthracene **3-1** and phenanthrene, which are minimal units of zigzag- and armchair-edged nanographenes, respectively. Important extra stabilization energy expected in aromatic hydrocarbons is aromatization energy derived from $(4n + 2)$ π cyclic conjugation. One can see two unpaired electrons on the 9,10-positions in anthracene after pairing electrons in the π-dot structure of anthracene so as to ensure the maximal number of the Clar sextet (Fig. 2(a)).[6c] These two unpaired electrons are located at positions separated each other, and pairing of the two electrons requires destruction of one sextet (Figs. 2(a)→2(b)). On the other hand, phenanthrene has two sextets and two unpaired electrons which are located at the neighboring 9,10-positions (Fig. 2(a')). These two electrons can participate in a π-bond formation with no destruction of the sextets (Figs. 2(a')→2(b')). Thus, in the Kekulé structures, anthracene is on a balance between stabilization and destabilization, whereas phenanthrene contains no unfavorable destabilization. The stabilization balance in anthracene might lead to its high reactivity at the 9,10-positions.[7]
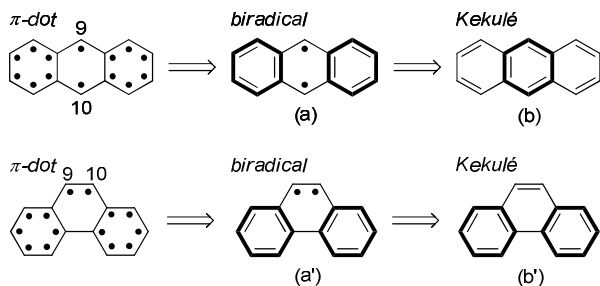
Fig. 2. Electron pairing process of anthracene **3-1** (upper) and phenanthrene (lower). The rings drawn in bold lines represent the Clar sextet.
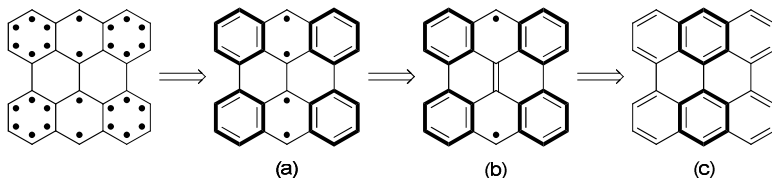
Fig. 3. Electron pairings in bisanthene **3-3**.

Fig. 4. Kekulé and biradical structures of polyacenes and polyperiacenes **a-b**. The numeral under each structure represents the number of the Clar sextets.

The consideration for the electronic structure of anthracene could be adapted to the edge-localization of electrons in polyperiacenes. Bisanthene **3-3**, which is the smallest polyperiacene of anthracene, has four unpaired electrons in the canonical form having a maximal number of the sextet (Fig. 3(a)). Two inner neighboring electrons can be paired with no destruction of the sextets, and consequently this pairing process is completely favorable in energy (Figs. 3(a)→3(b)). Remaining two electrons reside on the zigzag-edge regions, and pairing of the two

outer electrons results in decrease of total number of the sextets (Figs. 3(b)→3(c)). Energy difference between before and after the pairing of the electrons on the zigzag edges should be smaller in **3-3** than in **3-1**, since the pairing in **3-3** causes the destruction of two sextets; leading to propensity of electrons to more localize in separated places in **3-3**.[8] For larger polyperiacenes of anthracene such as **3-5** and **3-7**, the difference in the number of the sextet between the biradical and Kekulé structures increase with increment of molecular size; three for **3-5** and four for **3-7** (Fig. 4). More sextets in the biradical structures would result in more dominant contribution of biradical electron configuration to the ground state. Two unpaired electrons localize at the zigzag-edge regions so as to gain π-bonding energy in the inner pairs of electrons, as was seen in Figs. 3(a)→3(b).

2.2. *Quantum chemical method*

The singlet open-shell character was estimated using the index defined by Yamaguchi[9] coupled to the symmetry-broken UBHandHLYP/6-31G* calculation.[10] The degree of the singlet open-shell character, y_i, can be determined from the following equations: $y_i = 1 - 2T_i/(1 + T_i^2)$, $T_i = (n_{HOMO-i} - n_{LUMO+i})/2$, where n_{HOMO-i} and n_{LUMO+i} represent natural orbital occupation numbers of HOMO–i and LUMO+i, respectively. The index y_0 which are determined from the HOMO–LUMO pair are related to a π-bond cleavage and vary continuously from zero to unity. A perfect biradical molecule has y_0 of unity. Table 1 shows y_0 of polyacenes and polyperiacenes. The series of polyperinathalene **2-b**, which have been extensively studied by Müllen and co-workers,[11] has no appreciable y_0, although theoretical calculation for larger systems has predicted a small HOMO–LUMO energy gap.[12] Actually even **2-7** shows high stability. On the other hand, bisanthene **3-3** has a small but non-negligible value of y_0, suggesting that **3-3** is basically classified into a closed-shell molecule with potential biradical character. High reactivity toward oxygen of **3-3** supports this idea.[13] Larger homolog **3-5** and **3-7** give large values of y_0, clearly indicating their appreciable biradical character. It is noteworthy that apparent biradical character is recognized

in the systems having three or more Clar sextets in the biradical structures in comparison with the Kekulé structures. Aromatic stabilization energy (ASE) of benzene based on homodesmic stabilization energy (HSE) is ca. 90 kJ/mol,[14] three times of which is comparable to the C–C π-bonding energy of 272 kJ/mol.[15] Thus two unpaired electrons in the biradical structure of **3-3** (the difference of the Clar sextet is two) prefer electron pairing to form a closed-shell ground state, whereas **3-5** (the difference of the Clar sextet is three) is subjected to competition between the pairing of two unpaired electrons and the aromatization of the six-membered rings.

Table 1. The degrees of open-shell character y_0 of polyacenes and polyperiacenes **a**-**b**. In parentheses, spin contaminations are indicated.

b \ a	2	3	4
1	0.00 (0.00)	0.00 (0.00)	0.01 (0.31)
3	0.00 (0.00)	0.12 (1.01)	0.60 (1.63)
5	0.01 (0.35)	0.59 (1.66)	0.91 (1.90)
7	0.05 (0.83)	0.84 (1.83)	0.98 (2.05)

2.3. *Aromaticity of each ring*

The nucleus-independent chemical shift (NICS) calculation[16a,b,c,d] is informative for an aromatic contribution of each six-membered ring. We performed the NICS calculation of polyperiacenes **a**-**b** with the GIAO[16e]-B3LYP/6-31G* method. Figure 5 shows the NICS(1) values of polyacenes and polyperiacenes. Bisanthene **3-3** has the largest aromatic contribution in the ring B, which suggests a dominant contribution of the Kekulé structure in Fig. 4 to the ground state.[17] On the other hand, the NICS(1) value of the ring B in **3-5** approaches the non-aromatic and a large aromatic contribution is found in the ring A and D. This finding clearly indicates decrease and increase of Kekulé and biradical contributions to the ground state of **3-5**, respectively. Larger homolog **3-7** shows more non-aromatic NICS(1) values in the ring B and E, supporting its more pronounced biradical character.

2.4. *More extended ring system*

Using these findings, one can easily recognize open-shell electronic structures in polyperiacenes of tetracene (**4-b**; b = 3, 5, 7). All of these compounds contain three or more sextets in the biradical structures in comparison with the Kekulé structures, indicating a large contribution of the biradical structures to the ground states. Unpaired electrons are prone
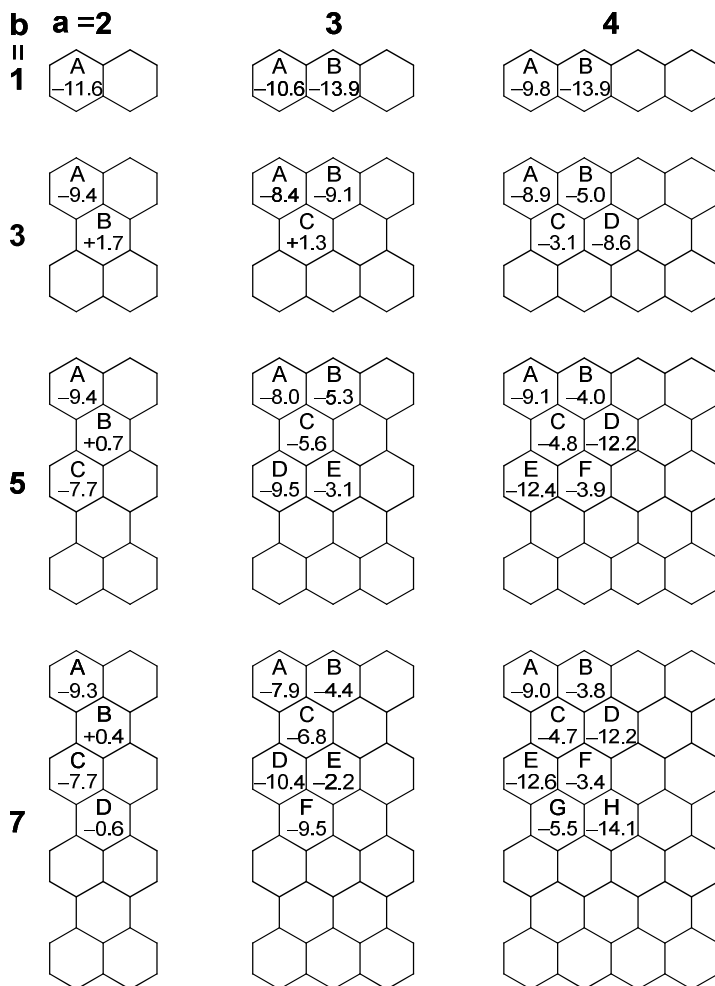
Fig. 5. NICS(1) values of polyacenes and polyperiacenes **a-b**.

to reside on the zigzag edges to ensure maximal numbers of the Clar sextets. Large negative NICS(1) values are found at the position where the sextet can be drawn in the biradical structures of Fig. 4.

3. Experimental Elucidation of the Smallest Polyperiacene

The smallest potential singlet biradical species in the polyperiacenes would be bisanthene **3-3**, which has been isolated as an air-sensitive crystalline powder.[18a] UV,[18a,b] photoelectron,[18c] fluorescence,[18d] and vibrational spectra[18e] of this labile compound have been measured, whereas there has been no direct determination of the experimental structure so far.[18f] Considering stability in air and solubility in common organic solvents, we decided to introduce *tert*-butyl groups on the rings of **3-3** and prepared a tetra-*tert*-butyl derivative **1** from commercially available diphenylmethane in 7 steps (Fig. 6). The structure of **1** was confirmed by X-ray crystallographic analysis.
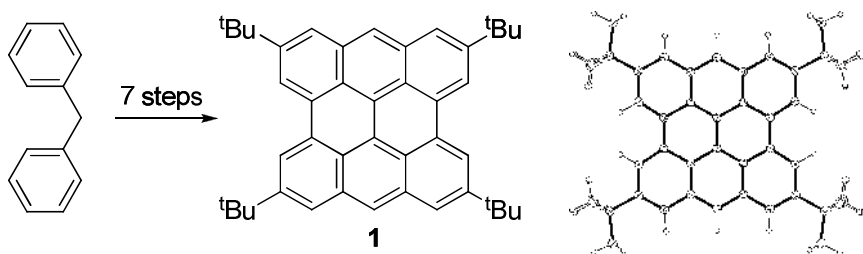
Fig. 6. Synthesis and ORTEP drawing of **1** at the 50% probability level.

3.1. *Geometrical consideration*

The bond lengths of **1** along with anthracene and phenanthrene are summarized in Fig. 7. The bond lengths in the ring *A* and *B* resemble to those of anthracene. The central C–C bond (1.451(2) Å) in **1** is quite long compared to the C–C double bond (1.338(5) Å) in the 9,10-position of phenanthrene whose structure can be drawn in the biradical resonance structure. The double bond character of the central C–C bond is
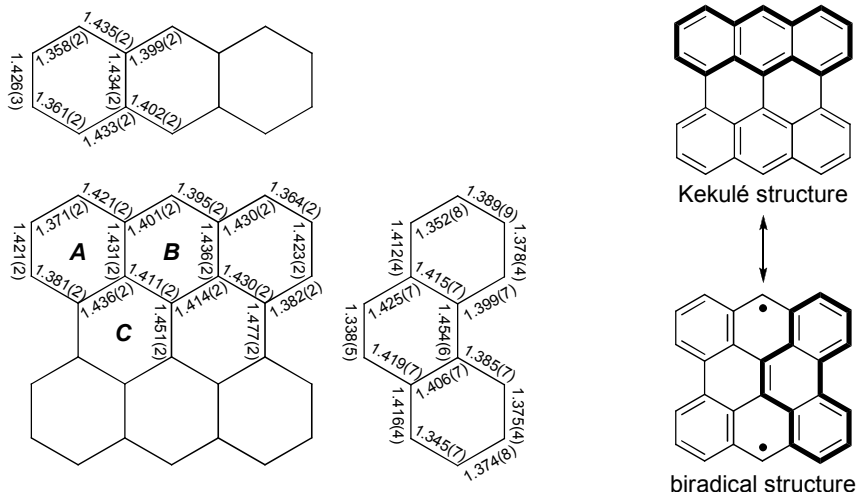
Fig. 7. (Left) Bond lengths of **1** (at 200 K), anthracene (94 K),[20a] and phenanthrene (295 K).[20b] (Right) Resonance structure of bisanthene **3-3**.

estimated to be only 21% according to the Pauling–Brockway relationship,[19] which represents C–C bond character as a function of an experimental bond length. Thus the X-ray data agree with the consideration of the Kekulé structure as having more importance in the resonance hybrid of **1**.

3.2. *Physical properties*

Physical properties of **1** also support the geometrical consideration on the ground state of **1**. In general, a small HOMO–LUMO energy gap is an essential factor for open-shell character of a molecule, because a HOMO–LUMO gap is closely related to the promotion of electrons from HOMO to LUMO. A single electron HOMO–LUMO excitation along with spin inversion leads to the triplet biradical state, whereas admixing a doubly excited configuration $^1\Phi_{H,H\rightarrow L,L}$ into a ground state leads to singlet biradical character of the system. Electronic absorption spectrum of **1** in a toluene solution gave an intense low-energy band at 662 nm ($\varepsilon = 32{,}500$), from which the optical HOMO–LUMO energy gap of **1**

was determined to be 1.87 eV. Cyclic voltammogram of **1** gave two oxidation ($E_{1,1/2}^{ox}$ = –0.07 V vs. Fc/Fc$^+$, $E_{2,pa}^{ox}$ = +0.49 V) and two reduction waves ($E_{1,1/2}^{red}$ = –1.75 V, $E_{2,pc}^{red}$ = –2.21 V), which led to the electrochemical HOMO–LUMO gap of 1.68 eV. The HOMO–LUMO energy gaps of **1** are larger than the energy gap border line (1.5 eV) for triplet biradical ground state that was suggested by Hofmann.[21] Actually, ESR signals typical for triplet species could not be detected in a powdered sample of **1** at 373 K. Theoretical singlet–triplet energy gap for **3-3** calculated with the B3LYP/6-31G* method was 52.4 kJ/mol (= 6300 K), from which the amount of triplet species at 373 K was estimated to be ~ 0.1 ppm according to the Boltzmann distribution. The non-biradical character of **1** was also supported by a variable temperature ^{1}H-NMR experiment, which showed no signal broadening of aromatic protons even at 383 K.[22] These observations indicate two unpaired electrons in the biradical resonance structure strongly coupled to form non-magnetic singlet ground state. On the other hand, chemical reactivity might suggest the potential open-shell character of **1**. The intense absorption band at 662 nm in the UV spectrum of **1** decayed with a half-life period of 19 days open to air. The absorption of the resulting product was the same as that of a quinone derivative, indicating the reaction with oxygen at the *meso*-positions where the largest spin density (±0.443) was predicted by means of the broken-symmetry UBHandHLYP calculation.

4. Conclusion

Open-shell character and edge-localization of unpaired electrons in polyperiacenes comes from acquiring as many aromatic sextets as possible. Energy balance between aromatization and π-bond formation determines the degree of open-shell character of the system. Tetra-*tert*-butyl derivative **1** of bisanthene **3-3**, which could be regarded as the smallest biradicaloid species in the series of polyperiacenes at the UBHandHLYP level of theory, had no appreciable biradical character in physical measurements, whereas its chemical reactivity might suggest the potential biradical character. These experimental results on **1** are consistent with the simple valence bond consideration based on the Clar

sextet model, as well as the quantum chemical calculation. This theoretical finding is a useful guidance to predict the ground state spin structures of polyperiacenes and hopefully of extraordinarily giant polycyclic aromatic compounds including graphene sheet.

Acknowledgments

References

1. a) Y. Kobayashi, K. Fukui, T. Enoki, K. Kusakabe, Y. Kaburagi, *Phys. Rev. B* **71**, 193406-1 (2005). b) Y. Kobayashi, K. Kusakabe, K. Fukui, T. Enoki, *Phys. E* **34**, 678 (2006). c) Y. Kobayashi, K. Fukui, T. Enoki, K. Kusakabe, *Phys. Rev. B* **73**, 125415-1 (2006). d) Y. Niimi, T. Matsui, H. Kambara, K. Tagami, M. Tsukada, H. Fukuyama, *Phys. Rev. B* **73**, 085421-1 (2006).

2. M. Fujita, K. Wakabayashi, K. Nakada, K. Kusakabe, *J. Phys. Soc. Jpn.* **65**, 1920 (1996).

3. a) A. K. Geim, K. S. Novoselov, *Nat. Mater.* **6**, 183 (2007). b) C. N. R. Rao, A. K. Sood, K. S. Subrahmanyam, A. Govindaraj, *Angew. Chem. Int. Ed.* **48**, 7752 (2009). c) C. N. R. Rao, K. Biswas, K. S. Subrahmanyam, A. Govindaraj, *J. Mater. Chem.* **19**, 2457 (2009). d) S. Dutta, S. K. Pati, *J. Mater. Chem.* **20**, 8207 (2010). e) C. Berger, Z. Song, X. Li, X. Wu, N. Brown, C. Naud, D. Mayou, T. Li, J. Hass, A. N. Marchenkov, E. H. Conrad, P. N. First, W. A. de Heer, *Science* **312**, 1191 (2006). f) K. S. Novoselov, Z. Jiang, Y. Zhang, S. V. Morozov, H. L. Stormer, U. Zeitler, J. C. Maan, G. S. Boebinger, P. Kim, A. K. Geim, *Science* **315**, 1379 (2007). g) Y. Son, M. L. Cohen, S. G. Louie, *Nature* **444**, 347 (2006). h) A. Ghosh, K. V. Rao, S. J. George, C. N. R. Rao, *Chem. Eur. J.* **16**, 2700 (2010). i) S. Dutta, S. Lakshmi, S. K. Pati, *Phys. Rev. B* **77**, 073412 (2008). j) K. S. Subrahmanyam, L. S. Panchakarla, A. Govindaraj, C. N. R. Rao, *J. Phys. Chem. C* **113**, 4257 (2009). k) A. Das, S. Pisana, B. Chakraborty, S. Piscanec, S. K. Saha, U. V. Waghmare, K. S. Novoselov, H. R. Krishnamurthy, A. K. Geim, A. C. Ferrari, A. K. Sood, *Nat. Nanotechnol.* **3**, 210 (2008).

4. J. Wu, W. Pisula, K. Müllen, *Chem. Rev.* **107**, 718 (2007).

5. a) K. Nakada, M. Fujita, G. Dresselhaus, M. S. Dresselhaus, *Phys. Rev. B* **54**, 17954 (1996). b) K. Wakabayashi, M. Sigrist, M. Fujita, *J. Phys. Soc. Jpn.* **67**, 2089 (1998). c) A. Yamashiro, Y. Shiomi, K. Harigaya, K. Wakabayashi, *Phys. Rev. B* **68**, 193410-1 (2003). d) T. Enoki, Y. Kobayashi, *J. Mater. Chem.* **15**, 3999 (2005). e) H. Lee, Y.-W. Son, N. Park, S. Han, J. Yu, *Phys. Rev. B* **72**, 174431-1 (2005). f) Y.-W. Son, M. L. Cohen, S. G. Louie, *Nature* **444**, 347 (2006). g) V. Barone, O. Hod, G. E. Scuseria, *Nano Lett.* **6**, 2748 (2006). h) Y.-W. Son, M. L. Cohen, S. G. Louie, *Phys. Rev. Lett.* **97**, 216803-1 (2006). i) D. Jiang, B. G. Sumpter, S. Dai, *J. Chem. Phys.* **27**, 124703-1 (2007). j) S. D. Dalosto, Z. H. Levine, *J. Phys. Chem. C* **112**, 8196 (2008). k) W. L. Wang, S. Meng, E. Kaxiras, *Nano Lett.* **8**, 241 (2008). l) O. Hod, V. Barone, G. E. Scuseria, *Phys. Rev. B* **77**, 035411-1 (2008).

6. a) E. Clar, *The Aromatic Sextet* (Wiley & Sons, London, 1972). b) Y. Ruiz-Morales, *J. Phys. Chem. A* **108**, 10873 (2004). c) The Clar's aromatic sextet is defined as a cyclic array of six π-electrons localized in a single benzene ring. In polycyclic aromatic systems, two sextets should not be adjacent but be separated by formal C–C single bonds.

7. a) E. Clar, *Polycyclic Hydrocarbon (Vol. 1)* (Academic Press, New York, 1964), p. 288–307. b) A. R. Reddy, M. Bendikov, *Chem. Commun.*, 1179 (2006).

8. Resonance effect results in delocalization of unpaired electron on the *meso*-position to neighbor rings. However, contribution of the formula **b-d** to the ground state of **3-3** would be smaller than the formula **a**, since the delocalization of unpaired electron from the *meso*-position accompanies destruction of one sextet.
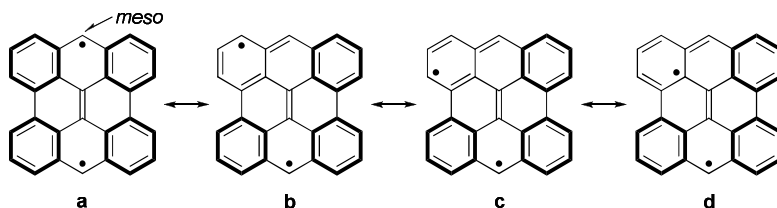
9. a) K. Yamaguchi, in *Self-Consistent Field: Theory and Applications*, Eds. R. Carbo, M. Klobukowski (Elsevier, Amsterdam, 1990), p. 727. b) S. Yamanaka, M. Okumura, M. Nakano, K. Yamaguchi, *J. Mol. Struct. (THEOCHEM)* **310**, 205 (1994).

10. The theoretical study on effective exchange interaction in phenalenyl radical dimer revealed that the symmetry broken UBHandHLYP calculation best reproduced the experimental value of the magnetic interaction, among unrestricted HF (UHF), pure DFT (UBLYP), hybrid DFT (UBHandHLYP and UB3LYP), and post HF (CASSCF) calculations. See, Y. Takano, T. Taniguchi, H. Isobe, T. Kubo, Y. Morita, K. Yamamoto, K. Nakasuji, T. Takui, K. Yamaguchi, *J. Am. Chem. Soc.* **124**, 11122 (2002).

11. a) A. Bohnen, K.-H. Koch, W. Lüttke, K. Müllen, *Angew. Chem. Int. Ed.* **29**, 525 (1990). b) M. Baumgarten, K.-H. Koch, K. Müllen, *J. Am. Chem. Soc.* **116**, 7341 (1994).

12. J. L. Brédas, R. H. Baughman, *J. Chem. Phys.* **83**, 1316 (1985).

13. a) H. Brockmann, R. Randebrock, *Chem. Ber.* **84**, 533 (1951). b) H. Kuroda, *J. Chem. Phys.* **33**, 1586 (1960). c) E. Clar, W. Schmidt, *Tetrahedron* **33**, 2093 (1977). d) S. M. Arabei, T. A. Pavich, *J. Appl. Spectrosc.* **67**, 236 (2000). e) G. G. D'yachenko, V. A. Petukhoc, S. M. Arabei, T. A. Pavich, *J. Appl. Spectrosc.* **70**, 208 (2003).

14. a) M. N. Glukhovtsev, R. D. Bach, S. Laiter, *J. Mol. Struct. (THEOCHEM)* **417**, 123 (1997). b) S. W. Slayden, J. F. Liebman, *Chem. Rev.* **101**, 1541 (2001).

15. The π-bonding energy is estimated from the rotational barrier in ethylene. See, B. S. Rabinovitch, F. S. Looney, *J. Chem. Phys.* **23**, 315 (1955).

16. a) P. v. R. Schleyer, C. Maerker, A. Dransfeld, H. Jiao, N. J. R. v. E. Hommes, *J. Am. Chem. Soc.* **118**, 6317 (1996). b) Z. Chen, C. S. Wannere, C. Corminboeuf, R. Puchta, P. v. R. Schleyer, *Chem. Rev.* **105**, 3842 (2005). c) P. Lazzeretti, *Phys. Chem. Chem. Phys.* **6**, 217 (2004). d) The NICS calculation might overgeneralize aromaticity, see A. Datta, S. S. Mallajosyula, S. K. Pati, *Acc. Chem. Res.* **40**, 213 (2007). e) G. Schreckenbach, T. Ziegler, *J. Phys. Chem.* **99**, 606 (1995).

17. The ring A also has a large negative NICS value. This can be explained by the sextet migration from the ring B to the ring A. See the reference 6a, and M. Randić, *Chem. Rev.* **103**, 3449 (2003).

18. a) H. Brockmann, R. Randebrock, *Chem. Ber.* **84**, 533 (1951). b) H. Kuroda, *J. Chem. Phys.* **33**, 1586 (1960). c) E. Clar, W. Schmidt, *Tetrahedron* **33**, 2093 (1977). d) S. M. Arabei, T. A. Pavich, *J. Appl. Spectrosc.* **67**, 236 (2000). e) G. G. D'yachenko, V. A. Petukhoc, S. M. Arabei, T. A. Pavich, *J. Appl. Spectrosc.* **70**, 208 (2003). f) Very recently the X-ray structure of a derivative of **3-3** has been reported; see, J. Li, K. Zhang, X. Zhang, K.-W. Huang, C. Chi, J. Wu, *J. Org. Chem.* **75**, 856 (2010).

19. L. Pauling, L. O. Brockway, *J. Am. Chem. Soc.* **59**, 1223 (1937).

20. a) C. P. Brock, J. D. Dunitz, *Acta Crystallogr., Sect. B: Struct. Sci.* **46**, 795 (1990). b) V. Petříček, I. Císařová, L. Hummel, J. Hroupa, B. Březina, *Acta Crystallogr., Sect. B: Struct. Sci.* **46**, 830 (1990).

21. R. Hoffmann, *J. Am. Chem. Soc.* **90**, 1475 (1968).

22. Appearance of NMR signals would be more sensitive to paramagnetic species, since it is well-known that paramagnetic species greatly reduce spin–lattice relaxation times T_1. Even very small amount of paramagnetic species influences the line-width of signals and can cause signal-broadening in NMR spectra.

Chapter 4

Doping of Graphene: A Computational Study

Arun K. Manna[*] and Swapan K. Pati[*,†]

*Theoretical Sciences Unit and †New Chemistry Unit,
Jawaharlal Nehru Centre for Advanced Scientific Research,
Jakkur Campus, Bangalore 560064, India
†pati@jncasr.ac.in

Recent experimental achievements in synthesizing single layer and a few layers graphene have provided a new platform to explore their novel electronic, mechanical and optical properties. This has created immense potential applications in this era of miniaturized electronic devices, which arises mainly due to the quantum confinement effects in this reduced dimension. In this chapter, we present the fascinating results obtained from first-principles density functional theory calculations on the structure and novel opto-electronic properties of two dimensional (2D) graphene subjected to tunable external perturbations induced by the presence of a few metal clusters and electron donor-acceptor molecules to explore the possible ways of enhancing their device applicabilities. We show that the nature of the deposited metal clusters and dopant molecules on graphene surface has significant effects in modulating its intriguing electronic properties through charge transfer, opening a new avenue for optoelectronic device applications. We find that the interaction strength for the metal clusters is relatively larger compared to the molecular systems, and consequently has more impacts in changing graphene's novel electronic structure. Interestingly, the type and concentrations of charge carriers in graphene can be controlled by appropriate external dopants. In fact, we suggest that the presence of suitable dopants can eventually tune the graphene electronic structure from semi-metallic to a perfect metallic and even if semiconducting behaviors. We also suggest that these charge transfer effects can be seen in optical conductivity profiles as the low frequency regions are affected by the extent and type of charge-transfer.

1. Introduction

Low dimensional carbon nanomaterials, like fullerenes, nanotubes, graphene, and their derivatives, have been of extensive research interest in condensed-matter physics and in materials sciences because of their intriguing novel electronic, mechanical and optical properties.[1,2,4–7] In fact, the diverse electronic properties of carbon nanomaterials strongly depend on their dimensionalities. The electronic confinement in these reduced dimensions give rise to many exotic phenomenon that have been of potential scientific interests over the decades.[1,8–11,13–16] The recent experimental realization of two and quasi-1D nanosystems have drawn a major attention of a large number of scientific communities for their possible applications in nanoelectronic devices.[2–4]

Owing to its versatile, unique properties, graphene, a strictly two-dimensional (2D) flat monolayer of carbon atoms tightly packed into a honeycomb lattice, among all class of nanomaterials, has become an ideal candidate for designing the next generation nanoelectronic devices.[2,7,17–22] In fact, graphene has been considered as the parental compound for the other conjugated carbon allotropes possessing various dimensionalities. The rhombus unit cell of graphene consists of two atoms coming from two different sublattices making graphene a bipartite lattice. According to Lieb's theorem[23] the graphene electronic spins prefer to align antiferromagnetically within the two sublattice points in a bipartite lattice. Tunable electronic properties from insulators through semiconductors to conductors make 2D graphene, a strictly zero band gap semi-metal, of practical interest in nanoscience and nanotechnology. Moreover, the finite termination of graphene results in quasi-1D nanoribbons like structures with two different possible edge geometries, namely zigzag and armchair; commonly termed as zigzag graphene nanoribbon (ZGNRs) and armchair graphene nanoribbons (AGNRs), respectively. These ribbons show completely different electronic behaviors arising from their two contrasting edge geometries. It has been demonstrated that in contrast to AGNRs, the ribbons with zigzag edges (ZGNRs) possess strongly localized edge states resulting from non-bonding molecular orbitals.[24] Interestingly, the half-metallic behavior of ZGNRs under a threshold external cross ribbon electric field is of practical interest since it, enables them for possible application in spintronics devices.[25–27] Thus, the dimensionalities and edge geometry play a very substantial role in governing the enticing electronic structure of these carbon nanomaterials.

In general, electronic properties of materials in reduced dimensions are mainly governed by their size, geometry, boundary conditions and more importantly by the nature of electronic correlations.[6,30] In addition to that, the carrier type and its concentrations play an important role in controlling the novel opto-electronic and transport properties. The *massless* Dirac fermions present in graphene that describe the low-energy electronic properties, result in very high carrier mobilities. Moreover, the carriers (electrons or holes) mobilities can be tuned by controlling the external electric field in graphene-based field effect devices.[2] Furthermore, the possible utilization of spin components in graphene-based electronic devices depends on the extent of spin polarization.[31,32] In this respect, the half-metallic materials as mentioned above, show zero band gap for electrons with one spin orientation and insulating or semiconducting band gap for the other, resulting in a completely spin-polarized current.[27,30,33–35] In fact, appropriate controlling and/or tuning the electronic structure of graphene have numerous applications in advanced device fabrications. The significant changes in properties of graphene, in particular of its phonon frequencies and electronic structure, are reported to occur when electrons or holes are added by electrochemical means.[36] It is indeed possible to achieve a high level of doping through electrochemical top-gating.[36–38] Apart from this, the other possible way of tuning the carrier type and its concentrations is by the incorporation of appropriate external electron donor or acceptor guests into the host carbon nanostructures. To achieve this, the boron and nitrogen atoms implantation,[35,39,40] chemical functionalization[41,42] and surface adsorption of selective donor and acceptor molecules[43–45] into graphene nanostructures, have been successfully considered to be the effective routes among others. As is well known, charge transfer is well known in molecular systems. This can be achieved in two different pathways, namely, intramolecular and intermolecular charge transfer processes. To materialize the intramolecular pathway, one has to form a new chemical bond between the electron donor and acceptor host-guest systems, and possibly loosing the intriguing electronic structure induced by the substantial structural deformation as a result of new bond formation. In sharp contrast to this, intermolecular pathways are more effective where one can add either electrons or holes by adsorbing various selective electron donor or acceptor dopants on the graphene surface through charge transfer processes. Such controlled adsorption of donor or acceptor dopant induces charge transfer, which in turn greatly changes the optoelectronic properties of 2D graphene, in particular the characteristic Raman spectra of graphene.[43–45]

In this chapter, we mainly describe the effect of external dopants of a few novel metal clusters and electron donor or acceptor molecules on the modification of electronic properties of a pure single layer 2D graphene using first-principles density functional theory calculations. We consider a few representative metal clusters of Pd, Ag, Pt and Au with 40 nuclearity embedded on graphene surface to model the metal nanoclusters doping. The molecular doping on the other hand is achieved by adsorbing selective donor and acceptor molecules onto the graphene surface.[45] For this, we consider a few representative donor and acceptor molecules with varying affinities of electron-withdrawing and donating power. Tetracyanoethylene (TCNE) and tetracyanoquinodimethane (TCNQ) have been chosen as electron acceptors, and tetrathiafulvalene (TTF) as the electron donor. Our study reveals that all the composite systems are stabilized in spin-polarized ground state. The type of the deposited dopants (metal clusters or donor/acceptor molecules) on graphene has significant effects in changing its intriguing electronic structure. Results obtained from molecular doping of graphene show that the donors and acceptors are adsorbed on the graphene surface through a physisorption process. Mülliken populations analysis predicts that there is an effective charge transfer between the adsorbed dopant and graphene, and its directionality follow the nature of the adsorbed dopants. The propensity of observed interaction strength is more for metal clusters doping compared to the molecular doping which in fact governed by the relative extent of charge transfer between the two. We analyze the effect of molecular charge transfer on the Raman active phonon frequencies in graphene. The band structures together with density of states (DOS) analysis clearly show the presence of discrete localized levels in between valence and conduction bands arising from dopants. We too have focused on the low-frequency profile of optical conductivity of these charge transfer complexes. Our theoretical findings[45] compare fairly well with recently reported experimental results.[43,44]

2. Computational Details

The first-principles calculations are carried out using the linear combination of atomic orbital density-functional theory (DFT) methods implemented in the SIESTA package.[46] The generalized gradient approximation (GGA) in the Perdew-Burke-Ernzerhof (PBE) form[47] and double ζ polarized (DZP) basis set are chosen for the spin-polarized DFT calculations. The interaction between ionic cores and valence electrons is described by norm

conserving pseudopotentials[48] in the fully non-local Kleinman-Bylander form.[49] The details of the computational methods can be found in ref. 45. We consider (8×8) supercell containing 128 carbon atoms of graphene for modelling the doping of 2D graphene.

3. Metal Nanoclusters Graphene Complexes

Possessing many exotic, interesting properties and the possibilities of their modulation in a controllable manner, the 2D graphene has been of great research interest in recent years. There are many potential modification routes to increase its device applicability. Here we describe the effect of metal clusters doping; i.e. embedding a few representative novel metal clusters of Pd, Ag, Pt and Au with sufficiently large nuclearity (40) to explore its responses in tuning of novel electronic structure, particularly designing an efficient way to engineer bandgaps which opens up a new avenue for optoelectronic device applications.
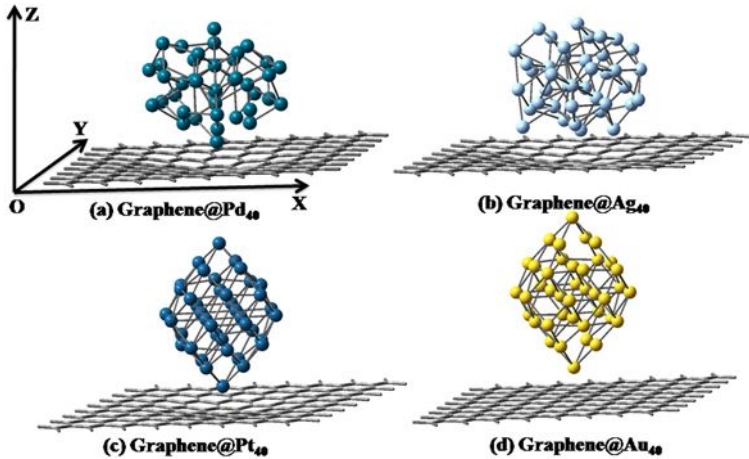
Fig. 1. (Color online) The optimized structures of four metal nanoclusters deposited on graphene surface (From reference 45a).

We first consider the two dimensional arrays of metal clusters deposited on graphene, as shown in Fig. 1 from the relaxed geometries of graphene and metal clusters. The initial structural guess for the metal clusters is

modeled by Sutton-Chen 12-6 potentials.[50] The relative stability of the
metal nanoclusters embedded on graphene surface (i.e., graphene@M_{40}) is
determined by the stabilization energies (E_{stab}) or the so-called binding
energy, calculated using equation (1). As is well known, the larger the sta-
bilization energy, the stronger is the binding of the guest dopant cluster to
the graphene surface. The stabilization energy per deposited metal cluster
is calculated by subtracting the energy of the optimized isolated cluster of
nuclearity 40, $E(M_{40})$ and the optimized equilibrium energy of the graphene
supercell, $E(graphene)$, from the total energy of the optimized composite
systems, $E(graphene@M_{40})$, :

$$\Delta E_{stab} = E_{graphene@M_{40}} - E_{graphene} - E_{M_{40}} \qquad (1)$$

A summary of the results for the optimized structures for all four com-
plexes is provided in Table 1.

Table 1.   Summary of results for metal nanoclusters deposited on graphene. The +ve
(-ve) sign indicates the electron transfer from graphene (metal cluster) to metal clus-
ter (graphene). The R_{eq} and C.T represent the equilibrium distances of separation and
amount of charge transfer, respectively. I.E_v (I.E_a) and E.A_v (E.A_a) represent the verti-
cal (adiabatic) ionization energy and electron affinity, respectively (From reference 45a).

Nanocomposites	R_{eq} (Å)	ΔE_{stab} (eV)	ΔE_{form} ($\Delta E_{form}{}^c$) (eV)	C.T (e)	I.E_v (I.E_a)	E.A_v (E.A_a)
Graphene@Pd_{40}	2.33	-4.74	-3.70 (-3.58)	3.62	5.78 (5.76)	-3.54 (-3.55)
Graphene@Ag_{40}	2.45	-2.19	-2.45 (-2.40)	2.00	4.68 (4.68)	-2.48 (-2.51)
Graphene@Pt_{40}	2.35	-2.86	-6.14 (-6.07)	2.41	6.82 (6.60)	-4.10 (-4.03)
Graphene@Au_{40}	2.83	-1.91	-4.13 (-4.03)	-0.17	4.10 (4.10)	-1.49 (-1.54)

We too have calculated the formation energies (E_{form}) per metal atom
defined by equation (2) and (3) of these metal nanoclusters in presence as
well as in absence of graphene to focus on the feasibility of spontaneous for-
mation of clustering from constitutional atomic metal moiety under suitable
experimental conditions. Our results indicate that the formation energy is
slightly increased in presence of graphene, acting as a catalyst, relative to
the free metal clustering.

$$\Delta E_{form} = [E_{graphene@M_{40}} - E_{graphene} - 40 * E_{M_{40}}]/40 \qquad (2)$$

$$\Delta E_{form}^c = [E_{M_{40}} - 40 * E_M]/40 \qquad (3)$$

where the $E(M_{40})$ and $E(M)$ are the energies of optimized metal nanocluster and of a single metal atom, respectively.

From the fully optimized geometries, we find that the shortest separation between a metal atom of the deposited metal cluster and the closest carbon atom of the graphene layer for the graphene@M_{40} complexes are between 2.3 and 2.8 (see Table 1). Also as given in table 1, the relative stabilization energies are higher in magnitude for Pd, Ag, Pt clusters embedded graphene complexes compared to the Au_{40} cluster which clearly indicates a relatively weak interaction between the Au nanoparticles and the graphene in comparison to others. The relatively higher binding energies combining with smaller equilibrium distances of separation dictate that all three (Pd, Ag, Pt) metal clusters do eventually adsorbed strongly on the graphene surface, inducing local structural deformation. An analysis of the Mülliken population suggests that there is an effective charge transfer between the adsorbed metal cluster and graphene. For the Pd, Ag, and Pt cluster deposition, the charge transfer occur from graphene to metal cluster at their equilibrium distances of separation, while for Au nanoclusters the direction of charge transfer is from metal cluster to graphene. It is also clear from the table 1 that the extent of charge transfer for Pd, Ag, Pt nanocluster is larger compared to that for the Au cluster with greater extent of charge transfer for Pd case, resulting in higher stabilization energy. To understand this, we have computed the vertical as well as adiabatic first ionization energy (I.E.) and electron affinity (E.A.) of individual metal clusters. Both the I. E. and E. A. values computed with the two different strategies follow the similar trend and can be analyzed to understand the extent of charge transfer. We find that the trend in extent of charge transfer which determines the overall stabilization energy of the complexes follow the same pattern in changes in either I. E. or E. A. of the metal clusters belonging to a particular period in the periodic table. In contrast to Pd, Ag, Pt clusters, the comparatively smaller magnitude of E. A. together with relatively lower value of I. E. make the Au_{40} cluster to act as weak electron donor towards the graphene.

In order to understand the mechanism and the extent of charge transfer, we have calculated the energy and difference in charge densities of the composites by varying the distance between the ad metal nanoclusters and the graphene. The interaction energy is found to change inversely with the distance between metal cluster and graphene, clearly predicting that such interactions are mainly due to Coulombic forces as already observed for SWCNT interacting with Pt, Au nanoclusters[51] and for electron

A. K. Manna and S. K. Pati

donor/acceptor adsorbed SWCNT[52] and graphene cases.[45] From the analysis of difference in charge density, we also find that the electron density at the outermost valence orbitals of Pd, Ag, and Pt increases while that at the orbitals of carbon in closer proximity to the metal cluster decreases. The situation is exactly reversed for the Au nanoparticle deposition on graphene as expected from the reverse directionality of charge transfer. Thus, our results predict that the changes in electronic properties of nanoclusters doped graphene is mainly due to direct charge transfer between the two.

We consider to focus on the changes in electronic band structures of the metal nanoclusters embedded graphene systems. From the fully relaxed configuration of all the nano composites, it is clear from Fig. 2 that the region of the graphene in close proximity to the metal cluster is slightly deformed for all the metal clusters deposition which is capable of breaking
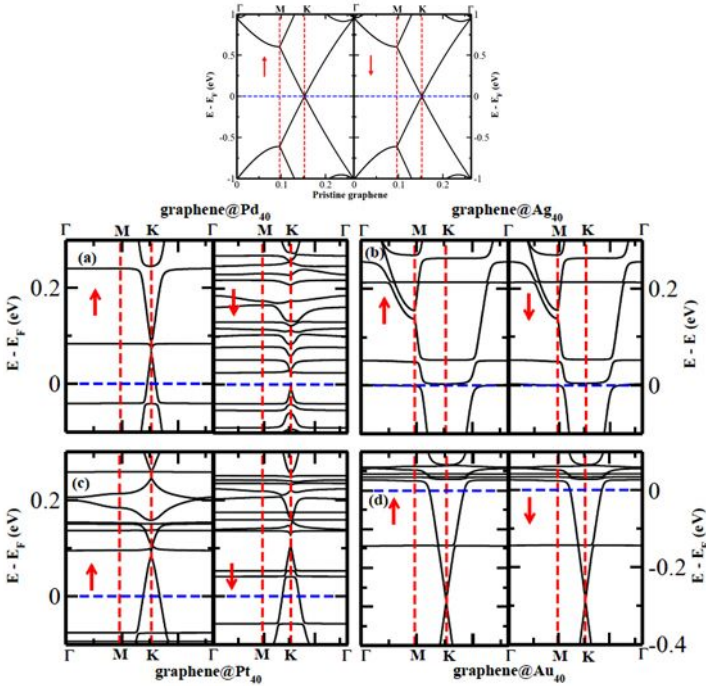
Fig. 2. (Color online) The electronic band structures of pristine graphene (top pannel) and of four metal nanoclusters embedded nanocomposites (bottom pannel). The energy is scaled with respect to the Fermi Energy (E_F). The up and down arrows indicate the majority and minority spin channel, respectively (From reference 45a).

the local A-B sublattice symmetry. Consequently, this can indeed cause an opening of band gap in the charge transfer complexes near the Fermi energy. Interestingly, we find that the band gap of a few meV opens near to the K-point, between the graphene-like bands which touches at the Dirac point in case of pure graphene, as can be seen from Fig. 2. The effect is very negligible for Au_{40} intercalated graphene as expected from small structural changes mentioned above. It is also to be noted that the energy-gap region is above (below) the Fermi energy due to electron transfer from the graphene (metal nanoclusters) to metal nanoclusters (graphene) for Pd, Ag, Pt (Au) and, therefore, the neutral systems are still metallic. The appropriate tuning of carriers concentration can result in placing the Fermi energy in the gap region, and the resulting system would behave as semiconductor. However, all the bands for composite systems are essentially a superposition of the bands arising from isolated systems. Moreover, the flat bands near the Fermi level arise from the localized electronic states of the metal nanoclusters, whereas the bands at the high symmetric K-points are mainly from graphene. The calculated density of states (DOS) and its projection on individual fragment present in nanocomposites show that the graphene is indeed still in its semi-metallic state for the deposition of nanoclusters Pd_{40} and Pt_{40}, while the same becomes metallic in presence of metal nanoclusters Ag_{40} and Au_{40}. The relatively strong adsorption of Pd_{40} and Pt_{40} nanoclusters on graphene induced by the larger extent of charge transfer result in a net spin polarization for the complexes. The spin-polarization of the two nanocomposite arises mainly from the adsorbed metal clusters. Interestingly, the graphene@Pd_{40} nanocomposite can act as perfect spin filter without any charge injection as can be seen from Fig. 2(a). This is because of the presence of metallic majority spin channel, whereas the minority spin channel is semiconducting, i.e., typical half-metallic behavior. Therefore, the doping of appropriate metal cluster on 2D graphene shows a new inroads towards designing of new nanomaterials of tunable electronic properties including room temperature half-metallicity for advanced device applications.

4. Molecule-Graphene Complexes

In this section, we discuss the changes in opto-electronic properties of 2D graphene induced by molecular charge transfer.[45] To achieve the goal, we have considered a few representative organic donor and acceptor molecules. The schematic diagram of which is shown in Fig. 3.
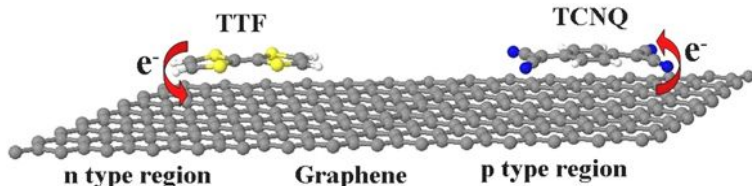
Fig. 3.   Schematic representation of charge transfer process between graphene and electron donor, TTF and electron acceptor, TCNQ molecules. The yellow, blue, grey, and white color atoms correspond to sulfur, nitrogen, carbon and hydrogen, respectively (From reference 45b).

From the relaxed geometries, we find that all the sorbed molecules surface adsorbed above the graphene at about 3.0 Å.[45] Moreover, the calculated adsorption energies that essentially examine the relative stability of adsorbate-graphene complexes are within a few kcal mol^{-1} (30 - 50 kcal mol^{-1}), suggesting a physisorption process[45] with larger adsorption energy for TCNQ adsorbed complex. An analysis of the Mülliken population suggests that there is an effective charge transfer between the adsorbed molecule and graphene. For both TCNE and TCNQ, the extent of electron transfer from graphene to adsorbed molecule is found to be ~ 0.31 e and ~ 0.39 e, respectively, consistent with their nature of electron-withdrawing tendency.[45] For electron donor, TTF, electron transfer of ~ 0.11 e is found from the molecule to graphene. The large value of adsorption energy for TCNQ on graphene compared to the others can be attributed to the fact that for TCNQ, the benzenoid structure provides a significant π surface for adsorption on graphene with a significant amount of charge transfer, and gains stability through electrostatic forces. Incidentally, the charge transfer between graphene and adsorbed molecule results in electrostatic attraction and thereby formation of a charge-transfer complex, in agreement with the UV/Vis spectrum reported by Rao and co-workers.[43,44] Furthermore, it is also indentified conclusively that the charge transfer occurs through Coulombic forces, as was the case for the interaction of carbon nanotubes with metal nanoparticles[51] and with donor and/or acceptor molecules, and nanocluster-graphene cases as discussed in previous section.[52]

To analyze the effect of charge transfer interaction on electronic structure, we plot band diagrams and corresponding DOS in Fig. 4. The band structures around the Dirac point are significantly affected by molecular adsorption in graphene. For pristine 2D graphene, spin-polarized DOS vanishes exactly at Fermi level due to the presence of *massless* Dirac
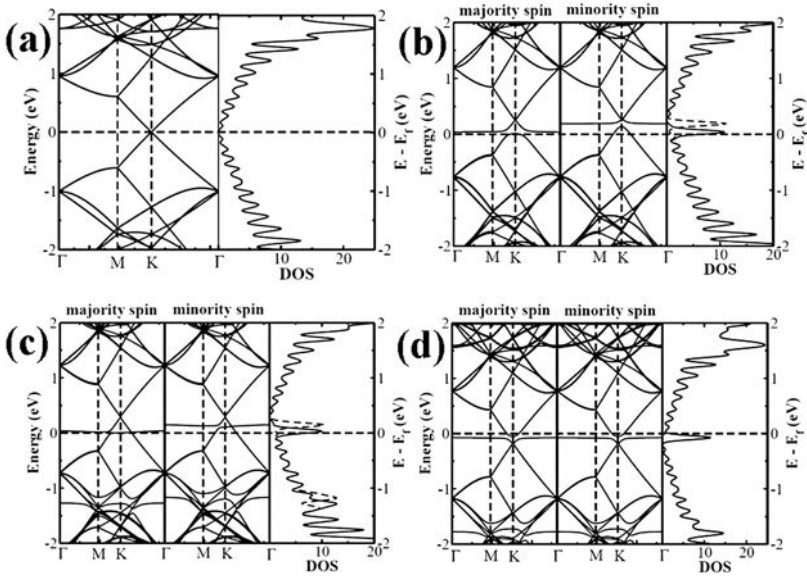
Fig. 4. The band structure and corresponding DOS for (a) pure Graphene, (b) Graphene-TCNE, (c) Graphene-TCNQ and (d) Graphene-TTF in the 8×8 supercell. The solid and dashed lines in DOS correspond to the majority and minority spins respectively. The Fermi level is set to zero. The DOS lines are broadened with Gaussian functions of width 0.05 eV (From reference 45b).

fermions and there is no net spin-polarization (see Fig. 4(a)). The calculated DOS and band structures of graphene in presence of donor and acceptor molecules clearly show the presence of discrete molecular levels around the Fermi energy. The flat molecular levels of TCNE and TCNQ in charge-transfer physisorbed systems at slightly above the Fermi level causes depletion of electrons from the uppermost valence bands, shifting the Fermi level down. In case of TTF adsorbed graphene, a flat band slightly below the Fermi level results in accumulation of electrons causing the upward shifting of the Fermi level, giving rise to finite DOS close to the Fermi level.[45] Also note that, in all three molecule-graphene complexes, breaking of the A-B sublattice symmetry induced by the local structural deformation creates a small band-gap. Injecting either electrons or holes can indeed change the electronic state from semi-metallic to metallic and even to a semiconducting state by placing the Fermi level in between the gap region. Note that, in a strict sense, the Dirac cone picture of graphene is absent in graphene-molecule complexes. Instead, as shown in Fig. 4, the
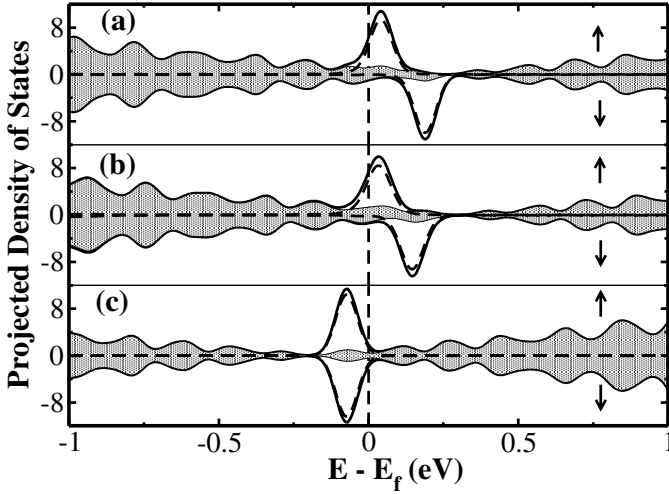
Fig. 5. The projected density of states (pDOS) for (a) Graphene-TCNE, (b) Graphene-TCNQ and (c) Graphene-TTF in the 8×8 supercell. The Fermi level is set to zero. The solid, dashed lines and filled dotted areas correspond to total DOS, molecule pDOS and graphene pDOS respectively. The DOS lines are broadened with Gaussian functions of width 0.05 eV (From reference 45b).

mixing of graphene band and discrete molecular level results in disappearance of cone picture for valance band for TCNE and TCNQ and conduction band for TTF. Interestingly, for electrochemical top-gating study, the linear dispersion near the Fermi level (cone picture) remains true even after doping to a high level.[36–38] In our case,[45] as has been mentioned, the charge-transfer is molecular in nature unlike the electrochemical gating.

From the pDOS analysis (see the Fig. 5), it is clear that the DOS at the Fermi level mainly comes from the adsorbed molecules. In fact, the graphene in graphene-molecule complex contributes only a little to the overall DOS at the Fermi energy. Note that, for pure graphene, there is no states at Fermi energy for transport process. It is also clear from Fig. 5 that at Fermi energy, a finite spin polarization exists for TCNE and TCNQ complexes with graphene, while for TTF adsorbed graphene such a spin polarization is absent.

Here, we also discuss about the Raman active bands (G and D) of graphene and graphene-molecule complexes for a direct comparison and detail understanding of the experimental results recently reported by Rao *et al.*[43,44] Experimentally, it was shown that G-band softens and stiffens

with increasing concentration of TTF and TCNE, respectively, with enhancement of the intensity ratio of D- to G-band.[44] In our calculations,[45] we have obtained qualitatively similar results. For pure 2D graphene, our calculations yield the optical phonon frequency at Brillouin zone center Γ-point corresponding to the Raman active G-band at around 1579 cm^{-1}. However, in presence of electron acceptors (TCNE and TCNQ), we find that the G-band frequency is shifted to a higher value ($\sim$ 1599 cm^{-1} and $\sim$ 1596 cm^{-1} for TCNE- and TCNQ-adsorbed graphene, respectively) because of the nonadiabatic removal of Kohn anomaly at Γ-point, while for the electron donor (TTF), it goes to a lower frequency region at about 1565 cm^{-1}, corroborating the experimental findings.[43,44] We also find that in presence of strong electron acceptors like TCNE and TCNQ, the intensity ratio of D- to G-band increases three orders of magnitudes ($\sim 10^3$), while for TTF adsorption, the intensity ratio increases only to two orders of magnitude ($\sim 10^2$), smaller than that for strong acceptors as found experimentally.[43,44] We find reasonably good agreement with previous calculations[53,54] and experimental results.[43,44,55]

To compare and contrast the low frequency optical excitations which can be affected by molecular charge transfer, we plot the low frequency regime of the optical conductivity for pure graphene along with donor (TTF) and acceptor (e.g; TCNE, TCNQ) intercalated graphene in Fig. 6. Note that, for pure 2D graphene, the Fermi level lies exactly at Dirac point resulting in only the possibility of inter band electronic transitions, giving rise to the optical conductivity peak only at above 0.50 eV. However, for molecule adsorbed on graphene, the shifting of Fermi level towards the valence band or conduction band from the Dirac point depending on the nature of the organic dopant as discussed earlier, creates the possibility of Drude like intra band transitions, resulting in the low frequency optical excitation below 0.50 eV.[45] This can also be accounted for the appearance of flat molecular levels in between the valence and conduction bands. Interestingly, the significant amount of charge transfer for TCNE- and TCNQ-adsorbed graphene induces spin-polarization effects on low-frequency optical conductivity profile. In fact, this induces asymmetry to the population of majority and minority spins at the Fermi level (see Fig. 4), which result in the difference in conductivity values for the carriers with different spins in the low frequency region (see Fig. 6). However, for TTF-adsorbed graphene, due to comparatively less charge transfer, both the majority and minority spins show symmetric population (see Fig. 4), with less intense low-frequency peaks in optical conductivity.
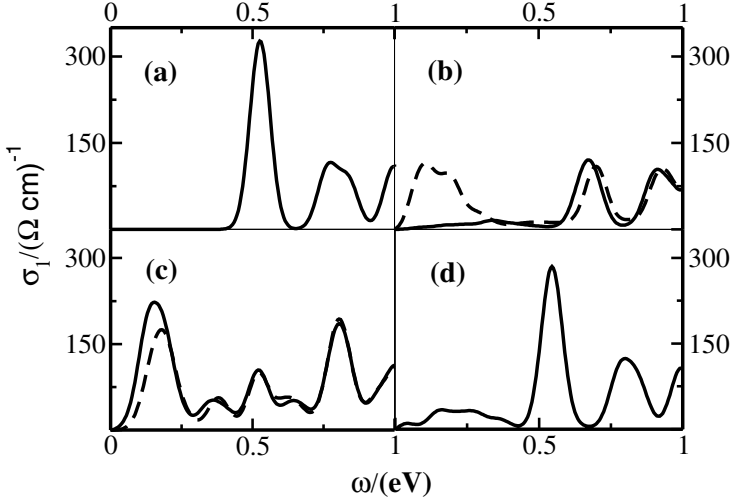
Fig. 6.   Low frequency optical conductivity for (a) pure Graphene, (b) Graphene-TCNE, (c) Graphene-TCNQ and (d) Graphene-TTF. The solid and dashed lines in conductivity profiles correspond to the majority and minority spins respectively. The lines are broadened with Gaussian functions of width 0.05 eV (From reference 45b).

5. Summary

In this chapter, we have presented emerging results on the effect of external doping induced by the deposition of a few metal clusters and donor/acceptor molecules in the modification of the intriguing electronic structure of pristine 2D graphene using first-principles density functional theory level of calculations. Our results show that the nature of the external dopants has a significant effect in tuning the electronic structure of graphene through charge transfer mechanisms. The presence of dopant metal clusters opens up a small band gap between the valence and conduction bands, and thus offers a possibile semi-metal to perfectly metallic transition. Interestingly, we find typical half-metallic behavior for graphene@Pd_{40} nanocomposite which has potential applications in spintronic device fabrication. We have also shown that the presence of organic donor or acceptor molecules on graphene can significantly change the electronic properties, in particular the characteristic Raman spectra of graphene. For all cases, the magnitude of adsorption energies are found to be moderate, suggesting physisorption process. Similar to the metal cluster dopants, in molecular cases also we find that there is an effective charge transfer, the signature of which is found

experimentally in UV-visible spectra. The stabilization energies are relatively larger for metal cluster dopants compared to the molecular dopants since it is governed by the extent of charge transfer. As a result, the effect in changes of the electronic structure is more pronounced for the former case. We find a downward shift of Fermi level relative to the Dirac point for TCNE and TCNQ adsorbed graphene, whereas the Fermi level shifts upward from the Dirac point for TTF intercalated graphene. Moreover, we have also found that a small band gap opens up in between the valence and conduction bands, and thus, tuning of carrier concentrations indeed can change the graphene electronic structure from semi-metallic to a perfect metallic through semiconducting behavior. Interestingly, we find that the molecular charge-transfer results in stiffening and softening of Raman active G-band frequency depending on the nature of the dopant molecule and an increase in the intensities ratio of D- to G-band in presence of dopants, as found experimentally. Thus, the Raman spectra can be used as a finger print for understanding the molecular charge-transfer interactions in graphene-adsorbate complexes. We also suggest that these charge-transfer effects can be seen in optical conductivity profiles as the low frequency regions are affected by the molecular charge transfer. Since adsorption of donor or acceptor dopants gives rise to tuning of band-gap as well as carrier type in graphene, we propose that it is possible to fabricate the graphene-based electronic devices through simple means, possibly even a p-n junction using both donor and acceptors.

Acknowledgments

References

1. G. Dresselhaus, M. S. Dresselhaus, P. C. Eklund, *Science of Fullerenes and Carbon Nanotubes: Their Properties and Applications*, Academic Press, New York, (1996).
2. K. S. Nonoselov, A. K. Geim, S. V. Morozov, D. Jiang, Y. Zhang, S. V. Dubonos, I. V. Grigorieva, A. A. Firsov, *Science*, **306**, 666, (2004).
3. K. S. Nonoselov, D. Jiang, F. Schedin, T. J. Booth, W. Khotkevich, S. V. Morozov, A. K. Geim, *Proc. Natl. Acd. Sci.*, **102**, 10451, (2005).

4. K. S. Novoselov, A. K. Geim, S. V. Morozov, D. Jiang, M. I. Katsnelson, I. V. Grigorieva, S. V. Dubonos, A. A. Firsov, *Nature*, **438**, 197, (2005).
5. Y. Zhang, Y. W. Tan, H. L. Stormer, P. Kim, *Nature*, **438**, 201, (2005).
6. S. Lakshmi, S. Dutta, S. K. Pati, *J. Phys. Chem. C*, **112**, 14718, (2008).
7. A. K. Geim, K. S. Novoselov, *Nat. Mater.*, **6**, 183, (2007).
8. R. Saito, G. Dresselhaus, M. S. Dresselhaus, *Physical Properties of Carbon Nanotubes*, Imperial College Press, London, (1998).
9. P. M. Ajayan, *Chem. Rev.*, **99**, 1787, (1999).
10. M. S. Dresselhaus, *Carbon*, **33**, 871, (1995).
11. T. W. Ebbesen, *Annul Rev. of Materials Sci.*, **24**, 235, (1994).
12. J. C. Charlier, X. Blase, S. Roche, *Rev. Mod. Phys.*, **79**, 677, (2007).
13. R. S. Baughman, A. A. ZAkhizov, W. A. de Heer, *Science*, **297**, 787, (2002).
14. S. J. Tans, A. R. M. Verschueren, C. Deeker, *Nature*, **393**, 49, (1998).
15. D. M. Guldi, M. Prato, *Acc. Chem. Res*, **33**, 695, (2000).
16. M. Prato, *J. Mater. Chem.*, **7**, 1097, (1997).
17. A. H. Castro Neto, F. Guinea, N. M. R. Peres, K. S. Novoselov, A. K. Geim, *Rev. Mod. Phys.*, **81**, 109, (2009).
18. M. I. Katsnelson, *Mater. Today*, **10**, 20, (2007).
19. C. Berger, Z. Song, X. Li, X. Wu, N. Brown, C. Naud, D. Mayou, T. Li, J. Hass, A. N. Marchenkov, E. H. Conrad, P. N. First, W. A. de Heer, *Science*, **312**, 1191, (2006).
20. M. Y. Han, B. Ozyilmaz, Y. Zhang, P. Kim, *Phys. Rev. Lett.*, **98**, 206805, (2007).
21. F. Schedin, A. K. Geim, S. V. Morozov, E. W. Hill, P. Blake, M. I. Katnelson, K. S. Novoselov, *Nat. Mater.*, **6**, 652, (2007).
22. B. Huard, J. A. Sulpizio, N. Stander, K. Todd, B. Yang, D. Goldhaber-Gordon, *Phys. Rev. Lett.*, **98**, 236803, (2007).
23. E. H. Leib, *Phys. Rev. Lett.*, **62**, 1201, (1989).
24. M. Fujita *et al.*, *J. Phys. Soc. Jpn.*, **65**, 8271, (1999).
25. R. A. de Groot *et al.*, *Phys. Rev. Lett.*, **50**, 2024, (1983).
26. J. -H. Park *et al.*, *Nature (London)*, **392**, 794, (1998).
27. S. M. Mallajosyula, S. K. Pati, *J. Phys. Chem. B*, **111**, 13877, (2007); **112**, 16982, (2008).
28. Y. W. Son *et al.*, *Nature (London)*, **444**, 347, (2006).
29. S. Dutta, S. K. Pati, *J. Phys. Chem. B*, **112**, 1333, (2008).
30. S. Dutta, S. Lakshmi, S. K. Pati, *Phys. Rev. B*, **77**, 073412, (2008).
31. W. Y. Kim, Y. C. Choi, K. S. Kim, *J. Mater. Chem.*, **18**, 4510, (2008).
32. W. Y. Kim, K. S. Kim, *J. Comput. Chem.*, **29**, 1073, (2008).
33. W. Y. Kim, K. S. Kim, *Nat. Nanotechnol.*, **3**, 408, (2008).
34. S. M. Sairam, P. Parida, S. K. Pati, *J. Mater. Chem.*, **19**, 1761, (2009).
35. S. Dutta, A. K. Manna, S. K. Pati, *Phys. Rev. Lett.*, **102**, 096601, (2009).
36. A. Das, S. Pisana, B. chakraborty, S. Piscanec, S. K. Saha, U. V. Waghmare, K. S. Novoselov, H. R. Krishnamurthy, A. K. Geim, A. C. Ferrari, A. K. Sood, *Nat. Nanotechnol.*, **3**, 210, (2008).
37. M. Kalbac, L. Kavan, L. Dunsch, M. S. Dresselhaus, *Nano. Lett.*, **8**, 1257, (2008).

38. M. A. Pimenta, G. Dresselhaus, M. S. Dresselhaus, L. G. Cancado, A. Jorio, R. Saito, *Phys. Chem. Chem. Phys.*, **9**, 1276, (2007).

39. J. Kotakoski, A. V. Krasheninnikov, Y. Ma, A. S. Foster, K. Nordlund, R. M. Nieminen, *Phys. Rev. B*, **71**, 205408, (2005).

40. L. Ci, L. Song, C. Jin, D. Jariwala, D. Wu, Y. Li, A. Srivastava, Z. F. Wang, K. Storr, L. Balicas, F. Liu, P. M. Ajayan, *Nat. Mater.*, **9**, 430, (2010).

41. J. Jhou, Q. Wang, Q. Sun, X. S. Chen, Y. Kawazoe, P. Jena, *Nano Lett.*, **9**, 3867, (2009).

42. E. -J. Kan, Z. Li, J. Yang, J. G. Hou, *J. Am. Chem. Soc.*, **130**, 4224, (2008).

43. B. Das, R. Voggu, C. S. Rout, C. N. R. Rao, *Chem. Commun.*, 5155, (2008); C. N. R. Rao, A. K. Sood, K. S. Subrahmanyam, A. Govindaraj, *Angew. Chem., Int. Ed.*, **48**, 7752, (2009).

44. R. Voggu, B. Das, C. S. Rout, C. N. R. Rao, *J. Phys. Condens. Mater.*, **20**, 472204, (2008).

45. a. K. S. Subrahmanyam, A. K. Manna, S. K. Pati, C. N. R. Rao, *Chem. Phys. Lett.*, **497**, 70, (2010).
    b. A. K. Manna, S. K. Pati, *Chem. Asian J*, **4**, 855, (2009).

46. J. M. Soler, E. Artacho, J. D. Gale, A. Garcia, J. Junquera, P. Ordejon, D. Sanchez-Portal, *J. Phys. : Cond. Matt.*, **14**, 2745, (2002); P. Ordejon, E. Artacho, J. M. Soler, *Phys. Rev. B*, **53**, R10441, (1996).

47. K. Burke, J. P. Perdew, M. Ernzerhof, *Int. J. Quantum Chem.*, **61**, 287, (1997).

48. N. Troullier, J. L. Martins, *Phys. Rev. B*, **43**, 1993, (1991).

49. L. Kleinman, D. M. Bylander, *Phys. Rev. Lett.*, **48**, 1425, (1982).

50. J. P. K. Doye, D. J. Wales, *New. J. Chem.*, **22**, 733, (1998).

51. R. Voggu, S. Paul, S. K. Pati, C. N. R. Rao, *J. Phys. : Cond. Matt.*, **20**, 215211, (2008).

52. A. K. Manna, S. K. Pati, *Nanoscale*, **2**, 1190 (2010).

53. O. Dubay, G. Kresse, *Phys. Rev. B*, **67**, 035401, (2003).

54. K. V. Christ, H. R. Sadeghpour, *Phys. Rev. B*, **75**, 195418 (2007).

55. D. Sanchez-Portal, E. Artacho, J. M. Soler, A. Rubio, P. Ordejon, *Phys. Rev. B*, **59**, 12678 (1999).

Chapter 5

Vibrations and Buckling of Uni-Axially Strained Graphene and BN-Monolayer: A First-Principles Study

K. P. S. S. Hembram and Umesh V. Waghmare

Theoretical Sciences Unit,
Jawaharlal Nehru Centre for Advanced Scientific Research,
Jakkur Campus, Bangalore 560064, India

We present a comparative first-principles analysis of phonons and buckling in graphene and BN-monolayer arising from compressive uni-axial strains along zigzag (Z) direction. We find that the changes in vibrational frequencies with compressive strain depend on (a) in-plane versus out-of-plane polarization of modes, (b) optic versus acoustic nature of the modes. While the responses of graphene and BN-monolayer are similar qualitatively, graphene exhibits a remarkable anisotropy in the changes in inter-atomic forces due to uni-axial strain compared to those of BN-monolayer. For modes with in-plane atomic displacements, optic modes at all the wave-vectors harden, while acoustic modes soften with compressive uni-axial strain. This hardening of optic modes is stronger at all wave vectors for graphene than for BN-monolayer, except at the Γ point. On the other hand, softening of acoustic modes are stronger in BN-monolayer than in graphene, revealing stronger hyperelastic nature of BN than graphene. For the modes with out-of-plane polarization, most modes of BN-monolayer and graphene soften with compressive uniaxial strain exhibiting a strong dependence on the direction of wave vector. Flexural acoustic modes with out-of-plane polarization, relevant to buckling, exhibit instabilities for compressive uni-axial strain greater than a nonzero value, demonstrating an intrinsic buckling strength of graphene and BN-monolayer. Analogus to strong electron-phonon coupling in graphene, we find that the electronic band-gap of BN-monolayer depends sensitively on strain and even vanishes for large enough compressive uni-axial strain of 0.2.

1. Introduction

Graphene composed of a layer of sp^2 bonded carbon (C) atoms arranged on a honeycomb lattice, possesses topologically different edge profiles such as

zigzag (Z) and armchair (A), which stay orthogonal to each other. Its fascinating electronic and vibrational properties have a great potential for variety of applications.These include effectively relativistic dynamics of charge carriers,[1] anomalous quantum Hall effect.[2] These phenomena discovered earlier, with different materials possess different structure and composition, but only carbon based material such as graphene showing the similar phenomena is quite interesting. Its use as a semiconductor in nano-electronic circuits is however limited due to its vanishing bandgap. In contrast to graphene which possess as zero bandgap, BN with a similar structure is an insulator. B and N atoms are one electron deficient and one electron rich compared to C, leading to polar bonding in BN which is analogous to graphene. Aming at the improved properties of BN over graphene various researchers have synthesized BN for various applications.[3–5]

Mermin and Wagner's argument for non-existence of truly long range 2D ordering crystal,[6] is refreshed by the discovery of graphene[7] with little buckling or corrugation.[8,9] The underlying mechanisms and quantitative analysis of buckling are necessary to answer fundamental features probed through sophisticated experiments, and also for technological applications.

The buckling strength can be estimated by applying compressive strain and measuring the critical stress. Critical strain is the amount of strain that graphene can withstand without buckling. Quantitatively thermal fluctutation is a measure for buckling at finite temperature. But at 0K, the linear along with the quadratic terms in the dispersion of flexural modes are responsible for buckling.[10] Various researchers have investigated graphene subjected to the tensile uni-axial strain to understand the underlying microscopic picture, not only theoretically,[11–16] but also with the support from properties, observed experimentally.[15–17] Theoretically, large strain shows clear features of opening of band gap, but for small strain it becomes controversial.[18] In the reality the maximum tensile strain realised experimentally has been a few percent. In this article, we study the flexural modes of uni-axially compressive strained BN and compare its results with graphene.

2. Methods

We use plane wave self consistent field (PWSCF)[19] implementation of density functional theory (DFT), with a local density approximation (LDA) to the exchange correlation energy of electrons, and ultrasoft pseudopotentials,[20,21] to represent interaction between ionic cores and valence electrons.

Kohn-Sham wave functions were represented with a plane wave basis with an energy cutoff of 40 Ry and charge density cutoff of 480 Ry. To facilitate a direct comparison, graphene and BN were simulated using the same periodic supercell with a vacuum of 16 Å in the direction perpendicular to the plane. Integration over the Brillouin zone was sampled with a 20 X 10 X 1 Monkhorst-Pack mesh[22] grid points and occupation numbers were semeard using Methfessel-Paxton scheme[23] with a broadening of 0.01 Ry. Convergence was checked with finer meshes of k-points in sampling the Brillouin zone.

3. Results

3.1. *Structure*

We use a unit cell containing 4 atoms as shown in Fig. 1(a) for graphene and in Fig. 1(b) for BN-monolayer. To ensure that no two B or N atoms are the nearest neighbors, we consider the homogeneous distribution of B and N in the ab-plane which is expected to be favored from configurational entropy minimization in the experimental synthesis procedure. Properties like conductivity differ from *Z*- to *A*-direction. Similarly the properties may be drastically different for the uni-axial strain applied along different directions.

When we apply a series of compressive strain along *Z*- and *A*-direction and simultaneously relax the structure, the system minimizes the energy
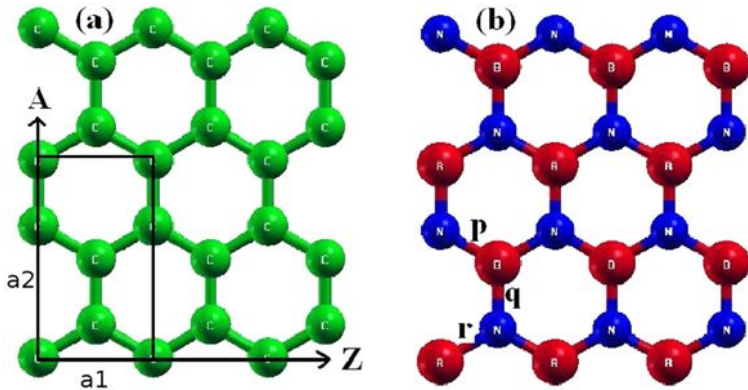
Fig. 1. (Color online) Two dimensional honeycomb structure with 4 atoms in the unit cell of (a) Graphene, (b) BN-monolayer.

using forces on each atom retaining the minimal residual stress. The stress on the graphene and BN-monolayer is shown in the Fig. 2(a). It is clear that the graphene possess slightly higher stress than that of BN at all values of applied strain.
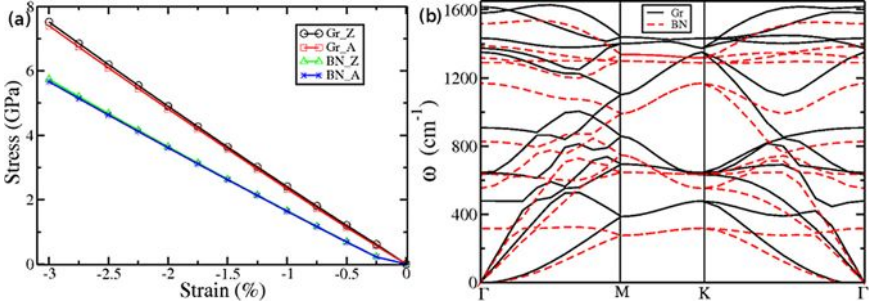
Fig. 2.　(Color online) (a) Stress on graphene and BN-monolayer as a function of uniaxial compressive strain. (b) Phonon dispersion of graphene and BN-monolayer.

3.2. *Phonons*

Phonon dispersion of graphene and BN-monolayer over the symmetry point on the Brillouin zone is shown in the Fig. 2(b). It is evident from the phonon dispersion that flexural acoustic modes are significantly softer in BN (310 cm^{-1} at K point) than those in graphene (527 cm^{-1} at K point). The Brillouin zone along with symmetry points of graphene and BN-monolayer with 4 atoms in the unit cell, with strain along Z-direction is shown in the Fig. 3. Comparison of flexural modes of graphene and BN-monolayer when the compressive strain is applied along Z-direction is shown in Fig. 4. It is clearly seen that the negative frequencies shown by both BN-monolayer and graphene indicate the structures are unstable with the applied compressive strain. The instability of BN-monolayer is stronger than that of graphene. The dependence of frequency on wave vector gives an indication of the elastic nature of the graphene or BN-monolayer. The best fit to omega (ω) vs q needs the following terms at the lowest order.

$$\omega^2_{flex} = \alpha * q^2 + \beta * q^4$$

The value of α does not change much for small strains, but drops to negative value for large enough compressive strain (see Fig. 5(a)). In the

unstrained case the value of α for graphene is 74 while that for BN-monolayer is 65 (*Z*-direction) with critical strains of -1.93 % and -1.77 % respectively.

Long-range structural order of an isolated 2D graphene sheet can be understood from the existence of the flexural modes. The number of flexural modes (if one assumes purely quadratic dispersion) per unit area at a certain temperature is given by

$$N_{flex} = \frac{1}{2\pi} \int_0^\infty dk \frac{k}{e^{\beta\sqrt{\kappa/\sigma}k^2} - 1}$$

with each flexural mode oscillating like quantum harmonic oscillator[24] with the frequency given by

$$\omega_{flex} = \left(\frac{\kappa}{\sigma}\right)^{\frac{1}{2}} k^2$$

The parameter σ is graphene's 2D mass density, κ is the bending stiffness, $\beta = 1/k_\beta T$. For $T \neq 0$ the above integral is logarithmically divergent in the long wavelength region indicating a divergent number of phonons in the thermodynamic limit. For a system with finite size L, with $L >> L_T$, (L_T is the thermal wavelength of the flexural modes) one finds the number of flexural modes diverges logarithmically with the size of the system. Hence

$$N_{flex} = \frac{2\pi}{L_T^2} ln(L/L_T)$$

where

$$L_T = \frac{2\pi}{\sqrt{k_\beta T}} (\kappa/\sigma)^{\frac{1}{4}}$$

indicating that the system cannot be structurally ordered at any finite temperature. This is nothing but the buckling instability.[24] For $L << L_T$, one finds that N goes to zero exponentially with the size of the system, indicating that systems with finite size can be flat at sufficiently low temperature.

Since our calculations here are based on 0K, we expect the similar characteristics. With applied compressive strain of a finite nonzero value, the scenario becomes different and hence the nature of the flexural modes. When compressive strain is applied uni-axially on the graphene, the atoms in the graphene adjust collectively remaining in the plane till the critical strain, beyond which they move out-of plane, causing the corrugation or buckling.
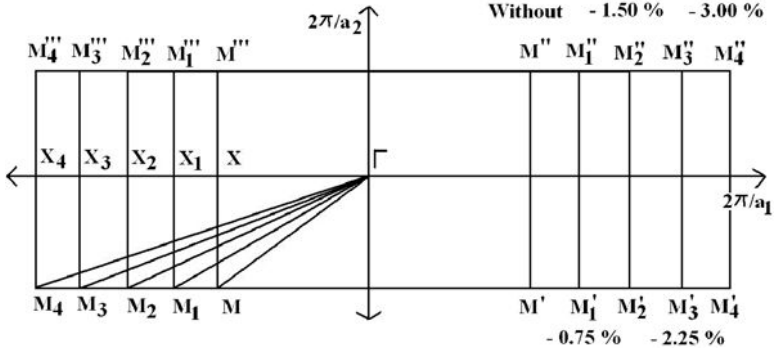
Fig. 3.   Schematic diagram of compressive strained Brillouin Zone along the Z-direction.
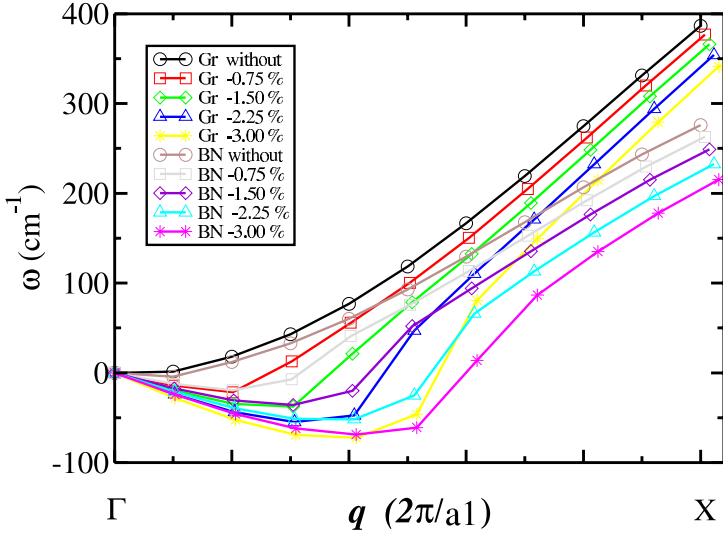
Fig. 4.   (Color online) Branch of flexural modes with compressive strain along Z-direction.

The values of acoustic and optical phonon frequency at the symmetry point on the Brillouin zone (listed in the Tables 1 and 2 for uni-axially strained along Z- and A-direction) suggest that the optical phonon modes at all the symmetry point harden and the acoustic phonon modes soften. Interestingly, optical phonon modes harden more for graphene than that of BN-monolayer in all the cases except at the Γ point, where the optical

phonon modes harden more for BN-monolayer than for graphene. On the other hand the acoustic phonon modes soften more for BN-monolayer than those of graphene.

Table 1. Calculated phonon frequencies of graphene and BN-monolayer (at different symmetry points on the Brillouin zone) with different uni-axial compressive strain along Z-direction.

System with strain	Γ (optic) cm^{-1}	X (acoustic) cm^{-1}	X (optic) cm^{-1}	M (acoustic) cm^{-1}	M (optic) cm^{-1}
Gr 0.00 %	1618	383	1435	474	1435
Gr-Z -0.75 %	1635	377	1465	470	1458
Gr-Z -1.50 %	1655	366	1487	462	1492
Gr-Z -2.25 %	1657	353	1514	454	1516
Gr-Z -3.00 %	1657	341	1543	446	1532
BN 0.00 %	1523	274	1337	313	1323
BN-Z -0.75 %	1543	263	1358	303	1337
BN-Z -1.50 %	1566	248	1380	298	1362
BN-Z -2.25 %	1587	234	1399	277	1381
BN-Z -3.00 %	1610	215	1422	269	1407

Table 2. Calculated phonon frequencies of graphene and BN-monolayer (at different symmetry points on the Brillouin zone) with different uni-axial compressive strain along A-direction.

System with strain	Γ (optic) cm^{-1}	X (acoustic) cm^{-1}	X (optic) cm^{-1}	M (acoustic) cm^{-1}	M (optic) cm^{-1}
Gr 0.00 %	1618	383	1435	474	1435
Gr-A -0.75 %	1651	382	1450	474	1457
Gr-A -1.50 %	1666	380	1463	469	1494
Gr-A -2.25 %	1674	374	1493	470	1518
Gr-A -3.00 %	1726	369	1523	466	1548
BN 0.00 %	1523	274	1337	313	1323
BN-A -0.75 %	1535	269	1354	307	1337
BN-A -1.50 %	1551	267	1372	303	1352
BN-A -2.25 %	1568	256	1394	299	1358
BN-A -3.00 %	1587	248	1419	291	1401

Figure 5(b) shows atomic displacements in flexural modes of graphene and BN-monolayer at different compressive strain. At M point, the flexural modes for compressive strain along Z-direction are larger than that of flexural modes for compressive strain along A-direction for both graphene and

BN-monolayer. The compressive strain along *Z*- or *A*-directions softens the M point optical modes with out-of plane displacements for graphene. Interesting features arise in the acoustic flexural modes. The acoustic flexural modes for q along *A*-direction hardly change with the application of compressive strain along *Z*-direction for graphene, but soften if the compressive strain along *A*-direction. On the other hand, the acoustic and optical flexural modes of BN-monolayer soften with compressive strain applied along either of *Z*- and *A*-directions.
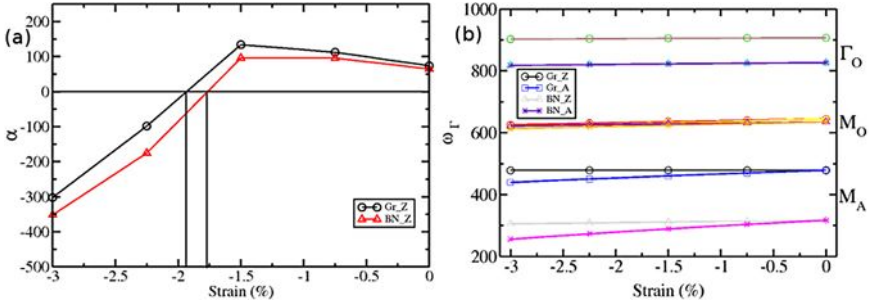
Fig. 5. (Color online) (a) The parameter α at different compressive strain, (b) Flexural modes of graphene and BN-monolayer at different compressive strain.
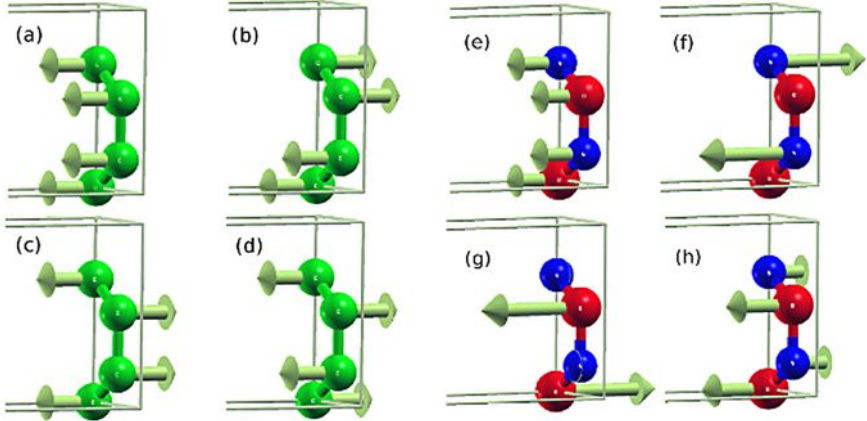
Fig. 6. (Color online) Eigen displacements of C atoms of graphene with compressive strain of -1.5 % along *Z*-direction (a) 0 cm^{-1} (b) 479 cm^{-1} (c) 636 cm^{-1} (d) 905 cm^{-1}, and those of B and N atom of BN-monolayer with compressive strain of -1.5 % along *Z*-direction (e) 0 cm^{-1} (f) 311 cm^{-1} (g) 629 cm^{-1} (h) 823 cm^{-1}.

The origin of buckling instability can be understood with the visualization of eigen displacement of the atoms at a definite strain. There are two equivalent sites in the unit cell of the hexagonal structure. We consider the atoms placed at the same sub-lattice as a-site and the other sub-lattice as b-site respectively. Figures 6(a)-(d) show the eigen displacement of C atoms when the compressive strain is applied along Z-direction. We note that modes in Figs. 6(a) and (d) are the z-polarized Γ-point acoustic and optic modes respectively and those in Figs. 6(b) and (c) are the M-point acoustic and optic modes respectively. The C atoms irrespective of the sites displaces out of plane at lower acoustic frequency (see Fig. 6(a)). Figure 6(b) shows that at frequency 479 cm^{-1} the two C atoms present at a-sites displaces in opposite direction and the other two C atoms present at b-sites also displaces oppositely w.r.t. each other. At higher frequency 636 cm^{-1}, (see Fig. 6(c)) the two C atoms present at a-sites displaces oppositely w.r.t. each other and the two other C atoms present at b-sites displaces oppositely w.r.t. each other. But the atoms present at b-sites changes their displacement direction at frequency 636 cm^{-1} opposite to that of at frequency 479 cm^{-1} while the atoms present at a-sites retain the same displacement direction. At higher frequency (905 cm^{-1}) the nature of displacement once more changes as shown in Fig. 6(d). The atoms at a-sites displace uni-directionally which are opposite to the atoms present at b-sites.

The eigen displacement of the B and N atoms are similar in nature to that of graphene, but vary with magnitude with the applied strain, irrespective of the strain direction. We consider the similar terminology retaining position of the B atoms at a-sites and N atoms at b-sites. The modes in Figs. 6(e) and (h) are the z-polarized Γ-point acoustic and optic modes respectively and those in Figs. 6(f) and (g) are the M-point acoustic and optic modes respectively. We comparatively show the eigen displacement of atoms when the compressive strain is applied along Z-direction as shown in Figs. 6(e)-(h).

In Fig. 6(e) the B and N atoms displacement are in phase, and directed out of the BN plane. In Fig. 6(f) there is hardly any eigen displacement of the B atoms which are placed at the a-sites at frequency 311 cm^{-1}. But N atoms which are present at b-sites show eigen displacement out-of-plane and opposite to each other. On the other hand in Fig. 6(g) the B atoms which are present at a-sites shows eigen displacement out-of-plane and opposite to each other and there is hardly any eigen displacement of the N atoms which are placed at the b-sites at frequency 629 cm^{-1}. Again at higher

frequency (823 cm^{-1}) the B atoms which are present at *a*-sites show eigen displacement out-of-plane with same phase and the N atoms which are present at *b*-sites shows eigen displacement out-of-plane with same phase (see Fig. 6(h)). But the eigen displacement of B atoms and N atoms are opposite in phase.

Thus, eigen displacement of modes at M-point are clearly different in BN-monolayer from those of graphene. Compressive strain along *Z*-direction causes softening only of the M-point optical phonon where as compressive strain on graphene along *A*-direction softens acoustic and optical phonon, at M point. But for BN-monolayer all optical phonon and acoustic phonon soften. Comparing the frequencies at each symmetry point, we infer that graphene is more sensitive than BN towards compressive strain.

3.3. *Electronic structure*
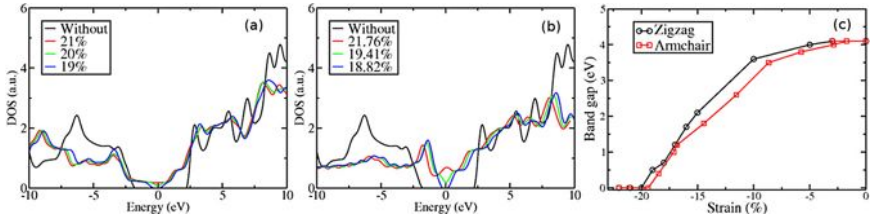
Fig. 7.   (Color online) Electronic density of states BN-monolayer with compressive strain along (a) *Z*-direction, (b) *A*-direction. (c) Band gap variation of BN-monolayer with applied compressive strain.
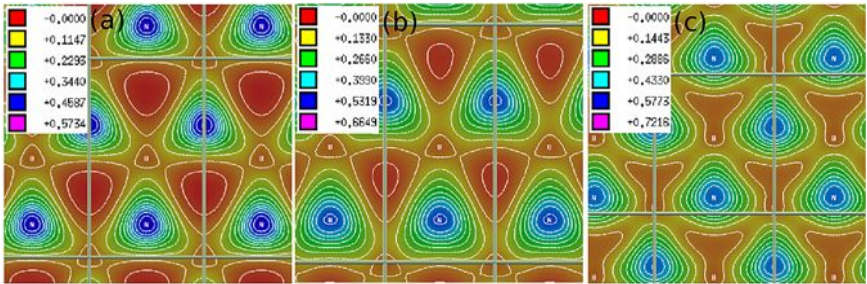
Fig. 8.   (Color online) Charge density contour plot on a planar surface of (a) unstrained BN-monolayer, (b) compressive strain along *Z*-direction, (c) compressive strain along *A*-direction.

We now determine effect of compressive strain on electronic structure by examining electronic density of states (EDOS) and visualising charge density contour plots of BN-monolayer. Calculated bandgap of unstrained BN-monolayer is about 4.1 eV which is comparable to 4.5 eV calculated by Terrones *et al*[25] and graphene shows a Dirac cone at K point in the Brillouin zone.[14] For small compressive strain, there is no significant change in EDOS of both in BN and graphene, which is also true for tensile strain investigated by other researchers.[15–17] As the compressive strain is increased the insulating BN turns metallic for a strain of 20 % (see Fig. 7(a)) for *Z*- and (see Fig. 7(b)) for *A*-directions. The variation of the band gap of BN-monolayer with applied compressive strain is shown in the Fig. 8(c). Although around 20 % uni-axial compressive strain causes insulator to metallic transition, its effect on the electronic structure depends on the direction of strain. We note that the insulator-metal transition occurs when buckling is not permitted. This may be possible experimentally with an appropriate choice of substrate.

Greater stability of graphene over BN-monolayer is due to the isotropic distribution of C atoms which are bonded with sp^2 hybridized orbitals and possess partially filled p_z orbital lying perpendicular to the graphene plane. In case of BN-monolayer B possess one electron less than that of C atom and N retains one extra electron than that of C atom. Further-more the electronegativity of B atom is 2.04 and that of N atom is 3.04 according to the Pauling scale.[26] Hence N atom tends to influence more the bonding electron than that of B atom in BN-monolayer which is clearly observed in the contour plot (see Fig. 8). Although in the unit cell the number of electrons participating in bonding are the same in both the cases, their nature is polar in BN. This local inhomogeneity of electron distribution in BN makes the structure more unstable with the application of compressive strain.

Local inhomogeneity of electron distribution can easily realised by observing the bond lengths summarised in Table 3. Around 20 % uni-axially

Table 3. Calculated bond length of B-N for BN-monolayer with different uni-axial strain where the transformation takes place from insulator to metallic nature.

B-N bond (See Fig. 1(b))	Unstrained (Å)	Strained along *Z*-direction (Å)	Strained along *A*-direction (Å)
p	1.43	1.29	1.26
q	1.43	1.32	1.23
r	1.43	1.29	1.26

stain, (irrespective of the *Z*-or *A*-direction) where the insulating nature of BN-monolayer changes to metallic, the bond lengths vary for strain applied in *Z*-direction and that of strain applied in *A*-direction. The dis-similarity in bond length along with the electronegative difference of B and N atoms, drives the electron cloud more towards the N atom, which is reflected in the contour plot in Fig. 8. With the applied strain the shape of the electron cloud also distorts as revealed from the Fig. 8(b) (compressive strain is applied along Z-direction) and Fig. 8(c) (compressive strain is applied along A direction), those differ from Fig. 8(a) where the electron cloud is distributed isotropically.

4. Conclusion

In conclusion, we have presented a comparative study of flexural modes of graphene and BN-monolayer. The critical uniaxial compressive strain along *Z*-direction of graphene is -1.93 % while it is -1.77 % for BN-monolayer at which buckling occurs. Compared to BN-monolayer, graphene exhibit a stronger anisotropy in changes in the inter-atomic forces due to uni-axial strain. At around 20 % of compressive strain insulating BN-monolayer becomes metallic. We suggest that strained BN-monolayer can be used as a tunable bandgap material for various applications.

Acknowledgment

References

1. K. S. Novoselov, A. K. Geim, S. V. Morozov, D. Jiang, M. I. Katnelson, I. V. Grigorieva, S. V. Dubonos, A. A. Firsov, *Nature*, **438**, 197 (2005).
2. Y. Zhang, Y. W. Tan, H. L. Stormer, P. Kim, *Nature*, **438**, 201 (2005).
3. W. Q. Han, L. Wu, Y. Zhu, K. Watanabe, T. Taniguchi, *Appl. Phys. Lett.*, **93**, 223103 (2008).
4. C. Zhi, Y. Bando, C. Tang, H. Kuwahara, D. Golberg, *Adv. Mater.*, **21**, 2889 (2009).
5. A. Nag, K. Raidongia, K. P. S. S. Hembram, R. Dutta, U. V. Waghmare, C. N. R. Rao, *ACS Nano*, **4**, 1539 (2010).
6. N. D. Mermin, *Phys. Rev.*, **176**, 250 (1968).
7. K. S. Novoselov, A. K. Geim, S. V. Morozov, D. Jiang, Y. Zhang, S. V. Dubonos, I. V. Grigorieva, A. A. Forsov, *Science*, **306**, 666 (2004).

8. J. C. Meyer, A. K. Geim, M. I. Katnelson, K. S. Novoselov, T. J. Booth, S. Roth, *Nature*, **446**, 60 (2007).
9. A. Fasolino, J. H. Los, M. I. Katnelson, *Nat. Mater.*, **6**, 858 (2007).
10. S. Kumar, K. P. S. S. Hembram, U. V. Waghmare, *Phys. Rev. B* (in press).
11. F. Liu, P. Ming, J. Li, *Phys. Rev. B*, **76**, 064120 (2007).
12. G. Gui, J. Li, J. Zhong, *Phys. Rev. B*, **78**, 075435 (2008).
13. M. Mohr, K. Papagelis, J. Maultzsch, C. Thomsen, *Phys. Rev. B*, **80**, 205410 (2009).
14. V. M. Pereira, A. H. C. Neto, *Phys. Rev. Lett.*, **103**, 046801 (2009).
15. T. M. G. Mohiuddin, A. Lombardo, R. R. Nair, A. Bonetti, G. Savini, R. Jalil, N. Bonini, D. M. Basko, C. Galiotis, N. Marzari, K. S. Novoselov, A. K. Geim, A. C. Ferrari, *Phys. Rev. B*, **79**, 205433 (2009).
16. C. Lee, X. Wei, J. W. Kysar, J. Hone, *Science*, **321**, 385 (2008).
17. Z. H. Ni, T. Yu, Y. H. Lu, Y. Y. Wang, Y. P. Feng, Z. X. Shen, *ACS Nano*, **2**, 2301 (2008).
18. S. M. Choi, S. H. Jhi, Y. W. Son, *Phys. Rev. B*, **81**, 081407(R) (2010).
19. S. Baroni, A. Dal Corso, S. de Gironcoli, P. Giannozzi, *http://www.pwscf.org.*
20. D. Vanderbilt, *Phys. Rev. B*, **41**, 7892 (1990).
21. J. P. Perdew, A. Zunger, *Phys. Rev. B*, **23**, 5048 (1981).
22. H. J. Monkhorst, J. D. Pack, *Phys. Rev. B*, **13**, 5188 (1976).
23. M. Methfessel, A. T. Paxton, *Phys. Rev. B*, **40**, 3616 (1989).
24. A. H. C. Neto, F. Guinea, N. M. R. Peres, K. S. Novoselov, A. K. Geim, *Rev. Mod. Phys.*, **81**, 109 (2009).
25. M. Terrones, J. M. R. Herrera, E. C. Silva, F. L. Urias, E. M. Sandoval, J. J. Velazquez, H. Terrones, Y. Bando, D. Golberg, *Mater. Today*, **10**, 30 (2007).
26. A. L. Allred, *J. Inorg. Nucl. Chem.*, **17**, 215 (1961).

Chapter 6

Raman Spectroscopy of Graphene Edges

Riichiro Saito

Department of Physics, Tohoku University, Sendai 980-8578, Japan
rsaito@flex.phys.tohoku.ac.jp

Raman spectroscopy of graphene edges is overviewed mainly from the theoretical point of view. There are two symmetric edge structures of graphene, armchair and zigzag edges. Because of the symmetry, a different Raman spectra and its polarization dependence are predicted within the bond-polarization theory. This result is useful for characterization of the edge structure.

1. Introduction

Graphene is a one atomic layer of graphite. Since graphite is known to be micro-clevaged into thin layers of graphene up to one atomic layer and up to 100μm in size on the substrate by a rather simple method using Scotch tape, many researchers have measured one atomic layer of graphene[1–8] without using a special nano-technology. Graphene is a two-dimensional solid and the electronic structure of graphene has a unique character at the Fermi energy, such as massless Fermion particle and zero energy gap at the hexagonal corner of two dimensional (2D) Brillouin zone. In the case of graphite, on the other hand, because of inter-layer interaction between two graphene layers smears out the uniqueness of the electronic structure and semi-metallic nature might be seen, though some exotic character of graphene (high mobility) can still be seen.

An important message of graphene physics especially in the transport properties is that the mobility of a suspended graphene is very high (up to 200,000cm^2/Vs) even at room temperature. Thus once we get an energy gap for graphene, we can make a field effect transistor with high on-off switching ratio which can operate at a high frequency up to 100GHz which is a big challenge for new semiconducting devices. In a graphene device,
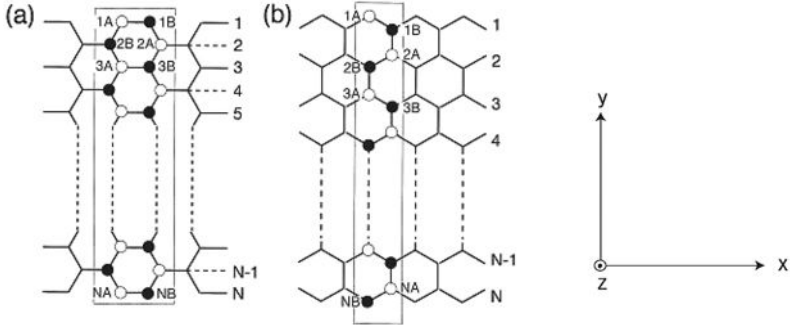
Fig. 1. The unit cell of (a) an armchair and (b) a zigzag graphene nano-ribbon (GNR). The graphene ribbon lies in the xy plane and the edge (periodic) direction is along x. The boxes in the figure are the one-dimensional unit cell of GNR.[58]

we make so-called graphene nano-ribbon (GNR) structure with finite width and periodic structure in one direction. If we make a GNR with a width in the order of 1nm, quantum confinement of an electron occurs and some energy gap would open,[9] which is similar to the case of semiconductor single wall carbon nanotubes.[10,11]

A GNR has two edges at the both sides. Finite size graphene can have two symmetric edge structures which are known as armchair and zigzag edges[12] as shown in Figs. 1(a) and (b), respectively. In Fig. 1, GNR lies on xy plane and the edge structure is along x direction with the finite width in y direction. Unlike carbon nanotubes where all chiralities are found, experiments show that armchair and zigzag edges of heat-treated GNRs are stable and dominant. Because of a lack of translational symmetries in the direction perpendicular to the edge, and because of the special symmetries that each of the two edges possesses, the electron and phonon states exhibit unique behaviors which affect the physical properties of graphene especially for small width graphene nanoribbons.[13] For example, localized electron states appear near the zigzag edge, and the zigzag edge states form a flat energy band at the Fermi energy.[12,14] Since the edge states are partially occupied by π electrons, the magnetic properties of edge states show ferromagnetic behavior because of the exchange interaction between spins in the flat energy band structure.[15] Another important fact about the edge state is that the amplitude of the wavefunction has a large value only on one of the two sub-lattices of graphene, that is, the one which enhances the electron-phonon interaction[16,17] only near the zigzag edge.

Thus possible superconductivity may appear at these edges.[18,19] Igami *et al.* discussed the possible phonon edge states of nano graphite-ribbons with zigzag edges.[20] Similar edge phonon modes are observed in a single wall carbon nanotube (SWNT) with finite length.[21]

Thus characterization of the edge structure is an important topic in the graphene physics. Although scanning tunneling microscope and spectroscopy (STM/STS) show a direct measurement of the edge structure and states of graphene,[22,23] respectively, it is not easy to get a high technique of (STM/STS) in high resolution of space and energy. Here we present calculations for the Raman spectra for GNRs with armchair and zigzag edges, which should be useful for characterization of the edge structure.

Raman spectroscopy of graphite, graphite intercalation compounds (GICs),[24,25] and n-layer graphene (n-LG)[26–28] have been widely investigated, which is useful for sample characterization and for understanding their electronic structure. The Raman spectra of the G′ band as well as the G′ band intensity for n-LG[26] shows that the G′ band intensity relative to that of the G band, which are both defect-free Raman spectra, depends on the number of layers n which is consistent with theoretical calculations.[29]

In the presence of edges, an elastic scattering of photo-excited carriers at each edge is expected, which is the origin of defect-induced Raman spectra, such as the D band ($\sim 1350 \text{cm}^{-1}$), and the D′ band ($\sim 1620 \text{cm}^{-1}$).[30–32] In fact, when D-band intensity imaging of graphene is shown for a finite size graphene sample, the D-band intensity is strong near the edges.[32] These defect-induced spectra are second-order, one-phonon Raman spectra which consist of non-zero q inelastic scattering and $-q$ elastic scattering events, or *vice versa*. When two of the three intermediate states, including the excited states produced by the electron-photon interaction, are real states of graphene, the Raman intensity can be greatly enhanced when two of the three energy denominators of the second-order Raman intensity expression are nearly zero, which is known as double resonance Raman spectroscopy.[33,34] In an earlier calculation, we simply considered the elastic scattering as a reflection of the photo-excited carrier in which the momentum parallel (perpendicular) to the edge is conserved (changes its sign).[35] Here we do not consider the D and D′ bands but instead restrict ourselves only to the zone-center phonon mode. Recent experiments and calculations show that there are edge-phonon oriented Raman spectra for zone-centered phonon features such as at 1450cm^{-1} and 1530cm^{-1} which are assigned to edge phonon spectra for zigzag and armchair edges, respectively.[36]

Thus it is of interest for us to distinguish between the Raman spectra of edge-phonon modes and the Raman spectra of zone-center phonon mode of the graphene crystal by changing the polarization direction of the light or by changing the edge structure, which is the main subject of this article. In II, the calculation method is briefly given. Then in III, the calculated Raman spectra of graphene edges are presented. In IV a discussion and summary of the results are given.

2. Method

The calculation of the Raman spectra consists of two home-made computer programs which calculate phonon eigenvectors and non-resonant Raman spectra.

The phonon eigenvectors are calculated by a tight-binding force constant model[11] in which the force constant sets have been recently updated up to the 14th nearest neighbors by fitting to inelastic X ray scattering measurements.[37] For the most distant force constant at the 14th nearest neighbor, we set it so as to satisfy the force constant sum rule[38,39] is applied to 2D graphene for obtaining zero frequencies of acoustic phonon mode at Γ point. For a graphene ribbon, since the long-distance neighbor atoms are missing near the edge carbon atoms, we use the force constants up to the existing atoms. It is confirmed that the calculated, lowest phonon frequencies of GNRs are sufficiently close to $0 \mathrm{cm}^{-1}$ within the accuracy of the calculation.

The Raman spectra calculated in this paper are based on the so-called bond-polarization theory which gives the non-resonant Raman spectrum intensity.[11,40,41] Since the resonance condition is always satisfied in the case of graphene for any laser excitation energies due to the continuous joint density of states, the relative intensity of each phonon mode can be discussed by a non-resonance Raman tensor.[a]

The scattering geometry of the light is specified by the symbols $iISs$ (i, $s = x$, y, z and I, $S = X$, Y, Z) in which i and s (I and S) denote propagating (polarization) directions of the incident and scattered light, respectively.[b] Here we consider the following four backscattering geometries, $zXX\bar{z}$, $zXY\bar{z}$, $zYY\bar{z}$, and $yZZ\bar{y}$. The propagating direction of the

---

[a]However, we should consider the optical transition matrix elements along the GNR direction if we calculate resonance Raman spectra.

[b]In the bond polarization theory, we can not specify the propagating direction but we can only specify the polarization direction. Because of the electromagnetic wave propagation, i and I (or s and S) should be perpendicular to each other.

incident and scattering light is selected as the z (y) direction for the XX, XY, and YY (ZZ) polarizations. The polarization direction is rotated along z (y) axis with keeping VV and VH geometry. Here VV (VH) configuration means that incident and scattered polarization of the light is parallel (perpendicular) to each other.

The ribbon width N is defined by the number of C-C lines parallel to the ribbon direction and the corresponding numbers of carbon atoms in the unit cell of armchair and zigzag GNRs are $2N$ for both cases as shown in Fig. 1. Here, we consider only N = odd for armchair (zigzag) GNRs in which the corresponding point group symmetry is D_{2h} (C_{2v}). We can also consider the other possibility of N = even for armchair (zigzag) GNRs with C_{2v} (D_{2h}) symmetry.[c] Point group theory tells us that the Raman-active modes belong to irreducible representations of D_{2h}: (A_g, x^2, y^2, z^2), (B_{1g}, xy), (B_{2g}, xz), and (B_{3g}, yz) and C_{2v}: (A_1, x^2, y^2, z^2), (A_2, xy), (B_1, xz), (B_2, yz). In particular, for geometries $zXX\bar{z}$ and $zYY\bar{z}$, the A_g (A_1) mode is Raman active, while for $zXY\bar{z}$ and $zYX\bar{z}$, the B_{1g} (A_2) mode is Raman active for D_{2h} (C_{2v}).

3. Calculated Raman Spectra

In Fig. 2, the non-resonant Raman intensities of $N = 9$ armchair GNR are plotted as a function of the polarization angle relative to a GNR direction where (a) and (b) the polarization direction of incident light is rotated from X to Y axis, while (c) the polarization direction is rotated from X to Z axis (See Fig. 1). Figures 2(a) and (c) are VV geometry while Fig. 2(b) is VH geometry. RBLM, EDGE, LO and TO denote, respectively, the radial breathing-like phonon mode (RBLM) at 310cm^{-1}, the edge phonon modes (EDGE) at 1217cm^{-1}, the longitudinal optical (LO) and in-plane transverse optical (TO) phonon modes which appear 1580cm^{-1}, whose vibration amplitudes are illustrated in Fig. 3. In Fig. 3, we also show the overtone of RBML mode as RBLM3 which is also Raman active whose frequency appears three times (900cm^{-1}) as large as that for RBLM. It is noted that the out-of-plane optical phonon mode is not a Raman-active mode. The LO, RBLM (RBLM3), and edge modes belong to A_g symmetry while TO belongs to B_{1g} (xy) symmetry, which are all Raman active.

---

[c]Further, in a special case of the zigzag case with N = half integer, a different type of edge (the so-called the Klein edge) appears.[15] The extension of the present calculation to this case will be given in the near future.
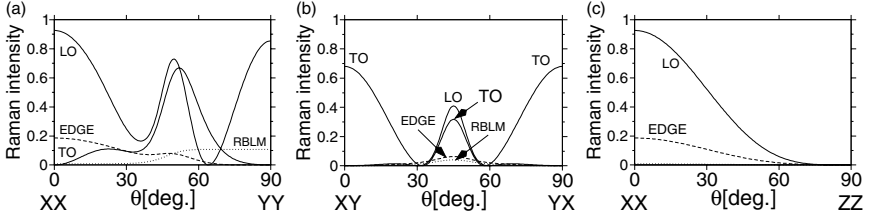
Fig. 2.   The non-resonance Raman spectra of an $N = 9$ armchair GNR as a function of the polarization angle of (a) from $zXX\bar{z}$ to $zYY\bar{z}$, (b) from $zXY\bar{z}$ to $zYX\bar{z}$, (c) from $zXX\bar{z}$ to $xZZ\bar{x}$. The Raman intensity is in arbitrary unit. Solid lines denote LO and TO phonons, while dashed and dotted lines denote, respectively, edge and RBML phonons.[42]
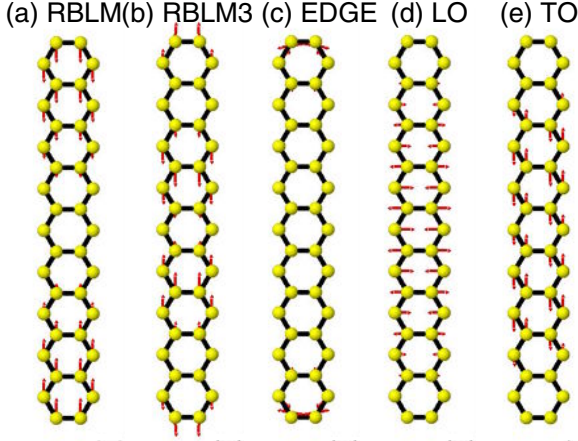
Fig. 3.   Phonon eigenvectors of an $N = 19$ armchair GNR for (a) RBLM, (b) RBLM3, (c) EDGE (d) LO and (e) TO phonon modes.[58]

The TO and LO modes are related to the Raman G band of sp^2 carbon materials whose vibrational amplitudes are perpendicular and parallel, respectively, to the armchair edge, that is, along the one dimensional k direction. As shown in Fig. 2(a), LO and EDGE Raman intensity is strong for $\theta = 0$, that is, $zXX\bar{z}$ while TO phonon modes have a maximum around θ=50 degree. RBML has a maximum around θ=90 degree ($zYY\bar{z}$). Since the ribbon width is vibrating in the RBLM mode, which is similar to the radial breathing mode of a single wall carbon nanotube,[43] it is reasonable that RBLM has a maximum Raman intensity for $zYY\bar{z}$ in the VV configuration.
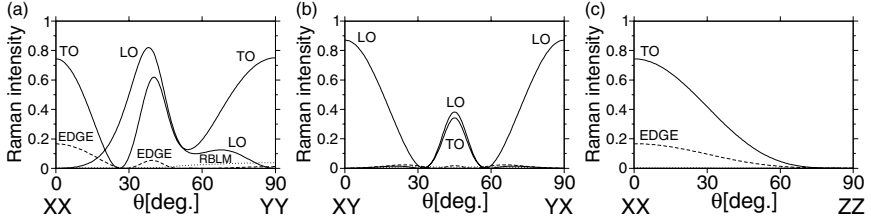
Fig. 4. The non-resonance Raman spectra of an $N = 9$ zigzag GNR as a function of the polarization angle of (a) from $zXX\bar{z}$ to $zYY\bar{z}$, (b) from $zXY\bar{z}$ to $zYX\bar{z}$, (c) from $zXX\bar{z}$ to $xZZ\bar{x}$. The Raman intensity is in arbitrary unit. Solid lines denote LO and TO phonons, while dashed and dotted lines denote, respectively, edge and RBML phonons.[42]

The RBLM frequency is inversely proportional to the ribbon-width.[d] The amplitude of the edge phonon mode has a significant value only near the armchair edge and its vibrating direction is parallel to the edge. Because of that, the edge mode has a larger intensity for the XX polarization geometry than for the YY geometry. The TO phonon modes have a large Raman intensity for the XY geometry since TO belongs to B_{1g} as shown in Fig. 2(b). Both LO and TO has a local maximum at 45 degree for Fig. 2(b). In the case of Fig. 2(c) only LO and EDGE phonon mode can be seen and their intensity decreases monotonically with increasing θ. This behavior is similar to A symmetry phonon mode of carbon nanotubes.[11,43]

In Fig. 4, the non-resonant Raman intensities for an $N = 9$ zigzag GNR are plotted as a function of the polarization angle relative to a GNR direction. The polarization geometries are the same as that for Fig. 2. The vibrational directions of the RBLM (180cm^{-1}), RBLM3 (530cm^{-1}), EDGE (1425cm^{-1}), TO and LO (1590cm^{-1}) phonon modes are illustrated in Fig. 5. In the case of zigzag GNRs, the TO, RBLM (RBLM3) and EDGE modes belong to A_1 symmetry while the LO mode belongs to A_2 symmetry. Thus the TO and EDGE phonon modes can be seen in the XX geometry and RBLM mode has a maximum for YY geometries as shown in Fig. 4(a). The LO phonon mode has a maximum and local maximum for XY (YX) geometries as shown in Fig. 4(b) which are symmetric to each other in the present calculation. Both LO and TO has a local maximum at 45 degree for VH configuration as shown in Fig. 4(b). When we rotate the polarization around y axis from XX to ZZ, TO and EDGE phonon modes monotonically decrease with increasing θ.

---

[d]In the experimental situation, we should consider the interaction of the GNR with the substrate which should be much larger than that for the RBM of a SWNT.

(a) RBLM   (b) RBLM3 (c) EDGE(d) LO (e) TO
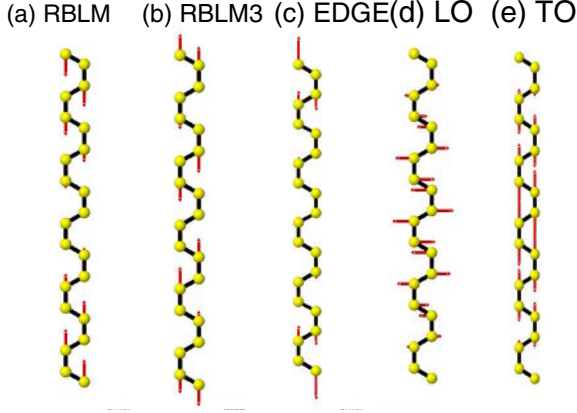
Fig. 5. Phonon eigenvectors of an $N = 11$ zigzag GNR for (a) RBLM, (b) RBLM3, (c) Edge, (d) TO and (d) LO phonon modes.[58]

It is important to note that the vibrational direction of the edge states for the zigzag GNR is perpendicular to the zigzag edge direction, while that for the armchair GNR is parallel to the armchair edge. It is a reason why TO and EDGE has a similar polarization angle dependence in the case of zigzag GNR. The edge phonon frequency of the zigzag edge is around 1430cm^{-1}, which is consistent with previous calculations[44] and experiments.[36] We can find a small intensities (not shown here) for two intermediate frequency spectra show higher RBLM modes with five, and seven nodes whose angular dependence is similar to RBLM.

4. Discussion and Summary

Separation of the LO and TO modes by changing the polarization directions is interesting. Especially when these mode measure the electro-chemical doping by applying a gate electrode, by which the Fermi energy can be controlled, and the LO and TO phonon mode frequencies become soft due to the Kohn anomaly effect.[45–56] Such Raman measurements for GNRs will be important for identifying LO and TO phonon modes.

In the Raman measurements for GNRs, we expect the D band intensity to be significant for armchair GNRs but not for zigzag GNRs. The present calculation can not include the D band Raman spectra since the D band is not a zone center phonon mode, but is rather a zone boundary phonon mode with inter-valley elastic scattering occurring at the edge.[33,34] As is

discussed in the Introduction, inter-valley elastic scattering occurs only at the armchair edge, while intra-valley elastic scattering occurs at the zigzag edge.[30–32] Raman imaging of the D band of graphite shows that the D-band intensity is strong about 20nm away from the edge.[32] Thus the D band of armchair GNRs is strong relative to the G-band intensity, especially for small width GNRs of around 20nm and smaller. The width dependence of the D band is another point that should be addressed by future experiments.

In the previous first principles calculations,[36,44] the C-C bond at the armchair edge becomes a triple bond, because the dangling bonds of the two carbon atoms at the edge make an additional π bond at the edges. The corresponding vibration frequency then becomes 2010cm^{-1} which is similar to the frequency of polyene in SWNTs.[57] In the present calculation, however, the change of the force constants at the edge is not included and thus the corresponding frequency appears at a much lower value. In the experiment, the dangling bonds are terminated by H atoms and form sp^2 covalent bonds. In this case, the frequency of the vibration is observed at 1530cm^{-1}.[36] Thus special care is needed in the case of a comparison with experiment if we uses the current force constant sets for graphene ribbon are used.

In summary, we have calculated the Raman intensity for an armchair and zigzag GNR within non-resonance bond polarization theory. Depending on the polarization direction, LO, TO, RBLM, and EDGE Raman-active phonon modes can be selected. Especially, the LO and TO modes show an opposite polarization dependence for their intensities and for the vibration direction for armchair and zigzag GNRs. The edge phonon vibration direction is parallel and perpendicular to the edge for armchair and zigzag GNRs, respectively. Such a behavior is therefore useful for determining the edge identification for these edges using Raman spectroscopy.

Acknowledgments

References

1. Novoselov, K. S., Geim, A. K., Morozov, S. V., Jiang, D., Katsnelson, M. I., Grigorieva, I. V., Dubonus, S. V. and Firsov, A. A., Two-dimensional gas of massless Dirac fermions in graphene, *Nature*, 438:197, 2005.

2. Y. Zhang, Y. W. Tan, H. L. Stormer, and P. Kim. Single-walled carbon nanotubes. *Nature*, 438:197, 2005.

3. Hubert B. Heersche, Pablo Jarillo-Herrero, Jeroen B. Oostinga, Lieven M. K. Vandersypen, and Alberto F. Morpurgo. Bipolar supercurrent in graphene. *Nature*, 446:56, 2007.

4. J.-C. Charlier, P. C. Eklund, J. Zhu, and A. C. Ferrari. Carbon nanotube synthesis and organization. In Ado Jorio, M. S. Dresselhaus, and G. Dresselhaus, editors, *Electron and Phonon Properties of Graphene: Their relationship with Carbon Nanotubes, Topics in the Synthesis, Structure, Properties and Applications*, volume 111 of *Springer Series on Topics in Appl. Phys.*, pages 673–709, Berlin, 2007. Springer-Verlag. Chapter 21 of Springer Series on Topics in Applied Physics, Vol. 111.

5. A. H. Castro Neto et al. Graphene. *Rev. Mod. Phys*, 81:181, 2009.

6. D. S. L. Abergel, V. Apalkov, J. Berashevich, K. Ziegler, and T. Chakraborty. Properties of graphene: A theoretical perspective. *Adv. in Phys.*, in press, 2010.

7. C. N. R. Rao, A. K. Sood, K. S. Subrahmanyam, and A. Govindaraj. *Angew. Chem. Int. Ed.*, 48:7752, 2009.

8. S. Dutta and S. K. Pati. Novel properties of graphene nanoribbons: A review. *J. Mater. Chem.*, 20:8207, 2010.

9. M. Y. Han, B. Ozyilmaz, Y. Zhang, and P. Kim. Energy band-gap engineering of graphene nanoribbons. *Phys. Rev. Lett.*, 98:206805, 2007.

10. R. Saito, M. Fujita, G. Dresselhaus, and M. S. Dresselhaus. Electronic structure of chiral graphene tubules. *Appl. Phys. Lett.*, 60:2204, 1992.

11. R. Saito, G. Dresselhaus, and M. S. Dresselhaus. *Physical Properties of Carbon Nanotubes*. Imperial College Press, London, 1998.

12. M. Fujita, K. Wakabayashi, K. Nakadw, and K. Kusakabe. Peculiar localized state at zigzag graphite edge. *J. Phys. Soc. Japan*, 65:1920, 1996.

13. K. Sasaki and R. Saito. Pseudospin and deformation-induced gauge field in graphene. *Prog. Theor. Phys.*, 176:253, 2008.

14. K. Nakada, M. Fujita, G. Dresselhaus, and M. S. Dresselhaus. Edge state in graphene ribbons: Nanometer size effect and edge shape dependence. *Phys. Rev. B*, 54:17954, 1996.

15. K. Kusakabe and M. Maruyama. Magnetic nanographite. *Phys. Rev.*, 67:092426, 2003.

16. L. M. Woods and G. D. Mahan. Electron-phonon effects in graphene and armchair (10,10) single-wall carbon nanotubes. *Phys. Rev. B*, 61:10651, 2000.

17. S. Dutta, S. Lakshmi, and S. K. Pati. Electron-electron interactions on the edge states of graphene: A many-body configuration interaction study. *Phys. Rev. B*, 77:073412, 2008.

18. K. Sasaki, K. Sato, R. Saito, J. Jiang, S. Onari, and Y. Tanaka. Local density of states at zigzag edges of carbon nanotubes and graphene. *Phys. Rev. B*, 75:235430, 2007.

19. K. Sasaki, J. Jiang, R. Saito, S. Onari, and Y. Tanaka. Theory of superconductiviy of carbon nanotubes and graphene. *J. Phys. Soc. Japan*, 76:033702, 2007.

20. M. Igami, M. Fujita, and S. Mizuno. Phonon dispersion of nano-graphite ribbons. *Appl. Surf. Sci.*, 130-132:870, 1998.
21. R. Saito, T. Takeya, T. Kimura, G. Dresselhaus, and M. S. Dresselhaus. Finite size effect on the Raman spectra of single-wall carbon nanotubes. *Phys. Rev. B*, 59:2388, 1999.
22. Y. Niimi, T. Matsui, H. Kambara, K. Tagami, M. Tsukada, and H. Fukuyama. *Appl. Surf. Sci.*, 241:43, 2005.
23. K. Fukui, Y. Kobayashi, T. Enoki, K. Kusakabe, and Y. Kaburagi. *Phys. Rev. B*, 71:193406, 2005.
24. J. J. Song, D. D. L. Chung, P. C. Eklund, and M. S. Dresselhaus. Raman scattering in graphite intercalation compounds. *Solid State Comm.*, 20:1111, 1976.
25. P. C. Eklund, G. Dresselhaus, M. S. Dresselhaus, and J. E. Fischer. Raman scattering from in-plane lattice modes in low stage graphite-alkali metal compounds. *Phys. Rev. B*, 16:3330, 1977.
26. A. Gupta, G. Chen, P. Joshi, S. Tadigadapa, and P. C. Eklund. Raman scattering from high-frequency phonons in sopported n-graphene layer films. *Nano Lett.*, 6:2667, 2006.
27. A. C. Ferrari, J. C. Meyer, V. Scardaci, C. Casiraghi, M. Lazzeri, M. Mauri, S. Piscanec, Da Jiang, K. S. Novoselov, S. Roth, and A. K. Geim. Raman spectrum of graphene and graphene layers. *Phys. Rev. Lett.*, 97:187401, 2006.
28. A. Das, S. Pisana, B. Chakraborty, S. Piscanec, S. K. Saha, U. V. Waghmare, K. S. Novoselov, H. R. Krishnamurthy, A. K. Geim, A. C. Ferrari, and A. K. Sood. Monitoring dopants by raman scattering in an electrochemically top-gated graphene transistor. *Nature Nanotechnology*, 3:210, 2008.
29. J. S. Park, Alfonso Reina Cecco, R. Saito, J. Jiang, G. Dresselhaus, and M. S. Dresselhaus. G' band raman spectrum of single, double and triple layer graphene. *Carbon*, 47:1303, 2009.
30. L. G. Cançado, M. A. Pimenta, R. A. Neves, G. Medeiros-Ribeiro, T. Enoki, Y. Kobayashi, K. Takai, K. Fukui, M. S. Dresselhaus, R. Saito, and A. Jorio. Anisotropy in the Raman spectra of nanographite ribbons. *Phys. Rev. Lett.*, 93:047403, 2004.
31. R. Saito, A. Grüneis, Ge. G. Samsonidze, V. W. Brar, G. Dresselhaus, M. S. Dresselhaus, A. Jorio, L. G. Cançado, C. Fantini, M. A. Pimenta, and A. G. Souza Filho. Double resonance Raman spectroscopy of single wall carbon nanotubes. *New Journal of Physics*, 5:157, 2003.
32. M. A. Pimenta, G. Dresselhaus, M. S. Dresselhaus, L. G. Cançado, A. Jorio, and R. Saito. Studying disorder in graphite-based systems by Raman spectroscopy. *Physical Chemistry Chemical Physics*, 9:1276, 2007.
33. C. Thomsen and S. Reich. Double resonant Raman scattering in graphite. *Phys. Rev. Lett.*, 85:5214, 2000.
34. R. Saito, A. Jorio, A. G. Souza Filho, G. Dresselhaus, M. S. Dresselhaus, and M. A. Pimenta. Probing phonon dispersion relations of graphite by double resonance Raman scattering. *Phys. Rev. Lett.*, 88:027401, 2002.
35. K. Sato, R. Saito, Y. Oyama, J. Jiang, L. G. Cançado, M. A. Pimenta, A. Jorio, Ge. G. Samsonidze, G. Dresselhaus, and M. S. Dresselhaus.

D-band Raman intensity of graphitic materials as a function of laser energy and crystallite size. *Chem. Phys. Lett.*, 427:117, 2006.

36. W. Ren, R. Saito, L. Gao, F. Zheng, B. Liu, Z. Wu, M. Furukawa, J. Zhao, Z. Chen, and H. M. Cheng. Edge phonon state of graphene nanoribbons observed by raman spectroscopy. *Phys. Rev. B*, 81:035412, 2010.

37. A. Gruneis, J. Serrano, A. Bosak, M. Lazzeri, S. L. Molodtsov, C. Attaccalite, L. Wirtz, M. Krisch, A. Rubio, F. Mauri, and T. Pichiler. Phonon surface mapping of graphite: Disentangling quasi-degenerate phonon dispersions. *Phys. Rev. B*, 80:085423, 2009.

38. O. Madelung. *Solid State Theory*. Springer-Verlag, Berlin, Berlin, 1978.

39. J. Zimmermann, P. Pavone, and Cuniberti G. Vibrational modes and low-temperature thermal properties of graphene and carbon nanotubes: Minimal force-constant model. *Phys. Rev. B*, 78:0454101, 2008.

40. S. Guha, J. Menéndez, J. B. Page, and G. B. Adams. Empirical bond polarizability model for fullerenes. *Phys. Rev. B*, 53:13106, 1996.

41. G. W. Chantry. *The Raman Effect*. Dekker, New York, NY, vol. 1 edition, 1971.

42. R. Saito, M. Furukawa, G. Dresselhaus, and M. S. Dresselhaus. *unpublished and Master Thesis: M. Furukawa, Tohoku University*, 2010.

43. R. Saito, T. Takeya, T. Kimura, G. Dresselhaus, and M. S. Dresselhaus. Raman intensity of single-wall carbon nanotubes. *Phys. Rev. B*, 57:4145, 1998.

44. J. Zhou and J. Dong. Vaibrational property and raman spectrum of carbon nanoribbon. *Appl. Phys. Lett.*, 91:173108, 2007.

45. W. Kohn. Image of the fermi surface in the vibration spectrum of a metal (Kohn anomaly). *Phys. Rev. Lett.*, 2:393, 1959.

46. S. Piscanec, M. Lazzeri, M. Mauri, A. C. Ferrari, and J. Robertson. Kohn anomalies and electron-phonon interaction in graphite. *Phys. Rev. Lett.*, 93:185503, 2004.

47. M. Lazzeri and F. Mauri. Nonadiabatic kohn anomaly in a doped graphene monolayer. *Phys. Rev. Lett.*, 97:266407, 2006.

48. K. Ishikawa and T. Ando. Optical phonon interacting with electrons in carbon nanotubes. *J. Phys. Soc. Jpn.*, 75:84713, 2006.

49. V. N. Popov and P. Lambin. Radius and chirality dependence of the radial breathing mode and the g-band phonon modes of single-walled carbon nanotubes. *Phys. Rev. B*, 73:085407, 2006.

50. H. Farhat, H. Son, Ge. G. Samsonidze, S. Reich, M. S. Dresselhaus, and J. Kong. Phonon softening in individual metallic carbon nanotubes due to the Kohn anomaly. *Phys. Rev. Lett.*, 99:145506, 2007.

51. K. Sasaki, R. Saito, G. Dresselhaus, M. S. Dresselhaus, H. Farhat, and J. Kong. Curvature-induced optical phonon frequency shift in metallic carbon nanotubes. *Phys. Rev. B*, 77:245441, 2008.

52. M. Kalbac, H. Farhat, L. Kavan, J. Kong, K. Sasaki, R. Saito, and M. S. Dresselhaus. Electrochemical charging of individual single-walled carbon nanotubes. *Nano (ACS)*, 3:2320, 2009.

53. K. Sasaki, R. Saito, G. Dresselhaus, M. S. Dresselhaus, H. Farhat, and J. Kong. Chirality dependent frequency shift of radial breathing mode in metallic carbon nanotubes. *Phys. Rev. B*, 78:235405, 2008.

54. H. Farhat, K. Sasaki, M. Kalbac, Mario Hofmann, R. Saito, M. S. Dresselhaus, and J. Kong. Softening of the radial breathing mode in metallic carbon nanotubes. *Phys. Rev. Lett.*, 102:126804, 2009.

55. J. S. Park, K. Sasaki, R. Saito, W. Izumida, M. Kalbac, H. Farhat, G. Dresselhaus, and M. S. Dresselhaus. Fermi energy dependence of the g -band resonance raman spectra of single-wall carbon nanotubes. *Phys. Rev. B*, 80(8):081402, 2009.

56. A. K. Manna and S. K. Pati. *Nanoscale*, 2:1190, 2010.

57. D. Nishide, H. Dohi, T. Wakabayashi, E. Nishibori, S. Aoyagi, M. Ishida, S. Kikuchi, R. Kitaura, T. Sugai, M. Sakata, and H. Shinohara. Single-wall carbon nanotubes encaging linear chain $c_{10}h_2$ polyyne molecules inside. *Chem. Phys. Lett.*, 428:356, 2006.

58. R. Saito, M. Furukawa, G. Dresselhaus, and M. S. Dresselhaus, *J. Phys. Cond. Matt.*, 22:334203, 2010.

Chapter 7

Probing Single and Bilayer Graphene Field Effect Transistors by Raman Spectroscopy

Anindya Das, Biswanath Chakraborty and A. K. Sood

Department of Physics, Indian Institute of Science,
Bangalore - 560012, India

This article is a review of our work related to Raman studies of single layer and bilayer graphenes as a function Fermi level shift achieved by electrochemically top gating a field effect transistor. Combining the transport and in-situ Raman studies of the field effect devices, a quantitative understanding is obtained of the phonon renormalization due to doping of graphene. Results are discussed in the light of time dependent perturbation theory, with electron phonon coupling parameter as an input from the density functional theory. It is seen that phonons near Γ and K points of the Brillouin zone are renormalized very differently by doping. Further, Γ-phonon renormalization is different in bilayer graphene as compared to single layer, originating from their different electronic band structures near the zone boundary K-point. Thus Raman spectroscopy is not only a powerful probe to characterize the number of layers and their quality in a graphene sample, but also to quantitatively evaluate electron phonon coupling required to understand the performance of graphene devices.

1. Introduction

Graphene as we know today was conclusively identified by Novoselov et al. in 2004[1–3] using micro-mechanical exfoliation of graphite and deposited on Si/SiO_2 substrate. The reason why it took such a long time may be that many people believed that a two dimensional graphene should not exist in nature based on Mermin theorem.[4] The theorem says that a pure two dimensional system is thermodynamically unstable at finite temperature because the root mean square thermal fluctuations of atomic positions are comparable to the inter-atomic distances. However, the discovery of graphene does not violate the Mermin theorem because the finite

size of graphene (~ 100 μm^2) becomes intrinsically stable by gentle crumpling called ripples.[5] Before 2004, a few layer graphene were prepared by chemical vapour deposition on metal surfaces[6] and studied mostly by electron energy loss spectroscopy.[7] Recently, single and few-layer graphene have been grown[8] epitaxially thermal decomposition of SiC,[9,10] by chemical vapor deposition of hydrocarbons on Ni and Cu metal substrates,[11,12] by , solution based approach from reduced graphitic oxide (RGO),[13] arc discharge method[14] and heating of nanodiamonds.[15] However, mechanical exfoliation technique produces the best quality graphene having mobility $\sim$ 10,000-200,000 cm^2/V.sec.[2,3,5,16–18] Even higher mobilities have been observed in single layer graphene suspended on a cavity, allowing the first observation of fractional quantum hall effect.[19,20]

The most interesting feature of graphene is that upto ~ 1 eV, the electronic energy dispersion is conical as if two inverted cones (conduction and valence bands) touch each other at a point called Dirac point.[21] In neutral graphene the Fermi energy is at the Dirac point. Upon doping, electrons and holes move through the layer with a velocity $v_F \sim 10^6$m/s and this velocity is energy independent as if the electrons and holes were massless particles and antiparticles moving at constant velocity. The effective Hamiltonian for the π-electrons near the K-points is expressed by the Dirac equation with zero mass: $H = \hbar v_F \vec{\sigma} . \vec{k}$. Here $\vec{\sigma}$ is the 2d pseudo spin Pauli matrix, taking into account the relative contributions of two different sublattices A and B of graphene to the electronic states near the K-point. Hence, many of the unusual properties[7,8,22] can show up in graphene compared to ordinary electrons such as Klein paradox[23,24] and anomalous integer quantum hall effect.[2,3]

It has been shown experimentally by Novoselov *et al.*[2] that in single layer graphene back gated field effect transistor, conductivity of the graphene increases linearly with gate voltage (V$_G$) except very close to the neutrality point (Dirac point (V$_D$)). It was seen that conductivity does not disappear in the limit of vanishing carrier concentration (n) but instead exhibits a minimum conductivity whose value varies from sample to sample. Another observation is that near the Dirac point conductivity does not increase sharply and indeed it remains constant for a range of gate voltages, V$_D \pm \Delta$V$_G$. It is known that due to pseudospin conservation there are no intra-valley and inter-valley back scattering.[21] As a result, the current flow in graphene is expected to be ballistic. Since the length of the samples in most of the experiments are more than few microns (5-10μm), much larger than than the ballistic transport length ($\sim$100nm) at room temperature,

diffusive transport[5,16,25] is sufficient to explain most of the conductivity results in graphene.

2. Vibrational Properties of Graphene

Single layer graphene has two atom basis (A and B) in the unit cell and belongs to the D_{6h} point group.[26] The zero-wave vector ($q = 0$ or Γ phonon) phonons in single layer graphene belong to the irreducible representations as E_{2g}, B_{2g}, E_{1u} and A_{2u}, where E_{2g} and B_{2g} are the optical modes; E_{1u} and A_{2u} are the acoustic modes. In the first column of Fig. 1, we have shown the eigenvectors of these six normal modes at $q = 0$ for a single layer graphene, where R and IR refer to Raman and infrared active modes.[26] E_{2g} is the doubly degenerate (longitudinal optic LO and transverse optic TO) with frequency 1582 cm^{-1}.[26] It can be seen from Fig. 1 that for optical vibrations two neighboring atoms vibrate opposite to one another, resulting in large bond distortions. The K phonon of single graphene belongs to C_{6v} space group[26,27] and the eigen vectors of TO branch at K point belongs to the irreducible representation A_1'-R, as shown in Fig. 2, where two sub-lattice atoms move circularly in opposite directions.[27]

Bilayer graphene belongs to D_{3d} point group,[26] with four atoms (A_1, B_1 and A_2, B_2) in the unit cell. Therefore, there will be total twelve (4×3) branches (three acoustic and nine optical). The vibration of a bilayer graphene can be obtained by combining the vibrations of two single layer graphenes either in phase or out of phase. In the second and third columns of Fig. 1 we have shown the eigen vectors of the twelve normal modes at Γ point. The second (third) column shows the in phase (out of phase) vibration. The Γ point of bilayer graphene belongs to the irreducible representations as E_{2g}, B_{2g}, E_{1u} and A_{2u} as shown in Fig. 1. The E_{2g} and E_{1u} are double degenerates (LO and TO). The $E_{2g}(LO/TO)$-R (in phase) modes have same energy (~ 1582 cm^{-1}) as single layer graphene but $E_{1u}(LO/TO)$-IR (out of phase) has slightly higher energy ~ 1589 cm^{-1}. The other $E_{2g}(LO/TO)$-R is called shear mode (see Fig. 1) with frequency ~ 40 cm^{-1} and $A_{2u}(ZO)$-IR of frequency ~ 868 cm^{-1}.

Many recent calculations have discussed the important issue of electron-phonon coupling (EPC) in graphene.[28–36] The degenerate E_{2g} phonon at Γ point and TO phonon at K point (A_1') have strong electron-phonon interactions, resulting in Kohn anomalies (KA) in the phonon-dispersion. Kohn anomaly refers to the anomalous screening of phonons of particular wave vector q which can connect two points k_1 and k_2 on the Fermi surface of
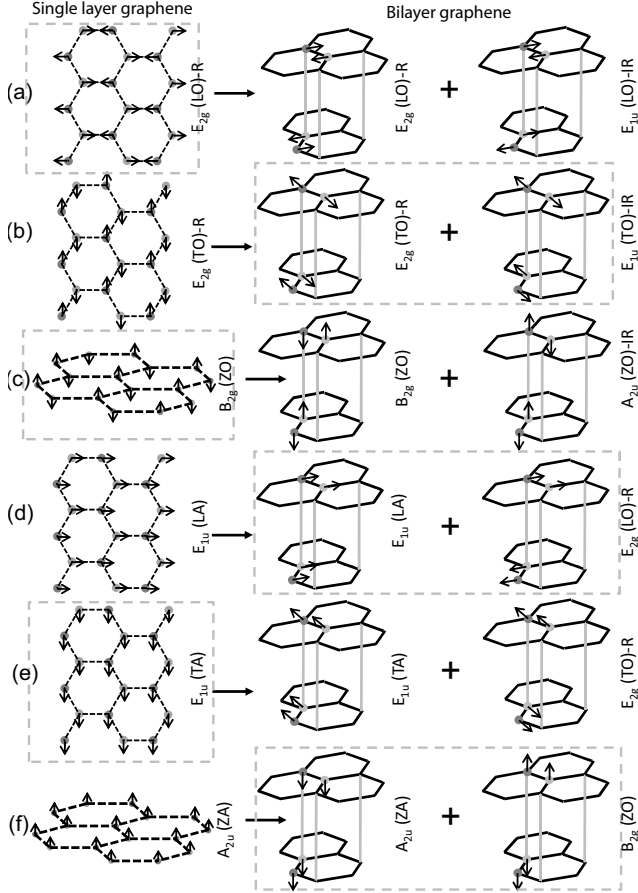
Fig. 1. (Left panel) Eigen vectors of six normal modes at Γ point of single layer graphene. Eigen vectors of six in phase (middle panel) and six out of phase (right panel) normal modes at Γ point of bilayer graphene. The R and IR correspond to the Raman active and infrared active modes, respectively.

the metal such that $\vec{k_2} = \vec{k_1} + \vec{q}$.[37] For graphene and metallic nanotubes, the Kohn anomalies occur at $q = 0$ and $q = K$.

3. Raman Spectra of Graphene

Raman spectroscopy has proved to be a powerful, non-invasive and non-destructive ideal tool to characterise the sp^2 and sp^3 carbon materials like
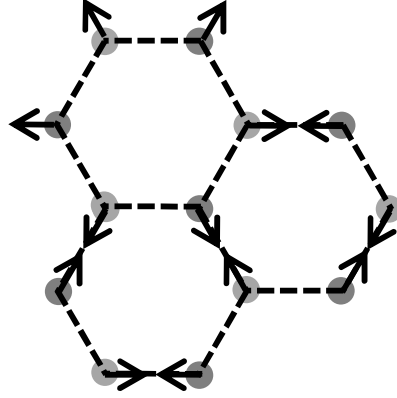
Fig. 2. The vibration of K point phonon. Two sub-lattice atoms move circularly in opposite directions.

graphite, diamond, poly-aromatic compounds, fullerenes and carbon nan-otubes.[8] It has been used uniquely to identify the number of graphene layers. Raman fingerprints of single and bilayer graphene are different and have been investigated by many groups.[38–45] The symmetry allowed E_{2g} mode at Γpoint, usually termed as G mode, appears at ~ 1583 cm^{-1}. Other Raman modes seen are at ~ 1350 cm^{-1}(D mode), 1620 cm^{-1}(D$'$ mode), 2680 (2D or D* mode), 2950 (D+G), 3245(2D$'$) and 4290 cm^{-1}(2D+G). The mode at ~ 1350 cm^{-1}, termed as D mode, is disorder activated mode associated with the TO branch near the K point.

Raman signatures of number of layers in the sample are reflected not in the G-band but in the line shape of the 2D band.[38–40,44,45] This occurs because Raman scattering from phonons occurs via electronic states, giving rise to double resonance Raman process.[46,47] In Fig. 3 we have shown the second order Raman process for the 2D band in single layer graphene. The Raman tensor (R) can be written in the fourth order perturbation theory as:[46]

$$R = \sum_{a,b,c} \frac{M_{er} M_{e-ph} M_{e-ph} M_{er}}{(E_I - E^e_{ai} - i\gamma_e)(E_I - \hbar\omega_{ph} - E^e_{bi} - i\gamma_e)(E_I - \hbar\omega_{ph} - \hbar\omega_{ph} - E^e_{ci} - i\gamma_e)} \quad (1)$$

Here M's are the matrix elements. It can be seen from Fig. 3(a) that there are four steps involved in the second order Raman process. (1) electron - radiation interaction with matrix element M_{er}, (2) electron-phonon interaction (M_{e-ph}) making a phonon assisted inter valley ($K \to K'$) transition, (3) electron-phonon interaction (M_{e-ph}) making a phonon assisted
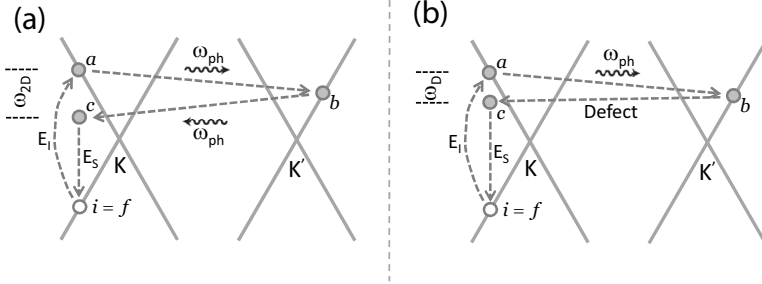
Fig. 3. (a) Second order Raman process for 2D mode. There are three intermediate (a, b and c) states. a and b are real states and the process is called double resonance process. Two phonons emit in opposite directions to conserve the momentum. (b) Second order Raman process for D mode, which is a defect mediated process.

inter valley ($K' \rightarrow K$) transition to take care of the momentum conservation, and (4) electron-radiation interaction. Thus, we can probe finite q phonon in the second order Raman process, where momentum conservation is obtained by creating two phonons with opposing wave vectors. Note that the intermediate states (a, b) are real and intermediate state (c) is virtual such that two of the energy denominator in Eq. (1) goes to zero. This is called double resonance process and as a result the momentum of the phonon wave vector, q depends on laser excitation energy (E_L) and the linear dispersion of phonon near K point. This $2D$ Raman band is highly dispersive with incident photon energy, $\sim$100 cm^{-1}/eV.[46] The 2D band in bilayer graphene splits into four bands arising due to different phonon assisted intervalley transitions shown in Fig. 4.[38] Please note that the third step of Fig. 3(a) can be defect mediated, as shown in Fig. 3(b), such that electron scatters from b to c elasticaly by a defect to conserve the momentum in the second order Raman process. This is known as D mode. Its frequency also depends on the incident laser energy ($\sim$50 cm^{-1}/eV),[46,47] almost half of dispersion of the $2D$ mode, due to double resonance Raman process. It can be seen that one can observe $2D$ band in Raman spectra, even though there is no D band because defect is not required for the observation of the $2D$ band. In bilayer graphene the position of the G mode remain the same as single layer graphene.

So far we have discussed intervalley transitions but there could be intravalley transitions similar to $2D$ and D modes, as shown in Fig. 5. These are called $2D'$ and D', respectively, where D' is the defect mediated process and the LO phonon near Γ point is involved for these Raman modes.[8]
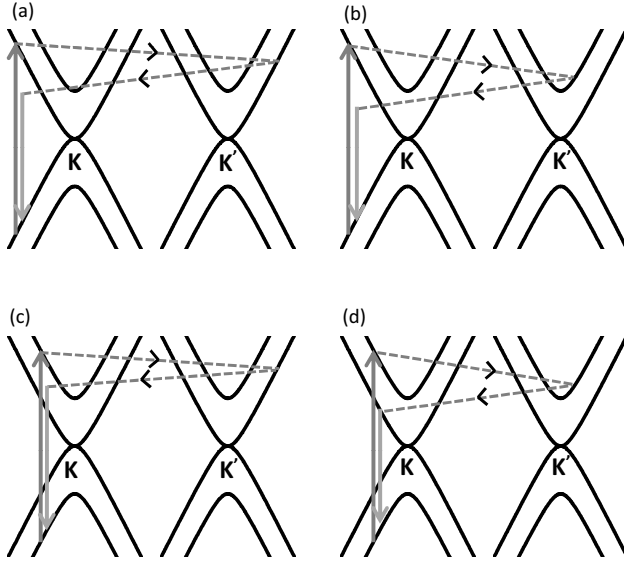
Fig. 4. Origin of four peaks in 2D band of a bilayer graphene. The processes (a) and (d) originate phonon with maximum and minimum momentum (q), respectively. The processes (b) and (c) have intermediate momentum. Therefore, (a) gives highest energy phonon and (d) gives lowest energy phonon among the four peaks of 2D band.
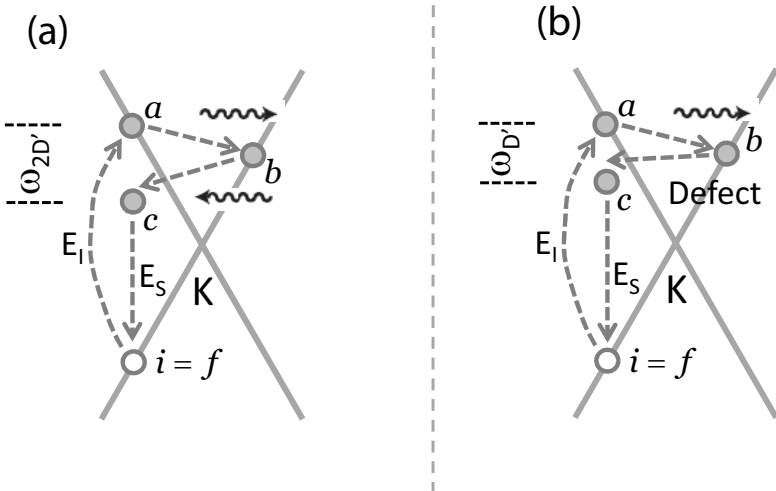
Fig. 5. Second order Raman process for intra-valley scattering of (a) $2D'$ mode and (b) D' mode.

4. Tuning the Fermi Energy by Field Effect Gating

The conventional way to shift the Fermi energy of a system is back gating. In Fig. 6 we have shown the schematic of a back gated field effect transistor using 300nm SiO$_2$ as a dielectric material. In this geometry a gate potential (V_{BG}) is applied between the sample graphene and the gate electrode (highly doped Si). Therefore, it act like a capacitor and amount of induced charges in the sample depends on the capacitance of the system, given by $C_G = \frac{\epsilon}{d}$, where ϵ is the dielectric constant of SiO$_2$. For a 300nm thick SiO$_2$ the $C_G \sim 12$ nF/cm^2.
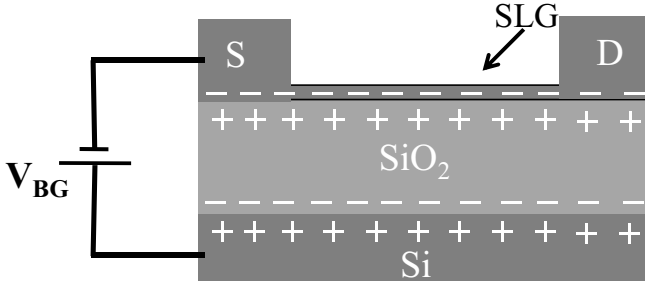
Fig. 6.   Schematic of a SiO$_2$ back gating.

An applied gate voltage (V_G) creates (i) electrostatic potential drop between the sample and the gate electrode and (ii) shift of the Fermi level of the sample. The first one depends on the geometrical gate capacitance (C_G) of the system and second one depends on the quantum capacitance (C_Q) of the sample. Now, for graphene $C_Q \sim 1\mu F/cm^2$ which is much larger compared to C_G. As a result maximum voltage drop occurs across the SiO$_2$ and thus, the conversion factor from V_G to E_F is very low ~ 0.003. For example by applying $V_G = 100V$ one can shift the Fermi energy by 300 meV in graphene. At higher gate voltages ($> 100V$) the dielectric of SiO$_2$ will break down. Therefore, the conversion factor and maximum Fermi level shift are limited by the C_G. One of the solutions to overcome this problems is to either reduce the thickness of the SiO$_2$ which needs sophisticated techniques like atomic layer deposition (ALD) etc or to use high dielectric insulator like HfO$_2$.

There is another way to increase the C_G by using the electrolyte gating.[48–52] Here we use solid polymer electrolyte gating, where polymer acts
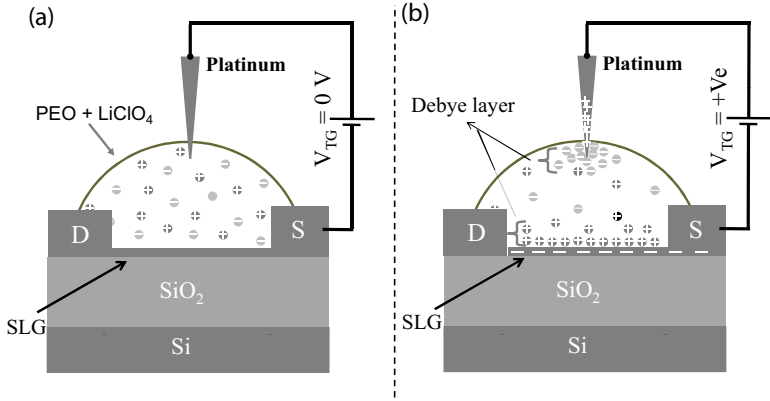
Fig. 7. (a) Schematic of an electrolyte gating in a top gated geometry when $V_G = 0$V. The '+' and '-' correspond to the Li$^+$ and ClO$_4^-$ ions. (b) After applying a +Ve voltage to the gate electrode.

as a dielectric material and Li$^+$ and ClO$_4^-$ act as electrolyte. We have used solid polymer rather than electrolyte solution (like LiClO$_4$ in water) because solid polymer is less reactive with the sample as well as with the gate electrodes and hence higher V_G can be applied.

In Fig. 7 we have shown the schematic of a top electrolyte gating where immersed platinum act as a gate electrode. When $V_{TG} = 0$V there is a uniform concentration of Li$^+$ and ClO$_4^-$, as shown in Fig. 7(a). Now +Ve (-Ve) voltage to the platinum gate electrode brings the Li$^+$ (ClO$_4^-$) ions closer to the sample and make up the Debye layer, as shown in Fig. 7(b). Debye layer is a diffuse layer of ions, which means there is a concentration gradient of Li$^+$ (when V_{TG} is positive) from the surface of the sample to the bulk such that it screens the electric field inside the Debye layer. Therefore, the applied V_{TG} drops across only the Debye layer and not inside the whole medium. As a result gating does not depend on the separation between the platinum electrode and sample. However, when the separation is larger the ions take more time to develop the Debye layer after applying V_{TG}, thereby decreasing the frequency response.

4.1. *Single layer top gating*

The application of a gate voltage (V_{TG}) results in creating an electrostatic potential difference ϕ between the graphene and the gate electrode as well

as Fermi level E_F shift, thereby

$$V_{TG} = \frac{E_F}{e} + \phi \qquad (2)$$

where ϕ and E_F/e are determined by the geometrical capacitance C_{TG} and the quantum capacitance (C_Q) of graphene, respectively. The two capacitors are in series, as shown in Fig. 8(a). In Fig. 8(b) we have shown schematically the electrostatic voltage drops in our experiment. The geometrical capacitance is $C_{TG} = \frac{\epsilon\epsilon_0}{d_{TG}}$, where ϵ is the dielectric constant of the PEO matrix and d_{TG} is the Debye length is given by $d_{TG} = (2ce^2/\epsilon\epsilon_0 k_B T)^{-1/2}$ for a monovalent electrolyte where c is the concentration of the electrolyte, e is the electric charge, $k_B T$ is the thermal energy. For polymer electrolyte gating the thickness of Debye layer is reported to be a few nanometers $(1 \sim 5 \text{ nm})$[48] and the dielectric constant (ϵ) of PEO is 5.[53] Assuming a Debye length of 2 nm, we get a gate capacitance $C_{TG} = 2.2 \times 10^{-6}$ F cm^{-2}, much higher than back gate capacitance. Therefore, the first term in Eq. (2) cannot be neglected. The Fermi energy in graphene changes as $E_F(n) = \hbar |v_F| \sqrt{\pi n}$, where $|v_F| = 1.1 \times 10^6 m/s$[2,3] is the Fermi velocity, hence:

$$V_{TG} = \frac{\hbar |v_F| \sqrt{\pi n}}{e} + \frac{ne}{C_{TG}} \qquad (3)$$

Using the values of C_{TG} and v_F,

$$V_{TG}(volts) = 1.16 \times 10^{-7}\sqrt{n} + 0.723 \times 10^{-13}n \qquad (4)$$

where n is in units of cm^{-2}. Equation (4) allows us to estimate the doping concentration at each top gate voltage (V_{TG}), as shown in Fig. 8(c). The inset in Fig. 8(c) shows that in the same voltage range the doping concentration obtained in 300 nm SiO$_2$ back gating is two orders of magnitude smaller compared to the present top gating. Recently, we have measured C_{TG} using back and top gate geometries and the value is $1.5 \mu F/cm^2$.[54]

We now consider the evolution of the Raman spectra. Figures 9(a) to 9(d) show the spectra recorded during the top gate experiment. Figure 9(a) is the PEO Raman spectrum. This has three prominent peaks at ~ 1282 cm^{-1} (P1), 1476 cm^{-1} (P2) and 2890 cm^{-1} (P3), which correspond to twisting, bending and stretching modes of the CH$_2$ bonds in the polymer.[55] Luckily they do not overlap the main features of graphene (see Figs. 9(b),(c),(d)). Furthermore these PEO Raman lines do not change with gating.

Fig. 8. (a) Geometrical capacitance and quantum capacitance are in series with V_G. (b) V_{TG} is the voltage applied between the gate and source. Φ is the electrostatic potential drop and E_F is the Fermi energy shift. (c) Doping as a function of V_{TG}.
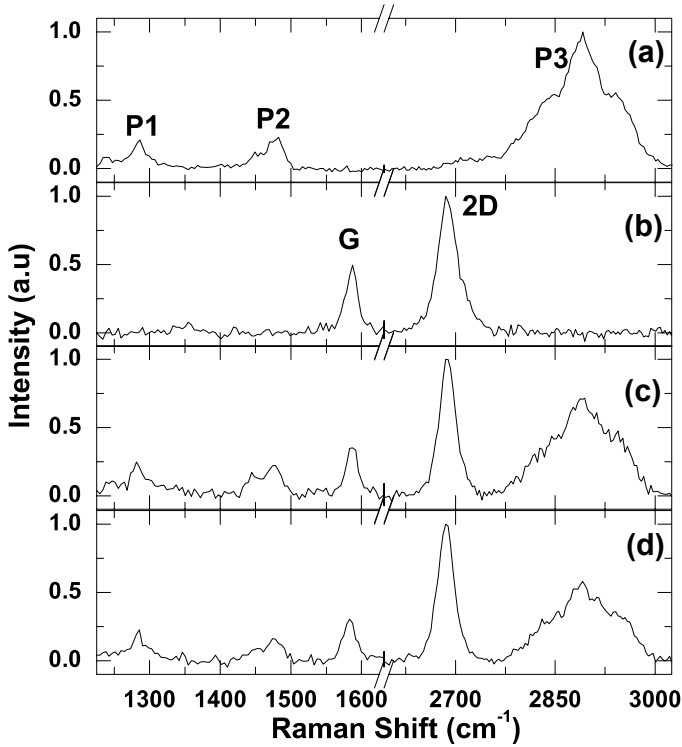
Fig. 9. (a) Raman spectra of PEO+LiClO$_4$ mixture. (b) Raman spectra of graphene before pouring the polymer electrolyte. (c) Raman spectra at $V_{TG} = 0.0$ V and (d) $V_{TG}=V_D=0.6$V. P1, P2 and P3 are the polymer peaks.[50,55]
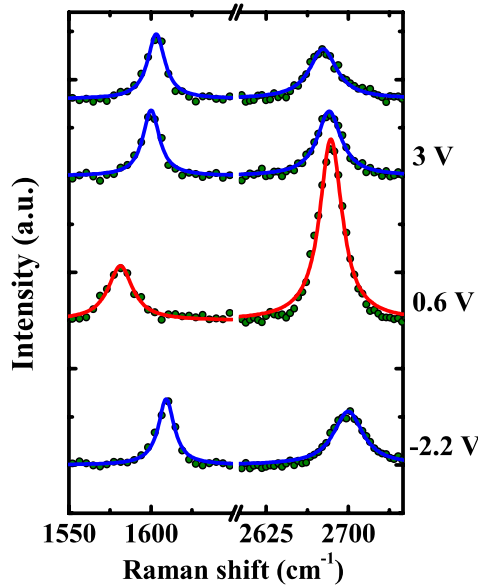
Fig. 10. Raman spectra at several V_{TG}. The dots are the experimental data. Black lines are fitted Lorentzians. The red line corresponds to the Dirac point.[50]

Figure 10 plots the Raman spectra in the G and 2D region at several top gate voltages. The peak positions and line-widths of G and 2D are plotted in Fig. 11 as a function of carrier concentration. The minimum Pos(G) (~ 1583.1 cm^{-1}) is at $V_{TG} = V_D \sim 0.6$ V. Pos(G) increases for positive (V_{TG} - V_D) and negative (V_{TG} - V_D), i.e. for both electron and hole doping, by up to 30 cm^{-1} for hole doping and 25 cm^{-1} for electron doping (see Fig. 11(a)). The decrease in FWHM(G) (see Fig. 11(b)) for both hole and electron doping is similar to earlier results,[56,57] even though extended to a much wider doping range. Most interestingly, the 2D peak shows a very different dependence on gate voltages when compared to the G mode. For electron doping, Pos(2D) does not change much (< 1 cm^{-1}) until gate voltage of ~ 3V. At higher gate voltages, there is a significant softening by ~ 20 cm^{-1} and for hole doping, Pos(2D) increases by ~ 20 cm^{-1} (see Fig. 11(c)). The FWHM (2D) remains constant from -1V to 3V and increases only at higher electron and hole doping (see Fig. 11(d)). In Fig. 11 we have plotted the Pos (G), FWHM (G), Pos (2D) and FWHM (2D) as a function of doping using Eq. (4). It can be seen from the Fig. 11 that the G peak position and the 2D peak position are very sensitive to
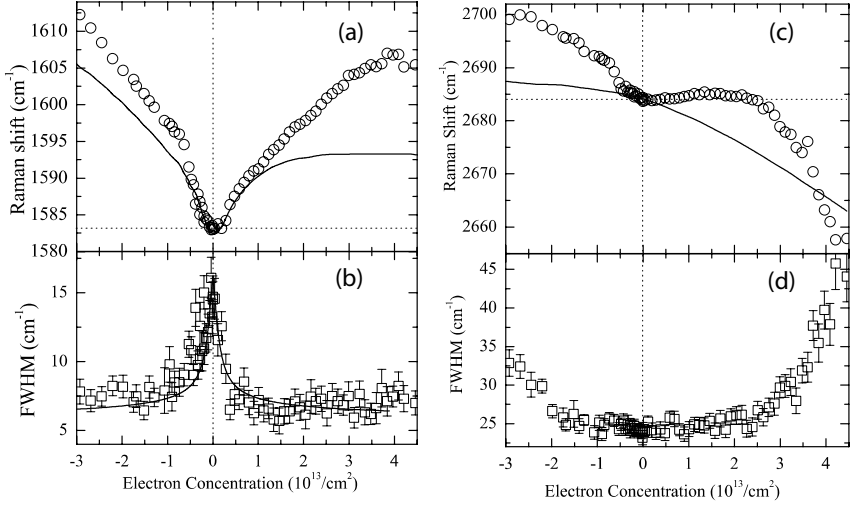
Fig. 11.   (a) Pos(G), (b) FWHM(G), (c)Pos(2D and (d) FWHM(2D) as a function of electron and hole doping. The solid lines are the theoretical predictions.[50]

the doping concentration and thus, the Raman spectroscopy is a noninvasive tool to determine the doping amount in graphene. The solid lines in Fig. 11 are the theoretical predication and will be discussed later.

4.2. *Bilayer top gating*

Experiments were done on a graphene bilayer which also had a single layer attached to it.[51] The G peak positions of SLG (circle) and BLG (square) are plotted in Fig. 12 as a function of V_{TG}. Please note that there is a change in slope for BLG at 2.5V, whereas it is absent in SLG.

4.2.1. *Conversion of V_{TG} into E_F*

To get a quantitative understanding, it is necessary to convert V_{TG} into a E_F shift. In Fig. 13(b) we have shown schematically the electrostatic voltage drops in our top gated experiment containing both the single and bilayer graphene. For a top gate experiment V_{TG} is applied between the gate and source. Φ^{SLG} is the electrostatic voltage drop between the Debye layer and single layer graphene. Similarly, the Φ^{BLG} is the voltage drop between the Debye layer and the bilayer graphene. In addition, there will be another voltage drop (δV) between the two layers of carbon sheets due to external
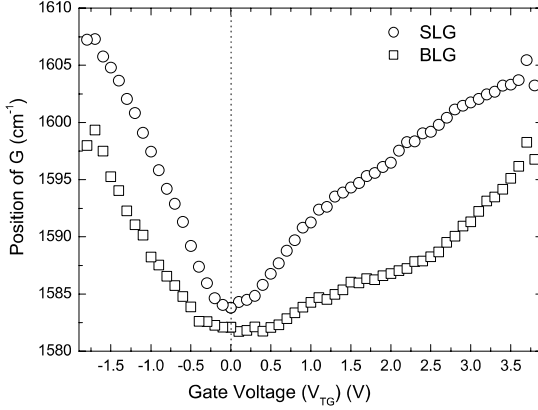
Fig. 12.   Peak position of G mode of SLG (circle) and BLG (square) as a function of V_{TG}.

electric field created by the gate electrode. Here, we assume equal charge density in the both the layers which means that there is no screening and hence the total electrostatic voltage drop in a bilayer graphene is $\Phi_T^{BLG} = \Phi^{BLG} + \delta V$.[51] This δV opens a band gap between the conduction band and valence band in a bilayer graphene. Now, in equilibrium both the single and bilayer graphene will have same chemical potential and therefore, $eV_{TG} = e\Phi^{SLG} + E_F^{SLG} = \Phi_T^{BLG} + E_F^{BLG}$ where E_F^{SLG} and E_F^{BLG} are Fermi energy shift in single and bilayer graphene, respectively. In our calculation we neglect the term δV as the value of δV is less compared to E_F^{BLG} as well as much less compared to Φ^{BLg}. Thus:

$$eV_{TG} = e\Phi^{SLG} + E_F^{SLG} \cong \Phi^{BLG} + E_F^{BLG}. \qquad (5)$$

Now, the electrostatic potential $\phi = \frac{ne}{C_{TG}}$, where n is the carrier concentration which can be calculated using the relation $n = \int_0^{\epsilon_F} D(\epsilon)d\epsilon$. For SLG, $n^{SLG} = \mu E_F^2$, where $\mu = \frac{g_s g_v}{4\pi\gamma^2} = \frac{1}{\pi(\hbar v_F)^2}$, $g_s = g_v = 2$ are spin and valley degeneracies and v_F is the Fermi velocity. Therefore for SLG:

$$eV_{TG} = \nu E_F^2 + E_F \qquad (6)$$

Similarly, for BLG:[58–60]

$$n^{BLG} = \mu[\gamma_1 E_F + E_F^2], \ E_F < \gamma_1 \qquad (7)$$
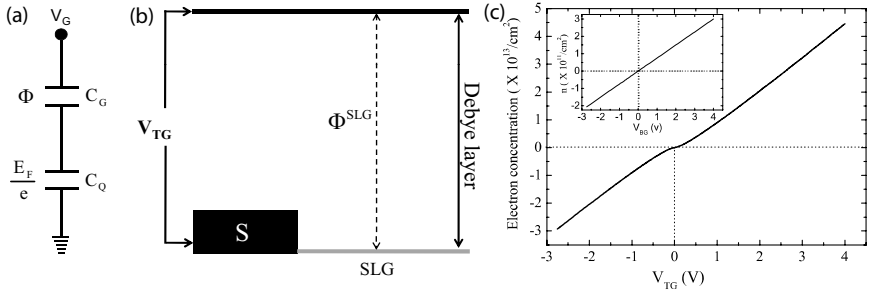$$= 2\mu E_F^2, \qquad E_F > \gamma_1$$
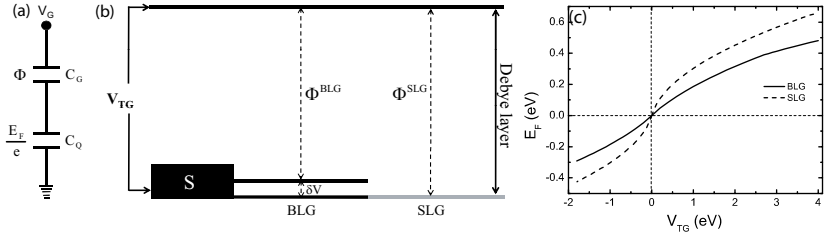
Fig. 13. (a) Geometrical capacitance and quantum capacitance are in series with V_G. (b) V_{TG} is the voltage applied between the gate and the source. The Φ is the electrostatic potential drop and E_F is the Fermi energy shift. The δV is the voltage drop between the layers of the bilayer graphene. (c) Fermi energy shift as a function of V_{TG}. The dashed and solid lines for single and bilayer graphene.[51]
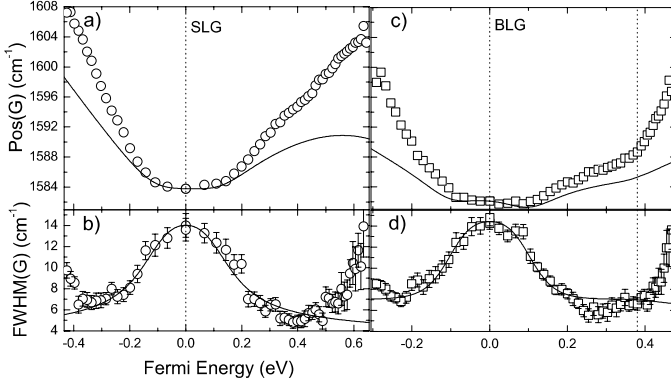
Fig. 14. Pos(G) for (a) SLG; (c) BLG as a function of Fermi energy. FWHM(G) of (b) SLG; (d) BLG as a function of Fermi energy. Solid lines are theoretical predictions.[51]

and hence for BLG:

$$eV_{TG} = \nu E_F^2 + (1 + \nu\gamma_1)E_F, \; E_F < \gamma_1 \qquad (8)$$
$$= 2\nu E_F^2 + E_F, \qquad E_F > \gamma_1$$

where $\nu = \frac{e^2}{\pi C_{TG}(\hbar v_F)^2}$. Using Eqs. (6) and (8) we have plotted the Fermi energy shift for SLG and BLG as a function of gate voltage in Fig. 13(c).

Figure 14 plots the resulting Pos(G), FWHM(G) as a function of E_F. In SLG, Pos(G) does not increase up to $E_F \sim 0.1$eV ($\sim \hbar\omega_0/2$), where ω_0 is the frequency of the E_{2g} phonon in the undoped case and then increases with E_F. Figures 14(b),(d) indicate that in SLG and BLG, FWHM(G) decreases

for both electron and hole doping. However, the FWHM increases at higher doping level for both SLG and BLG. Figure 14(c) plots Pos(G) of BLG. We note that (i) Pos(G) does not increase until $E_F \sim 0.1$eV ($\sim \hbar\omega_0/2$). (ii) Between 0.1 and 0.4eV, the BLG slope R=$\frac{dPos(G)}{dE_F}$ is smaller than the SLG one. (iii) A kink is observed in Fig. 14(c) at $E_F \sim 0.4$eV. (iv) Beyond $E_F > 0.4$eV the slope is larger than in SLG. (v) The kink position does not significantly depend on γ_1 used to convert V_{TG} in E_F (e.g. a $\sim 66\%$ change in γ_1 modifies E_F by $\sim 6\%$).

Prof. Rao *et al.* group[61,62] has extensively studied the effect of doping by molecular charge transfer from electron-donor molecules such as tetrathiafulvalene (TTF) and electron acceptor molecules such as tetracyanoethylene (TCNE). Here, unlike electrochemical gate doping, the G band shifts shifts to lower frequency with TTF and to higher frequency with TCNE. However, the effects of doping achieved by substitution with boron (hole doping) and nitrogen (electron doping)[63] are similar to the electrochemical doping.

4.3. *Theoretical calculations*

G mode

In doped graphene, the shift of the Fermi energy induced by doping gives two major effects: (i) a change of the equilibrium lattice parameter with a consequent stiffening/softening of the phonons, and (ii) the onset of effects beyond the Adiabatic Born-Oppenheimer approximation that modify the phonon dispersion close to the Kohn anomalies.[30,56] The excess (defect) charge results in an expansion (contraction) of the crystal lattice. This was extensively investigated in order to understand graphite intercalation compounds.[64] Dynamic effects beyond the Born-Oppenheimer approximation play a fundamental role in the description of the KA in single wall carbon nanotubes and in graphene.[29–31,56]

The main contribution comes from the non-adiabatic or "dynamic" effects due to electron-phonon coupling, denoted by $\Delta Pos(G)^{dyn}$. The physics behind the "dynamic" effect is basically how the carriers screen the phonon vibrations. The carrier screening can be expressed in terms of phonon decay into interband real (solid) and virtual (dashed) electron-hole excitations, as shown in Fig. 15. Now, as the Fermi energy enters in the conduction or valence band, some of the electron-hole excitations will be blocked because of Pauli exclusion principle, as shown schematically in Figs. 15(b),(c), which will reduce the screening of phonons by the carriers,
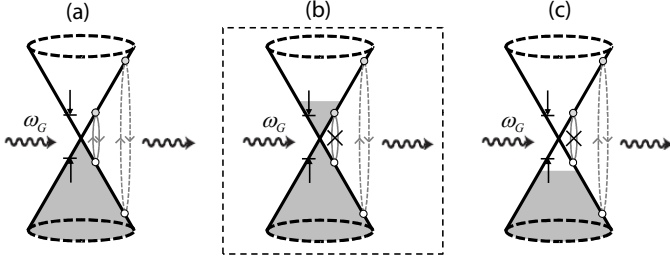
Fig. 15. (a). Phonon decay into real (solid) and virtual (dashed) electron-hole excitations. The gap between the vertical arrows corresponds to the phonon energy $\hbar\omega_G$. (b) Electron doped: ($E_F > \hbar\omega_G/2$) no real transitions, only virtual transitions. (c) Hole doped: ($E_F < \hbar\omega_G/2$) again only virtual transitions.

resulting in upshift of the phonon frequency with respect to the undoped case. This effect will be symmetric for both the electron and hole doping. $\Delta Pos(G)^{dyn}$ is calculated from the phonon self energy Π.[30,51,65,66]

$$\hbar\Delta Pos(G)^{dyn} = \text{Re}[\Pi(E_F) - \Pi(E_F = 0)]. \tag{9}$$

The electron-phonon coupling (EPC) contribution to FWHM(G) is given by:

$$\text{FWHM(G)}^{EPC} = 2\text{Im}[\Pi(E_F)] \tag{10}$$

The self energy corrections are calculated using the time dependent perturbation (TDPT) theory and can be written for phonon with wave vector q as:

$$\Pi(E_F) = \sum_{\mathbf{k},\mathbf{k}',\mathbf{s},\mathbf{s}'} |W_{\mathbf{kq}}|^2 \frac{[f(\epsilon_{sk}) - f(\epsilon_{s'k'})]}{\epsilon_{\mathbf{sk}} - \epsilon_{s'\mathbf{k}'} + \hbar\omega_{\mathbf{q}} + i\delta} \tag{11}$$

where $W_{\mathbf{kq}}$ is the strength of the electron-phonon interaction, $f(\epsilon) = 1/[\exp(\frac{\epsilon - E_F}{k_B T}) + 1]$ is the Fermi-Dirac distribution, $\mathbf{k}' = \mathbf{k} + \mathbf{q}$ and δ is a broadening factor accounting for charge inhomogeneity. Thus, the self energy for the $q = 0$ phonon (E_{2g}) mode at $\mathbf{\Gamma}$ in SLG is:[30,66]

$$\Pi(E_F) = \alpha' \int_0^\infty \gamma^2 k dk \sum_{s,s'} \phi_{ss'} \frac{f(\epsilon_{sk}) - f(\epsilon_{s'k})}{\epsilon_{sk} - \epsilon_{s'k} + \hbar\omega_0 + i\delta} \tag{12}$$

Here $\phi_{ss'}$ is weightage of the electron-phonon coupling (EPC) for transitions between conduction and valence bands in a bilayer graphene and $s=+1$ and $s=-1$ are band indices for the conduction and valence bands respectively.

Equation (12) can be rewritten as:

$$\Pi(E_F) = \alpha' \int_{-\infty}^{\infty} \frac{f(\epsilon) - f(-\epsilon)}{2\epsilon + \hbar\omega_0 + i\delta} |\epsilon| d\epsilon, \tag{13}$$

where $\alpha' = \frac{\hbar A_{uc} EPC(\Gamma)^2}{\pi M \omega_0 (\hbar v_F)^2}$, $A_{uc} = 5.24$ Å^2 is the graphene unit-cell area, M is the carbon atom mass and EPC(Γ) is the electron-phonon coupling constant. $f(\epsilon) = 1/[\exp(\frac{\epsilon - E_F}{k_B T}) + 1]$ is the Fermi-Dirac distribution and δ is a broadening factor accounting for charge inhomogeneity. By converting E_F into electron density n $(E_F = \hbar |v_F| \sqrt{\pi n})$ we can plot $\Delta Pos(G)^{dyn}$ as a function of n.

Lattice relaxation effect

The non-adiabatic effect alone does not explain the electron-hole asymmetry seen in Fig. 11(a). To explain this we need to consider the effect of doping on the phonons due to the doping induced change of the equilibrium lattice parameter, termed as $\Delta Pos(G)^{st}$ and has been calculated using the relation:[30]

$$\Delta Pos(G)^{st} = -2.13n - 0.0360n^2 - 0.00329n^3 - 0.226 |n|^{3/2} \tag{14}$$

where n, in units of 10^{13}cm^{-2}, is positive and negative for electron and hole doping, respectively.

Comparison between the experiment and theory (Single layer)

The theoretical trend (solid line) in Fig. 11(a) is generated from $\Delta Pos(G)^{dyn} + \Delta Pos(G)^{st}$ at T = 300K using the value of parameter $\alpha' = 4.4 \times 10^{-3}$ and $\delta = 0.1$eV, where α' is obtained from the density functional theoretical (DFT) values of EPC(Γ) = 45.6 (eV)^2/ Å^2 and δ is obtained by fitting the experimental FWHM using Eq. (10), as shown in Fig. 11(b). The quantitative agreement between the experiment and theory (Fig. 11(a)) is poor for large doping, and requires to reconsider the non-adiabatic calculations of Ref. [30] incorporating electron-electron interactions.

Line-width

As mentioned in the previous section, the FWHM (solid line) in Fig. 11(b) is plotted using the Eq. (10) to get the best fit with the experimental data (open squares). The reduction of line-width at higher doping can be understood from how the phonon decays into real electron-hole excitations

which conserve the energy and the momentum and this is possible if $|E_F| < \hbar\omega_G/2$. Now, at higher doping $|E_F| > \hbar\omega_G/2$, to satisfy the Pauli principle the real transitions are blocked, as a result life time increases or in other words line-width decreases.

2D mode

The depencence of 2D peak position as a function of doping is very different from the G peak. As mentioned earlier 2D-peak originates from a second order, double resonant (DR) Raman scattering mechanism.[38,46,68] In this process, the incoming laser radiation creates an electron-hole pair close to the Fermi point $\mathbf{k}_F = \mathbf{K}$. The photo-excited electron is then scattered towards the second inequivalent Fermi point $\mathbf{k}_F = \mathbf{K}'$ by a phonon of energy $\hbar\omega_q$ and wavevector $\mathbf{q}$. A scattering event with a second phonon, of the same energy but opposite momentum, brings the electron back to its original position in reciprocal space. The recombination of the electron-hole pair finally results in the emission of a photon, whose energy is decreased by $2\hbar\omega_{\mathbf{q}}$ with respect to the incoming laser radiation. The order of these four events is not fixed, and all their combinations are possible and have to be taken into account.[68]

The position of the 2D-peak is calculated such that the the second-order, double resonant scattering cross section is maximized. The trigonal warping of the $\pi - \pi^*$ bands and the angular dependence of the electron-phonon coupling (EPC) matrix elements,[38] results in phonons oriented along the **ΓKM** direction and with $\mathbf{q} > \mathbf{K}$ giving a non-negligible contribution to the 2D-peak. The exact value of q is determined by the constraint that the energy of the incoming photons $\hbar\omega_L$ has to exactly match a real electronic transition: $\hbar\omega_L = \epsilon(\pi^*, \mathbf{q}') - \epsilon(\pi, \mathbf{q}')$, where $\epsilon(n, \mathbf{k})$ is the energy of an electron of band index n and wave vector $\mathbf{k}$, and $\mathbf{q}'$ is measured from $\mathbf{K}$ and is in the **ΓKM** direction. Recall, $q = 2q' + K$. The D mode is associated with the phonon near K-point on the TO branch. For laser energy of 2.41eV, the magnitude of wave vector $\mathbf{q}$ is 0.844 in $\frac{2\pi}{a_0}$ units, a_0 being the lattice parameter of graphene.

For the 2D peak measured at 514nm the influence of dynamic effects is expected to be negligible, since the phonons giving rise to the 2D-peak are far away from the Kohn anomaly at $\mathbf{K}$. Therefore, the dynamic corrections for 2D mode are small and hence the 2D-peak position as a function of doping is calculated from the lattice relaxation effect within a DFT framework and has been given in Ref. [50]. The comparison between the theoretical

and the experimental position of the 2D peak is shown in Fig. 11(c) by
a solid line. Indeed, as experimentally determined, the position of the 2D
peak is predicted to decrease for an increasing electron concentration in the
system. This allows to use the 2D peak to discriminate between electron
and hole doping. The FWHM(2D) (Fig. 11(d)) increases at higher doping
and this is not related to disorder as we do not see any appearance of the
D mode (defect mode) in the Raman spectra even at higher doping level.
We have not yet understood this result.

Intensity ratio

Figure 16(a) shows how the G mode and 2D mode Raman intensities in
single layer graphene change with doping. For this we have normalized
the Raman spectra with respect to the polymer peak at ~ 2890 cm^{-1} to
exclude any external effects like power change or defocusing etc. The G peak
increases with doping and then decreases at higher doping level. However,
2D peak decreases sharply with doping. Figure 16(b) plots the variation
of 2D and G intensity ratio (I(2D)/I(G)) as a function of doping. It shows
a strong dependence on doping. Hence the 2D/G intensity ratio is an
important parameter to estimate the doping concentration. Figures 16(b)
and 11(a) also show that the I(2D)/I(G) ratio and G peak position should
not be used to estimate the number of graphene layers.

Now, for BLG:[58]

$$\Pi(E_F)^{BLG} = \alpha' \int_0^\infty \gamma^2 k dk \sum_{s,s'} \sum_{j,j'} \phi^+{}_{jj'}$$
$$\times \frac{[f(\epsilon_{sjk}) - f(\epsilon_{s'j'k})][\epsilon_{sjk} - \epsilon_{s'j'k}]}{(\epsilon_{sjk} - \epsilon_{s'j'k})^2 - (\hbar\omega_0 + i\delta)^2} \tag{15}$$

where s,s' are the band indices and j,j' are the subband indices. It can
be seen from Eq. (15) that for BLG both interband and intraband tran-
sitions contribute. The $\phi^+_{jj'}$ is weightage of the electron-phonon coupling
(EPC) for transitions between different subbands in a bilayer graphene.
The '+' sign is for the symmetric mode which is Raman active G mode.
The values of $\phi^+_{jj'}$ are given in Ref. [58] and can be expressed as:

$$\phi_{11} = \phi_{22} = 0.5 \frac{(\gamma k)^2}{(\gamma_1/2)^2 + (\gamma k)^2} \tag{16}$$
$$\phi_{12} = \phi_{21} = 0.5 \frac{(\gamma_1/2)^2}{(\gamma_1/2)^2 + (\gamma k)^2}$$
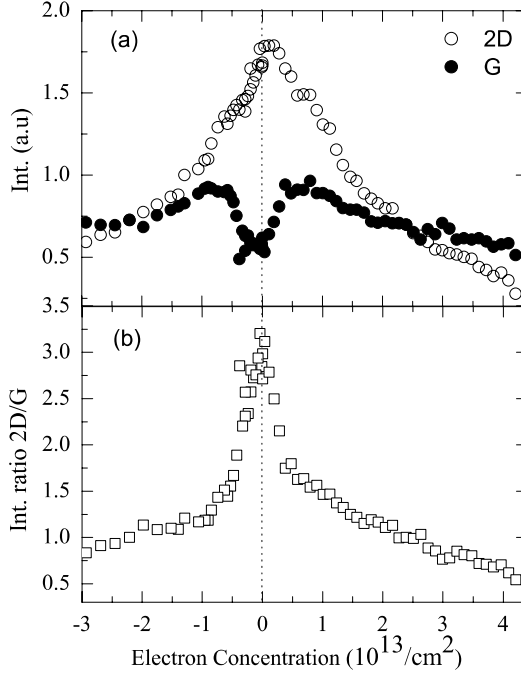
Fig. 16. (a) Intensity of G and 2D as a a function of doping. (b) I(2D)/I(G) as a function of hole and electron doping.[50]

Equation (15) can be decoupled for different transitions and shown pictorially in Figs. 17(a),(b), where the blue lines and red lines correspond to interband and intraband transitions, respectively. The contribution of interband and intraband transitions to the Eq. (15) are plotted separately in Fig. 17(c) as a function of Fermi energy shift at T=4K and δ=0.001eV. The dashed line, dotted line and solid line in Fig. 17(c) correspond to the interband, intraband and total (interband plus intraband) contribution, respectively. We see a change of slope at $\sim$ 0.4 eV, which is the signature of the second subband filling. It is clear from Fig. 17(c) that the sharp change of slope at $\sim$ 0.4 eV becomes pronounced due to intraband contribution. Note that the slope of $\Delta Pos(G)^{dyn}$ just above $E_F = \gamma_1$ is double than that just below γ_1.

Figure 18 shows the theoretical results for the change in peak positions of G mode and FWHM for both SLG and BLG at different temperatures (T) and broadening factors (δ) using the value of parameter
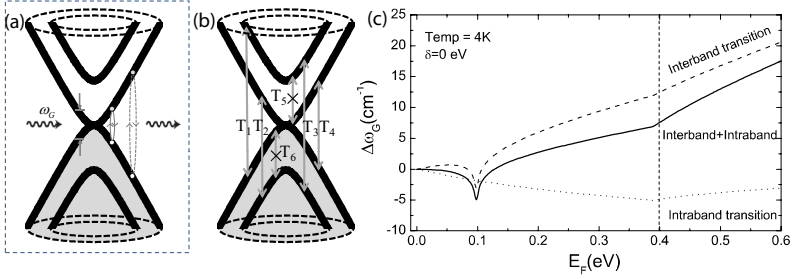
Fig. 17. (a) Phonon decay into real (solid circle) and virtual (dotted circle) electron-hole excitations. The gap between the vertical arrows corresponds to the phonon energy. (b) Different transitions. Blue lines and red lines for interband (T_1, T_2, T_3 and T_4) and intraband (T_5 and T_6) transitions, respectively. (c) Frequency shift of G peak as a function of Fermi energy. Dashed line and dotted line correspond to interband and intraband transition, respectively. Black line is the total contribution.
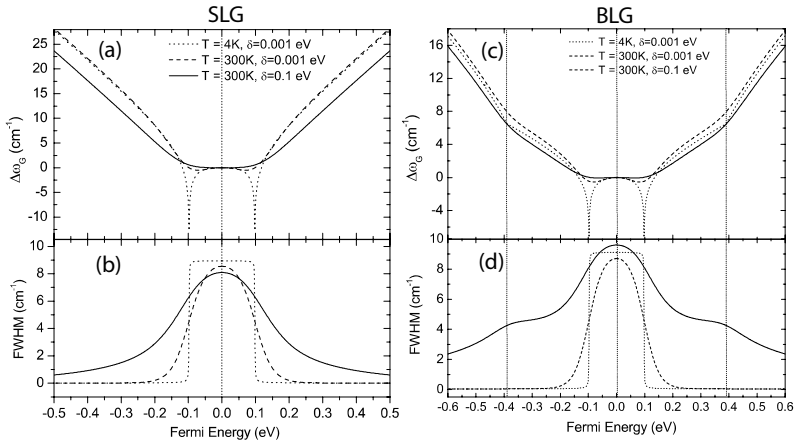
Fig. 18. (a) Pos(G) for (a) SLG; (c) BLG as a function of Fermi energy. FWHM(G) of (b) SLG; (d) BLG as a function of Fermi energy at different temperatures (T) and broadening factors δ.

$\alpha' = 4.4 \times 10^{-3}$, where the value of α' is obtained from the density functional theoretical values of EPC(Γ) = 45.6 (eV)^2/ $\mathring{A}^2$ and $v_F = 0.84 \times 10^6$ m/sec[29,56]). It can seen from Fig. 18 that the logarithmic divergences at $E_F = \hbar\omega_G/2$ are only visible at low temperatures but at room temperature with cleaner sample ($\delta \sim 0$) it will be of the order of ~ -1cm^{-1}. Therefore, at room temperature the frequency position remains constant upto 0.1eV

and then increases linearly with E_F. For BLG there is a change of slope at $E_F \sim 0.4$ eV, as seen in Fig. 18(c).

The FWHM of SLG and BLG decreases with E_F, as shown in Figs. 18(b),(d). Only the real transitions contribute to the life time of phonon. Therefore, with Fermi energy shift ($E_F > \hbar\omega_0/2$) there will be blockage of interband real transitions due to Pauli exclusion principle and as a result FWHM will decrease. Note that there is a kink in FWHM at $E_F \sim 0.4$ eV for BLG with $\delta = 0.1$eV, as seen in Fig. 18(d). This is due to the blockage of real intraband transitions. However, there are no real intraband transitions in BLG for $\delta = 0$.

4.3.1. *Comparison between the experiment and theory (Bilayer)*

To compare calculations with the experimental data, we need to know exact value of δ in our sample. The parameter δ is obtained by fitting the experimental FWHM(G) to FWHM(G)= FWHM(G)^{EPC}+FWHM(G)^0, with FWHM(G)^0 a constant accounting for non-EPC effects (e.g. resolution and anharmonicity). From Fig. 14(b) and Fig. 14(d) we determine $\delta = 0.13$eV for SLG and $\delta = 0.03$eV for BLG. We get FWHM(G)$^0 = 4.3$cm^{-1} and 5.1cm^{-1} for SLG and BLG, respectively. These δ values are then used to compute Pos(G). Note that the relation between n and E_F implies that same amount of charge inhomogeneity causes different E_F broadening in SLG and BLG (e.g. $\delta n \sim 10^{12}$cm^{-2} would give $\delta = 0.13$eV and 0.03eV in SLG and BLG, respectively).

The solid lines in Fig. 14 are the theoretical Pos(G) and FWHM(G) trends at 300K. The FWHM(G) of SLG and BLG increases at higher doping, similar to the FWHM(2D) of SLG. The kink at ~ 0.4 eV in BLG is the most striking difference between SLG and BLG. It is the signature of the second subband filling in BLG.

4.3.2. *Physical interpretation*

A shift of E_F changes $f(\epsilon)$ in Eq. (15) thereby modifying the type and number of transitions contributing to Π. A positive contribution to Π arises when $|\epsilon_{s,j,k} - \epsilon_{s',j',k}| < \hbar\omega_0$, i.e. a subset of those between ($s = -1; j = 1$) and ($s = 1; j = 1$) (interband transitions, solid blue lines in Fig. 19). On the other hand interband transitions with $|\epsilon_{s,j,k} - \epsilon_{s',j',k}| > \hbar\omega_0$ (solid red lines in Fig. 19) and all intraband (between ($s = \pm 1; j = 1$) and ($s = \pm 1, j = 2$), dashed red lines in Fig. 19) contribute to Π as negative
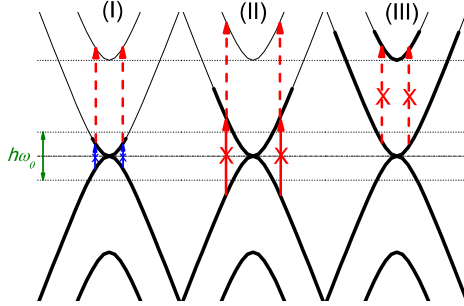
Fig. 19. Phonon renormalization for BLG: (I) $E_F < \hbar\omega_0$, (II) $\hbar\omega_0 < E_F < \gamma_1$, (III) $E_F > \gamma_1$. Blue and red arrows correspond respectively to positive and negative contributions to Π. Solid and dashed arrows correspond to interband and intraband processes respectively.

terms. Let see what happen to Π with Fermi energy shift. We discuss three different cases: (I), $|E_F| < \hbar\omega_0$, (II) $\hbar\omega_0 < |E_F| < \gamma_1$, and (III) $|E_F| > \gamma_1$. Taking $E_F > 0$ (the same applies for $E_F < 0$). Case (I), $|E_F| < \hbar\omega_0$: the positive contributions from interband transitions are suppressed, whereas new negative intraband transitions are created, resulting in strong phonon softening. Experimentally it has been observed at low temperatures in Ref. [69]. At T=300K, these effects are blurred by the broadening of the Fermi function, resulting in an almost doping independent phonon energy. Case (II), $\hbar\omega_0 < |E_F| < \gamma_1$: the shift of E_F decreases negative interband contributions and creates new negative intraband transitions.

Taking into account their number and relative weight (given by $\Phi_{jj'}/(\epsilon_{s,j,k} - \epsilon_{s',j',k})$), it has been shown that interband transitions outweight intraband ones, leading to in phonon hardening. Case (III), $|E_F| > \gamma_1$: this is similar to (II), with a significant difference that the second subband filling suppresses negative intraband transitions at $\mathbf{k} \sim \mathbf{K}$, thereby leading to the phonon hardening. Therefore, the kink in Fig. 14 is a direct measurement of the interlayer coupling strength.

Bilayer graphene exhibits an inversion symmetry. As shown in Fig. 1, the in plane lattice vibrations (G phonon) are classified into symmetric (with displacement of two layers oscillating in-phase) and antisymmetric (with displacement of two layers oscillating out-of-phase). The symmetric mode is Raman active and the antisymmetric mode is IR active. Under inversion operation through the inversion center of the bilayer structure, the in- phase motion is invariant while the out-of-phase motion changes sign. In an unperturbed bilayer graphene the in-phase phonon and the out-of-phase
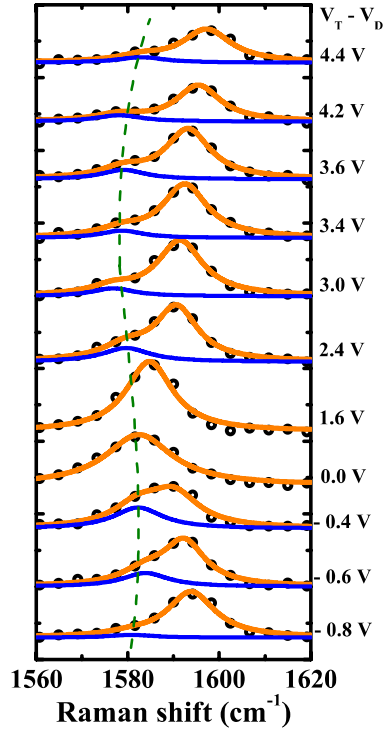
Fig. 20. G mode spectra of top gated bilayer graphene for different top gate voltages. Lines are Lorentzian fit to the experimental data denoted by squares. The dotted line shows the evolution of the lower mode. Note, that that the Dirac point voltage is subtracted from applied voltages.[75]

phonon are the eigenstates of the bilayer.[71,72] However, as the bilayer is doped either with electrons or with holes, owing to the existence of an inter-layer electric field, the inversion symmetry is broken, mixing the symmetric and the antisymmetric modes. The breaking of this inversion symmetry is manifested in the splitting of Raman G mode, with energy and spectral weight evolving as the doping increases.[73–75] Figure 20 shows the bilayer G band splitting as a function of top gate voltage in our experiments.[75] The resulting phonon eigenstates can be viewed as a superposition of both the in-phase and out-of-phase displacements and both the modes become Raman active. Near the charge neutral point, Raman G peak is a single line peak which is attributed to the in-phase motion of the two layers. As the doping increases, the separation between the two bands widens,

one decreasing in energy (lower mode) while the other mode increasing in energy (higher mode) and the intensity is determined by the content of symmetric component in each mode. This results are being understood in the light of recent calculations of bilayer phonons.[71,72]

5. Conclusions

Raman spectroscopy is a powerful probe to look into vibrational signatures of undoped and doped graphene layers. Owing to the high electron-phonon coupling strength in graphene, Kohn anomalies occur in graphene's phonon dispersion at the Γ and K point phonons. The doping reduces the screening of the and the G phonon's energy increases for both electron and hole doping. The FWHM of G mode decreases on doping because of the blockage of the decay channels of phonons into electronhole pairs due to the Pauli exclusion principle. The frequency of Raman G mode can be used to estimate the carrier concentration whereas the 2D peak position determine the sign of induced carriers. Additionally, Raman spectroscopy can be used to probe breaking of inversion symmetry in bilayer graphene where G peak splits for moderate doping concentration due to mixing of symmetric and antisymmetric modes. The agreement of time dependent perturbation calculations for the phonon frequencies with the experimental results for single and bilayer graphene as a function of doping is rather modest at high concentrations. This brings out a need to look into the theory of phonon renormalization further, incorporating electron-electron correlations and other possible effects.

In near future, it will be interesting to study doping dependence of Raman phonons in graphene nanoribbons, functionalized graphenes, graphanes[22] and graphenes prepared by heating of SiC, chemical vapour deposition on metal surfaces and chemical methods. The study of hot phonons[76] at large drain-source bias voltage will also be important from the point of view of graphene devices.

Acknowledgments

References

1. K. S. Novoselov, A. K. Geim, S. V. Morozov, D. Jiang, Y. Zhang, S. V. Dubonos, I. V. Grigorieva, and A. A. Firsov, *Science*, **306**, 666 (2004).
2. K. S. Novoselov, A. K. Geim, S. V. Morozov, D. Jiang, M. I. Katsnelson, I. V. Grigorieva, S. V. Dubonos, and A. A. Firsov, *Nature*, **438**, 197 (2005).
3. Y. Zhang, Y.-W. Tan, H. L. Stormer, and P. Kim, *Nature*, **438**, 201 (2005).
4. N. D. Mermin, *Phys. Rev.*, **176**, 250 (1968).
5. A. K. Geim and K. S. Novoselov, *Nat. Mater.*, **6**, 183 (2007).
6. A. Nagashima, Ayato Nagashima, Kenji Nuka, Hiroshi Itoh, Takeo Ichinokawa, Chuhei Oshima, and Shigeki Otani, *Surf. Sci.*, **291**, 93 (1993).
7. C. N. R. Rao, A. K. Sood, Rakesh Voggu, and K. S. Subrahmanyam, *J. Physical Chem. Letters*, **1**, 572 (2010).
8. C. N. R. Rao, A. K. Sood, K. S. Subrahmanyam, and A. Govindaraj, *Angew. Chem. Int. Ed.*, **48**, 7752 (2009).
9. C. Berger, Z. Song, T. Li, X. Li, A. Y. Ogbazghi, R. Feng, Z. Dai, A. N. Marchenkov, E. H. Conrad, P. N. First, and W. A. de Heer, *J. Phys. Chem. B*, **108**, 19912 (2004).
10. T. Ohta *et al.*, *Science*, **313**, 951 (2006).
11. A. N. Obraztsov, *Nature Nanotechnology*, **4**, 212 (2009).
12. A. Reina, X. Jia, J. Ho, D. Nezich, H. Son, V. Bulovic, M. S. Dresselhaus, and J. Kong, *Nano Lett.*, **9**, 30 (2009).
13. V. C. Tung *et al.*, *Nature Nanotechnology*, **4**, 25 (2009).
14. K. S. Subrahmanyam *et al.*, *J. Phys. Chem. C*, **113**, 4257 (2009).
15. S. R. C. Vivekchand *et al.*, *J. Chem. Sci.*, **120**, 9 (2008).
16. S. V. Morozov, K. S. Novoselov, M. I. Katsnelson, F. Schedin, D. C. Elias, J. A. Jaszczak, and A. K. Geim, *Phys. Rev. Lett.*, **100**, 016602 (2008).
17. X. Du, I. Skachko, A. Barker, and E. Y. Andrei, *Nat. Nanotechnol.*, **3**, 491 (2008).
18. K. I. Bolotin, K. J. Sikes, Z. Jiang, G. Fundenberg, J. Hone, P. Kim, and H. L. Stormer, *Solid State Commun.*, **146**, 351 (2008). K. I. Bolotin, K. J. Sikes, J. Hone, H. L. Stormer, and P. Kim, *Phys. Rev. Lett.*, **101**, 096802 (2008).
19. X. Du, I. Skachko, F. Duerr, A. Luican, and E. Y. Andrei, *Nature*, **462**, 192 (2009).
20. K. I. Bolotin, F. Ghahari, M. D. Shulman, H. L. Stormer, and P. Kim, *Nature*, **462**, 196 (2009).
21. A. H. Castro Neto, F. Guinea, N. M. R. Peres, K. S. Novoselov, and A. K. Geim, *Rev. Mod. Physics*, **81**, 109 (2009).
22. A. K. Geim, *Science*, **324**, 1530 (2009).
23. M. I. Katnelson, K. S. Novoselov, and A. K. Geim, *Nature Physics*, **2**, 620 (2006).
24. A. F. Young and P. Kim, *Nature Physics*, **462**, 1 (2009).
25. Y. -W. Tan, Y. Zhang, K. Bolotin, Y. Zhao, S. Adam, E. H. Hwang, S. Das Sarma, H. L. Stormer, and P. Kim, *Phys. Rev. Lett.*, **99**, 246803 (2007).
26. S. Reich and C. Thomsen, *Phil Trans. Royal Soc. London*, **A362**, 2271 (2004).

27. J. A. Yan, W. Y. Ruan, and M. Y. Chou, *Phys. Rev. B*, **77**, 125401 (2008).
28. O. Dubay and G. Kresse, *Phys. Rev. B*, **67**, 035401 (2003).
29. S. Piscanec, M. Lazzeri, F. Mauri, A. C. Ferrari, and J. Robertson, *Phys. Rev. Lett.*, **93**, 185503 (2004).
30. M. Lazzeri and F. Mauri, *Phys. Rev. Lett.*, **97**, 266407 (2006).
31. S. Piscane, M. Lazzeri, J. Robertson, A. C. Ferrari, and F. Mauri, *Phys. Rev. B*, **75**, 035427 (2007).
32. A. H. Castro-Neto and F. Guinea, *Phys. Rev. B*, **75**, 045404 (2007).
33. S. K. Saha, U. V. Waghmare, H. R. Krishnamurthy, and A. K. Sood *Phys. Rev. B*, **76**, 201404(R) (2007).
34. C. H. Park, F. Giustino, M. L. Cohen, and S. G. Louie, *Nano lett.*, **8**, 4229 (2008).
35. J. Yan, W. Y. Ran, and M. Y. Chou, *Phys. Rev. B*, **79**, 115443 (2009).
36. C. Attaccalite, L. Wirtz, M. Lazzeri, F. Mauri, and A. Rubio, *Nano Lett.*, **10**, 1172 (2010).
37. W. Kohn, *Phy. Rev. Lett.*, **2**, 393 (1959).
38. A. C. Ferrari, J. C. Meyer, V. Scardaci, C. Casiraghi, M. Lazzeri, F. Mauri, S. Piscanec, D. Jiang, K. S. Novoselov, S. Roth, and A. K. Geim, *Phys. Rev. Lett.*, **97**, 187401 (2006).
39. A. Gupta, G. Chen, P. Joshi, S. Tadigadapa, and P. C. Eklund, *Nano Lett.*, **6**, 2667 (2006).
40. D. Graf, F. Molitor, K. Ensslin, C. Stampfer, A. Jungen, C. Hierold, and L. Wirtz, *Nano Lett.*, **7**, 238 (2007).
41. A. C. Ferrari, *Solid State Comm.*, **143**, 47 (2007).
42. C. Casiraghi, S. Pisana, K. S. Novoselov, A. K. Geim, and A. C. Ferrari, *Appl. Phys. Lett.*, **91**, 233108 (2007).
43. C. Stampfer, F. Molitor, D. Graf, K. Ensslin, A. Jungen, C. Hierold, and L. Wirtz, *Appl. Phys. Lett.*, **91**, 241907 (2007).
44. A. Das, B. Chakraborty, and A. K. Sood, *Bull. Mat. Sci.*, **31**, 579 (2008).
45. M. S. Dresselhaus, A. Jorio, M. Hofmann, G. Dresselhaus, and R. Saito, *Nano Lett.*, **10**, 751 (2010).
46. C. Thomsen and S. Reich, *Phys. Rev. Lett.*, **85**, 5214 (2000).
47. A. K. Sood, R. Gupta, and S. A. Asher, *J. Appl. Phys.*, **90**, 4494 (2001).
48. C. Lu, Q. Fu, S. Huang, and J. Liu, *Nano Lett.*, **4**, 623 (2004).
49. A. Das, A. K. Sood, A. Govindaraj, A. M. Saitta, M. Lazzeri, F. Mauri, and C. N. R. Rao, *Phys. Rev. Lett.*, **99**, 136803 (2007).
50. A. Das, S. Pisana, B. Chakraborty, S. Piscanec, S. R. Saha, U. V. Waghmare, K. S. Novoselov, H. R. Krishnamurthy, A. K. Geim, A. C. Ferrari, and A. K. Sood, *Nature Nanotech.*, **3**, 210 (2008).
51. A. Das, B. Chakraborty, S. Piscanec, S. Pisana, A. K. Sood, and A. C. Ferrari, *Phys. Rev. B*, **79**, 155417 (2009).
52. A. Das and A. K. Sood, *Phys. Rev. B*, **79**, 235429 (2009).
53. Richard H. Boyd, *J. Polym. Sci. Polym. Phys. Ed.*, **21**, 505 (1983).
54. B. Chakraborty, A. Das, and A. K. Sood, *Nanotechnology*, **20**, 365203 (2009).
55. T. Yoshihara, H. Tadokoro, and S. Murahashi, *J. Chem. Phys.*, **41**, 2902 (1964).

56. S. Pisana, M. Lazzeri, C. Casiraghi, K. Novoselov, A. K. Geim, A. C. Ferrari, and F. Mauri, *Nature Materials*, **6**, 198 (2007).
57. J. Yan, Y. Zhang, P. Kim, and A. Pinczuk, *Phys. Rev. Lett.*, **98**, 166802 (2007).
58. T. Ando, *J. Phys. Soc. Jpn.*, **76**, 104711 (2007).
59. Note that in Fig. 3 of Ref. [58] both SLG density of states and electron concentration are multiplied by a factor 2.
60. A. H. Castro Neto *et al.*, *cond-mat/0709.1163v1* (2007).
61. R. Voggu, B. Das, C. S. Rout, and C. N. R. Rao, *J. Phys. Condens. Matter*, **20**, 4772204 (2008).
62. A. K. Manna and S. Pati, *Chem. Asian J*, **4**, 855 (2009).
63. L. S. Panchakarla, K. S. Subrahmanyam, S. K. Saha, A. Govindaraj, H. R. Krishnamurthy, U. V. Waghmare, and C. N. R. Rao, *Adv. Mater.*, **21**, 4726 (2009).
64. L. Pietronero and S. Strassler, *Phys. Rev. Lett.*, **47**, 593 (1981).
65. W. E. Pickett and P. B. Allen, *Phys. Rev. B*, **16**, 3127 (1977).
66. T. Ando, *J. Phys. Soc. Jpn.*, **75**, 124701 (2006).
67. M. Lazzeri, S. Piscanec, F. Mauri, A. C. Ferrari, and J. Robertson, *Phys. Rev. B*, **73**, 155426 (2006).
68. J. Maultzsch, S. Reich, and C. Thomsen, *Phys. Rev. B*, **61**, 121407 (2001).
69. J. Yan, E. A. Henriksen, P. Kim, and A. Pinczuk, *Phys. Rev. Lett.*, **101**, 136804 (2008).
70. D. M. Basko, *Phys. Rev. B*, **76**, 081405(R) (2007).
71. T. Ando and Mikito Koshino, *J. Phys. Soc. Jpn.*, **78**, 034709 (2009).
72. P. Gava, M. Lazzeri, A. M. Saitta, and F. Mauri, *Phys. Rev. B*, **80**, 155422 (2009).
73. L. M. Malard, D. C. Elias, E. S. Alves, and M. A. Pimenta, *Phys. Rev. Lett.*, **101**, 257401 (2008).
74. J. Yan, T. Villarson, E. A. Henriksen, P. Kim, and A. Pinczuk, *Phys. Rev. B*, **80**, 241417(R) (2009).
75. B. Chakraborty, A. Das, and A. K. Sood, Unpublished (2010).
76. S. Berciaud, M. Y. Han, L. E. Brus, P. Kim, and T. F. Heinz, *cond-mat/1003.6101v1* (2010).

Chapter 8

Phonons and Electron-Phonon Interaction in Graphene and Nanotube

Tsuneya Ando

Department of Physics, Tokyo Institute of Technology,
2–12–1 Ookayama, Meguro-ku, Tokyo 152-8551, Japan
ando@phys.titech.ac.jp

A brief review is given on long-wavelength acoustic phonons, long-wavelength optical phonons, and zone-boundary phonons in graphene and carbon nanotubes together with effects of their interaction with electrons from a theoretical point of view.

1. Introduction

Monolayer graphene was fabricated using the so-called scotch-tape technique[1] and the magnetotransport was measured including the integer quantum Hall effect.[2,3] Since then the graphene became the subject of extensive theoretical and experimental study.[4,5] The carbon nanotube is graphene rolled into a cylindrical form, discovered and synthesized earlier than graphene.[6] The purpose of this paper is to give a brief review on phonons and effects of electron-phonon interaction in graphene and nanotubes.

2. Monolayer Graphene and Nanotube

In a monolayer graphene the conduction and valence bands consisting of π orbitals cross at K and K' points of the Brillouin zone, where the Fermi level is located.[7,8] Electronic states near a K point are described by the $\mathbf{k} \cdot \mathbf{p}$ equation equivalent to Weyl's equation or a Dirac equation with vanishing rest mass.[6,9–14] In the vicinity of the K point, in particular, we have

$$\gamma(\vec{\sigma} \cdot \hat{\mathbf{k}})\mathbf{F}(\mathbf{r}) = \varepsilon \mathbf{F}(\mathbf{r}), \quad \mathbf{F}(\mathbf{r}) = \begin{pmatrix} F_A(\mathbf{r}) \\ F_B(\mathbf{r}) \end{pmatrix}, \tag{1}$$

where F_A and F_B describe the amplitude at sublattice points A and B, respectively, γ is a band parameter, $\hat{\mathbf{k}} = (\hat{k}_x, \hat{k}_y)$ is the wave-vector operator, and $\vec{\sigma} = (\sigma_x, \sigma_y)$ is the Pauli matrix. The equation of motion for the K' point is obtained by replacing $\vec{\sigma}$ with $\vec{\sigma}^*$ in the above equation.

Electronic states in a carbon nanotube (CN) are obtained by imposing generalized periodic boundary condition $\mathbf{F}(\mathbf{r}+\mathbf{L}) = \exp(\mp 2\pi\nu i/3)\mathbf{F}(\mathbf{r})$ (upper sign for K and lower for K') in the circumference direction specified by chiral vector $\mathbf{L}$ with $\nu = 0$ or ± 1 determined by the CN structure. We have $\nu = 0$ for a metallic CN and $\nu = \pm 1$ for a semiconducting CN. The direction of $\mathbf{L}$ is called chiral angle and denoted by η.

3. Acoustic Phonon

Acoustic phonons important in the electron scattering are described well by a continuum model.[15] The potential-energy functional for displacement $\mathbf{u} = (u_x, u_y, u_z)$ is written as

$$U[\mathbf{u}] = \int dx dy \, \frac{1}{2}\Big(B(u_{xx}+u_{yy})^2 + S\big[(u_{xx}-u_{yy})^2 + 4u_{xy}^2\big]\Big), \qquad (2)$$

$$u_{xx} = \frac{\partial u_x}{\partial x} + \frac{u_z}{R}, \;\; u_{yy} = \frac{\partial u_y}{\partial y}, \;\; 2u_{xy} = \frac{\partial u_x}{\partial y} + \frac{\partial u_y}{\partial x}, \qquad (3)$$

as in a homogeneous and isotropic two-dimensional (2D) system. The parameters B and S denote the bulk modulus and the shear modulus, respectively ($B = \lambda + \mu$ and $S = \mu$ with λ and μ being Lame's constants). In carbon nanotubes with finite radius R, we should add u_z/R in the expression of u_{xx} as in the above equation, where the x axis is chosen along the circumference direction. In order to discuss out-of-plane distortions, we should consider the potential energy due to nonzero curvature. It is written as

$$U_c[\mathbf{u}] = \frac{1}{2}a^2 \Xi \int dx dy \Big[\Big(\frac{\partial^2}{\partial x^2} + \frac{1}{R^2} + \frac{\partial^2}{\partial y^2}\Big)u_z\Big]^2, \qquad (4)$$

where Ξ is a force constant for curving of the plane. This curvature energy is of the order of the fourth power of the wave vector and therefore is usually much smaller than $U[\mathbf{u}]$.

In nanotubes, the phonon modes are specified by angular momentum n along the circumference direction. Figure 1 shows phonon dispersions calculated in this continuum model.[15] The twisting mode with a linear dispersion and the stretching and breathing modes coupled with each other at their crossing are given by the solid lines. There exist modes $n = \pm 1$ with frequency which vanishes in the long wavelength limit $q \to 0$. These
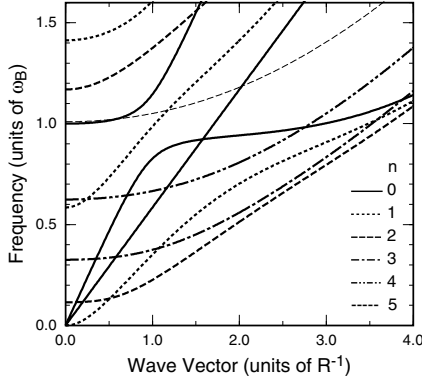
Fig. 1.   Frequencies of acoustic phonons obtained in the continuum model in carbon nanotubes. ω_B is the frequency of the breathing mode and R is the radius.

modes correspond to bending motion of the tube and therefore have the dispersion $\omega \propto q^2$ like a similar mode of a rod. Modes with other n involve displacement from the circular shape of the tube cross section.

A long-wavelength acoustic phonon gives rise to an effective potential called the deformation potential

$$V_1 = g_1(u_{xx} + u_{yy}), \tag{5}$$

proportional to a local dilation, where g_1 of the order of the Fermi level measured from the bottom of the σ bands, i.e., $g_1 \sim 30$ eV. This term appears as a diagonal term in the matrix Hamiltonian in the effective-mass approximation and cannot give rise to backscattering in metallic nanotubes. A higher order term appears due to the modification of local bond length,

$$V_2 = g_2 e^{3i\eta}(u_{xx} - u_{yy} + 2iu_{xy}), \tag{6}$$

where η is the chiral angle in nanotubes and vanishes in graphene, and $g_2 \sim \gamma_0/2$ or $g_2 \sim 1.5$ eV, which is much smaller than the deformation potential constant g_1. This term appears as an off-diagonal term. The total Hamiltonian is written as

$$\mathcal{H}'_K = \begin{pmatrix} V_1 & V_2 \\ V_2^* & V_1 \end{pmatrix}, \quad \mathcal{H}'_{K'} = \begin{pmatrix} V_1 & -V_2^* \\ -V_2 & V_1 \end{pmatrix}. \tag{7}$$

In the following, we shall discuss resistivity and/or conductivity limited by these acoustic phonons in carbon nanotubes. In metallic nanotubes, V_1 does not give rise to backscattering as in the case of impurity scattering.[16,17] Further, phonon modes contributing to backscattering through V_2 depend
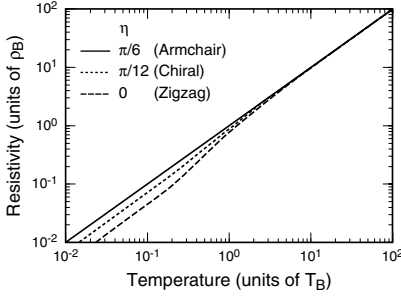
Fig. 2. The resistivity of armchair and zigzag nanotubes in units of $\rho_A(T_B)$ which is the resistivity of the armchair nanotube at $T = T_B$, and T_B denotes the temperature of the breathing mode, $T_B = \hbar\omega_B/k_B$.
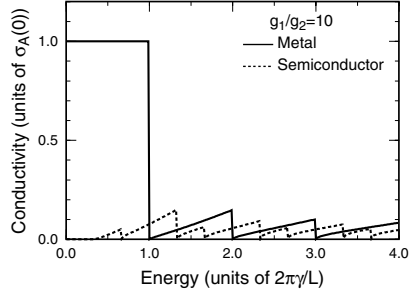
Fig. 3. Fermi-energy dependence of conductivity for metallic and semiconducting CN's with $g_1/g_2 = 10$ in units of $\sigma_A(0)$ denoting the conductivity of an armchair CN with $\varepsilon = 0$.

on chirality η. In fact, transverse twisting modes contribute to the resistivity, while longitudinal stretching and breathing modes contribute to it in zigzag nanotubes. Figure 2 shows calculated temperature dependence of the resistivity, where $\rho_A(T) = (\hbar/e^2)R^{-1}(g_2^2 k_B T/2\gamma^2 S)$. The difference between a zigzag and armchair nanotube appears at temperatures lower than the frequency of the breathing mode ω_B.

Figure 3 shows the Fermi-energy dependence of conductivity for metallic and semiconducting CN's. In metallic CN's, when $\varepsilon(2\pi\gamma/L)^{-1} < 1$, the diagonal potential g_1 causes no backward scattering between two bands with linear dispersion and smaller off-diagonal potential g_2 determines the resistivity. However, when the Fermi energy becomes higher and the number of subbands increases, g_1 dominates the conductivity due to interband scattering. This is the reason that the conductivity changes drastically depending on the Fermi energy in metallic CN's. On the other hand, such a drastic change disappears for semiconducting CN's and smaller conductivity compared to that of a metallic CN shows dominance of the diagonal potential independent of the Fermi energy.

4. Optical Phonon

Long-wavelength optical phonons are known to be measured directly by the Raman scattering.[18–20] Usually, they are described perfectly well in a continuum model. Such a model was developed and the Hamiltonian for electron-phonon interactions was derived,[21] and effects of electron-phonon interaction on optical phonons were recently studied in graphene.[22,23]

Optical phonons are represented by the relative displacement of two sub-lattice atoms A and B,

$$\mathbf{u}(\mathbf{r}) = \sum_{\mathbf{q},\mu} \sqrt{\frac{\hbar}{2NM\omega_0}} (b_{\mathbf{q}\mu} + b^{\dagger}_{-\mathbf{q}\mu})\mathbf{e}_{\mu}(\mathbf{q})e^{i\mathbf{q}\cdot\mathbf{r}}, \tag{8}$$

where N is the number of unit cells, M is the mass of a carbon atom, ω_0 is the phonon frequency at the Γ point, $\mathbf{q} = (q_x, q_y)$ is the wave vector, μ denotes the modes ('t' for transverse and 'l' for longitudinal), and $b^{\dagger}_{\mathbf{q}\mu}$ and $b_{\mathbf{q}\mu}$ are the creation and destruction operators, respectively. Define $q_x = q\cos\varphi_{\mathbf{q}}$ and $q_y = q\sin\varphi_{\mathbf{q}}$ with $q = |\mathbf{q}|$. Then, we have $\mathbf{e}_{\mathrm{l}}(\mathbf{q}) = i(\cos\varphi_{\mathbf{q}}, \sin\varphi_{\mathbf{q}})$ and $\mathbf{e}_{\mathrm{t}}(\mathbf{q}) = i(-\sin\varphi_{\mathbf{q}}, \cos\varphi_{\mathbf{q}})$.

The interaction between optical phonons and an electron in the vicinity of the K and K' points is given by[21]

$$\mathcal{H}^{\mathrm{K}}_{\mathrm{int}} = -\sqrt{2}\frac{\beta_{\Gamma}\gamma}{b^2}\vec{\sigma}\times\mathbf{u}(\mathbf{r}), \quad \mathcal{H}^{\mathrm{K'}}_{\mathrm{int}} = +\sqrt{2}\frac{\beta_{\Gamma}\gamma}{b^2}\vec{\sigma}^*\times\mathbf{u}(\mathbf{r}), \tag{9}$$

where the vector product for vectors $\mathbf{a} = (a_x, a_y)$ and $\mathbf{b} = (b_x, b_y)$ in 2D is defined by $\mathbf{a}\times\mathbf{b} = a_x b_y - a_y b_x$. This means that the lattice distortion gives rise to a shift in the origin of the wave vector or an effective vector potential, i.e., u_x in the y direction and u_y in the x direction. The interaction strength is characterized by the dimensionless coupling parameter

$$\lambda_{\Gamma} = \frac{36\sqrt{3}}{\pi}\frac{\hbar^2}{2Ma^2}\frac{1}{\hbar\omega_0}\left(\frac{\beta_{\Gamma}}{2}\right)^2. \tag{10}$$

For $M = 1.993\times10^{-23}$ g and $\hbar\omega_0 = 0.196$ eV, we have $\lambda_{\Gamma} \approx 3\times10^{-3}(\beta_{\Gamma}/2)^2$. This shows that the interaction is not strong and therefore the lowest order perturbation gives sufficiently accurate results.

The phonon Green's function is written as

$$D_{\mu}(\mathbf{q}, \omega) = \frac{2\hbar\omega_0}{(\hbar\omega)^2 - (\hbar\omega_0)^2 - 2\hbar\omega_0\Pi_{\mu}(\mathbf{q}, \omega)}. \tag{11}$$

The phonon frequency is determined by the pole of $D_{\mu}(\mathbf{q}, \omega)$. In the case of weak interaction, the shift of the phonon frequency, $\Delta\omega_{\mu}$, and the broadening, Γ_{μ}, are given by

$$\Delta\omega_{\mu} = \frac{1}{\hbar}\mathrm{Re}\,\Pi_{\mu}(\mathbf{q}, \omega_0), \quad \Gamma_{\mu} = -\frac{1}{\hbar}\mathrm{Im}\,\Pi_{\mu}(\mathbf{q}, \omega_0). \tag{12}$$

When we calculate the self-energy of optical phonons starting with the known phonon modes in graphene, its direct evaluation causes a problem of double counting.[24] In fact, if we apply the above formula to the case of
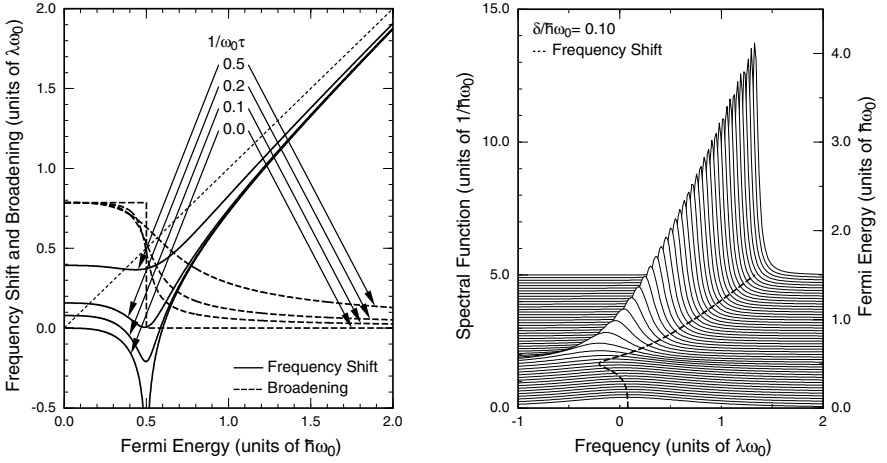
Fig. 4. (Left) The frequency shift and broadening of optical phonons in monolayer graphene as a function of the Fermi energy. τ is a phenomenological relaxation time characterizing the level broadening effect due to disorder. (Right) Calculated spectral function of optical phonon for varying Fermi energy.

vanishing Fermi energy, we get the frequency shift due to virtual excitations of all electrons in the π bands. However, this contribution is already included in the definition of the frequency ω_0. In order to avoid such a problem, we have to subtract the contribution in the undoped graphene for $\omega = 0$ corresponding to the adiabatic approximation.

Figure 4 shows the frequency shift and broadening for various values of $1/\omega_0\tau$ and an example of the spectral function, $(-1/\pi)\text{Im}D(q, \omega_0)$. For nonzero δ or $1/\omega_0\tau$, the logarithmic singularity of the frequency shift and the sharp drop in the broadening disappear, but the corresponding features remain for $1/\omega_0\tau \ll 1$. Similar results were reported independently[25] and experiments giving qualitatively similar results were reported.[26–28]

The calculation can easily be extended to the case in the presence of magnetic field B, where discrete Landau levels are formed and oscillations due to resonant interactions appear in the frequency shift and the broadening.[23] The Landau-level energy is given by $\varepsilon_n = \text{sgn}(n)\sqrt{|n|}\hbar\omega_B$ $(n = 0, \pm 1, \cdots)$, where $\text{sgn}(n)$ denotes the sign of n and $\hbar\omega_B = \sqrt{2}\gamma/l$ with magnetic length $l = \sqrt{c\hbar/eB}$. Figure 5 shows calculated frequency shift and broadening when $\varepsilon_F^0/\hbar\omega_0 = 1/4$ and the corresponding phonon spectral function, where ε_F^0 is the Fermi energy in the absence of a magnetic field. All resonant transitions from $-n$ to $n+1$ and from $-n-1$ to n with $n > 0$
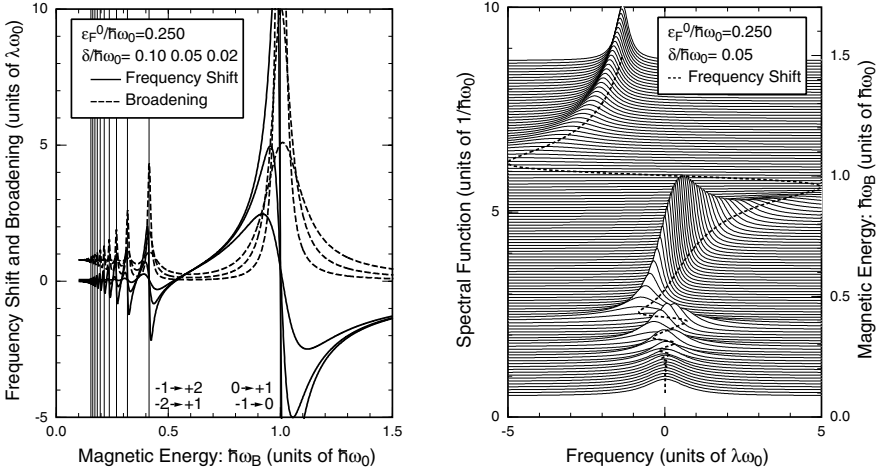
Fig. 5. (Left) The frequency shift and broadening of optical phonons in monolayer graphene as a function of effective magnetic energy $\hbar\omega_B$. Thin vertical lines show resonance magnetic fields. $\varepsilon_F^0/\hbar\omega_0 = 1/4$. The results for $\delta/\hbar\omega_0 = 0.1$, 0.05, and 0.02 are shown. (Right) The phonon spectral function for $\varepsilon_F^0/\hbar\omega_0 = 1/4$ and $\delta/\hbar\omega_0 = 0.05$. The dotted line shows the peak position as a function of $\hbar\omega_B$.

appear at the field where their energy difference becomes equal to $\hbar\omega_0$. At resonances, the phonon spectrum exhibits characteristic behavior. Recently this magneto-phonon resonance was observed in Raman experiments.[29]

The same tuning of the optical-phonon frequency and broadening due to change in the Fermi level is also possible in carbon nanotubes. In fact, effects of the electron-phonon interaction on the optical phonon in carbon nanotubes were theoretically studied earlier than in graphene.[21] In nanotubes, the modes are classified into longitudinal and transverse, depending on their displacement in the axis or circumference direction. Figure 6 shows the results of the similar calculations in carbon nanotubes.[30]

In semiconducting nanotubes, the imaginary part vanishes identically because of the presence of a gap. The frequency of the longitudinal and transverse modes is both shifted to higher frequency side and the shift is smaller for the longitudinal mode for small k_F. The behavior of two modes as a function of k_F is similar to that of "level crossing." In metallic nanotubes, the transverse mode is not affected by the doping at all. For the longitudinal mode, the energy shift exhibits a downward shift and considerable broadening.[21] For nonzero k_F, the self-energy has a logarithmic divergence at $\gamma k_F = \hbar\omega_0/2$ and increases logarithmically with k_F for $\gamma k_F > \hbar\omega_0/2$ for
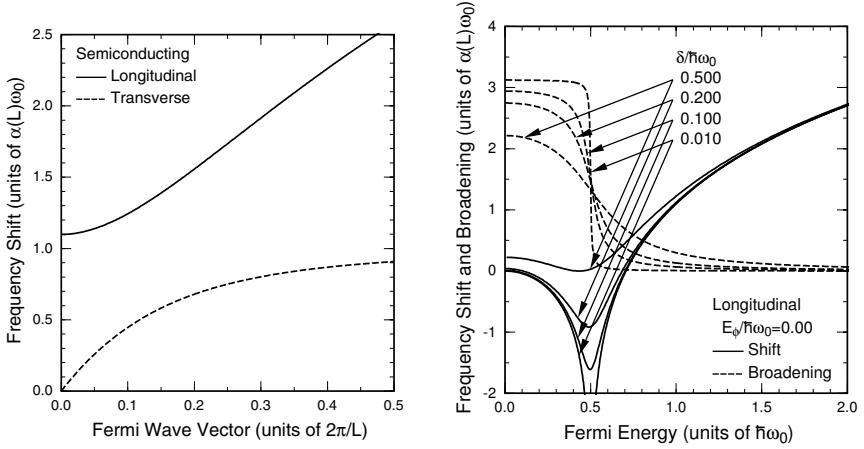
Fig. 6.   (Left) The frequency shift in a semiconducting nanotube as a function of the Fermi wave vector k_F. The solid and dashed lines represent the longitudinal and transverse modes, respectively. (Right) The frequency shift and broadening of the longitudinal mode in metallic nanotubes as a function of the Fermi energy.

vanishing δ. This behavior in CN, the same as in graphene theoretically predicted[22,23,25,31] and experimentally observed,[26,27] was also observed in Raman experiments[32,33] and discussed theoretically.[34,35]

5. Zone-Boundary Phonon

Phonons near the K and K' point, called zone-boundary phonons, can play important roles in intervalley scattering between the K and K' points. In general, there exist four independent eigen modes for each wave vector. However, after straightforward calculations, we can see that only one mode with the highest frequency contributes to the electron-phonon interaction.[36] This mode is known as a Kekulé type distortion generating only bond-length changes. The interaction Hamiltonian is given by

$$\mathcal{H}_{\text{int}} = 2\frac{\beta_K \gamma}{b^2} \begin{pmatrix} 0 & \omega^{-1}\Delta(\boldsymbol{r})\sigma_y \\ \omega\Delta^{\dagger}(\boldsymbol{r})\sigma_y & 0 \end{pmatrix}, \tag{13}$$

where $\omega = e^{2\pi i/3}$ and β_K is another appropriate parameter, which is equal to β_Γ for the tight-binding model. In the second quantized form,

$$\Delta(\boldsymbol{r}) = \sum_{\boldsymbol{q}} \sqrt{\frac{\hbar}{2NM\omega_K}}(b_{K\boldsymbol{q}} + b_{K'-\boldsymbol{q}}^{\dagger})e^{i\boldsymbol{q}\cdot\boldsymbol{r}}, \tag{14}$$

where ω_K is the frequency of the Kekulé mode. It is worth noting that Δ cannot be given by a simple summation over the K and K' modes. We should take a proper linear combination of the K and K' modes in order to make the lattice displacement a real variable. We can easily understand the operator form of Δ and $\Delta^\dagger$ in the interaction Hamiltonian by considering the momentum conservation with the fact that $2\mathbf{K} - \mathbf{K}'$ and $\mathbf{K} - 2\mathbf{K}'$ are reciprocal lattice vectors, where $\mathbf{K}$ and $\mathbf{K}'$ are the wave vectors at the K and K' point. The dimensionless coupling parameter, λ_K, is given by the same expression as Eq. (10) except that ω_0 is replaced with ω_K and β_Γ with β_K. For $\hbar\omega_K = 161.2$ meV, we have $\lambda_K = 3.5 \times 10^{-3}(\beta_K/2)^2$.

The lifetime of an electron with energy ε is given by the scattering probability from the initial state to possible final states via emission and absorption of one phonon. For the zone-center phonon, the summation of the contributions of longitudinal and transverse modes gives isotropic scattering probability in each of the K and K' points. For the zone-boundary phonon, any scattering processes are classified into two types: One is the transition between "one K-electron with one K-phonon" and "one K'-electron," and the other is between "one K-electron" and "one K'-electron with one K'-phonon." For example, an electron around the K point can be scattered to the K' point accompanied by absorption of one phonon around the K point, and this belongs to the former process. The electron scattering from the K to K' point can also be induced by the emission of one phonon around the K' point, while this is classified into the latter one.

In graphene, the calculated scattering probabilities for both phonons are given by the same formula,

$$\frac{\hbar}{\tau} = \pi\lambda_\alpha|\varepsilon - \hbar\omega_\alpha|. \tag{15}$$

where α represents Γ or K and we have neglected the phonon occupation due to large ω_α at room temperature. This simply shows that the electron lifetime is inversely proportional to the coupling parameter λ_α and to the density of states at the energy of the final state. What should be stressed here is that the phonon emission is possible only when the energy of the initial electron is larger than that of the phonon to be emitted. Otherwise, the final states are fully occupied at zero temperature and the phonon emission never takes place. In this sense, the zone-boundary phonon has another advantage over the zone-center phonon. Therefore, the zone-boundary phonon gives dominant scattering for high-field transport in graphene and in nanotube owing to its smaller frequency and larger coupling constant.

6. Spontaneous Lattice Distortion

In the presence of strong electron-phonon interaction, metallic systems are often unstable against lattice distortion causing band-gap opening. In fact, Peierls distortion, or bond alternation, is known to spontaneously occur in many organic conductors. Such lattice instability is expected to exist also in graphene and carbon nanotubes. In fact, there have been several theoretical studies on lattice instability in metallic nanotubes. Some considered an in-plane Kekule distortion corresponding to the zone-boundary phonon[24,37–39] and effects of magnetic fields in metallic nanotubes and in graphene.[40–42] Effects of out-of-plane distortion destroying the sublattice symmetry were also considered,[24,43] and distortions corresponding long-wavelength acoustic and optical modes were pointed out because they can open up a gap in metallic nanotubes.[44–47] The lattice instability is certainly the subject always attracting considerable interest.[48–55]

7. Bilayer Graphene

We consider a bilayer graphene which is arranged in the AB (Bernal) stacking. The upper layer is denoted as 1 and the lower layer denoted as 2. In each layer, the unit cell contains two carbon atoms denoted by A_1 and B_1 in layer 1 and A_2 and B_2 in layer 2. For the inter-layer coupling, we include only the coupling between vertically neighboring atoms. Then, electronic states are described by the $\mathbf{k} \cdot \mathbf{p}$ Hamiltonian:[56,57]

$$\mathcal{H} = \begin{matrix} & A_1 & B_1 & A_2 & B_2 \\ & \begin{pmatrix} 0 & \gamma \hat{k}_- & 0 & 0 \\ \gamma \hat{k}_+ & 0 & \Delta & 0 \\ 0 & \Delta & 0 & \gamma \hat{k}_- \\ 0 & 0 & \gamma \hat{k}_+ & 0 \end{pmatrix} \end{matrix}, \tag{16}$$

where Δ (≈ 0.4 eV) represents the inter-layer coupling between sites B_1 and A_2.

Let us define

$$\varepsilon(k) = \sqrt{\left(\frac{\Delta}{2}\right)^2 + (\gamma k)^2}, \quad \gamma k = \varepsilon(k) \sin \psi, \quad \frac{\Delta}{2} = \varepsilon(k) \cos \psi, \tag{17}$$

where ψ vanishes for $k = 0$ and approaches $\pi/2$ with increasing k. Then, the eigen energies are given by

$$\varepsilon_{\pm 1}(k) = \pm 2\varepsilon(k) \sin^2(\psi/2), \quad \varepsilon_{\pm 2}(k) = \pm 2\varepsilon(k) \cos^2(\psi/2). \tag{18}$$
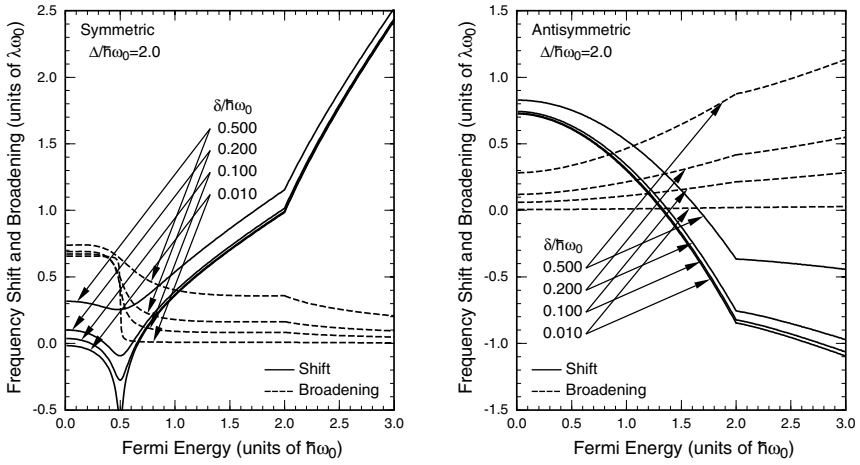
Fig. 7. Some examples of calculated frequency shift and broadening of the symmetric (left) and antisymmetric mode (right) at the Γ point in a bilayer graphene. $\Delta/\hbar\omega_0 = 2$. The amount of the broadening due to disorder is denoted by δ.
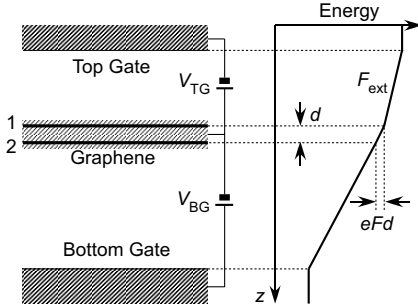
Fig. 8. A schematic illustration of the bilayer graphene with a top gate and a bottom gate and the potential energy diagram. The distance between the layers is given by d, the potential difference by eFd, and F_{ext} represents the field due to the top gate.
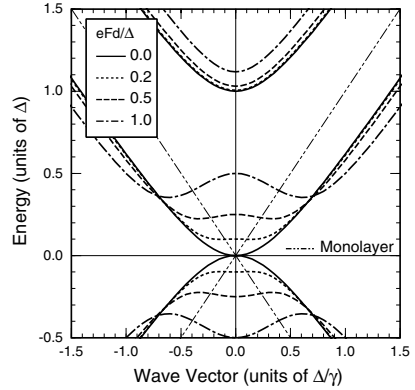
Fig. 9. The energy dispersion for varying values of the potential difference eFd. The dot-dot-dashed lines show that of a monolayer graphene.

The band $\varepsilon_{+1}(k)$ represents the lowest conduction band which touches the highest valence band $\varepsilon_{-1}(k)$ at $k = 0$. The bands $\varepsilon_{\pm2}(k)$ are the excited conduction and valence bands and $\varepsilon_{+2}(k) - \varepsilon_{+1}(k) = \delta$ independent of k.

In bilayer graphene, optical phonons are classified into symmetric and antisymmetric modes in which the displacement of the top and bottom

layers are in-phase and out-of-phase, respectively. They are affected by electron-phonon interactions in a different manner.[31] The symmetric mode causes interband transitions between $\varepsilon_{\pm1}(k)$ and therefore exhibits logarithmic singularity in a manner same as monolayer graphene when $\varepsilon_F = \hbar\omega_0/2$. On the other hand, this transition is not allowed for the antisymmetric mode but interband transitions between $\varepsilon_{+1}(k)$ and $\varepsilon_{+2}(k)$ contribute to the phonon renormalization. Figure 7 shows calculated frequency shift and broadening for two phonon modes.

One important feature is that the band structure can be strongly modified due to opening-up of a band gap by applied electric field.[58,59] Figure 8 shows a schematic illustration of the device structure, where eFd represents the potential difference between layers 1 and 2 (F is the effective electric field and $d = 0.334$ nm is the interlayer distance). The effective Hamiltonian becomes

$$
\mathcal{H} = \begin{pmatrix}
eFd/2 & \gamma\hat{k}_- & 0 & 0 \\
\gamma\hat{k}_+ & eFd/2 & \Delta & 0 \\
0 & \Delta & -eFd/2 & \gamma\hat{k}_- \\
0 & 0 & \gamma\hat{k}_+ & -eFd/2
\end{pmatrix}.
\tag{19}
$$

Figure 9 shows the energy bands obtained by the diagonalization of this Hamiltonian. The band gap appears and the minimum gap is located at a nonzero value of k depending on the field.

The effective field is determined in a self-consistent manner because the electron density distribution between two layers becomes different, giving rise to interlayer potential difference. Some examples of the results of such calculations are shown in Fig. 10.[60] The unit $n_s^0 = g_v g_s \Delta^2 / 2\pi\gamma^2$ is the electron concentration at $\varepsilon_F = \Delta$ for $eFd = 0$. We have $n_s^0 \approx 2.5 \times 10^{13}$ cm^{-2} for $\Delta \approx 0.4$ eV. We can see eFd can become as large as $\sim \Delta/2$ although being dependent on $eF_{ext}d$.

Figure 11 shows the frequency shift (top panel), broadening (middle panel), and the spectral intensity (bottom panel) of the symmetric component as a function of the electron concentration for $eF_{ext}d = 0$.[61] We have assumed $\Delta/\hbar\omega_0 = 2$ corresponding to $\Delta \approx 0.4$ eV and $\hbar\omega_0 \approx 0.2$ eV and $\delta/\hbar\omega_0 = 0.1$. The symmetric component shown in the figure describes the relative intensity of the Raman scattering. At $n_s = 0$ with $eFd = 0$, the optical phonons are exactly classified into symmetric and antisymmetric modes. With the increase of n_s, they become mixed with each other, which becomes particularly important when they cross each other.
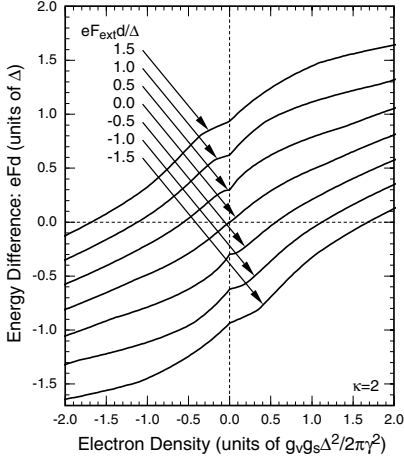
Fig. 10. Calculated energy difference eFd as a function of the electron concentration for various values of $eF_{ext}d$. The static dielectric constant of the environment is chosen as $\kappa = 2$.
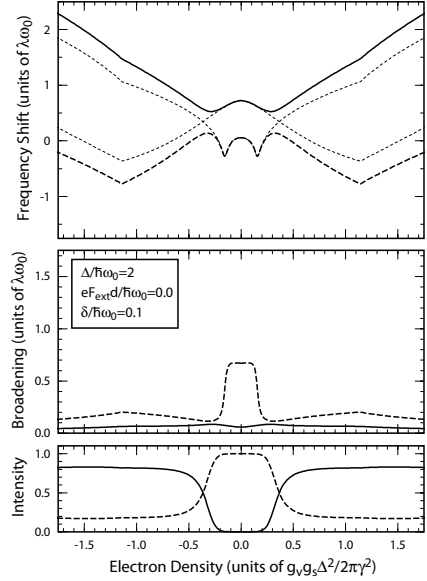
Fig. 11. Calculated frequency shift, broadening, and strength of the symmetric component. The solid and dashed lines denote the high- and low-frequency modes, respectively. The thin dotted lines in the top panel show the frequencies for symmetric and antisymmetric modes calculated without inclusion of their mixing. $\Delta/\hbar\omega_0 = 2$. $\delta/\hbar\omega_0 = 0.1$. $eF_{ext}d/\Delta = 0$.

The appearance of two peaks at sufficiently high electron concentration is in agreement with that of recent experiments showing double peaks in a highly doped bilayer graphene.[62] In order to make detailed comparison with experiments, we may have to consider a small frequency splitting of symmetric and antisymmetric modes which is independent of the change in the electron concentration.

Acknowledgments

"Nanoscience and Quantum Physics" from Ministry of Education, Culture, Sports, Science and Technology Japan.

References

1. K. S. Novoselov, A. K. Geim, S. V. Morozov, D. Jiang, Y. Zhang, S. V. Dubonos, I. V. Grigorieva, and A. A. Firsov, Science **306**, 666 (2004).
2. K. S. Novoselov, A. K. Geim, S. V. Morozov, D. Jiang, M. I. Katsnelson, I. V. Grigorieva, S. V. Dubonos, and A. A. Firsov, Nature **438**, 197 (2005).
3. Y. Zhang, Y.-W. Tan, H. L. Stormer, and P. Kim, Nature **438**, 201 (2005).
4. T. Ando, Physica E **40**, 213 (2007).
5. A. H. Castro Neto, F. Guinea, N. M. Peres, K. S. Novoselov, and A. K. Geim, Rev. Mod. Phys. **81**, 109 (2009).
6. T. Ando, J. Phys. Soc. Jpn. **74**, 777 (2005) and references cited therein.
7. P. R. Wallace, Phys. Rev. **71**, 622 (1947).
8. G. S. Painter and D. E. Ellis, Phys. Rev. B **1**, 4747 (1970).
9. J. W. McClure, Phys. Rev. **104**, 666 (1956).
10. J. C. Slonczewski and P. R. Weiss, Phys. Rev. **109**, 272 (1958).
11. D. P. DiVincenzo and E. J. Mele, Phys. Rev. B **29**, 1685 (1984).
12. G. W. Semenoff, Phys. Rev. Lett. **53**, 2449 (1984).
13. H. Ajiki and T. Ando, J. Phys. Soc. Jpn. **62**, 1255 (1993).
14. C. L. Kane and E. J. Mele, Phys. Rev. Lett. **78**, 1932 (1997).
15. H. Suzuura and T. Ando, Phys. Rev. B **65**, 235412 (2002).
16. T. Ando and T. Nakanishi, J. Phys. Soc. Jpn. **67**, 1704 (1998).
17. T. Ando, T. Nakanishi, and R. Saito, J. Phys. Soc. Jpn. **67**, 2857 (1998).
18. A. C. Ferrari, J. C. Meyer, V. Scardaci, C. Casiraghi, M. Lazzeri, F. Mauri, S. Piscanec, D. Jiang, K. S. Novoselov, S. Roth, and A. K. Geim, Phys. Rev. Lett. **97**, 187401 (2006).
19. A. Gupta, G. Chen, P. Joshi, S. Tadigadapa, and P. C. Eklund, Nano Lett. **6**, 2667 (2006).
20. C. N. R. Rao, A. K. Sood, K. S. Subrahmanyam, and A. Govindaraj, Angew. Chem. **48**, 7752 (2009).
21. K. Ishikawa and T. Ando, J. Phys. Soc. Jpn. **75**, 084713 (2006).
22. T. Ando, J. Phys. Soc. Jpn. **75**, 124701 (2006).
23. T. Ando, J. Phys. Soc. Jpn. **76**, 024712 (2007).
24. N. A. Viet, H. Ajiki, and T. Ando, J. Phys. Soc. Jpn. **63**, 3036 (1994).
25. M. Lazzeri and F. Mauri, Phys. Rev. Lett. **97**, 266407 (2006).
26. S. Pisana, M. Lazzeri, C. Casiraghi, K. S. Novoselov, A. K. Geim, A. C. Ferrari, and F. Mauri, Nat. Mat. **6**, 198 (2007).
27. J. Yan, Y. Zhang, P. Kim, and A. Pinczuk, Phys. Rev. Lett. **98**, 166802 (2007).
28. A. Das, S. Pisana, B. Chakraborty, S. Piscanec, S. K. Saha, U. V. Waghmare, K. S. Novoselov, H. R. Krishnamurthy, A. K. Geim, A. C. Ferrari, and A. K. Sood, Nat. Nanotech. **3**, 210 (2008).

29. C. Faugeras, M. Amado, P. Kossacki, M. Orlita, M. Sprinkle, C. Berger, W. A. de Heer, and M. Potemski, Phys. Rev. Lett. **103**, 186803 (2009).
30. T. Ando, J. Phys. Soc. Jpn. **77**, 014707 (2008).
31. T. Ando, J. Phys. Soc. Jpn. **76**, 104711 (2007).
32. H. Farhat, H. Son, Ge. G Samsonidze, S. Reich, M. S. Dresselhaus, and J. Kong, Phys. Rev. Lett. **99**, 145506 (2007).
33. Y. Wu, J. Maultzsch, E. Knoesel, B. Chandra, M. Huang, M. Y. Sfeir, L. E. Brus, J. Hone, and T. F. Heinz, Phys. Rev. Lett. **99**, 027402 (2007).
34. K. Sasaki, R. Saito, G. Dresselhaus, M. S. Dresselhaus, H. Farhat, and J. Kong, Phys. Rev. B **78**, 235405 (2008).
35. J. S. Park, K. Sasaki, R. Saito, W. Izumida, M. Kalbac, H. Farhat, G. Dresselhaus, and M. S. Dresselhaus, Phys. Rev. B **80**, 081402 (2009).
36. H. Suzuura and T. Ando, J. Phys. Soc. Jpn. **77**, 044703 (2008).
37. J. W. Mintmire, B. I. Dunlap, and C. T. White, Phys. Rev. Lett. **68**, 631 (1992).
38. K. Harigaya, Phys. Rev. B **45**, 12071 (1992).
39. K. Harigaya and M. Fujita, Phys. Rev. B **47**, 16563 (1993).
40. H. Ajiki and T. Ando, J. Phys. Soc. Jpn. **64**, 260 (1995).
41. H. Ajiki and T. Ando, J. Phys. Soc. Jpn. **65**, 2976 (1996).
42. H. Ajiki and T. Ando, Physica B **227**, 342 (1996).
43. R. Saito, M. Fujita, G. Dresselhaus, and M. S. Dresselhaus, Phys. Rev. B **46**, 1804 (1992).
44. L. Yang, M. P. Anantram, J. Han, and J. P. Lu, Phys. Rev. B **60**, 13874 (1999).
45. L. Yang and J. Han, Phys. Rev. Lett. **85**, 154 (2000).
46. H. Suzuura and T. Ando, *Proc. 25th Int. Conf. Physics of Semiconductors*, eds. N. Miura and T. Ando (Springer, Berlin, 2001), p. 1625.
47. H. Suzuura and T. Ando, *Nanonetwork Materials*, edited by S. Saito, T. Ando, Y. Iwasa, K. Kikuchi, M. Kobayashi, and Y. Saito (American Institute of Physics, New York, 2001), p. 269.
48. D. Connetable, G.-M. Rignanese, J.-C. Charlier, and X. Blase, Phys. Rev. Lett. **94**, 015503 (2005).
49. S. Piscanec, M. Lazzeri, J. Robertson, A. C. Ferrari, and F. Mauri, Phys. Rev. B **75**, 035427 (2007).
50. A. Fasolino, J. H. Los, and M. I. Katsnelson, Nat. Mat. **6**, 858 (2007).
51. F. Guinea, B. Horovitz, and P. Le Doussal, Phys. Rev. B **77**, 205421 (2008).
52. F. Varchon, P. Mallet, J.-Y. Veuillen, and L. Magaud, Phys. Rev. B **77**, 235412 (2008).
53. L. Covaci and M. Berciu, Phys. Rev. Lett. **100**, 256405 (2008).
54. V. Mohan and A. Datta, J. Phys. Chem. Lett. **1**, 136 (2010).
55. A. Datta, arXiv:1003.5270v1.
56. E. McCann and V. I. Falko, Phys. Rev. Lett. **96**, 086805 (2006).
57. M. Koshino and T. Ando, Phys. Rev. B **73**, 245403 (2006).
58. E. McCann, Phys. Rev. B **74**, 161403 (2006).
59. H. Min, B. Sahu, S. K. Banerjee, and A. H. MacDonald, Phys. Rev. B **75**, 155115 (2007).

60. T. Ando and M. Koshino, J. Phys. Soc. Jpn. **78**, 104716 (2009).
61. T. Ando and M. Koshino, J. Phys. Soc. Jpn. **78**, 034709 (2009).
62. L. M. Malard, D. C. Elias, E. S. Alves, and M. A. Pimenta, Phys. Rev. Lett. **101**, 257401 (2008).

Chapter 9

Magnetic Structures of Edge-State Spins in Nanographene and a Network of Nanographene Sheets

Toshiaki Enoki[*], V. L. Joseph Joly and Kazuyuki Takai

*Department of Chemistry, Tokyo Institute of Technology,
2-12-1 Ookayama, Meguro-ku, Tokyo 152-8551, Japan*
[*]tenoki@chem.titech.ac.jp

The electronic structure of a nanographene sheet crucially depends on the shape of its edges. In the zigzag-shaped edges, a nonbonding π-electron state (edge state) is created in contrast to the absence of such state in the armchair edges. Strong spin polarization of the edge state gives rise to unconventional magnetism in nanographene. Ultra-high vacuum STM/STS experiments confirm the presence of the edge state in graphene edges. The magnetism of a 3 dimensional disordered network of nanographene sheets is understood on the basis of ferrimagnetic structure of the edge-state spins in individual constituent nanographene sheet. Electron localization in the electron transport between nanographene sheets seriously affects the dynamical magnetic feature of the edge-state spins. The strengthening of the inter-nanographene-sheet magnetic interaction brings about a spin glass state.

1. Introduction

After the discovery of graphene (a single layer of graphite) in 2004,[1-4] graphene has attracted rapidly growing attention not only as a central issue in basics science but also as a target in cutting-edge nanotechnology. What is most interesting in graphene is the unconventional physics behind the electronic behavior observed experimentally. Indeed, the electronic structure of graphene is described in terms of massless Dirac fermion, which plays in giving the unprecedented electronic phenomena, such as anomalous quantum Hall

effect,[5] spin Hall effect,[6] etc. When an infinite graphene sheet is cut into nano-sized graphene (nanographene) sheets or semi-infinite graphene sheets, another important issue arises related to the creation of graphene edges, as evidenced by early theoretical[7-10] and experimental works,[12-15] which have been performed several years before the discovery of graphene.

Depending on the direction of the cutting line of a graphene sheet, there can be two types of edges created; that is, armchair and zigzag edges.[15] What is important here is that the electronic structure of nanographene depends crucially on the geometrical shape of the edges. Indeed, according to the theoretical and experimental studies,[7-15] a nonbonding π-electron state called "edge state" is created along the zigzag edges, whereas no such state is present in the armchair edges. In connection to the presence/absence of edge state, we should remind the issue on the aromaticity in condensed polycyclic hydrocarbon molecules.[16-20] The nonbonding π-electron state is created also in these molecules with the geometrical dependence same to that in nanographene and graphene edges. The edge state well localized in the vicinity of the zigzag edge is therefore a kind of surface state and plays an important role in giving electronic features that are specific to nanographene sheet. In addition, the edge state, which is singly occupied and strongly spin polarized, contributes to create strong spin magnetism. Interestingly, the localized spins of the edge state are ferromagnetically arranged through a strong ferromagnetic intra-zigzag-edge exchange interaction ($\sim 10^3$ K).[21] The circumference of a nanographene sheet can be described in terms of a combination of zigzag and armchair edges. Therefore, depending on the shape of a nanographene sheet, the interplay between intra-zigzag-edge ferromagnetic interaction and inter-zigzag-edge ferromagnetic/antiferromagnetic exchange interaction is expected to gives rise to a variety of magnetic structures, taking into account that the magnetic feature of edge state is sensitive to the detailed edge geometry and chemical modifications of edges.

In this paper, we present the electronic structure of the edge state and the magnetic properties of a disordered network of nanographite domains, each of which consists of a stack of 3-4 nanographene sheets.

2. Electronic Structure of Edge State and STM/STS Observations

Let us start with the relationship between aromaticity in small hydrocarbon molecules and the issue on edge state in nanographene/graphene edges. Benzene, which is a typical Kekulé molecule and the primary building block of graphene, consists of three bonding π- and three antibonding π*-orbitals split mutually with a large HOMO-LUMO gap, which corresponds to energy stabilization of aromaticity. When benzene rings are fused to each other to form condensed polycyclic hydrocarbon molecules, the Kekulé structure with a large HOMO-LUMO gap is usually conserved, as evidenced in naphthalene, anthracene, etc. However, there are exceptional molecules called non-Kekulé molecules, in which the energy stabilization is failed.[16-20] A typical example is phenalenyl radical consisting of three benzene rings fused in a triangle shape as shown in Fig. 1(b). In this molecule, an additional π-electron state is present at the Fermi level in the energy gap as a nonbonding π-electron state, which works to destabilize the molecule. A similar situation in the electronic structure is present in triangle molecules having larger sizes, as shown in Figs. 1(c) and (d), where the triangle molecules consisting of 6 and 10 benzene rings have 2 and 3 nonbonding π-electron states, respectively. Here, Lieb's theorem[17] can tell us how large number of nonbonding states is present in a molecule concerned. According to the Lieb's theorem, the
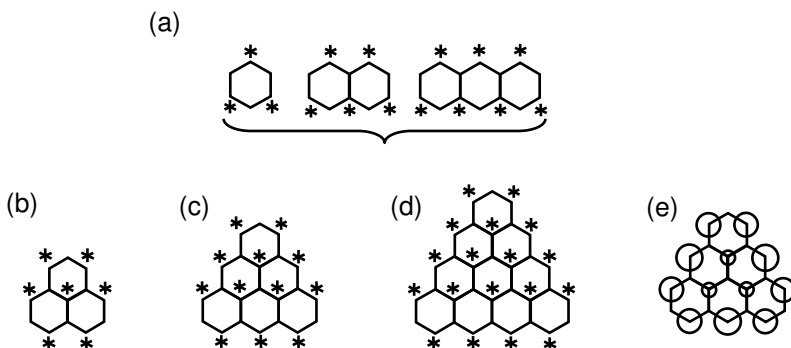
Fig. 1. (a) Kekulé molecules, (b), (c), (d) triangle-shaped non-Kekulé molecules consisting of 3, 6 and 10 benzene rings, (e) spatial distribution of the nonbonding π-electron state.

number of nonbonding state N_n is given as the difference in the numbers of the starred (N_*) and unstarred (N_{un*}) sites: $N_n = |N_* - N_{un*}|$, where the carbon sites belonging to a given subgroup (starred) are directly bonded to the sites belonging to another subgroup (unstarred). This implies that Kekulé molecules (Fig. 1(a)), in which N_* is always equal to N_{un*}, have no nonbonding state and are nonmagnetic. In contrast, the triangle-shaped molecules consisting of 3, 6 and 10 benzene rings have 1, 2 and 3 nonbonding states and are ferromagnetic with S=1/2, 1 and 3/2, respectively, since the electrons occupying these degenerate nonbonding states at E_F obey the Hund rule with the parallel spin arrangement as shown in Figs. 1(b)-(d).

It should be noted here that the nonbonding π-electron states are populated around the peripheral zigzag shaped region of the molecules as illustrated in Fig. 1(e) for triangulene consisting of 6 benzene rings. This indicates that the nonbonding π-electron state is the small molecule version of the edge state. Indeed, an extrapolation of the electronic state to nano-sized graphene demonstrates the presence of the nonbonding state when a nanographene sheet is zigzag edged, in contrast to the absence of such a state in the armchair-edged sheet. Figure 2 presents the spatial distribution of the HOMO level for armchair-edged and zigzag-edged nanographene sheets.[7] The armchair-edged nanographene sheet has a uniform distribution of the HOMO state. On the contrary, the zigzag-edged nanographene sheet has a large local-density-of-states, which is assigned to the edge state, around the zigzag edge region.
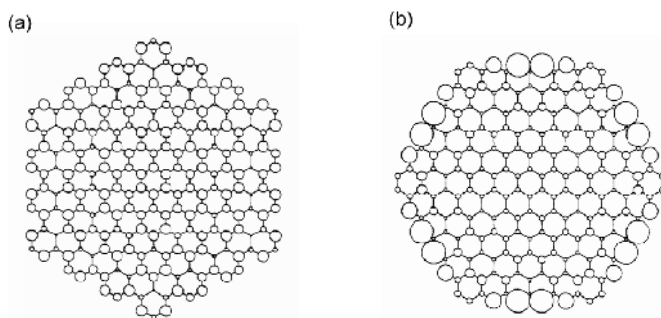
Fig. 2. The spatial distribution of the HOMO level in (a) armchair-edged and (b) zigzag-edged nanographene sheets. The HOMO level is assigned to the edge state in the zigzag-edged nanographene sheet. (Ref. 7)

It is particularly important to show the evidence on the presence of edge state using scanning tunneling microscopy/spectroscopy (STM/STS) technique in atomic resolution.[11-15] However, the as-prepared graphene edges are usually covered with oxygen-containing functional groups due to the easy oxidation of graphene edges in the ambient condition.[22] STM observations with well defined graphene edges are required to examine the electronic structure of the graphene edges. For this reason, the graphene edges are heat-treated to remove the functional groups and hydrogen terminated in ultra-high vacuum (UHV) condition.[11,13] Figure 3 exhibits the typical examples of the UHV-STM lattice images and STS spectra of graphene edges which are hydrogen terminated.[11] Figures 3(a) and (b) are the STM and STS results for a
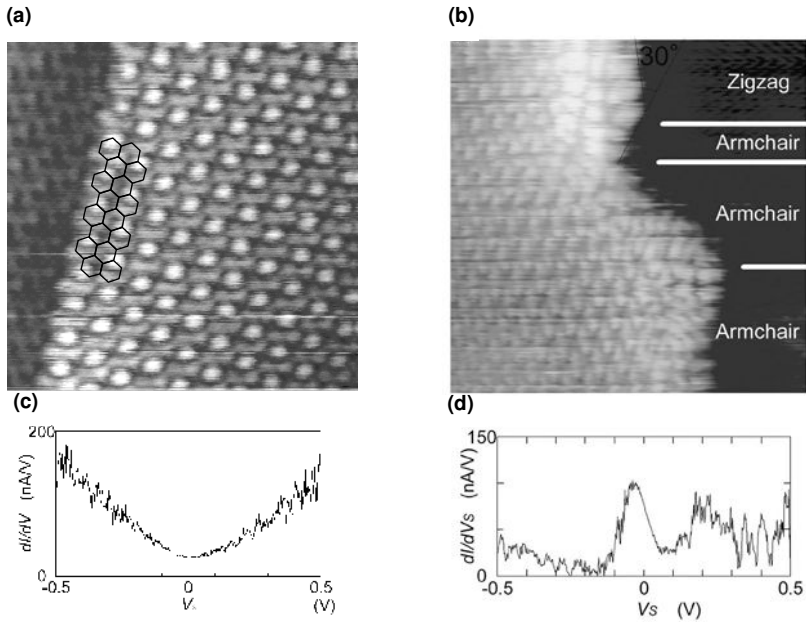
Fig. 3. (a) Atomically resolved UHV STM images (5.6×5.6 nm^2) of a homogeneous armchair edge in constant-height mode with bias voltage V_s=0.02 V and current I=0.7 nA. For clarity of edge structures, a model of the honeycomb lattice is drawn on the image. (b) A dI/dV_s curve from STS measurements taken at the edge in (a). (c) An atomically-resolved UHV STM image of zigzag and armchair edges (9×9 nm^2) observed in constant-height mode with bias voltage V_s=0.02 V and current I=0.7 nA. (d) The dI/dV_s curve from STS data at a zigzag edge (From reference 11).

uniform armchair edge, respectively. The STS spectrum demonstrates that the electronic structure in the vicinity of the Fermi level (E_F) is same to that of infinite graphene sheet with a feature of massless Dirac fermion described in terms of linear valence π- and conduction π^*-bands which touch to each other at E_F.[4] This reflects the lattice image which shows a $\sqrt{3} \times \sqrt{3}$ superlattice structure with no additional contribution. Armchair edges observed are generally long and less defective, being suggested to be energetically stable, in accordance with the theoretical prediction.[20] Zigzag edges have features that is different from armchair edges. Zigzag edges tend to be defective and short. They are observed frequently to be embedded between armchair edges, as shown in Fig. 3(c). This is a consequence of the energetically unstable structure of zigzag edges.[20] What is important in zigzag edges is the presence of edge state.[9] The STS spectrum (Fig. 3(d)) at the zigzag edge shows a sharp peak of the density-of-states at E_F in addition to the linear π- and π^*-bands, giving evidence for the edge state. The bright spots observed in the zigzag edge region (Fig. 3(c)) are ascribed to the edge state.

3. Magnetic Properties of Nanographene and Nanographite

As discussed in Secs. 1 and 2, edge states localized in the zigzag edge region have localized spins, which interact with each other through exchange interactions in a nanographene sheet. This gives a variety of magnetic structures depending on the geometry of a nanographene sheet. Activated carbon fibers (ACFs) are a good model system in investigating the magnetism of nanographene sheets.[23,24] The structure of ACF is featured with a 3 dimensional (3D) disordered network of nanographite domains, each of which consists of a stack of 3-4 nanographene sheets with a mean intra-sheet size of 2-3 nm, as shown in Fig. 4(a).[23] The magnetic structure of an individual nanographene sheet having irregular shape is depicted in Fig. 4(b).[25] The periphery of the nanographene sheet is described with a combination of zigzag and armchair edge regions. In the zigzag edge region, a strong ferromagnetic intra-zigzag-edge interaction $J_0 \sim 10^3$ K acts to arrange the edge-state spins in parallel.[21] In addition, the inter-zigzag-edge interaction J_1, which is mediated by the conduction π-electron carriers and has intermediate strength

$(J_1 \sim (10^{-1} - 10^{-2})J_0)$, works to couple the ferromagnetically-arranged edge-state spin clusters between the zigzag edge regions embedded in the circumference. The strength and sign (ferromagnetic/antiferromagentic) of J_1 vary depending on the mutual geometrical relation between the zigzag edges concerned. The cooperation of J_0 and J_1 therefore creates ferrimagnetic spin structure with a non-zero net magnetic moment in an individual nanographene sheet as shown in Fig. 4(b).[25,26] In the network of nanographite domains, there are two kinds of additional exchange interactions; inter-nanographene-sheet interaction (J_2) and inter-nanographite-domain interaction (J_3), which are both weakly antiferromagnetic $(J_0>J_1>>J_2>J_3)$.[24-26] Eventually, the magnetism of ACFs is given as a consequence of the cooperation of J_0, J_1, J_2 and J_3.
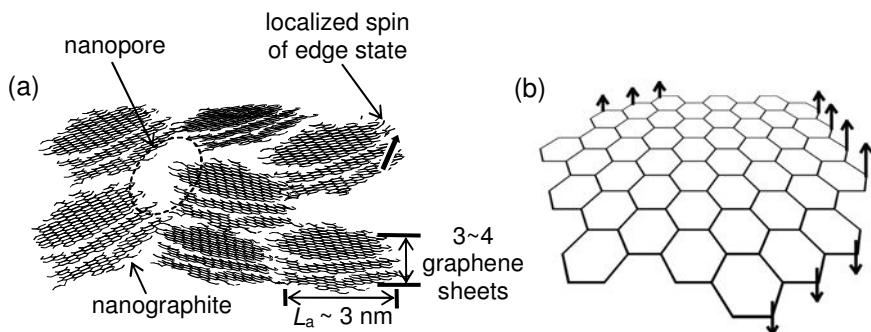
Fig. 4. (a) The schematic structural model of activated carbon fiber (ACF). (b) An individual nanographene sheet in a nanographite domain of ACF, and the spatial distribution of edge-state spins. J_0 and J_1 are intra- and inter-zigzag-edge interactions, respectively.

3.1. *Effect of electron localization on the magnetism of the edge-state spins*

Before discussing the magnetism of ACFs, let us see the electron transport properties of ACFs. The non-treated ACF shows insulating behavior in their electron transport properties as shown in Figs. 5(a) and (b) with the temperature dependence of the conductivity/resistivity. The resistivity obeys the formula of the Coulomb-gap type variable range hopping in a fractal geometry network in Anderson insulator;[24,27-29]

$$\sigma(T) = \sigma_0 \exp\left[-\left(T_0/T\right)^\gamma\right], \tag{1}$$

where

$$T_0 = \frac{e^2}{4\pi\varepsilon_0\varepsilon_r L} \frac{(1-\gamma)^{1-1/\gamma}}{\gamma}. \tag{2}$$

Here, L, ε_r and ε_0 are the localization length, the relative permittivity of ACFs and the dielectric constant of vacuum, respectively. With T_0=324 K from the experiment, the estimates are obtained as γ=0.57 and L~17 nm. This satisfied the criteria of Coulomb-gap variable range hopping on fractal (average nanographene size a~2-3 nm < L), suggesting that the electron transport is governed by the electron hopping between conductive nanographite domains under the influence of charging process in the network having a fractal geometry.[28,29]
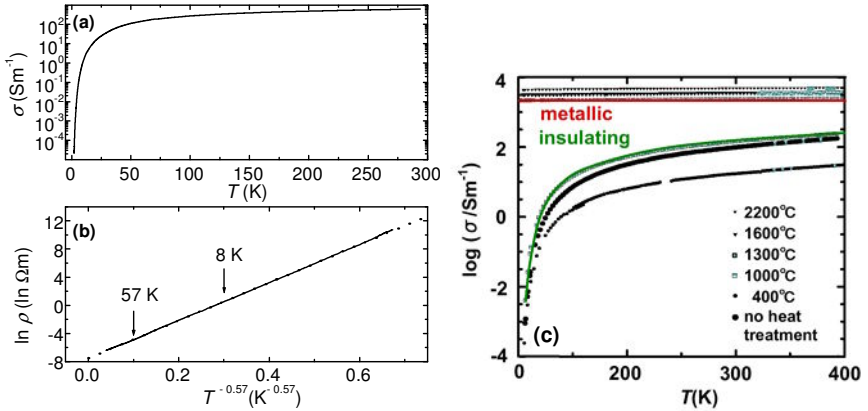
Fig. 5. The electrical conductivity (σ) / resistivity (ρ) of ACFs and their heat-treated samples with the heat treatment temperature being up to 2200 °C. (a) Non-heat-treated sample. (b) ln ρ vs T^{-n} plot of the data in (a), n=0.57. (c) Heat treatment temperature dependence of the conductivity vs T plots. ((a), (b) after Ref. 26, (c) after Ref. 24)

The magnetism of ACFs reflects the feature of the electron transport and the underlying hierarchical network structure, in which the nanographene sheets playing as the primary units are expected to be ferrimagnetic. Figure 6 exhibits the temperature dependence of the ESR
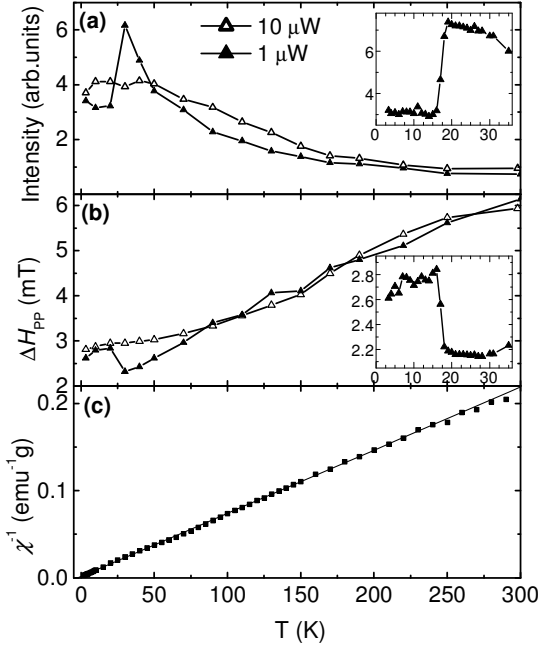
Fig. 6. The temperature dependence of the ESR intensity, ESR line width, and the reciprocal of the static susceptibility of the non-heat-treated ACFs. The ESR signals are observed with microwave powers of 1 and 10 μW (From reference 26).

intensity, ESR line width ΔH_{PP} and static magnetic susceptibility of the edge-state spins in the non-heat-treated ACFs.[26] The intensity at 1 μW obeys the Curie law down to 30 K, and suddenly drops by 50 % below 20 K. ΔH_{PP} follows a trend corresponding to the behavior of the intensity. ΔH_{PP} decreases linearly from 6.2 to 2.2 mT upon lowering of the temperature down to 30 K, and suddenly increases by 30 % (0.6 mT) below 20 K. In the elevated microwave power (10 μW) the sudden change in the signal properties becomes a smooth variation as shown in Figs. 6(a) and (b). Such sensitive nature of the ESR signal below 20 K is also evident in the microwave power dependence of the intensity. The power saturation at 30 K has a feature of a homogeneous spin system. On the other hand, at 10 K, increasing the power above 200 μW doubles the intensity suddenly and then it is easily saturated in the higher microwave power range above 1 mW, showing inhomogeneity in the spin system. Unlike the ESR intensity that represents the dynamical susceptibility, the
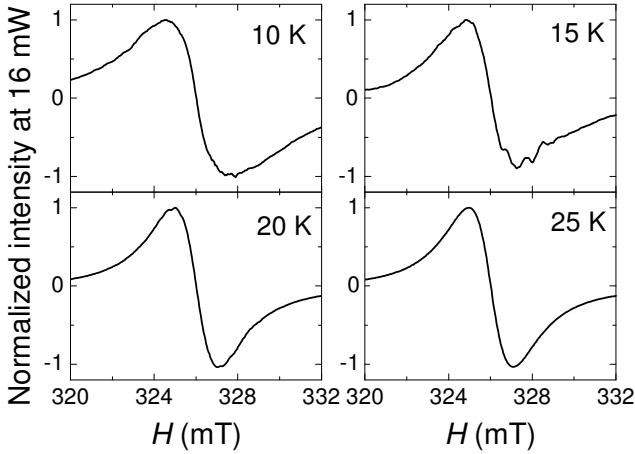
Fig. 7. The ESR signals in vacuum at 10, 15, 20, and 25 K measured with 16 mW (From reference 26).

static susceptibility does not show any indications of non-Curie behavior down to 2 K as shown in Fig. 6(c). These experimental findings are therefore understood by the presence of a transition from the homogeneous state to an inhomogeneous one at ca.20 K. This is clearly evident in observing a change in the line profile in the vicinity of the transition temperature ($T_c \sim 20$ K). Figure 7 exhibits the ESR signal at a strong microwave power of 16 mW in the vicinity of T_c.[26] The broadened signal at 10 K shows a slight deviation from the Lorentzian shape indicating an inhomogeneous line-broadening. Interestingly, a prominent hole-burning effect (irregular feature in the ESR signal) appears at 15 K, which is just below T_c, and it is reproducible in repeated runs. The hole-burning feature is an important evidence of serious inhomogeneity appearing in this temperature range. On going to higher temperatures, hole-burning is gradually suppressed and the line-shape tends to become Lorentzian. Above 25 K the line shape becomes sharpened and purely Lorentzian, exchange/motional narrowing being indicated.

The experimental findings presented above allow us to understand the magnetic structure and dynamics of the edge-state spin system. The conductivity result suggests strong electron localization with the aid of Coulomb interaction, particularly in the lower temperature region. In

addition to the electron hopping in the 3D random network of metallic nanographene sheets, the π-electron carriers interact strongly with the edge-state localized spins of a given sheet. At high temperatures, the fast hopping process evidenced by the high conductivity (Fig. 5(a)) makes the edge-state spins subjected to the motional narrowing, yielding a homogeneous spin system in the entire of the network. This is justified by the Lorentzian shape of the ESR signal and its less saturated behavior in the high temperature range. Therefore, the spin system is modeled merely as a metallic system with the interaction between the localized edge-state spins and conduction π-carriers. Here, the strong coupling between the edge-state spins and the conduction π-carriers, and a weak spin-orbit interaction, the latter of which is evident from a considerably small deviation of the g-value from that of the free electron spin ($\Delta g \sim 10^{-3}$),[30] lead to a bottleneck in energy dissipation from the conduction carriers to the lattice. In the bottleneck regime, the effective spin-lattice relaxation time, which is inversely proportional to the line width, is given as;[31,32]

$$\Delta H \sim 1/T_{1,\text{eff}} = \left(1/T_{n\pi}\right)\left(T_{\pi n}/T_{\pi L}\right),\tag{3}$$

where $T_{n\pi}$, $T_{\pi n}$ and $T_{\pi L}$ are the relaxation times of from the edge-state spin to the π-carrier, from the π-carrier to the edge-state spin, and from the π-carrier to the lattice, respectively. The relaxation from the edge-state spins to the π-carriers, $T_{\pi n}$ is given by the Korringa relation with temperature dependence of $T_{n\pi} \propto 1/T$.[33] Then, as shown in Eq. (3), the line width is narrowed by $\left(T_{\pi n}/T_{\pi L}\right)$ due to the bottleneck effect with a slow relaxation rate $1/T_{\pi L}$ Here, it should be noted that $T_{\pi n}$ is independent of temperature[31] and $T_{\pi L}$, which is governed by the boundary scattering in the nanographene, is also less temperature dependent.[34] Eventually, the linear temperature dependence of the line width observed above $T_c \sim 20$ K (Fig. 6(b)) is in good agreement with that expected by Eq. (3). This suggests the importance of the interplay between the edge-state spins and conduction π-carriers strongly interacting with each other in the metallic medium.

The situation becomes different in the magnetism in the low temperature regime below T_c. The appearance of the hole-burning in the vicinity of the transition temperature demonstrates the serious effect of

the structural inhomogeneity on the edge-state spins. Indeed, an inhomogeneous distribution of on-resonance fields is owing to the structural inhomogeneity originating from the hierarchical feature of the 3D network with irregular shaped nanographene sheets as the fundamental unit, as discussed with Fig. 4. In an individual nanographene sheet, the compensation of randomly distributed ferromagnetic clusters of the edge-state spins at zigzag edges, which are coupled by randomly varying inter-zigzag-edge interaction J_1, creates a net nonzero ferrimagnetic moment with its own strength. Therefore, the strengths of the ferrimagnetic moments, which depend on the shape of a nanographene sheet, are randomly distributed in the network of nanographene sheets, causing an inhomogeneous distribution of the on-resonance fields. The inhomogeneous distribution of the on-resonance fields does not appear in the high temperature range due to the motional narrowing operated by the fast inter-nanographene-sheet hopping. However, as the temperature is lowered, electron localization develops and nanographene sheets become independent from each other due to the slowdown of electron hopping. Finally, the inhomogeneity survives at lower temperatures below T_c, where the electron hopping frequency becomes small enough to unveil the inhomogeneous line width.

3.2. *Spin glass state in the nanographite network*

In the pristine ACFs, the periphery of an individual nanographene sheet is covered with oxygen-containing functional groups,[22] which disturb the inter-nanographene-sheet electron transfer. Heat-treatment removes the functional groups, working to enhance the inter-sheet interaction and create coherent electron transfer paths between nanographene sheets. The development of coherent electron transfer paths enhances the conductivity, as indicated in Fig. 5(c), which shows the temperature dependence of the conductivity for the ACF samples heat-treated at temperatures up to 2200 °C.[24] The extension of a percolation path networks in the electron transport to the entire of the sample eventually brings about metallic conductivity through an insulator-to-metal (I-M) transition around the heat-treatment temperature (HTT) of 1200 °C. The
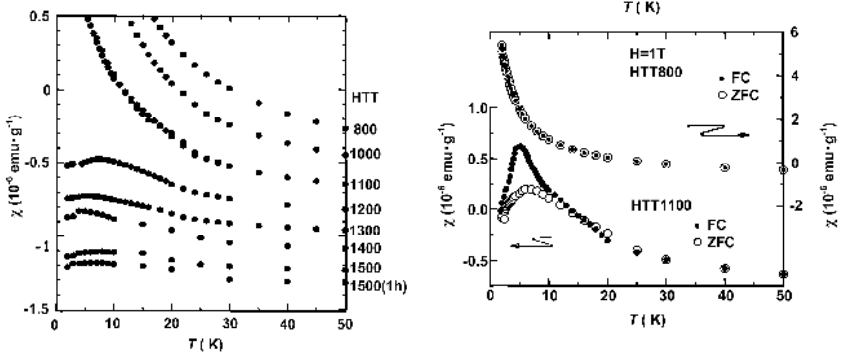
Fig. 8. (a) Temperature dependence of the magnetic susceptibility for ACF samples heat-treated at various temperature up to 1500 °C. (b) The field cooling effect on the susceptibility vs temperature plots at HTT1100 and 800, which are in the vicinity of the insulator-metal transition and far from the transition, respectively. Open and full circles represent data for the zero field cooling and field cooling (*H*=1T) processes, respectively (From reference 35).

change in the conductivity is faithfully tracked by the susceptibility as given in Fig. 8(a).[35] Namely, the Curie-Weiss behavior featured with the localized spins of edge state in the Anderson insulator regime is converted to a less temperature dependent susceptibility of conduction electrons in the metallic regime, where the net negative susceptibility is a combination of small positive Pauli paramagnetic and large negative orbital contributions. Here it should be noted that an anomalous feature appears in the vicinity of the I-M transition, that is; the susceptibility has a cusp at ca.7 K with a negative Weiss temperature (antiferromagnetic) of –2 to –3 K. This is reminiscent of the onset of an antiferromagnetic ordering. However, this is not the case, as a large field cooling effect on the susceptibility evidences in Fig. 8(b).[35] Figure 8(b) indicates that the susceptibility for the sample in the vicinity of the insulator-metal transition has a large field cooling effect, particularly around the temperature range in which the cusp emerges. The presence of a cusp and its large field cooling effect are a consequence of the development of spin glass state. In general, a spin glass state develops when the strengths of exchange interactions *J* vary randomly in space. From the magnetization curve analysis, a large randomness in the strengths of exchange interactions is evident, the width of the distribution being

estimated at $\sqrt{\langle \Delta J^2 \rangle} / \langle J \rangle \approx 0.8$, which is safely involved in the region of a spin glass. The heat-treatment well above the I-M transition converts the feature of the electrons from the localized to an itinerant one, where the localized spins of edge states diminish as the fusion of nanographene sheets takes place upon the elevation of heat-treatment temperature in the metallic phase. However, a considerable amount of edge-state spins still survive in the vicinity of the I-M transition. The inter-nanographene-sheet interaction J_2 and inter-nanographite-domain interaction J_3 are enhanced by strengthening the electron transfer paths, and works to couple strongly the ferrimagnetic moments of nanographene sheets. This causes the anomalous spin glass state appearing in the I-M transition region.

4. Summary

The electronic structure of a nanographene sheet, which is considered to be a condensed polycyclic hydrocarbon molecule extended to nano-dimension, crucially depends on the shape of its edges, same to small sized molecules in this family. The geometry of an arbitrary shaped nanographene sheet is described in terms of a combination of zigzag and armchair edges. In zigzag edges, the nonbonding π-electron state localized in the edge region is created, in contrast to the absence of such state in the armchair edges. As the edge state is strongly spin polarized, the localized edge-state spins contribute to form an unconventional magnetic system in nanographene.

The electronic structure of graphene edges is investigated experimentally to confirm the presence of edge state using UHV-STM/STS techniques. The magnetic properties of the edge-state spins are investigated using activated carbon fibers consisting of a 3D network of nanographene sheets. The constituent individual nanographene sheet is found to have a ferrimagnetic feature. Electron localization in the electron transport between the nanographene sheets in the network affects seriously the magnetism of the nanographene network. Strengthening of the inter-nanographene-sheet interaction brings about the formation of a spin glass state.

Acknowledgments

References

1. K. S. Novoselov, A. K. Geim, S. V. Morozov, D. Jiang, Y. Zhang, S. V. Dubonos, I. V. Grigorieva, and A. A. Firsov, *Science* **306**, 666 (2004).
2. C. Berger, Z. Song, T. Li, X. Li, A. Y. Ogbazghi, R. Feng, Z. Dai, A. N. Marchenkov, E. H. Conrad, P. N. First, and W. A. de Heer, *J. Chem. Phys. B* **108**, 19 912 (2004).
3. V. V. Cheianov, V. Fal'ko, and B. L. Altshuler, *Science* **315**, 1252 (2007).
4. A. H. Castro Neto, F. Guinea, N. M. R. Peres, K. S. Novoselov, and A. K. Geim, *Rev. Mod. Phys*. **81**, 109-162 (2009).
5. Y. Zhang, Y. Tan, H. L. Stormer, and P. Kim, *Nature* **438**, 201 (2005).
6. C. L. Kane and E. J. Mele, *Phys. Rev. Lett.* **95**, 226801 (2005).
7. S. E. Stein and R. L. Brown, *J. Amer. Chem. Soc*. **109**, 3721 (1987).
8. K. Yoshizawa, K. Okahara, T. Sato, K. Tanaka, and T. Yamabe, *Carbon* **32**, 1517 (1994).
9. M. Fujita, K. Wakabayashi, K. Nakada, and K. Kusakabe, *J. Phys. Soc. Jpn.* **65**, 1920 (1996).
10. K. Nakada, M. Fujita, G. Dresselhaus, and M. S. Dresselhaus, *Phys. Rev. B* **54**, 17954 (1996).
11. Y. Kobayashi, K. Fukui, T. Enoki, K. Kusakabe, and Y. Kaburagi, *Phys. Rev. B* **71**, 193406 (2005).
12. Y. Niimi, T. Matsui, H. Kambara, K. Tagami, M. Tsukada, and H. Fukuyama, *Appl. Surf. Sci.* **241**, 43 (2005).
13. Y. Kobayashi, K. Fukui, T. Enoki, and K. Kusakabe, *Phys. Rev. B* **73**, 125415 (2006).
14. Niimi, T. Matsui, H. Kambara, K. Tagami, M. Tsukada, and H. Fukuyama, *Phys. Rev. B* **73**, 085421 (2006).
15. T. Enoki, Y. Kobayashi, and K. Fukui, *Int. Rev. Phys. Chem.* **26**, 609 (2007).
16. E. Clar, "The Aromatic Sextet", Wiley, London, 1972.
17. E. Lieb, *Phys. Rev. Lett.* **62**, 1201 (1989).
18. K. Nakasuji and T. Kubo, *Bull. Chem. Soc. Jpn.* **77**, 1791 (2004).
19. Z. B. Maksic, D. Baric, and T. Muller, *J. Phys. Chem. A* **110**, 10135 (2006).
20. T. Wassmann, A. P. Seitsonen, A. M. Saitta, M. Lazzeri, and F. Mauri, *Phys. Rev. Lett.* **101**, 096402 (2008).

21. K. Wakabayashi, M. Sigrist, and M. Fujita, *J. Phys. Soc. Jpn.* **67**, 2089 (1998).
22. G. U. Sumanasekera, G. Chen, K. Takai, J. Joly, N. Kobayashi, T. Enoki, and P. C. Eklund, *J. Phys.: Condens. Matter.* **22**, 334208 (2010).
23. K. Kaneko, C. Ishii, M. Ruike, and H. Kuwabara, *Carbon* **30**, 1075 (1992).
24. Y. Shibayama, H. Sato, T. Enoki, X. Xin Bi, M. S. Dresselhaus, and M. Endo, *J. Phys. Soc. Jpn.* **69**, 754 (2000).
25. T. Enoki and K. Takai, *Solid State Commun.* **49,** 1144 (2009).
26. V. L. Joseph Joly, K. Takahara, K. Takai, M. Koshino, H. Tanaka, K. Sugihara, and T. Enoki, *Phys. Rev. B* (2010), in press.
27. A. W. Fung, Z. H. Wang, M. S. Dresselaus, G. Dresselhaus, R. W. Pekala, and M. Endo, *Phys. Rev. B* **49**, 17325 (1994).
28. A. Aharony, O. Entin-Wohlman, and A. Brooks Harris, *Physica* A **200**, 171 (1993).
29. D. van der Putten, J. T. Mooren, H. B. Bron, J. C. M. Brokken-Zijp, and M. A. Michels, *Phys. Rev. Lett.* **69**, 494 (1992).
30. K. Matsubara, T. Tsuzuki, and K. Sugihara, *Phys. Rev. B* **44**, 11845 (1991).
31. H. Hasegawa, *Progr. Theor. Phys.* **21**, 483 (1959).
32. J. H. Pifer and R. T. Longo, *Phys. Rev. B* **4**, 3797 (1971).
33. J. Korringa, *Physica* **16**, 601 (1950).
34. O. E. Andersson, B. L. V. Prasad, H. Sato, T. Enoki, Y. Hishiyama, Y. Kaburagi, M. Yoshikawa, and S. Bandow, *Phys. Rev. B* **58**, 16387 (1998).
35. Y. Shibayama, H. Sato, and T. Enoki, *Phys. Rev. Lett.* **84**, 1744 (2000).

Chapter 10

Electronic and Transport Properties of Graphene Nanoribbons

Katsunori Wakabayashi

International Center for Materials Nanoarchitectonics (MANA),
National Institute for Materials Science (NIMS),
Namiki 1-1, Tsukuba 305-0044, Japan
ka.wakaba@gmail.com

Low-energy electronic states of graphene are described by the massless Dirac Fermions. In nano-graphene, however, this description is strongly modified due to the existence of edges. In this chapter, we discuss the electronic transport properties of graphene nanoribbons, and clarify the role of edge boundary condition. Here we show that the graphene nanoribbons with zigzag edges subjected to the long-ranged impurities provide on-perfectly conducting channel, i.e. the absence of Anderson localization, because in each valley the balance between left- and right-going modes is violated due to the central subband originating from the edge states. We also study the electron transport through the graphene junction structures, where the zero-conductance anti-resonances is observed.

1. Introduction

Recently graphene, a single-layer hexagonal lattice of carbon atoms, has emerged as a fascinating system for fundamental studies in condensed matter physics, as well as the promising candidate material for future application in nanoelectronics and molecular devices.[1] The honeycomb crystal structure of single layer graphene consists of two nonequivalent sublattices and results in a unique band structure for the itinerant π-electrons near the Fermi energy which behave as massless Dirac Fermion. The valence and conduction bands touch conically at two nonequivalent Dirac points, called K_+ and K_- point, which form a time-reversed pair, i.e. opposite chirality. The chirality and a Berry phase of π at the two Dirac points provide an environment for highly unconventional and fascinating two-dimensional

electronic properties,[2] such as the half-integer quantum Hall effect,[3] the absence of backward scattering.[4,5]

The successive miniaturization of the graphene electronic devices inevitably demands the clarification of edge effects on the electronic structures and electronic transport properties of nanometer-sized graphene. The presence of edges in graphene has strong implications for the low-energy spectrum of the π-electrons.[6] There are two basic shapes of edges, *armchair* and *zigzag* which determine the properties of graphene ribbons. It was shown that ribbons with zigzag edges (zigzag ribbon) possess localized edge states with energies close to the Fermi level.[6] These edge states correspond to the non-bonding molecular orbitals,[6] and responsible for the magnetism.[6–9] In contrast, edge states are completely absent for ribbons with armchair edges. Recent experiments support the evidence of edge localized states.[10,11] Also, graphene nanoribbons can experimentally be produced by using lithography techniques and chemical techniques.[12–17]

In this chapter, we focus on edge and geometry effects of the electronic transport properties of graphene nanoribbons. In zigzag nanoribbons, for disorder without inter-valley scattering a single perfectly conducting channel emerges associated with a chiral mode due to edge states, i.e. the absence of the localization.[18] Nano-graphene junctions are shown to have the zero-conductance anti-resoances associated with the edge states.[19,20] The relation between the condition of the resonances and geometry is discussed.

2. Electronic States of Graphene Nanoribbons

We describe the electronic states of graphene nanoribbons by the tight-binding model. The Hamiltonian is written as,

$$H = -t \sum_{\langle i,j \rangle} c_i^\dagger c_j + \sum_i V_i c_i^\dagger c_i, \qquad (1)$$

where the operator $c_i^\dagger$ creates an π-electron on the site i. $\langle i,j \rangle$ denotes the summation over the nearest neighbor sites. t the transfer integrals between all the nearest neighbor sites are set to be unity for simplicity. This is sufficient to show the intrinsic difference in the electronic states originating from the topological nature of each system. The value of t is considered to be about 2.75eV in a graphene system. The second term in Eq. (1) represents the impurity potential, $V_i = V(\boldsymbol{r}_i)$ is the impurity potential at a position $\boldsymbol{r}_i$. The effect of impurity potential on the electronic transport properties will be discussed in the next section.
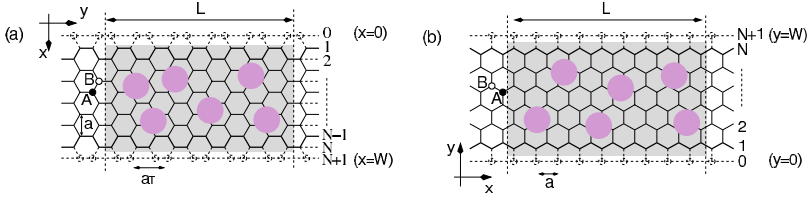
Fig. 1. Structure of graphene nanoribbon with (a) armchair edges (armchair ribbon) and (b) zigzag edges (zigzag ribbon). The lattice constant is a and N defines the ribbon width. The circles with dashed line indicate the missing carbon atoms for the edge boundary condition of massless Dirac equation. The disordered region with randomly distributed impurities lines in the shaded region and has the length L (see text in Sec. 3). Randomly distributed circles schematically represent the long-ranged impurities.

The energy band structures of (a) armchair nanoribbons and (b) zigzag nanoribbons for $N = 30$ are shown in Figs. 2(a)–(b), together with the density of states. The wave number k is normalized by the length of the primitive translation vector of each graphene nanoribbon, and the energy E is scaled by the transfer integral t. For armchair nanoribbons, the system is metallic when $N = 3M - 1$, where M is an integer. For the semiconducting ribbons, the direct gap decreases with increasing ribbon width and tends to zero in the limit of very large N. For narrow non-doped metallic armchair nanoribbons, the energy gap can acquire due to Peierls instabilities toward low-temperatures,[21] which is consistent with the recent density functional theory calculation.[22] For zigzag ribbons, however, a remarkable feature arises in the band structure, as shown in Fig. 2(b). We see that the highest valence band and lowest conduction band are always degenerate at $k = \pi$. It is found that the degeneracy of the center bands at $k = \pi$ does not originate from the intrinsic band structure of graphene sheet. These two special center bands get flatter with increasing ribbon width. A pair of partial flat bands appears within the region of $2\pi/3 \leq |k| \leq \pi$, where the bands sit in the vicinity of the Fermi level. The electronic state in the partial flat bands of the zigzag ribbons can be understood as the localized state near the zigzag edge.[6]

3. Electronic Transport Properties

We numerically discuss the electronic transport properties of the disordered graphene nanoribbons. In general, electron scattering in a quantum wire is described by using a scattering matrix.[23] Through the scattering matrix
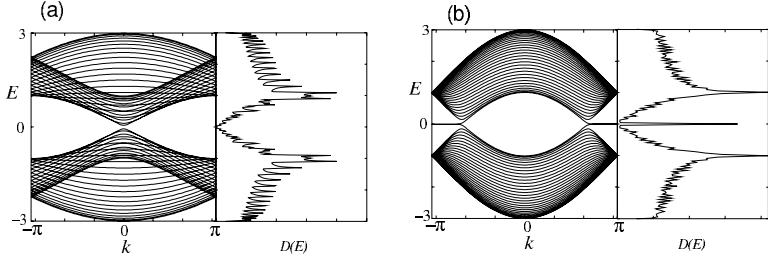
Fig. 2. Energy band structure $E(k)$ and density of states $D(E)$ of (a) armchair nanorib-bon and (b) zigzag nanoribbon. Here $N = 30$.

S, the an amplitude of scattered waves O are related to an amplitude of incident waves I,

$$\begin{pmatrix} O_L \\ O_R \end{pmatrix} = S \begin{pmatrix} I_L \\ I_R \end{pmatrix} = \begin{pmatrix} r & t' \\ t & r' \end{pmatrix} \begin{pmatrix} I_L \\ I_R \end{pmatrix}. \quad (2)$$

Here, r and r' are reflection matrices, t and t' are transmission matrices, L and R denote the left and right lead lines. The Landauer-Büttiker formula[24] relates the scattering matrix to the conductance of sample. The electrical conductance is calculated using the Landauer-Büttiker formula,

$$G(E) = \frac{e^2}{\pi\hbar}\mathrm{Tr}(tt^\dagger) = \frac{e^2}{\pi\hbar}g(E). \quad (3)$$

Here $t(E)$ is the transmission matrix through the disordered region. For simplicity, throughout this paper, we evaluate electronic conductance in the unit of quantum conductance ($e^2/\pi\hbar$), i.e. dimensionless conductance $g(E)$.

3.1. *One-way excess channel system*

In this subsection, we consider the conductance of zigzag nanoribbons in the clean limit, which is simply given by the number of the conducting channel. As can be seen in Fig. 3(a), there is always one excess left-going channel in the right valley (K_+) within the energy window of $|E| \leq 1$. Analogously, there is one excess right-going channel in the left valley (K_-) within the same energy window. Although the number of right-going and left-going channels are balanced as a whole system, if we focus on one of two valleys, there is always one excess channel in one direction, i.e. a chiral mode.

Now let us consider to inject electrons from left to right-side through the sample. When the chemical potential is changed from $E = 0$, the quantization rule of the dimensionless conductance (g_{K_+}) in the valley of K_+ is given as

$$g_{K_+} = n, \tag{4}$$

where $n = 0, 1, 2, \cdots$. The quantization rule in the K_--valley is

$$g_{K_+} = n + 1. \tag{5}$$

Thus, conductance quantization of the zigzag nanoribbon in the clean limit near $E = 0$ has the following odd-number quantization, i.e.

$$g = g_{K_+} + g_{K_-} = 2n + 1. \tag{6}$$
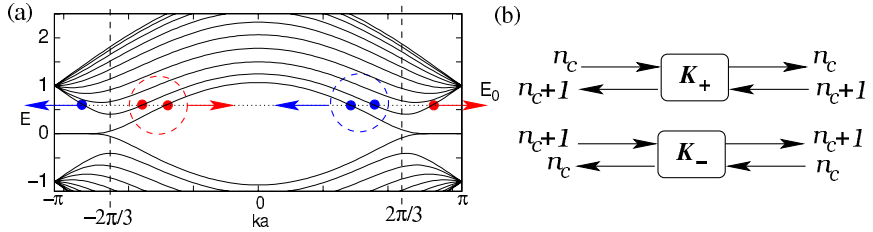
Fig. 3. (a) Energy dispersion of zigzag ribbon with $N = 10$. The valleys in the energy dispersion near $k = 2\pi/3a$ $(k = -2\pi/3a)$ originate from the Dirac $K_+(K_-)$-point of graphene. The red-filled (blue-unfilled) circles denote the right (left)-moving open channel at the energy E_0(dashed horizontal line). In the left(right) valley, the degeneracy between right and left moving channels is missing due to one excess right(left)-going mode. The time-reversal symmetry under the intra-valley scattering is also broken. (b) Schematic figure of scattering geometry at K_+ and K_- points in zigzag nanoribbons, where a single excess right-going mode exists for K_- point. But a single excess left-going mode exists for K_- point. Here $n_c = 0, 1, 2, \cdots$.

Since we have an excess mode in each valley, the scattering matrix has some peculiar features which can be seen when we explicitly write the valley dependence in the scattering matrix. By denoting the contribution of the right valley (K_+) as $+$, and of the left valley (K_-) as $-$, the scattering matrix can be rewritten as

$$\begin{pmatrix} O_L^+ \\ O_L^- \\ O_R^+ \\ O_R^- \end{pmatrix} = \begin{pmatrix} r & t' \\ t & r' \end{pmatrix} \begin{pmatrix} I_L^+ \\ I_L^- \\ I_R^+ \\ I_R^- \end{pmatrix}. \tag{7}$$

Here we should note that the dimension of each column vector is not identical. Let us denote the number of the right-going channel in the valley $\boldsymbol{K}_+$ or the left-going channel in the valley $\boldsymbol{K}_-$ as n_c. For example, $n_c = 1$ at $E = E_0$ in Fig. 3(a). Figure 3(b) shows the schematic figure of scattering geometry for $\boldsymbol{K}_+$ and $\boldsymbol{K}-$ points. Thus, the reflection matrices have the following matrix structures,

$$\boldsymbol{r} = \begin{array}{c} \\ n_c+1 \\ n_c \end{array} \overset{\displaystyle \begin{array}{cc} n_c & n_c+1 \end{array}}{\left(\begin{array}{cc} \boldsymbol{r}_{++} & \boldsymbol{r}_{+-} \\ \boldsymbol{r}_{-+} & \boldsymbol{r}_{--} \end{array} \right)}. \tag{8}$$

The reflection matrices become non-square when the intervalley scattering is suppressed, i.e. the off-diagonal submatrices ($\boldsymbol{r}_{+-}$, $\boldsymbol{r}_{-+}$ and so on) are zero.

When the electrons are injected from the left lead of the sample and the intervalley scattering is suppressed, a system with an excess channel is realised in the $\boldsymbol{K}_-$-valley. Thus, for single valley transport, the $\boldsymbol{r}_{--}$ and $\boldsymbol{r}'_{--}$ are $n_c \times (n_c+1)$ and $(n_c+1) \times n_c$ matrices, respectively, and $\boldsymbol{t}_{--}$ and $\boldsymbol{t}'_{--}$ are $(n_c+1) \times (n_c+1)$ and $n_c \times n_c$ matrices, respectively. Noting the dimensions of $\boldsymbol{r}_{--}$ and $\boldsymbol{r}'_{--}$, we find that $\boldsymbol{r}^\dagger_{--}\boldsymbol{r}_{--}$ and $\boldsymbol{r}'_{--}\boldsymbol{r}'^\dagger_{--}$ have a single zero eigenvalue. Combining this property with the flux conservation relation ($\boldsymbol{S}^\dagger \boldsymbol{S} = \boldsymbol{S}\boldsymbol{S}^\dagger = \boldsymbol{1}$), we arrive at the conclusion that $\boldsymbol{t}_{--}\boldsymbol{t}^\dagger_{--}$ has an eigenvalue equal to unity, which indicates the presence of a perfectly conducting channel (PCC) only in the right-moving channels. Note that $\boldsymbol{t}'_{--}\boldsymbol{t}'^\dagger_{--}$ does not have such an anomalous eigenvalue. If the set of eigenvalues for $\boldsymbol{t}'_{--}\boldsymbol{t}'^\dagger_{--}$ is expressed as $\{T_1, T_2, \cdots, T_{n_c}\}$, that for $\boldsymbol{t}_{--}\boldsymbol{t}^\dagger_{--}$ is expressed as $\{T_1, T_2, \cdots, T_{n_c}, 1\}$, i.e. a PCC. Thus, the dimensionless conductance g for the right-moving channels is given as

$$g_{\boldsymbol{K}_-} = \sum_{i=1}^{n_c+1} T_i = 1 + \sum_{i=1}^{n_c} T_i, \tag{9}$$

while that for the left-moving channels is

$$g'_{\boldsymbol{K}_-} = \sum_{i=1}^{n_c} T_i. \tag{10}$$

We see that $g_{\boldsymbol{K}_-} = g'_{\boldsymbol{K}_-} + 1$. Since the overall time reversal symmetry (TRS) of the system guarantees the following relation:

$$\begin{aligned} g'_{\boldsymbol{K}_+} &= g_{\boldsymbol{K}_-}, \\ g'_{\boldsymbol{K}_-} &= g_{\boldsymbol{K}_+}, \end{aligned} \tag{11}$$

the conductance $g = g_{K_+} + g_{K_-}$ (right-moving) and $g' = g'_{K_+} + g'_{K_-}$ (left-moving) are equivalent.

3.2. *Perfectly conducting channel*

The dimensionless electrical conductance, $g(E) = \text{Tr}(\boldsymbol{t t^\dagger})$ ($\boldsymbol{t}(E)$ is the transmission matrix through the disordered region), is calculated by means of the recursive Green function method.[25] As shown in Fig. 1, the impurities are randomly distributed with a density n_{imp} in the nanoribbons. In our model we assume that the each impurity potential has a Gaussian form of a range d

$$V(\boldsymbol{r}_i) = \sum_{\boldsymbol{r_0}(random)} u \exp\left(-\frac{|\boldsymbol{r}_i - \boldsymbol{r}_0|^2}{d^2}\right) \qquad (12)$$

where the strength u is uniformly distributed within the range $|u| \leq u_M$. Here u_M satisfies the normalization condition:

$$u_M \sum_{\boldsymbol{r}_i}^{(full\ space)} \exp\left(-r_i^2 d^2\right) / (\sqrt{3}/2) = u_0. \qquad (13)$$

In this work, we set $n_{\text{imp.}} = 0.1$, $u_0 = 1.0$ and $d/a = 1.5$ for LRI and $d/a = 0.1$ for SRI. Since the momentum difference between two valleys is rather large, $\Delta k = k_+ - k_- = 4\pi/3a$, only short-range impurities (SRI) with a range smaller than the lattice constant causes *inter-valley scattering*. Long-range impurities (LRI), in contrast, restrict the scattering processes to *intra-valley scattering*.[4]

We focus first on the case of LRI using a potential with $d/a = 1.5$ which is already sufficient to avoid inter-valley scattering. Figure 4(a) shows the averaged dimensionless conductance as a function of L for different incident energies(Fermi energies), averaging over an ensemble of 40000 samples with different impurity configurations for ribbons of width $N = 10$. The potential strength and impurity density are chosen to be $u_0 = 1.0$ and $n_{imp.} = 0.1$, respectively. As a typical localization effect we observe that $\langle g \rangle$ gradually decreases with growing length L (Fig. 4). However, $\langle g \rangle$ converges to $\langle g \rangle = 1$ for LRIs (Fig. 4(a)), indicating the presence of a single *perfectly conducting* channel. It can be seen that $\langle g \rangle(L)$ has an exponential behavior as

$$\langle g \rangle - 1 \sim \exp(-L/\xi) \qquad (14)$$

with ξ as the localization length. Deviations from the limit $\langle g \rangle \to 1$ also occur, if the incident energy lies at a value close to the change between $g = 2n - 1$ and $g = 2n + 1$ for the ribbon without disorder. This is for example visible in above calculations for $E = 0.4$ where the limiting value $\langle g \rangle < 1$ (Fig. 4(a)).
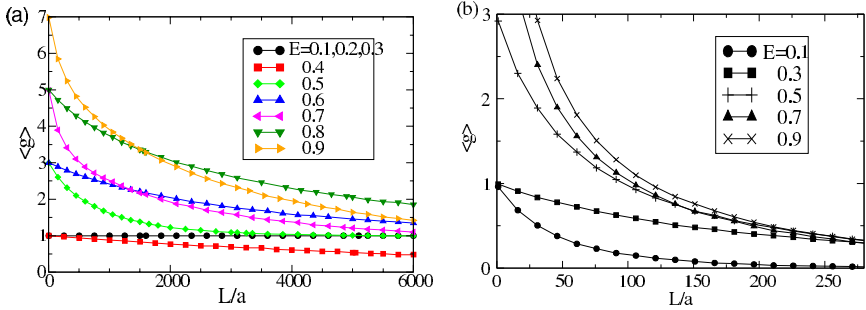
Fig. 4. L-dependence of the averaged dimensionless conductance, $\langle g \rangle$ for zigzag nanoribbon with $N = 10$, (a) $d/a = 1.5$ (no inter-valley scattering), (b) $d/a = 0.1$ (inter-valley scattering). Here $u_0 = 1.0$, and $n_{imp.} = 0.1$. More than 9000 samples with different impurity configuration are included in the ensemble average.

In Fig. 4(b), the nanoribbon length dependence of the averaged conductance for SRIs is shown. Since SRI causes the inter-valley scattering for any incident energy, the electrons tend to be localized and the averaged conductance decays exponentially, $\langle g \rangle \sim \exp(-L/\xi)$, without developing a perfect conduction channel.

As the effect is connected with the subtle feature of an excess mode in band structure, it is natural that the result can only be valid for sufficiently weak potentials. For potential strengths comparable to the energy scale of the band structure, e.g. the energy difference between the transverse modes, the result should be qualitatively altered.[26]

3.3. Graphene nanoribbons with generic edge structures

As we have seen, zigzag ribbons with long-ranged impurity potentials retain a single PCC. This PCC originates for the following two reasons: (i) The spectrum contains two valleys (two Dirac $K_{\pm}$-points) which are well enough separated in momentum space as to suppress intervalley scattering due to the long-ranged impurities, (ii) the spectrum in each valley is chiral by
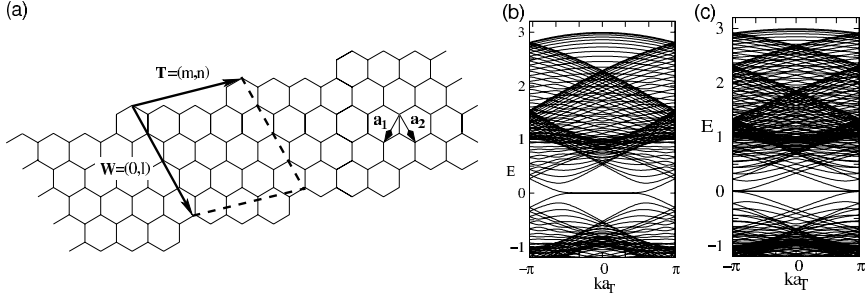
Fig. 5. (a) The primitive vectors for nanoribbon with the general edge structures. The translational vector is defined as $\boldsymbol{T} = (m, n) = m\boldsymbol{a_1} + n\boldsymbol{a_2}$, and the ribbon width is defined by the vector $\boldsymbol{W} = (0, l) = l\boldsymbol{a_2}$. The number of carbon atoms in the unit cell is $2(l+1)m$. The corresponding energy band structures of $\boldsymbol{W} = (0, 20)$ for (b) $\boldsymbol{T} = (-4, 3)$ and (c) $\boldsymbol{T} = (-6, 5)$. Here a_T is the effective lattice constant which is given as $|\boldsymbol{T}|$.

possessing a right- and left-moving modes which differ by one in number, and so scattered electrons can avoid in one channel backscattering.

We extend our analysis to the electronic spectrum of nanoribbons for which the ribbon axis is tilted with respect to the zigzag axis and keep the balance between A- and B-sublattice sites. In Fig. 5(a), we show the definitions of coordinates and primitive vectors which specifies the geometry of the ribbon. For this purpose we introduce the two vectors, $\boldsymbol{T} = (m, n) = m\boldsymbol{a_1} + n\boldsymbol{a_2}$ and $\boldsymbol{W} = (0, l) = l\boldsymbol{a_2}$, where l, m, n are integers. The pure zigzag ribbon corresponds to $m = -n$ and the pure armchair edge is given by $m = n$.

Figures 5(b) and (c) show the energy band structures of ribbons with the general edge structures of $\boldsymbol{W} = (0, 20)$ and (b) $\boldsymbol{T} = (-4, 3)$ and (c) $\boldsymbol{T} = (-6, 5)$ are shown. As we expected, the partially flat bands due to localized edge modes appear which break the balance between left- and right-going modes in the two valleys. Both examples are rather close to the zigzag edge so that the two valleys are well separated. In this case PCC can appear. If the geometry of the ribbons deviates more strongly from the zigzag condition, the valley structure will become less favorable for creating a PCC, as the momentum difference between valleys shrinks. It is important to note that the extended unit cell along these generalized ribbons reduces the valley separation drastically through Brillouin zone folding. The length scale is the new effective lattice constant a_T along the ribbon. Under these circumstances the condition for long-ranged impurity potentials is more stringent, d being larger than a_T and not a.
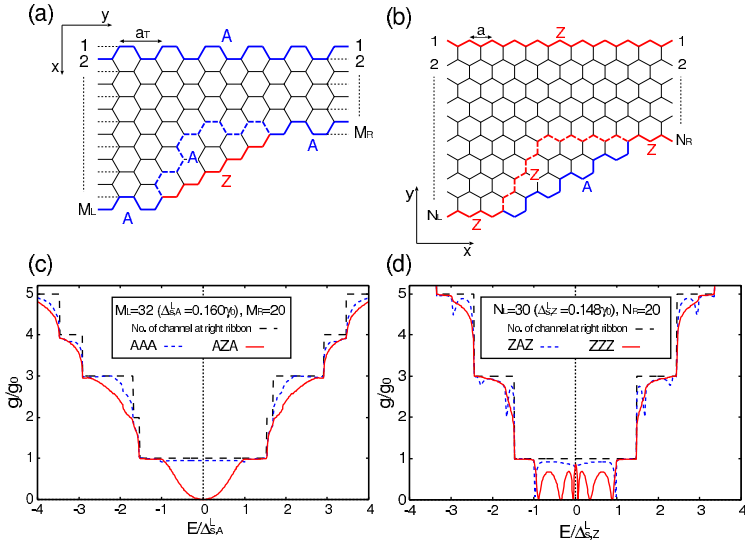
Fig. 6. (a) Armchair ribbons with armchair junction (AAA-junction, bule dotted line) and zigzag junction (AZA-junction, red solid line). (b) Zigzag ribbons with armchair junction (ZAZ-junction, blue solid line) and zigzag junction (ZZZ-junction, red dotted line). (c) Conductance as a function of energy in armchair ribbon junctions. The width of left and right ribbons are $M_L = 32$ and $M_R = 20$. Conductance mostly remains unity in the AAA-junction while the zero conductance dip appears in the AZA-junction at $E = 0$ for the single-channel energy regime ($|E| < \Delta_{s,A}^L$). (d) Conductance as a function of energy in zigzag ribbon junctions. The width of left and right ribbons are $N_L = 30$ and $N_R = 20$. Conductance mostly remains unity in the ZAZ-junction while several zero conductance dips appear in the ZZZ-junction at non-zero energies for the single-channel energy regime ($|E| < \Delta_{s,Z}^L$).

4. Transport Properties through Graphene Junction

In this section, we study the electronic transport in GNR junctions. Here, we consider GNR junctions as shown in Figs. 6(a) and (b). Junctions are classified into the armchair ribbon with armchair edge junction (AAA-junction), that with zigzag one (AZA-junction), the zigzag ribbon with armchair edge junction (ZAZ-junction) and that with zigzag one (ZZZ-junction). The width of left (right) armchair ribbon is defined by $M_L(M_R)$ while that of zigzag one is by $N_L(N_R)$. Here we note that the armchair ribbon is metallic only for $M_{(L,R)} = 3I - 1$ (I : integer) while the zigzag ribbon is always metallic.

Figures 6(c) and (d) show the energy dependence of the conductance for armchair and zigzag ribbon junctions, respectively. We set $(M_L, M_R) =$

$(32, 20)$ and $(N_L, N_R) = (30, 20)$. The energy is normalized by $\Delta^L_{s,A} (\Delta^L_{s,Z})$, denoting the end of single-channel energy regime of the left wider armchair (zigzag) ribbon. These energy scales are related to the ribbon width by $\Delta^L_{s,A} \simeq \sqrt{3}\pi\gamma_0 a/2W$ and $\Delta^L_{s,Z} \simeq 3\sqrt{3}\pi\gamma_0 a/8W$ where $W = (M_L + 1)a/2$ and $W = \sqrt{3}(N_L + 1)a/2$ for armchair and zigzag ribbons, respectively. The maximum conductance is limited by the number of channel at the right narrower ribbon (black dotted line in Figs. 6(c) and (d)).

The behaviour of conductance strongly depends on junction structure in the single-channel energy regime ($|E| < \Delta^L_{s,(A,Z)}$) while it does not in the multi-channel one ($|E| > \Delta^L_{s,(A,Z)}$). In the single-channel energy regime, the conductance mostly remains unity in the AAA-junction while the zero conductance dip appears in the AZA-junction at $E = 0$. This zero conductance dip is due to the anti-resonance induced by the coupling between a continuous state at ribbon and a localized state at zigzag edge junction. In addition, the junction region is mainly semiconducting and works as a barrier for low-energy transport in the AZA-junction since the ribbon width are narrowed as $M_L - 1, M_L - 2, \cdots$. Hence, by the combination of a resonance and a barrier effect, the width of zero conductance dip in the AZA-junction is rather wide and the FWHM (full width at half maximum) can be roughly estimated as $\Delta^L_{s,A}$. On the other hand, the junction region is always metallic or semiconducting in the AAA-junction since the ribbon width are narrowed as $M_L - 3, M_L - 6, \cdots$.

In the ZAZ-junction, the sharp zero conductance dips appear in the vicinity of the end of single-channel energy regime ($E \simeq \pm\Delta^L_{s,Z}$). In zigzag ribbons, propagating electrons belong to one of two valleys in the single-channel energy regime while the second channel will be opened in both valleys as the energy of incident electrons increases. Since the group velocity of a second channel is almost zero at the bottom of subband, the second channel in the other valley works as a bound state similar to the zigzag edge state at $E = 0$. The FWHM of dips can be roughly estimated as $\Delta^L_{s,A}/20$ in our numerical simulation performed for several different values of the ribbon width N_L and the width difference $\Delta N = N_L - N_R$ within the range $N_L/3 \leq \Delta N \leq 2N_L/3$.

In the ZZZ-junction, several zero conductance dips appear at non-zero energies. This is due to the energy level splitting induced by the coupling between the edge-localized state on A-sublattice at ribbon and the edge-localized states on B-sublattice at junction. Moreover, the coupled states have different nodes as the width difference ΔN is getting larger.[20]

5. Summary

In this paper, we have presented a brief overview on the transport properties of graphene nanoribbons focusing on the effect of edge shapes and impurity scattering. We have seen that the degree of freedoms with respect to edge structures can be a source of wide variety of electron transport phenomena such as perfectly conducting channel and zero-conductance Fano-resonances, which will serve to design the nano-carbon electronics devices.

References

1. K. S. Novoselov *et. al.*, *Science* **306**, 666 (2004).
2. A. H. Castro Neto, F. Guinea, N. M. R. Peres, K. S. Novoselov, and A. K. Geim, *Rev. Mod. Phys.* **81**, 109 (2009).
3. K. S. Novoselov, A. K. Geim, and S. V. Morozov *et. al.*, *Nature* **438**, 197 (2005); Y. Zhang, Y. W. Tan, H. L. Stormer, and P. Kim, *Nature* **438**, 201 (2005).
4. T. Ando, *J. Phys. Soc. Jpn.* **74**, 777 (2005).
5. T. Ando and T. Nakanishi, *J. Phys. Soc. Jpn.* **67**, 1704 (1998).
6. M. Fujita and K. Wakabayashi *et. al.*, *J. Phys. Soc. Jpn.* **65**, 1920 (1996); K. Wakabayashi *et. al.*, *Phys. Rev. B* **59**, 8271 (1999).
7. K. Wakabayashi, M. Sigrist, and M. Fujita, *J. Phys. Soc. Jpn.* **67**, 2089 (1998).
8. K. Kusakabe and M. Maruyama, *Phys. Rev. B* **67**, 092406 (2003).
9. S. Dutta and S. K. Pati, *J. Mater. Chem.* **20**, 8207 (2010).
10. Y. Kobayashi *et. al.*, *Phys. Rev. B* **71**, 193406 (2005).
11. Y. Niimi *et. al.*, *Phys. Rev. B* **73**, 085421 (2006).
12. M. Y. Han *et. al.*, *Phys. Rev. Lett.* **98**, 206805 (2007).
13. X. Li *et. al.*, *Science* **319**, 1229 (2008).
14. X. Yang *et. al.*, *J. Am. Chem. Phys.* **130**, 4216 (2008).
15. L. Jiao *et. al.*, *Nature* **458**, 877 (2009); D. V. Kosynkin *et. al.*, *Nature* **458**, 872 (2009).
16. X. Jia *et. al.*, *Science* **323**, 1701 (2009).
17. C. N. R. Rao *et. al.*, *Angew. Chem. Int. Ed.* **48**, 7752 (2009).
18. K. Wakabayashi *et. al.*, *Phys. Rev. Lett.* **99**, 036601 (2007); *New. J. Phys.* **11** , 095016 (2009).
19. M. Yamamoto and K. Wakabayashi, *Appl. Phys. Lett.* **95**, 082109 (2009).
20. K. Wakabayashi, *Phys. Rev. B* **64**, 125428 (2001).
21. M. Fujita, M. Igami, and K. Nakada, *J. Phys. Soc. Jpn.* **66**, 1864 (1997).
22. Y.-W. Son, M. L. Cohen, and S. G. Louie, *Phys. Rev. Lett.* **97**, 216803 (2006).
23. C. W. J. Beenakker, *Rev. Mod. Phys.* **69**, 731 (1997).
24. M. Büttiker, Y. Imry, R. Landauer, and S. Pinhas, *Phys. Rev. B* **31**, 6207 (1985).
25. T. Ando, *Phys. Rev. B* **44**, 8017 (1991).
26. K. Wakabayashi, *J. Phys. Soc. Jpn.* **71**, 2500 (2002).

Chapter 11

Gate-Voltage Modulation in Graphene

K. Tsukagoshi,[*,†,¶] H. Miyazaki,[*,†] S.-L. Li,[*] A. Kumatani,[*]
H. Hiura,[*,‡] and A. Kanda[†,§]

MANA, NIMS, Namiki, Tsukuba, Ibaraki 305-0047, Japan
†*CREST, JST, Kawaguchi, Saitama 332-0012, Japan*
‡*NEC, Tsukuba, Ibaraki 305-8501, Japan*
§*University of Tsukuba, Tsukuba, Ibaraki 305-8571, Japan*
¶*TSUKAGOSHI.Kazuhito@nims.go.jp*

We present a review of our experiments on graphene transistors in its potential use as atomic film switching devices. As the preparation of the bilayer graphene, a quick formation method to precisely confirm the number of layers is required. Fabrication of gate electrodes specialized for the graphene system is also useful in the application of a high electric field in the graphene transistor. In this short review paper, our original method of fabrication and structure of gate electrodes for the graphene transistor will be introduced.

1. Introduction

A thin graphite film with atomic scale thickness will be one of the key materials for future electronics. Besides its high mobility [1,2], graphene is conductive without doping, which eliminates its limitation in device miniaturization due the uncertainty of dopant position [3]. Furthermore, the atomic film is ideal to confine conduction carrier into a real two-dimensional space. The ideal two-dimensional conductor can achieve efficient switching of the conduction during gate voltage changes even though transistor size is miniaturized to nano-scale [4]. However, the intrinsic metallic nature and high carrier density of graphene prevents the use of graphene channel in semiconductor switching devices. The resistance tunability under a gate electric field is at most several tens,

which is far lower than the on/off ratio exhibited in the current switching transistor. The enhancement of resistance tunability is strongly desired in order to realize high-performance in atomic graphene transistors [5]. Therefore, further investigation of the gate voltage characteristics in the graphene is required [6-10].

Here, we introduced our experiments to fabricate graphene transistor on SiO_2/Si substrate to investigate electric conduction under a high electric field. An original graphene mapping method on the SiO_2/Si substrate and a fabrication method of gate electrode have been introduced. We also experimentally investigated the transport properties in the fabrication of graphene transistors with top and back gates.

2. Experimental

2.1. *Quick and precise judgment method for number of layers*

The graphite films are prepared using the micromechanical cleavage method [1] from kish, HOPG, or natural graphite on a highly doped silicon wafer with a 300-nm-thick or 90-nm-thick SiO_2 layer. On the SiO_2 surface, thin graphite films with various thicknesses, including the graphenes, are randomly spread around. Among the graphite films, suitable graphene films should be efficiently selected. Monolayer graphene is commonly judged from the color of the optical-microscope image [1,11,12]. Precise determination of the number of layers by Raman spectroscopy [13,14] shows that the optical-microscope method is reliable and reproducible for an experienced observer. It is known that a green optical filter improves visibility of thin layers in the optical microscope observations [11,12]. Oostinga et al. successfully distinguished between the monolayer and bilayer graphene by using the absolute green intensity in digital images [15].

We use a charge-coupled device (CCD) mounted on an optical microscope to obtain direct green images of graphene films. The light detected by the CCD is separated into red, green, and blue (RGB) components for each pixel. Each component is recorded in 256
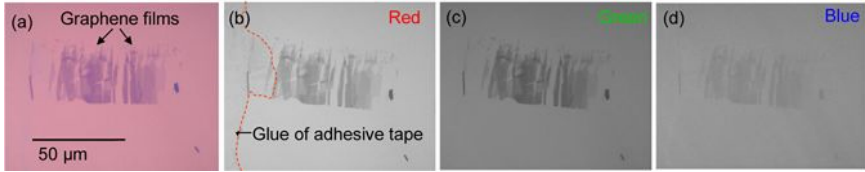
Fig. 1. (a) Original image of the graphene films on 300-nm-thick SiO$_2$/Si substrate. The image was taken using a CCD mounted on an optical microscope. The image can be separated into the (b) red, (c) green, and (d) blue images by a conventional graphics software.

intensity-levels, and combined in a picture image. In this way, the picture image (Fig. 1(a)) can be resolved into R/G/B images (Figs. 1(b)-(d)) by conventional graphic software. The residual glue from adhesive tape is prominent and causes noise in the red image. The blue image has relatively poor contrast in comparison with the green image. This difference is consistent with the use of the green filter to obtain better contrast in the optical-microscope observations. The green image taken by the CCD has the advantage of direct and clear pixel-bit information on the green intensity over other optical methods.

From the green image map (Fig. 2(a)), the pixel percentage histogram in the dotted frame is obtained (the dotted line in Fig. 2(b)). Five peaks with equal intensity intervals are separately observed (inset in Fig. 2(b)), indicating that these are five pixel regions with different green-contrast. The peak with the highest green-intensity (at ~133 in the intensity level) is from the substrate, as confirmed by the image without graphene. Then, the framed region in Fig. 2(a) contains four different thicknesses. Each percentage of the observed pixels depends on the occupied area in the dotted frame. This histogram is used as a reference to judge the number of layers of a target sample (in a red frame in Fig. 2(c)). We also make a green intensity histogram for the target sample (a red curve in Fig. 2(b)). After normalizing the intensity of the sample by using the intensity from the substrate, we compare the peak positions in the histogram of the target with those in the reference (Fig. 2(d)) to judge the number of layers in the target.
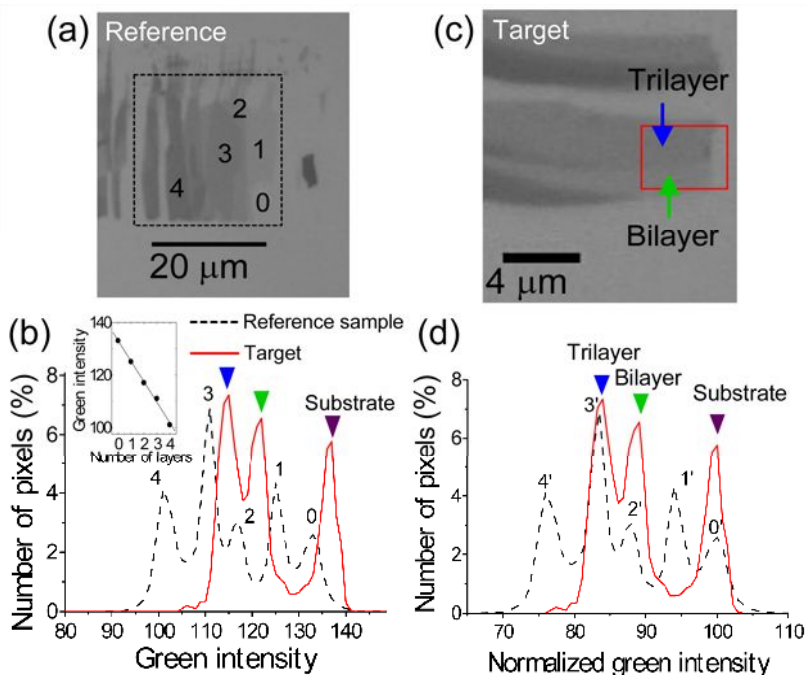
Fig. 2. (a) Green data image of graphene films containing various number of layers. (b) Number of pixels in the dotted frame in (a) was plotted as a dotted line with respect to the detected green intensity (b). The inset shows the Green intensity plot depending on the number of layers of the graphene film. Another example of a film from the red frame in (c) is shown as a red line. These two films are directly compared after normalization with respect to the green intensity of the substrate, as shown in (d). Here, the absolute intensity was slightly changed when the image was slightly defocused, or the optical light intensity was changed. However, the interval of the normalized green intensity is always nearly constant. This method can recognize 1 to 6 layers as discrete intensity peaks.

2.2. *Device fabrication process*

Graphene films cleaved from Madagascar natural graphite are fabricated into field effect transistor. Source and drain electrodes (50-nm-thick Au with 5-nm-thick Ti) are fabricated by electron-beam lithography and thermal evaporation of the metals. The electrodes show ohmic contact with the graphene with a typical resistance of less than a few kΩ. Subsequently, a 30-nm-thick aluminum film is directly deposited
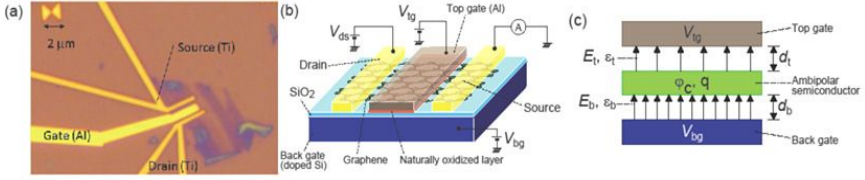
Fig. 3. (a) Optical microscope image of the graphene transistor fabricated on SiO$_2$/Si substrate. After forming the source and drain electrodes, the aluminum gate was directly evaporated onto the graphene surface. Although this process has no intentional insulator layer at the interface between the graphene and the aluminum film, the interface aluminum can be partially oxidized in air. Because the oxidation is only around the surface of the film and the interface and the inside of the aluminum film remains as the conductive aluminum, the aluminum film evaporated on the graphene can be used as the gate electrode. (b) Schematic of the transistor structure with measurement circuit system. (c) Schematic of the ambipolar semiconductor film with a top-gate and a back-gate. In the experiment, the ambipolar semiconductor was the graphene channel. The channel was separated from the back gate by a distance d_b (d_b=300 nm in the experiment) with a gate insulator SiO$_2$ film (dielectric constant ε_i=3.9ε_0), and from the top-gate by a distance d_t with a self-assembled insulating layer (ε_t).

between the source-drain electrodes using the process similar to the contact formation (Figs. 3(a) and (b)). Although an intentional insulator layer was not introduced between the Al top gate and the graphene, the Al electrode and the graphene were naturally insulated after exposing the device to air for several hours [8]. The resistance between the gate and the source (or drain) electrodes automatically far exceeds 100 MΩ, and the interior remains intact because the Al electrode remains conductive. The most possible oxidation source is the atmospheric oxygen, which could diffuse into the interface layer between the Al and the graphene, due to the fairly weak physical contact between Al and graphite [16-18]. The oxygen gas absorbed on the graphite surface could also contribute to the oxidization process. However, the amount of oxygen atoms adsorbed on the graphene surface would be insufficient to form the nm-thick oxidation layer (the thickness is estimated below). Thus, we speculate that the oxygen was mainly supplied from the air. Once the top gate dielectric layer is formed, the current from the top gate electrode to the graphite can hardly be measured, thus exhibiting insulating properties. The proposed top gate fabrication method is superior to other methods

with high gate efficiency and it is a simple fabrication process. The highly doped substrate is used as a bottom gate electrode, while the Al electrode with the self-formed insulator is used as the top gate electrode in the dual gate graphene transistor. Electric conduction of the graphene can be tuned by the two gate voltages in the dual-gate structure.

2.3. *Top gate capacitance*

Capacitance between the top gate and the graphene channel is estimated. We consider the relation of an electric field E_t (E_b) between the channel and the top-gate (back-gate) to the electric potential of the channel φ_c (Fig. 3(c)). The electric fields and the electric potentials are related by $V_{bg} - \varphi_c = E_b d_b$ and $\varphi_c - V_{tg} = E_t d_t$. When the channel contains charges with density q, an equality $\varepsilon_t E_t - \varepsilon_b E_b = q$ is obtained from Gauss's law, where ε_t and ε_b are the dielectric constant of the top gate and the back gate insulators respectively. From these three equations, we have the following equation:

$$\frac{\varepsilon_t}{d_t} V_{tg} + \frac{\varepsilon_b}{d_b} V_{bg} = (1+\alpha) \frac{\varepsilon_t}{d_t} \varphi_c - q \tag{1}$$

where $\alpha = (\varepsilon_b/d_b)/(\varepsilon_t/d_t)$. At the charge neutrality point ($q=0$ and $V_{tg} = V_{tg}^*$), the Eq. (1) becomes $\frac{\varepsilon_t}{d_t} V_{tg}^* + \frac{\varepsilon_b}{d_b} V_{bg} = (1+\alpha) \frac{\varepsilon_t}{d_t} \varphi_c$. When the source-drain bias is small enough, φ_c is approximately zero, giving $\frac{dV_{tg}^*}{dV_{bg}} = -\frac{\varepsilon_b/d_b}{\varepsilon_t/d_t} = -\alpha$. The quantity α corresponds to the ratio of the back gate capacitance $c_b = \varepsilon_b/d_b$ to the top gate capacitance $c_t = \varepsilon_t/d_t$ for unit area. Using $\alpha = -\frac{dV_{tg}^*}{dV_{bg}} = 0.013$ obtained as a device parameter in the experiment (Fig. 3), $\varepsilon_b = 3.9\varepsilon_0$ (ε_0: dielectric constant of vacuum) from dielectric constant of SiO_2, and $d_b = 300$ nm, we can estimate the top gate capacitance per unit area, $c_t = \varepsilon_t/d_t = (\varepsilon_d/d_b)/\alpha = 8.9 \times 10^{-3}$ F/m^2. Assuming that $\varepsilon_t = 5\text{-}9\varepsilon_0$ for Al-oxide, the thickness of the top-gate insulator is estimated to be 5-9 nm. Note that formation of such a thin insulating layer would be difficult using conventional method, such as vacuum evaporation.
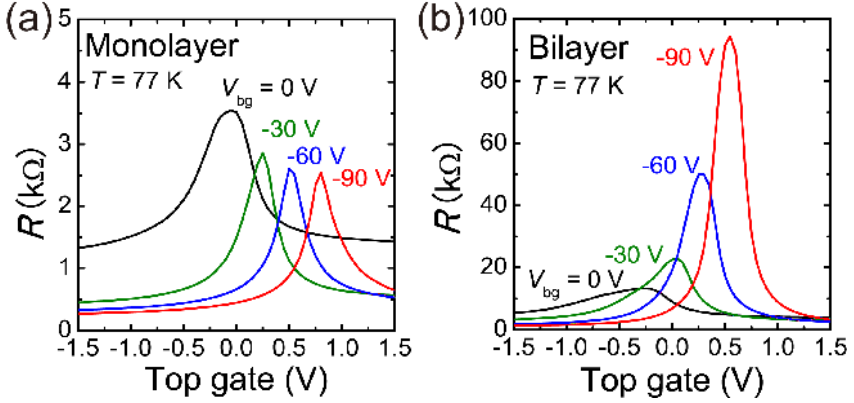
Fig. 4. Resistance as a function of V_{tg} at V_{bg}= -90, -60, -30, 0 V for (a) monolayer and for (b) bilayer graphene. The resistance enhancement can be observed in the bilayer graphene under the high electric field.

2.4. *Conductance control in graphene by dual gate voltages*

The electric conduction in the bilayer graphene can be changed by the electric filed generated by the dual gate voltages (Fig. 4). The charge neutrality resistance peak indicated that the transition between the p-type and the n-type conduction was observed commonly in any graphene and thin graphite films. In a monolayer graphene, the charge neutrality resistance was never enhanced even though the high electric field between the dual gates was increased (Fig. 4(a)). In a bilayer, however, a clear resistance enhancement was observed as the electric field was increased (Fig. 4(b)). The difference in the electric conduction was attributed to the intrinsic conduction mechanism in the monolayer or the bilayer graphene.

The conduction possibly contains two important components. One of them stems from the conduction due to the variable range hopping conduction via localized states [13]. Another component is assumed to be transport related to the band gap enhanced only in the electric field. In a conductance plot of the ambipolar behavior in a top-gate voltage scan, when the resistance is enhanced in the bilayer graphene, the conductance closely approached zero conduction. Voltage difference extracted from

the threshold of the p-type and the n-type region in the top-gate voltage scan is typically 0.5 V at the gate electric field of 1.4 V/nm, and strongly dependent on the applied electric field. The subthreshold region in the bilayer graphene implies an existence of the band gap when the electric field is applied.

Acknowledgments

References

1. K. S. Novoselov, A. K. Geim, S. V. Morozov, D. Jiang, Y. Zhang, S. V. Dubonos, I. V. Grigorieva and A. A. Firsov, *Science* **306**, 666 (2004).
2. C. N. R. Rao, A. K. Sood, K. S. Subrahmanyam and A. Govindaraj, *Angew. Chem. Int. Ed.* **48**, 7752 (2009).
3. J. D. Meindl, Q. Chen and J. A. Davis, *Science* **293**, 2044 (2001).
4. see for example, Chapter 7 in Physics of semiconductor devices (2nd edition), S. M. Sze, New York, Wiley, 1981.
5. A. K. Geim and K. S. Novoselov, *Nat. Mater.* **6**, 183 (2007).
6. H. Miyazaki, S. Odaka, T. Sato, S. Tanaka, H. Goto, A. Kanda, K. Tsukagoshi, Y. Ootuka and Y. Aoyagi, *Appl. Phys. Exp.* **1**, 024001 (2008).
7. H. Miyazaki, S. Odaka, T. Sato, S. Tanaka, H. Goto, A. Kanda, K. Tsukagoshi, Y. Ootuka and Y. Aoyagi, *Appl. Phys. Exp.* **1**, 034007 (2008).
8. H. Miyazaki, S. Li, A. Kanda and K. Tsukagoshi, *Semiconductor Science and Technology* **25**, 034008 (2010).
9. H. Goto, A. Kanda, T. Sato, S. Tanaka, Y. Ootuka, S. Odaka, H. Miyazaki, K. Tsukagoshi and Y. Aoyagi, *Appl. Phys. Lett.* **92**, 212110 (2008).
10. A. Das, S. Pisana, B. Chakraborty, S. Piscanec, S. K. Saha, U. V. Waghmare, K. S. Novoselov, H. R. Krishnamurthy, A. K. Geim, A. C. Ferrari and A. K. Sood, *Nature Nanotechnology* **3**, 210 (2008).
11. P. Blake, E. W. Hill, A. H. Castro Neto, K. S. Novoselov, D. Jiang, R. Yang, T. J. Booth and A. K. Geim, *Appl. Phys. Lett.* **91**, 063124 (2007).
12. S. Soddaro, P. Pingue, V. Piazza, V. Pellegrini and F. Beltram, *Nano Lett.* **7**, 2707 (2007).

13. A. C. Ferrari, J. C. Meyer, V. Scardaci, C. Casiraghi, M. Lazzeri, F. Mauri, S. Piscanec, D. Jiang, K. S. Novoselov, S. Roth and A. K. Geim, *Phys. Rev. Lett.* **97**, 187401 (2006).

14. D. Graf, F. Molitor, K. Ensslin, C. Stampfer, A. Jungen, C. Hierold and L. Wirtz, *Nano Lett.* **7**, 238 (2007).

15. J. B. Oostinga, H. B. Heersche, X. Liu, A. F. Morpurgo and L. M. K. Vandersypen, *Nat. Mater.* **7**, 151 (2007).

16. Y. Qi, L. G. Hector Jr., N. Ooi and J. B. Adams, *Surface Science* **581**, 155 (2005).

17. G. Ziovannetti, P. A. Khomyakov, G. Brocks, V. M. Karpan, J. van den Brink and P. J. Kelly, *Phys. Rev. Lett.* **101**, 026803 (2008).

18. P. A. Khomyakov, G. Giovannetti, P. C. Rusu, G. Brocks, J. Zan den Brink and P. J. Kelly, *Phys. Rev.* B **79**, 195425 (2009).

Chapter 12

Kondo Physics in Graphene

K. Sengupta

Department of Theoretical Physics,
Indian Association for the Cultivation of Sciences,
Jadavpur-700032, Kolkata, India

We review a part of the recent progress on Kondo physics in graphene stressing on the gate voltage induced crossover phenomenon. We also point out that a signature of the unconventional nature of this Kondo physics can be probed by STM experiments.

1. Introduction

Graphene, a two-dimensional single layer of graphite, has been recently fabricated by Novoselov *et. al.*[1] This has provided an unique opportunity for experimental observation of electronic properties of graphene which has attracted theoretical attention for several decades.[2] In graphene, the energy bands touch the Fermi energy at six discrete points at the edges of the hexagonal Brillouin zone. Out of these six Fermi points, only two are inequivalent; they are commonly referred to as K and K' points.[3,4] The quasiparticle excitations about these K and K' points obey linear Dirac-like energy dispersion. The presence of such Dirac-like quasiparticles is expected to lead to a number of unusual electronic properties in graphene including relativistic quantum Hall effect with unusual structure of Hall plateaus.[5] Recently, experimental observation of the unusual plateau structure of the Hall conductivity has confirmed this theoretical prediction.[6] Further, as suggested in in a recent work,[7] the presence of such quasiparticles in graphene provides us with an experimental test bed for Klein paradox,[8] and leads to novel Lorenz boost type phenomena.[9] Further, the normal metal-superconductor (NS) and normal metal-insulator-superconductor (NIS) junctions of graphene also exhibit unconventional

behavior of tunneling conductance.[10–13] In particular, it has been shown in Refs. 11, 12 that the subgap tunneling conductance of graphene NIS junctions, in contrast to its counterpart in conventional NIS junctions, is an oscillatory function of the barrier strength of the applied barrier strength. Similar unconventional oscillatory behavior was also observed in for critical current I_c in graphene Josephson tunnel junctions.[13,14]

An extremely interesting phenomenon in conventional metal systems is the Kondo effect which occurs in the presence of dilute concentration of localized quantum spins coupled to the spin-degenerate Fermi sea of metal electrons.[15] The impurity spin-electron interaction then results in perfect or partial screening of the impurity spin as one approaches zero temperature. It also results in a sharp 'Kondo Resonance' in electron spectral functions. Recent developments in quantum dots and nano devices have given new ways in which various theoretical results in Kondo physics, which are not easily testable otherwise, can be tested and confirmed experimentally.[16] Most of the early studies in Kondo effect were carried on for conventional metallic systems with constant density of states (DOS) at the Fermi surface.[17] Some studies on Kondo effect in possible flux phases,[18] nodal quasiparticles in d-wave superconductors,[19] Luttinger liquids,[20] and hexagonal Kondo lattice,[21] for which the DOS of the associated Fermions vanishes as some power law at the Fermi surface, has also been undertaken. Recently, there has been a interest in study of the physics of magnetic impurities in graphene.[23–27] The purpose of this article is to articulate a part of this recent progress.

2. Analysis of the Kondo Model

The crucial requirement for occurrence of Kondo effect is that the embedded impurities should retain their magnetic moment in the presence of conduction of electrons of graphene. We will not quantitatively address the problem of local moment formation in the presence of Dirac sea of electrons; this has been recently addressed in Ref. 27. A shown in Ref. 27, the large band width and small linearly vanishing density of states at the fermi level in graphene should make survival of impurity magnetic moment easier than in the conventional 3D metallic matrix. In fact, a detailed calculation shows that Cobalt atoms may lead to an effective moment of $\hbar$ or $\hbar/2$ when placed at the center of the graphene hexagon.[27] In the rest of this article, we shall therefore use the Kondo Hamiltonian[28] as our staring point.

Our analysis begins with the Hamiltonian for non-interacting Dirac electron in graphene. In the presence of a gate voltage V, the Hamiltonian can be expressed in terms of electron annihilation operators $\Psi_{A(B)\alpha}^s$ at sublattice $A(B)$ and Dirac point $s = K, K$ with spin $\alpha = \uparrow, \downarrow$ as

$$H = \int \frac{d^2k}{(2\pi)^2} \left(\Psi_{A\alpha}^{s\dagger}(\mathbf{k}), \Psi_{B\alpha}^{s\dagger}(\mathbf{k}) \right)$$
$$\times \begin{pmatrix} eV & \hbar v_F(k_x - i\mathrm{sgn}(s)k_y) \\ \hbar v_F(k_x + i\mathrm{sgn}(s)k_y) & eV \end{pmatrix} \begin{pmatrix} \Psi_{A\alpha}^s(\mathbf{k}) \\ \Psi_{B\alpha}^s(\mathbf{k}) \end{pmatrix} \quad (1)$$

where $\mathrm{sgn}(s) = 1(-1)$ for $s = K(K')$, v_F is the Fermi velocity of graphene, and all repeated indices are summed over. In Eq. (1) and in rest of the work, we shall use an upper momentum cutoff $k_c = \Lambda/(\hbar v_F)$, where $\Lambda \simeq 2\mathrm{eV}$ corresponds to energy up to which the linear Dirac dispersion is valid, for all momenta integrals.

Equation (1) can be easily diagonalized to obtain the eigenvalues and eigenfunctions of the Dirac electrons: $E_\pm = eV \pm \hbar v_F k$ where $\mathbf{k} = (k_x, k_y) = (k, \theta)$ denote momenta in graphene and

$$\left(u_A^{s\pm}, u_B^{s\pm} \right) = 1/\sqrt{2} \left(1, \pm \exp\left(i\mathrm{sgn}(s)\theta\right) \right). \quad (2)$$

Following Ref. 18, we now introduce the ξ fields, which represents low energy excitations with energies $E_\pm$, and write

$$\Psi_{A\alpha}^s(\mathbf{k}) = \sum_{j=\pm} u_A^{sj} \xi_{j\alpha}^s = 1/\sqrt{2}(\xi_{+\alpha}^s(\mathbf{k}) + \xi_{-\alpha}^s(\mathbf{k})),$$
$$\Psi_{B\alpha}^s(\mathbf{k}) = \exp(i\theta)/\sqrt{2}(\xi_{+\alpha}^s(\mathbf{k}) - \xi_{-\alpha}^s(\mathbf{k})). \quad (3)$$

In what follows, we shall consider a single impurity to be centered around $\mathbf{x} = 0$. Thus to obtain an expression for the coupling term between the local moment and the conduction electrons, we shall need to obtain an expression for $\Psi(\mathbf{x} = 0) \equiv \Psi(0)$. To this end, we expand the ξ fields in angular momentum channels

$$\xi_{+\alpha}^s(\mathbf{k}) = \sum_{m=-\infty}^{\infty} e^{im\theta} \xi_{+\alpha}^{ms}(k), \quad (4)$$

where we have written $\mathbf{k} = (k, \theta)$. Substituting Eq. (4) in Eq. (3), we obtain, after some straightforward algebra,

$$\Psi_{B\alpha}^s(0) = \frac{1}{\sqrt{2}} \int_0^{k_c} \frac{kdk}{2\pi} \left(\xi_{+\alpha}^{-\mathrm{sgn}(s)s}(k) - \xi_{-\alpha}^{-\mathrm{sgn}(s)s}(k) \right),$$
$$\Psi_{A\alpha}^s(0) = \frac{1}{\sqrt{2}} \int_0^{k_c} \frac{kdk}{2\pi} \left(\xi_{+\alpha}^{0s}(k) + \xi_{-\alpha}^{0s}(k) \right). \quad (5)$$

Note that $\Psi_B(0)$ receives contribution from $m = \pm 1$ channel while for $\Psi_A(0)$, the $m = 0$ channel contributes. The Kondo coupling of the electrons with the impurity spin is given by

$$H_K = \frac{g}{2k_c^2} \sum_{s=1}^{N_s} \sum_{l=1}^{N_f} \sum_{\alpha,\beta=1}^{N_c} \sum_{a=1}^{N_c^2-1} \Psi_{l\alpha}^{s\,\dagger}(0)\tau_{\alpha\beta}^a \Psi_{l\beta}^s(0)S^a, \qquad (6)$$

where g is the effective Kondo coupling for energy scales up to the cutoff Λ, **S** denotes the spin at the impurity site, τ are the generators of the SU(N_c) spin group, and we have now generalized the fermions, in the spirit of large N analysis, to have N_s flavors (valley indices) N_f colors (sublattice indices) and N_c spin. For realistic systems $N_f = N_c = N_s = 2$. Here we have chosen Kondo coupling g to be independent of sublattice and valley indices. This is not a necessary assumption. However, we shall avoid extension of our analysis to flavor and/or color dependent coupling term for simplicity. Also, the Dirac nature of the graphene conduction electrons necessitates the Kondo Hamiltonian to mix $m = \pm 1$ and $m = 0$ channels (Eqs. (5) and (6)). This is in complete contrast to the conventional Kondo systems where the Kondo coupling involves single angular momentum channel.

The kinetic energy of the Dirac electrons can also be expressed in terms of the ξ fields:

$$H_0 = \int_0^\infty \frac{kdk}{2\pi} \sum_{m=-\infty}^{\infty} \sum_{s,\alpha} \left(E_+(k)\xi_{+\alpha}^{ms\,\dagger}\xi_{+\alpha}^{ms} \right.$$
$$\left. + E_-(k)\xi_{-\alpha}^{ms\,\dagger}\xi_{-\alpha}^{ms} \right). \qquad (7)$$

Typically such a term involves all angular momenta channels. For our purpose here, it will be enough to consider the contribution from electrons in the $m = 0, \pm 1$ channels which contribute to scattering from the impurity (Eqs. (5) and (6)). To make further analytical progress, we now unfold the range of momenta k from $(0, \infty)$ to $(-\infty, \infty)$ by defining the fields $c_{1(2)\alpha}^s$

$$c_{1(2)\alpha}^s(k) = \sqrt{|k|}\xi_{+\alpha}^{0(-\mathrm{sgn}(s))s}(|k|), \quad k > 0,$$
$$c_{1(2)\alpha}^s(k) = +(-)\sqrt{|k|}\xi_{-\alpha}^{0(-\mathrm{sgn}(s))s}(|k|), \quad k < 0, \qquad (8)$$

so that one can express the Ψ fields as $\Psi_{A(B)\alpha}^s(0) = \int_{-\infty}^{\infty} \frac{dk}{2\pi} \sqrt{|k|}c_{1(2)\alpha}^s(k)$. In terms of the $c_{1(2)\alpha}^s$ fields, the kinetic energy (in the $m = 0, \pm 1$ channels)

and the Kondo terms in the Hamiltonian can therefore be written as

$$H_0 = \int_{-k_c}^{k_c} dk/(2\pi) E_k c_{l\alpha}^{s\,\dagger} c_{l\alpha}^s$$

$$H_K = g/(8\pi^2 k_c^2) \int_{-k_c}^{k_c} \int_{-k_c}^{k_c} \sqrt{|k|}\sqrt{|k'|} dk dk'$$

$$\times \left(c_{l\alpha}^{s\,\dagger}(k) \, \tau_{\alpha\beta}^a \, c_{l\beta}^s(k') \, S^a \right), \tag{9}$$

where $E_k = eV + \hbar v_F k$ and summation over all repeated indices are assumed.

Next we follow standard procedure[29] of representing the local spin by $SU(N_c)$Fermionic fields f_α and write the partition function of the system in terms of the f and c fields

$$Z = \int \mathcal{D}c\mathcal{D}c^\dagger \mathcal{D}f \mathcal{D}f^\dagger \mathcal{D}\epsilon \, e^{-S/\hbar}, \quad S = S_0 + S_1 + S_2$$

$$S_0 = \int_0^{\beta\hbar} d\tau \int_{-k_c}^{k_c} dk/(2\pi) \left(c_{l\alpha}^{s\,\dagger}(k,\tau) G_0^{-1} c_{l\alpha}^s(k,\tau) \right),$$

$$S_1 = J/(4\pi^2 N_c k_c^2) \int_0^{\beta\hbar} d\tau \int_{-k_c}^{k_c} \int_{-k_c}^{k_c} \sqrt{|k|}\sqrt{|k'|} dk dk'$$

$$\times \left[c_{l\alpha}^{s\,\dagger}(k,\tau) \, \tau_{\alpha\beta}^a \, c_{l\beta}^s(k',\tau) f_\gamma^\dagger(\tau) \tau_{\gamma\delta}^a f_\delta(\tau) \right]$$

$$S_2 = \int_0^{\beta\hbar} d\tau \left[\left(f_\alpha^\dagger(\tau) \left[\hbar\partial_\tau + \epsilon(\tau) \right] f_\alpha(\tau) \right) - \epsilon(\tau)Q \right], \tag{10}$$

where $G_0^{-1} = \hbar\partial_\tau + E_k$ is the propagator for c fields, $J = gN_c/2$ is the renormalized Kondo coupling, we have imposed the impurity site occupancy constraint

$$\sum_\alpha f_\alpha^\dagger f_\alpha = Q \tag{11}$$

using a Lagrange multiplier field $\epsilon(\tau)$.

We now use the identity[29]

$$\tau_{\alpha\beta}^a \tau_{\gamma\delta}^a = N_c \delta_{\alpha\delta}\delta_{\beta\gamma} - \delta_{\alpha\beta}\delta_{\gamma\delta} \tag{12}$$

and decouple S_1 using a Hubbard-Stratonovitch field ϕ_l^s. In the large N_c limit one has $S = S_0 + S_2 + S_3 + S_4$, where

$$S_3 = \int_0^{\beta\hbar} d\tau \int_{-k_c}^{k_c} \frac{\sqrt{|k|} dk}{(2\pi)} \left(\phi_l^{*\,s}(\tau) c_{l\alpha}^{s\,\dagger}(k,\tau) f_\alpha(\tau) + \text{h.c} \right)$$

$$S_4 = N_c k_c^2/J \int_0^{\beta\hbar} d\tau \phi_l^{*\,s}(\tau) \phi_l^s(\tau). \tag{13}$$

Note that at the saddle point level $\langle \phi_l^s \rangle \sim \left\langle \sum_\alpha c_{l\alpha}^{s\,\dagger} f_\alpha \right\rangle$ so that a non-zero value of ϕ_l^s indicates the Kondo phase. In what follows, we are going to look for the static saddle point solution with $\phi_l^s(\tau) \equiv \phi_0$ and $\epsilon(\tau) \equiv \epsilon_0$.[29] In this case, it is easy to integrate out the c and f fields, and obtain an effective action in terms of ϕ_0 and ϵ_0 and one gets $S' = S_5 + S_6$ with

$$S_5 = -\beta\hbar N_c \mathrm{Tr}\left[\ln\left(i\hbar\omega_n - \epsilon_0 - N_s N_f \phi_0^* G_0'(i\omega, V)\phi_0\right)\right],$$
$$S_6 = \beta\hbar\left(N_s N_c N_f k_c^2 |\phi_0|^2 / J - \epsilon_0 Q\right), \tag{14}$$

where Tr denotes Matsubara frequency sum as well as trace over all matrices and the Fermion Green function $G_0'(ip_n, q) \equiv G_0'$ is given by[18]

$$G_0' = \frac{-\Lambda}{2\pi(\hbar v_F)^2}(ip_n - q)\ln\left[1/|ip_n - q|^2\right], \tag{15}$$

where, in the last line we have switched to dimensionless variables $p_n = \hbar\omega_n/\Lambda$ and $q = eV/\Lambda$.

One can now obtain the saddle point equations from Eq. (14) which are given by $\delta S'/\delta\phi_0 = 0$ and $\delta S'/\delta\epsilon_0 = 0$. Using Eqs. (14) and (15), one gets (after continuing to real frequencies and for $T = 0$)

$$1/J = -\Lambda/(\pi\hbar v_F k_c^2)^2 \int_{-1}^0 dp\, G_0(p - \nu - \Delta_0 G_0/2)^{-1},$$
$$Q/N_c = 1/(2\pi)\int_{-1}^0 dp\, \nu(p - \nu - \Delta_0 G_0/2)^{-1}, \tag{16}$$

where we have defined the dimensionless variable $\Delta_0 = N_f N_s |\phi_0|^2/(\pi\hbar^2 v_F^2)$, $p = \hbar\omega/\Lambda$, $G_0 = 2\pi(\hbar v_F)^2 G_0'/\Lambda$, $\nu = \epsilon_0/\Lambda \geq 0$, and have used the energy cutoff Λ for all frequency integrals. At the critical value of the coupling strength, putting $\nu = 0$ and $\Delta_0 = 0$, we finally obtain the expression for $J_c(q, T)$

$$J_c(q, T) = J_c(0)\left[1 - 2q\ln\left(1/q^2\right)\ln\left(k_B T/\Lambda\right)\right]^{-1} \tag{17}$$

where the temperature $k_B T$ is the infrared cutoff, $J_c(0) = (\pi\hbar v_F k_c^2)^2/\Lambda = \pi^2\Lambda$ is the critical coupling in the absence of the gate voltage, and we have omitted all subleading non-divergent term which are not important for our purpose. For $V = 0 = q$, we thus have, analogous to the Kondo effect in flux phase systems,[18] a finite critical Kondo coupling $J_c(0) = \pi^2\Lambda \simeq 20\mathrm{eV}$ which is a consequence of vanishing density of states at the Fermi energy for Dirac electrons in graphene. Of course, the mean-field theory overestimates J_c. A quantitatively accurate estimate of J_c requires a more sophisticated analysis which we have not attempted here.

The presence of a gate voltage leads to a Fermi surface and consequently $J_c(q, T) \to 0$ as $T \to 0$. For a given experimental coupling $J < J_c(0)$ and temperature T, one can tune the gate voltage to enter a Kondo phase. The temperature $T^*(q)$ below which the system enters the Kondo phase for a physical coupling J can be obtained using $J_c(q, T^*) = J$ which yields

$$k_B T^* = \Lambda \exp\left[(1 - J_c(0)/J)/(2q \ln[1/q^2])\right] \qquad (18)$$

For a typical $J \simeq 2$eV and voltage $eV \simeq 0.5$eV, $T^* \simeq 35$K.[30] We stress that even with overestimated J_c, physically reasonable J leads to experimentally achievable T^* for a wide range of experimentally tunable gate voltages.

Next, we discuss the possible ground state in the Kondo phase. In the absence of the gate voltage a finite J_c implies that the ground state will be non-Fermi liquid as also noted in Ref. 18 for flux phase systems. In view of the large J_c estimated above, it might be hard to realize such a state in undoped graphene. However, in the presence of the gate voltage, if the impurity atom generates a spin half moment and the Kondo coupling is independent of the valley(flavor) index, we shall have a realization of two-channel Kondo effect in graphene owing to the valley degeneracy of the Dirac electrons. This would again lead to overscreening and thus a non Fermi-liquid like ground state.[17] The study of details of such a ground state necessitates an analysis beyond our large N mean-field theory. To our knowledge, such an analysis has not been undertaken for Kondo systems with angular momentum mixing. In this work, we shall be content with pointing out the possibility of such a multichannel Kondo effect in graphene and leave a more detailed analysis as an open problem for future work.

The role of the scattering of graphene electrons from the impurity needs to be analyzed in details for the above assertion of two channel Kondo phenomenon. At first glance it seems that it would be impossible to achieve this phenomenon in graphene since large momenta scattering from point-like impurities will necessarily lead to channel mixing. However, it has been recently shown that when the impurity resides at the center of the graphene this does not happen.[25] To understand this phenomenon qualitatively, let us consider an impurity at the center of the graphene hexagon with short-range potential. Then the contribution to the scattering amplitude of this electrons from this impurity is given by $S \sim \sum_{\vec{r}} V(\vec{r}) \psi_G^\dagger(\vec{r}) \psi_G(\vec{r})$, where $V(r)$ is a short range potential and $\psi(\vec{r})$ denotes the wavefunction of the graphene electrons, and the sum over $\vec{r}$ can be thought as sum over graphene lattice point due to the short spread of the p_z orbital wavefunctions in the graphene plane.[25] Thus the major contribution to the scattering comes

from the sum of graphene wavefunctions over the six surrounding sites around the impurity. In graphene, as shown in Ref. 25, the sums of these wavefunctions at momenta K or K' vanish; consequently the scattering from K to K' is negligibly small. This destructive interference phenomenon, together with the finite size of the impurity, makes two-channel Kondo physics in graphene a distinct possibility.

3. Experiments

Next, we discuss experimental observability of the Kondo phenomena in graphene. The main problem in this respect is creation of local moment in graphene. There are several routes to solving this problem. First, substitution of a carbon atom by a transition metal atom. This might in principle frustrate the strong sp^2 bonding and thus locally disturb the integrity of graphene atomic net. However, nature has found imaginative ways of incorporating transition metal atoms in p-π bonded planar molecular systems such as porphyrin.[31] Similar transition metal atom incorporation in extended graphene, with the help of suitable bridging atoms, might be possible. Second, one can try chemisorption of transition metal atoms such as Fe on graphene surface through sp-d hybridization in a similar way as in intercalated graphite.[32] Third, it might be possible to chemically bond molecules or free radicals with magnetic moment on graphene surface as recently done with cobalt pthalocyanene (CoPc) molecule on AU(111) surface.[33] This might result in a strong coupling between graphene and impurity atom leading to high Kondo temperatures as seen for CoPc on AU(111) surface ($T_K \simeq 280K$). Fourth, recently ferromagnetic cobalt atom clusters with sub nano-meter size, deposited on carbon nanotube, have exhibited Kondo resonance.[34] Similar clusters deposition in graphene might be a good candidate for realization of Kondo systems in graphene. Finally, from quantum chemistry arguments, a carbon vacancy, or substitution of a carbon atom by a boron or nitrogen might lead to a spin-half local moment formation. In particular, it has been shown that generation of local defects by proton irradiation can create local moments in graphite.[35] Similar irradiation technique may also work for graphene.

For spin one local moments and in the presence of sufficiently large voltage and low temperature, one can have a conventional Kondo effect in graphene. The Kondo temperature for this can be easily estimated using $k_B T_K \sim D \exp(-1/\rho J)$ where the band cutoff $D \simeq 10$eV, $J \simeq 2-3$eV and DOS per site in graphene $\rho \simeq 1/20$ per eV. This yield $T_K \simeq 6-150$K. The

estimated value of T_K has rather large variation due to exponential dependence on J. However, we note that Kondo effect due to Cobalt nano-particle in graphitic systems such as carbon nanotube leads to a high $T_K \approx 50K$ which means that a large J may not be uncommon in these systems. Recent STM experiments seems to suggest a Kondo temperature of $T \simeq 17K$ for Cobalt doped graphene.[37] We note that this experiment also shows a $\sqrt{V}$ behavior for the tunneling conductance $G(V)$ over a range of the applied voltage V from the experimental temperature T to the Kondo temperature T_K confirming the two-channel Kondo behavior in graphene.

4. Conclusion

In conclusion, we have pointed out that Kondo effect in graphene is unconventional and can be tuned by a gate voltage. Kondo effect of such unconventional nature, where the different angular momentum channels mix, has previously been theoretically predicted for possible flux phases in cuprates.[18] However, such phases have not been experimentally verified till date in cuprates. Therefore graphene might provide the first example of experimental realization of such Kondo physics. Moreover, we have also shown that it may also be possible to realize non-Fermi liquid ground states in graphene via multichannel Kondo effect. A detailed study of such ground states and properties of several physical quantities associated with them is left as a subject of future research.

References

1. K. S. Novoselov, A. K. Geim, S. V. Morozov, D. Jiang, Y. Zhang, S. V. Dubonos, I. V. Grigorieva, and A. A. Firsov, *Science,* **306**, *666 (2004).*
2. P. R. Wallace, *Phys. Rev.* **71**, *622 (1947).*
3. T. Ando, *J. Phys. Soc. Jpn.* **74**, *777 (2005).*
4. A. H. Castro Neto, F. Guinea, N. M. R. Peres, K. S. Novoselov, and A. K. Geim, *Rev. Mod. Phys.* **81**, *109 (2009).*
5. V. P. Gusynin and S. G. Sharapov, *Phys. Rev. Lett.* **95**, *146801 (2005)*; N. M. R. Peres, F. Guinea, and A. Castro Neto, *Phys. Rev, B* **73**, *125411 (2006).*
6. K. S. Novoselov, A. K. Geim, S. V. Morozov, D. Jiang, M. I. Katsnelson, I. V. Grigorieva, S. V. Dubonos, and A. A. Firsov *Nature (London)* **438**, *197 (2005)*; Yuanbo Zhang, Yan-Wen, Tan Horst, L. Stormer, and Philip Kim *Nature* **438**, *201 (2005)*; K. S. Novoselov, E. McCann, S. V. Morozov, V. I. Fal'ko, M. I. Katsnelson, U. Zeitler, D. Jiang, F. Schedin, and A. K. Geim. *Nat. Phys.* **2**, *177 (2006).*
7. M. I. Katsnelson, K. S. Novoselov, and A. K. Geim, *Nat. Phys.* **2**, *620 (2006).*

8. O. Klein, *Z. Phys.* **53***, 157 (1929).*

9. V. Lukose, R. Shankar, and G. Baskaran, *Phys. Rev. Lett.* **98***, 116802 (2007).*

10. C. W. J. Beenakker, *Phys. Rev. Lett.* **97***, 067007 (2006)*; M. Titov and C. W. J. Beenakker, *Phys. Rev. B* **74***, 041401(R) (2006).*

11. S. Bhattacharjee and K. Sengupta, *Phys. Rev. Lett.* **97***, 217001 (2006).*

12. S. Bhattacharjee, M. Maiti, and K. Sengupta, *Phys. Rev. B* **76***, 184514 (2007).*

13. C. W. J. Beenakker, *Rev. Mod. Phys.* **80***, 1337 (2008).*

14. M. Maiti and K. Sengupta, *Phys. Rev. B* **76***, 054513 (2007).*

15. See for example A. C. Hewson, *The Kondo Problem to Heavy Fermions*, Cambridge University Press (1993).

16. M. Pustilnik and L. Glazman, *J. Phys.: Condens. Matter* **16***, R 513 (2004).*

17. For a review see I. Affleck, *Acta Phys. Polon.* **B26***, 1869 (1995); cond-mat/9512099.*

18. C. R. Cassanello and E. Fradkin, *Phys. Rev. B* **53***, 15079 (1996)*; D. Withoff and E. Fradkin, *Phys. Rev. Lett.* **64***, 1835 (1990)*; K. Insergent, *Phys. Rev. B* **54***, 11936 (1996).*

19. A. Polkovnikov, S. Sachdev, and M. Vojta, *Phys. Rev. Lett.* **86***, 296 (2001).*

20. A. Furusaki and N. Nagaosa, *Phys. Rev. Lett.* **72***, 892 (1994).*

21. S. Saremi and P. A. Lee, *cond-mat/0610273 (unpublished).*

22. C. Bena and S. Kivelson, *Phys. Rev. B* **72***, 125432 (2005);* T. O. Wehling *et al.*, *cond-mat/0609503 (unpublished).*

23. K. Sengupta and G. Baskaran, *Phys. Rev. B* **77***, 045417 (2008).*

24. M. Hentschel and F. Guinea, *Phys. Rev. B* **76***, 115407 (2007).*

25. K. Saha, I. Paul, and K. Sengupta, *Phys. Rev. B* **81***, 165446 (2010).*

26. B. Uchoa *et al.*, *Phys. Rev. Lett.* **103***, 206804 (2009).*

27. T. Wehling *et al.*, *arXiv:0907.1111 (unpublished).*

28. J. Kondo, *Prog. Theor. Phys.* **32***, 37 (1964).*

29. N. Read and C. J. Newns, *J. Phys. C* **16***, 3273 (1983).*

30. Note that J in our analysis is an effective coupling valid below the scale Λ *i.e.* $J > J_{\text{bare}}$. This might further enhance T^*.

31. *Porphyrin Hand Book*, Eds. K. M. Kadish, K. M. Smith, and R. Guilard (Academic Press, New York) 1999.

32. M. E. Vol'pin and Yu. N. Novikov, *Pure and Appl. Chem., vol.* **60***, No. 8, 1133 (1988).*

33. A. Zhao *et al.*, *Science* **309***, 1542 (2005).*

34. T. W. Odom *et al.*, *Science* **290***, 1459 (2000).*

35. P. O. Lehtinen *et al.*, *Phys. Rev. Lett.* **93***, 187202 (2004).*

36. T. O. Wehling *et al.*, *cond-mat/0703390 (unpublished);* S. Adam, S. Das Sarma, and A. K. Geim, *cond-mat/0610834 (unpublished).*

37. L. Mattos *et al.*, (private communications).

Chapter 13

Noise in Graphene Transistors

Atindra Nath Pal[*] and Arindam Ghosh[†]

*Department of Physics, Indian Institute of Science,
Bangalore 560 012, India*
[*]*atin@physics.iisc.ernet.in*
[†]*arindam@physics.iisc.ernet.in*

Graphene, single atomic layer of hexagonal carbon atoms, has drawn
a lot of interest because of its unusual electronic properties. As an
emerging new material, an investigation of the effect of time dependent
disorder of graphene devices is hence necessary for both application and
fundamental understanding. Here, we present a systematic study of low-
frequency noise in graphene-based field-effect transistors with varying
number of layers. In single-layer devices, the noise magnitude decreases
with increasing carrier density, which behaved oppositely in the devices
with two or larger number of layers. We have developed a theoretical
model of noise based on a correlated number and mobility fluctuations
due to the underlying traps inside SiO_2 substrate. We show that the
variation of noise with carrier density is opposite for linear and parabolic
band structure, and hence can act as a sensitive transport-based tool to
separate single layer graphene from others.

1. Introduction

Graphene, a single sheet of carbon atoms, has become a potential candidate
for future electronics.[1–6] It is the thinnest available material in the world
and the strongest[7] ever measured. Its charge carriers have the zero effective
mass and can travel micrometer-long distances without scattering at room
temperature. Carrier mobilities as high as 1×10^4 cm^2/Vs are now obtained
on SiO_2 substrate,[8] which is considerably enhanced (2×10^5 cm^2/Vs) in
suspended graphene.[9–11] Graphene can sustain 2 orders higher current
densities than copper,[12] shows record thermal conductivity[13] and stiff-
ness. Electron transport in graphene is described by a Dirac-like equation,

which allows the investigation of relativistic quantum phenomena in a table-top experiment. In particular, extensive research on single layer graphene (SLG) and bilayer graphene (BLG) has led to significant improvement in both material properties, as well as fundamental understanding, for nanoelectronic applications. Recently, BLG has also emerged as a promising material in nanoelectronics[14] because of its ability to control the energy gap between valence and conduction bands through external means.[2,4–6,15,16] In contrast, however, the behavior of few-layer graphene (FLG) devices with three or more atomics layers remains relatively unexplored.

Graphene was first isolated[1] by mechanical exfoliation of layered graphite using a scotch tape. Although delicate and time consuming, this simple technique provides crystals of high structural and electronic quality. The alternative route is to grow graphene epitaxially on top of silicon carbide. Several chemical methods, such as those involving reduction of graphite oxide,[18,19] ultrasonic cleavage of intercalated graphite[20] are available to make graphene and graphene based composite materials in large scale. Recently, large area single crystals of graphene have been grown on Ni,[21,22] Cu[23] and iridium(Ir),[24] and can be put on top of any substrate like plastic or Si wafers also,[25,26] which has opened a new possibility for flexible electronics. The ease of processing can make graphene applicable to many other fields other than electronics, especially in sensors[27] and photovoltaic.[28,29]

The most explored aspect of graphene physics is its electronic properties. The linear Dirac-like electronic spectrum has made graphene a unique condensed matter system. The most direct consequence of Dirac fermion is the half-integer quantum hall effect,[8,30] which has been well explained using relativistic quantum mechanics. Due to the massless carriers and little scattering, quantum effects in graphene are robust and can survive even at room T.[31] Based on the quantum electrodynamics study, already there are several predictions of such phenomena as Klein tunneling, zitterbewegung, the Schwinger production,[32] supercritical atomic collapse[33] and Casimir-like interactions between adsorbates on graphene.[34] As for experiment, only the Klein tunneling has been verified in sufficient detail.[35,36] However, for graphene on SiO_2, scattering of electrons by optical phonons of the substrate and the formation of electron-hole puddles limit the mobility to $40,000$ $cm^2V^{-1}s^{-1}$,[37] which limits graphene to observe the above such predictions. By removing the substrate, graphene mobility has increased to several orders of magnitude, which makes the Dirac-physics more accessible to us. This has led to the observation of fractional quantum hall effect

(FQHE) in graphene[38,39] and new broken symmetry phase at $n = 0$ Landau level in case of bilayer graphene.[40] Although, there are several emerging phenomena, some basic questions about graphene's electronic properties need to be addressed. For example, there is no clear understanding about the scattering mechanism, which limits the mobility, and very little understanding about transport properties near n=0 Landau level.[41]

One of the important parameter that needs better understanding is the source of disorder. There are three sources of disorder that are often discussed in the literature: (1) Intrinsic lattice imperfection and defects, such as dislocations, point vacancies etc., (2) Rippling of graphene[42] when it is supported by an underlying substrate, which also creates local curvature,[43] and hence fluctuation in local chemical potential and effective gauge fields.[2] Both intrinsic ripples and extrinsic roughness of surface have been considered. Finally, (3) a major source of disorder arises from the Coulomb potential from the trapped charges buried in the oxide substrate (the adsorbed atom on the graphene surface, such as the water molecules, have also been shown to have adverse effects on its mobility).

The conventional time-averaged transport measurements seem to be inadequate in understanding the effect of disorder in graphene transistors. Being directly sensitive to the ability of an electronic device to screen external potential fluctuations, the low frequency noise in electrical transport has recently been shown to reflect the low-energy band structure in single and BLG devices.[44,45] The noise in both cases was found to originate primarily from the fluctuating charge traps inside the SiO_2 substrate, similar to carbon nanotube field effect devices.[46] Also, the dependence of noise magnitude on the gate electric field was found to be opposite for single and BLG, and was attributed to a field-induced gap formation in the latter. Noise experiments on multilayer graphene[47] also shows the similar gate voltage dependence like bilayer graphene, which ensure that the bandgap is not the only reason for the increase in noise with gate voltage.

Here, we propose an analytical model of noise which is based on the number and correlated mobility fluctuation model described earlier. Then we show a systematic study of low-frequency noise measurements in four categories of graphene devices: single layer graphene (SLG), BLG, FLG with three to five atomic layers, and many-layer graphene (MLG) with greater than five layers in the device. The gate voltage dependence of noise in all kind of graphene devices seem to be consisting with our proposed model. For BLG,[45] we have used double gated FET devices to tune the zero gap and charge neutrality points independently, which offers a unique

mechanism to investigate the low-energy band structure, charge localization and screening properties of bilayer graphene.
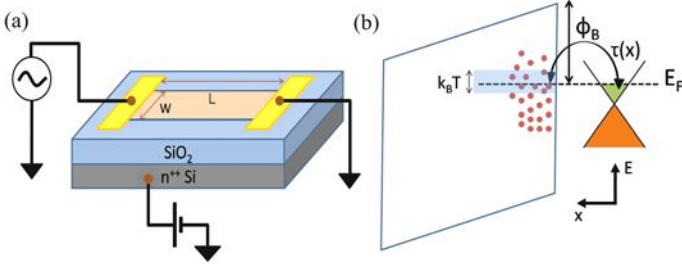
Fig. 1. (a) Schematic of graphene-transistor consisting of channel dimension WL. (b) Schematic diagram of energy scale description of trapping-detrapping event where the tunneling of carriers occurs mainly due to the trap states near the quasi-Fermi level of graphene. ϕ_B is the height of tunneling barrier, the distance between the graphene Fermi level and SiO_2 conduction band edge and $\tau(x)$ is the time constant associated with the trapping event at a distance x from the graphene-SiO_2 interface.

2. The Correlated Number and Mobility Fluctuation Model

Oxide traps located at the SiO_2 and 2D electron interface are responsible for low frequency noise in conventional MOSFETs. Among various models proposed to explain $1/f$ noise behaviors in MOS transistors, two most popular models are the number fluctuation and mobility fluctuation model. The number fluctuation model, originally proposed by McWhorter,[48] arises due to the tunneling transition between the oxide traps and MOSFET channel. The other model is the mobility fluctuation model, based on Hooge's empirical relationship[49] to fit the noise data for homogeneous semiconductor and devices.

Due to the underlying similarity in device layout and operating principle, we consider that noise in graphene-FET originates from both number and mobility fluctuations.[50] The number fluctuations are caused by the tunneling of carriers to and from the interfacial oxide traps, while the Coulomb scattering from the occupied oxide taps gives rise to the mobility fluctuation in graphene channel.

Figure 1 shows the schematic of a graphene device consisting of channel of dimension WL. For a carrier density of n, Drude conductivity $\sigma = ne\mu = \mu Q_n$, where total charge density $Q_n = en$. Hence the change in σ

for infinitesimal changes in μ and σ can be written as,

$$\frac{\delta\sigma}{\sigma} = \frac{\delta\mu}{\mu} + \frac{\delta Q_n}{Q_n} \tag{1}$$

For sufficiently large oxide thickness, $|\delta Q_n| = |\delta Q_T|$, where δQ_T is the change in trapped charge.

To calculate the contribution from number fluctuations, let's take a volume element ΔV and energy element ΔE inside the SiO$_2$ such that the trapping events inside $\Delta V \Delta E$ can be characterized by a single time constant τ_T. We assume that the fluctuations come from the traps situated a few $k_B T$ above or below the quasi-Fermi level of graphene. The power spectral density of the fluctuation arising from $\Delta V \Delta E$ is found by taking the Fourier transform of the autocorrelation of $\delta n_{\Delta V \Delta E}$, given by

$$S_{n\Delta V \Delta E} = \frac{\tau_T}{1 + \omega^2 \tau_T^2} n_{tr}(x, E) f_T (1 - f_T) \Delta V \Delta E \tag{2}$$

where n_{tr} is the trap density of states per unit volume times energy, ω is the frequency expressed in radians, f_T is the probability of a trap being filled.

In our model, we assume that the Coulomb potential due to a trapped charge will also give rise to the fluctuation in mobility. Using Mathiessen's rule[51] we can write

$$\frac{1}{\mu} = \frac{1}{\mu_{avg}} + \frac{1}{\mu_T} \tag{3}$$

where μ is the instantaneous mobility, μ_{avg} is the time averaged mobility, from all static scattering mechanism. The term μ_T^{-1} arises from the Coulomb scattering off the trapped charge that fluctuates between the oxide and graphene. Consider a channel element $\Delta y \Delta z$, where we concentrate on the fluctuation in number and mobility of the graphene channel due to the fluctuation of trap charges in $\Delta V \Delta E$ inside SiO$_2$. So

$$\frac{1}{\mu_T} = \Sigma(x) \left(\frac{\delta Q_n \Delta y \Delta z}{WL} \right) \tag{4}$$

where $\Sigma(x)$ is related to the scattering rate entirely due to the Coulomb potential of the trapped charge located inside the substrate at a distance x from graphene.

Simple mathematical calculations show that power spectral density in the source-drain current consists of three terms

$$S_V = S_{V1} + S_{V2} + S_{V3} \tag{5}$$

where

$$S_{V1} = \frac{V_{DS}^2 e^2}{(WL)Q_n^2} \int\limits_{x1}^{x2} \int\limits_{E1}^{E2} \frac{n_{tr}(x,E)\tau_T(x)}{1+\omega^2\tau_T^2(x)} f_T(E)(1-f_T(E))dxdE \qquad (6)$$

$$S_{V2} = \frac{V_{DS}^2 e^2}{(WL)Q_n} \int\limits_{x1}^{x2} \int\limits_{E1}^{E2} 2\mu_{avg}\Sigma(x)\frac{n_{tr}(x,E)\tau_T(x)}{1+\omega^2\tau_T^2(x)} f_T(E)(1-f_T(E))dxdE$$

$$(7)$$

$$S_{V3} = \frac{V_{DS}^2 e^2}{(WL)} \int\limits_{x1}^{x2} \int\limits_{E1}^{E2} \mu_{avg}^2\Sigma^2(x)\frac{n_{tr}(x,E)\tau_T(x)}{1+\omega^2\tau_T^2(x)} f_T(E)(1-f_T(E))dxdE \quad (8)$$

The first term arises entirely due to number fluctuation, the second term describes the joint effect of both number and mobility fluctuation, and the final term represents the mobility fluctuation alone.

Number fluctuation: For a uniform trap distribution, the integral over E of $n_{tr}f_T(E)(1-f_T(E))$ is approximately $k_B T n_{tr}(E_F)$. The limits $x1$ and $x2$ are such that all the traps are taken into account, in our experimental frequency range. The first term can be calculated by integrating over τ as

$$S_{V1} = \frac{V_{DS}^2 e^2}{(WL)Q_n^2 \alpha} n_T(E_F)\frac{1}{f}(\frac{V^2}{Hz}) \qquad (9)$$

Using typical values of $n_{tr}(E_F)$, we get $S_{V1}/V_{DS}^2 \sim 10^{-30}/Hz$, which is far lower compared to the experimental values obtained in recent experiments. Moreover, $S_{V1} \propto 1/n^2$, irrespective of the number of graphene layers in the device. However, in recent noise experiments in graphene it has been observed that the conductivity noise magnitude in single and multilayer device behaves oppositely with gate voltage. In case of SLG devices the noise magnitude goes down with increasing carrier density, while it increases in case of multilayer devices. These inconsistencies indicate that the number fluctuations to be only of minor importance in graphene.

Mobility fluctuation: Calculating the integral exactly in (8) is not straightforward. From (8), we find the mobility fluctuation term mainly depends on average mobility μ_{avg} and Σ. Hence,

$$\frac{S_{V3}}{V_{DS}^2} \sim \Sigma^2\mu_{avg}^2 \qquad (10)$$

To get the density dependence of S_{V3} we should calculate the density dependence of Σ and μ_{avg}. Within the semiclassical model of conductivity $\Sigma(x)$ can be expressed as

$$\Sigma(x) = \frac{\pi}{e} \frac{n}{k_F v_F} \left(\frac{\hbar}{\tau_C}\right) \frac{1}{n_{imp}} \qquad (11)$$

where τ_c as the scattering time arising due to the Coulomb scattering only and we have taken $\delta Q \sim n_{imp}$, the density of charge impurities trapped at the SiO_2 interface. Using the expressions for the scattering rates, calculated for both single[52,53] and bilayer/multilayer graphene[54] for Coulomb scattering, it can be shown from (9) that $\Sigma(x)$ is independent of density for both single and multilayer graphene.[55] Hence, the density dependence of noise only arises due to that of μ_{avg} only. The important fact is that the average mobility of graphene transistors comes from all scattering mechanisms, whereas only Coulomb scattering is responsible for the mobility fluctuations. So one can extract the dependence of μ_{avg} from the density dependence of the Drude conductivity $\sigma = ne\mu_{avg}$. We focus on the most relevant experimental situation, where $q_{TF}/2k_F > 1$. Recently,[52–54] the density dependence of σ has been calculated within Thomas-Fermi approximation for both single and bilayer/multilayer graphene for all possible scattering mechanisms. In Table 1, a comparison of density dependence of σ for various scattering mechanisms has been summarized.

Table 1. Dependence of σ for various scattering mechanisms in experimentally relevant situation where $q_{TF}/2k_F > 1$.

	SLG	BLG/MLG
Bare Coulomb Scattering	$\sigma \sim n$	$\sigma \sim n^2$
Screened Coulomb	$\sigma \sim n$	$\sigma \sim n$
Short-range scattering	$\sigma \sim n^0$	$\sigma \sim n$

Using Table 1, one can write $\mu_{avg} \sim n^\beta$, where $-1 < \beta < 0$ for SLG and $0 < \beta < 1$ for BLG and MLG. Hence, the contribution from mobility fluctuations $S_{V3}/V_{DS}^2 \sim n^{2\beta}$, which predicts that in case of SLG the noise magnitude always decreases with density, whereas, for BLG, the noise power spectral density increases with increasing density. This opposite behavior is a direct consequence of the band structures. In case of multilayer graphene we expect noise to behave in the same way as BLG because of their similar parabolic band structure. Noise can form an excellent probe to detect SLG from other forms of graphene.

3. Experimental Section

3.1. *Sample preparation and characterization*
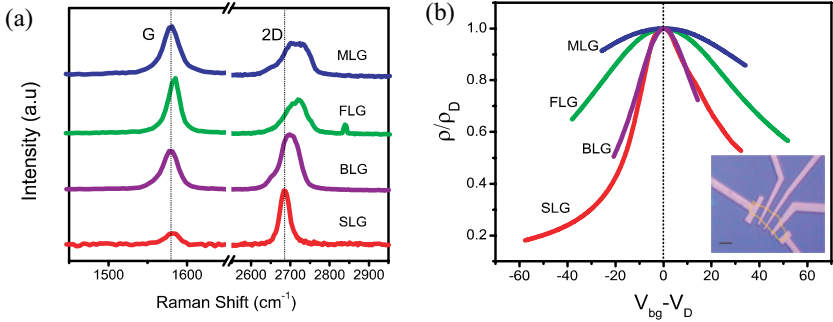
Fig. 2. (a) Raman spectra for SLG, BLG, FLG, and MLG showing the characteristic G and 2D peaks (b) Gate voltage characteristics of graphene devices: for comparison, the ratio of resistivity (ρ) and the resistivity at the CNP (ρ_D) are plotted as a function of ($V_{bg} - V_D$) at T = 100 K. The inset shows the optical micrograph and outline of a typical graphene device. The scale bar is 5μm.

Graphene flakes were prepared on 300 nm SiO_2 on n^{++} doped silicon substrate (the backgate) by micromechanical exfoliation of highly oriented pyrolytic graphite (HOPG). All flakes were characterized by Raman spectroscopy,[56] and subsequent atomic force microscopy indicated the FLG and MLG devices in the present case to consist of $3-4$ and ~ 14 layers, respectively. 40 nm gold (99.99%) contacts were defined using standard electron beam lithography technique. To keep the disorder level comparable, we have cleaned the Si/SiO$_2$ substrates in standard RCA solution (1:1:5 solution of NH$_4$OH (ammonium hydroxide) + H$_2$O$_2$ (hydrogen peroxide) + H$_2$O (water) at 75 or 80 ^{0}C) followed by acetone and isopropyl alcohol prior to the graphene deposition. Figure 2(a) shows the characteristic Raman spectra for different graphene flakes where the intensity ratio of the G peak to the 2D peak can be seen to increase with increasing layer number. Figure 2(b) shows the gate voltage characteristics of the devices. In all the cases, charge neutrality point (CNP) was shifted to a finite gate voltage due to the intrinsic doping (see Fig. 3 also), primarily arising from the impurities inside the SiO$_2$. Hence in order to compare the influence of gating we have plotted the ratio of resistivity to that at the CNP as a function of

$(V_{bg} - V_D)$, where V_D is the backgate voltage at CNP. Figure 2(b) clearly demonstrates the ambipolar transistor action in all devices, although the effect of gating decreases with increasing layer numbers. Mobility of SLG, BLG, FLG, and MLG devices was calculated to be $1100, 1160, 2450$, and 1200 cm^2 V^{-1} s^{-1} respectively.
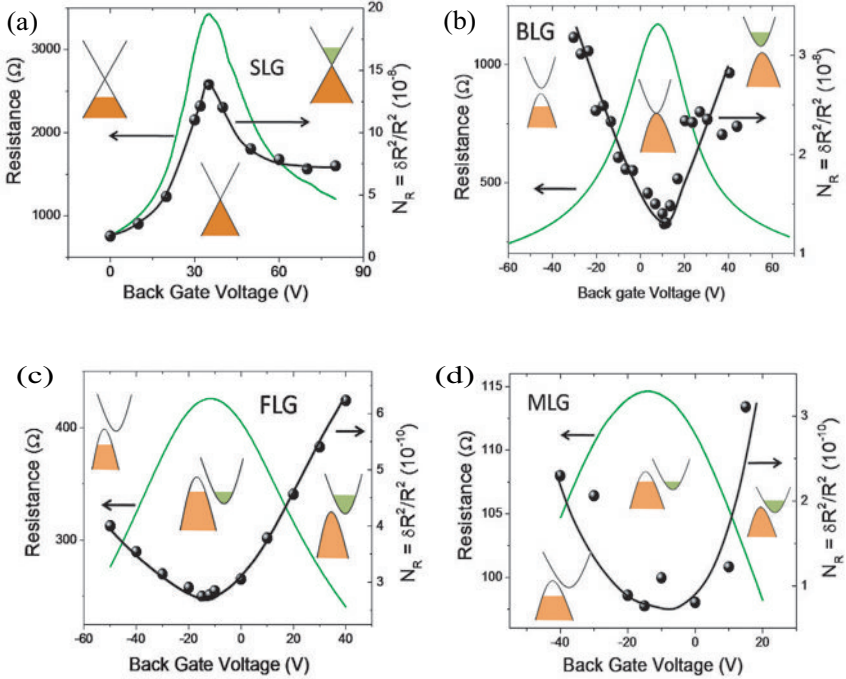
Fig. 3. The resistance and the normalized noise power spectral density (N_R) as functions of back gate voltages are shown for: (a) SLG (b) BLG (c) FLG and (d) MLG devices at T = 100 K. The thick solid lines are guide to the eye. The insets in each figure correspond to the bandstructure at particular voltages for corresponding graphene flake.

3.2. *Noise characteristics in graphene based FET devices*

Noise in the graphene devices were measured in low frequency ac four-probe method.[57] In all devices, the normalized resistance noise PSD behaved as $S_R(f)/R^2 \sim 1/f^\alpha$, with α ranging from $0.8 - 1.2$.[45] Here, instead of focusing on noise magnitude at a specific frequency, we compute and

analyze the total variance of resistance fluctuations (N_R) integrated over the experimental bandwidth. Figures 3(a)–(d) shows the variation of N_R and the corresponding average resistance as a function of backgate voltage (V_{bg}) for SLG, BLG, FLG, and MLG devices, respectively. The most striking observation of Fig. 3 is the unique gate voltage dependence of noise in case of SLG,[44,47] noise decreases with increasing n on either side of the CNP (the Dirac point). But in all other cases, noise magnitude behaves oppositely. The observed characteristics can be qualitatively explained by our model described in Sec. 2, which shows that the bandstructure plays an important role in determining the behavior of noise in graphene. To compare the noise performance from different devices, people often calculate the dimensionless parameter γ_H from the empirical relation given by Hooge,[49] $S_R/R^2 = \gamma_H(1/(A_G n f^\alpha)$, where A_G is the area of graphene channel between two voltage probes and n is the density of charge carriers inside graphene.
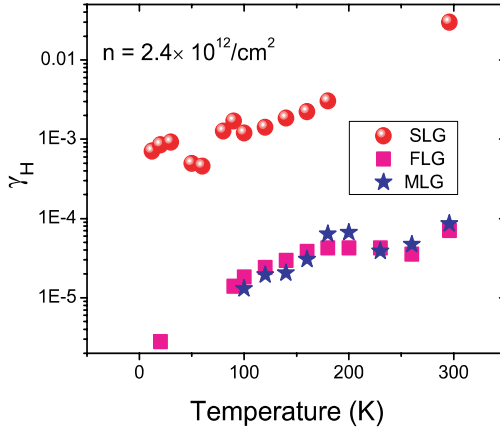
Fig. 4.   (Color Online) Temperature dependence of Hooge parameter for SLG, FLG and MLG devices, far from the CNP ($n = 2.4 \times 10^{12}/\text{cm}^2$).

Figure 4 shows the variation of Hooge parameter γ_H in SLG, FLG and MLG, at a particular density n (2×10^{12} /cm^2) over a wide temperature (T) range. The exponential increase in γ_H in all devices with increasing T could be readily understood in the framework of charging/discharging of the trap states at SiO$_2$ and graphene interface which are known to be activated processes. Our analysis indicates the activation energies (17 ± 1.5), (17 ± 0.6), and (22 ± 2) meV in SLG, FLG, and MLG respectively,[47] being

expectedly similar since the devices were fabricated on the same Si/SiO$_2$ wafer. However, the most intriguing aspect of Fig. 4 is nearly two orders of magnitude lower noise in FLG and MLG in comparison to SLG that was consistently observed in other similar devices as well. A simple understanding of this can be obtained by considering efficient screening of underlying trap potential fluctuations for FLG and MLG due to their nearly three dimensional character, and existence of parabolic bands that provide finite DOS at low energies. The three dimensional nature increases with increasing number of layers making most of FLG/MLG structure insensitive to extraneous fluctuations. Indeed, with considerable field effect behavior, and with $\gamma_H \sim 10^{-5} - 10^{-6}$ FLG forms a promising material for low noise nanoelectronic applications, outperforming competing nanomaterials such as carbon nanotubes in this respect.

3.3. *Noise in dual gated BLG device*

In case of BLG, one can break the interlayer symmetry by applying a perpendicular electric field across the flake, resulting in a gap between the conduction and valence band.[4,15,16] Recently, the low-frequency fluctuations, or the $1/f$ noise, in electrical resistance of bilayer graphene has been shown to be sensitive to its band structure and the increase in noise with density has been explained by the diminished ability of BLG to screen the external potential fluctuations in the presence of finite bandgap (Δ_g).[44,45] However, in noise experiments on BLG so far,[44] Δ_g has been tuned only by varying n with a single (back) gate, where a partial screening of the gate potential leads to excess charge in the upper layer, and hence an electric field between the graphene layers.[16] Here, we have measured the low-frequency resistance noise in spatially extended double-gated BLG devices. The main objective is to achieve an independent tunability of Δ_g with both n and E, where E is the transverse electric field across the electrodes, to separate the influence of band structure and carrier density on screening. A micrograph of a typical dual gated device is shown in Fig. 5(a). The resistance (R)- V_{tg} characteristics of the device at $T \approx 107\ K$ are shown in Fig. 5(b) for several different values of V_{bg} spanning between -30 and $+30\ V$. The charge mobility of the device was estimated to be $1160\ \mathrm{cm^2\ V^{-1}\ S^{-1}}$, which contained an intrinsic hole doping of $-n_0 \approx 5.82 \times 10^{11} cm^{-2}$. When V_{bg} and V_{tg} are different, a finite E is established between the electrodes. Existence of the electric field-induced band gap becomes increasingly prominent at higher V_{bg} with increasing R at charge neutrality point.
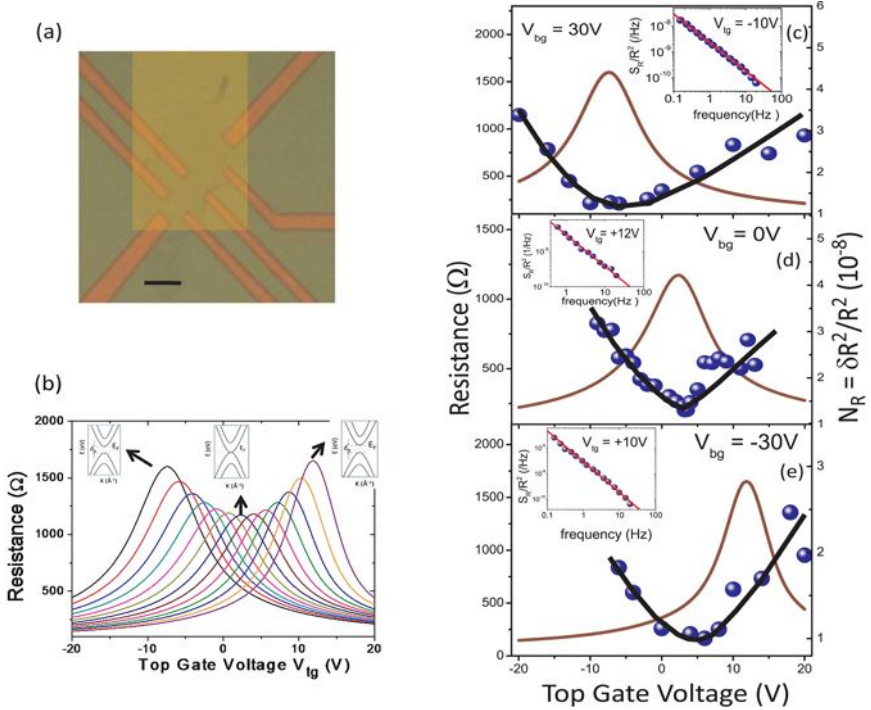
Fig. 5. (a) Optical micrograph of the dual gated BLG device used in the experiment. The scale bar is 10μm.(b) Resistance versus topgate voltage for various back gate voltages, ranging from 30 V to -30 V (left to right) with an interval of 5 V. Insets show schematics of corresponding band structures. (c-e) Electrical transport and noise characterization of a BLG device. The resistance and the normalized noise power spectral density (N_R) as functions of top gate voltages are shown for various back gate voltages: (c) 30 V, (d) 0 V, and (e) -30 V. The thick solid lines are guide to the eye. The insets show typical normalized noise power spectra S_R/R^2, far from the charge neutrality point for each back gate voltage. Note that the charge neutrality points and the noise minimum points are not necessarily the same. This can be explained quantitatively by considering the noise minimum point in graphene to correspond to zero band gap between the conduction and the valence bands.

Typical power spectra of resistance noise are shown in the insets of Figs. 5(c)–(e). Figures 5(c)–(e) show the variation of N_R and the corresponding average resistance as functions of V_{tg} at three different values of V_{bg}. For all V_{bg}, N_R shows a minimum at a specific V_{tg}, denoted as V_{tg}^{Nmin}, and increases monotonically on both sides of V_{tg}^{Nmin}. Similar behavior was observed for noise in BLG nanoribbons as well,[44] which confirms this to be an intrinsic characteristic of BLG, although V_{tg}^{Rmax} and V_{tg}^{Nmin} are

not equal in our measurements, indicating that noise minimum has been shifted away from charge neutrality in the presence of finite E. More detailed analysis shows that multiple processes involving the charge traps are active in producing the resistance noise which is intimately connected to the BLG band structure, being minimum at $\Delta_g \sim 0$ even if it corresponds to a nonzero n.[45]

4. Conclusion

In summary, we have done a comparative study of low frequency fluctuations in electrical resistance of graphene based field-effect devices with varying layer thickness. An analytical model of noise has been proposed based on the number fluctuation between the interfacial oxide traps and the correlated mobility fluctuation. Gate voltage dependence of noise in various graphene devices can well be explained using our model, showing its intimate connection to the bandstructure. Apart from opposite gate voltage characteristics between multilayer graphene and SLG, a striking observation in this study is the extremely low magnitude of noise in case of multilayer graphene, with Hooge parameter as low as 10^{-6} at low temperatures. This makes few/multilayer graphene an attractive candidate for future nanoelectronics. Also, we have measured the low-frequency resistance noise in bilayer graphene flakes as a function of charge density and inter-electrode electric field. The absolute magnitude of noise is intimately connected with the BLG band structure, and shows a minimum when the band gap of the system is zero. The experiments also reveal the charge organization in BLG-based electronic devices, and the microscopic mechanism of resistance noise.

Acknowledgments

References

1. K. S. Novoselov, A. K. Geim, S. V. Morozov, D. Jiang, Y. Zhang, S. V. Dubonos, I. V. Grigorieva, and A. A. Firsov, *Science* **306**, 666 (2004).

2. A. H. Castro Neto, F. Guinea, N. M. R. Peres, K. S. Novoselov, and A. K. Geim, *Rev. Mod. Phys.* **81**, 109 (2009).
3. A. K. geim and K. S. Novoselov, *Nature Mater.* **6**, 183 (2007).
4. E. V. Castro, K. S. Novoselov, S. V. Morozov, N. M. R. Peres, J. M. B. Lopes dos Santos, J. Nilsson, F. Guinea, A. K. Geim, and A. H. Castro Neto, *Phys. Rev. Lett.* **99**, 216802 (2007).
5. T. Ohta, A. Bostwick, T. Seyller, K. Horn, and E. Rotenberg, *Science* **313**, 951 (2006).
6. J. B. Oostinga, H. B. Heersche, X. Liu, A. F. Morpurgo, and L. M. K. Vandersypen, *Nature Mater.* **7**, 151 (2008).
7. C. Lee, X. Wei, J. W. Kysar, and J. Hone, *Science* **321**, 385 (2004).
8. K. S. Novoselov, A. K. Geim, S. V. Morozov, D. Jiang, M. I. Katsnelson, I. V. Grigorieva, S. V. Dubonos, and A. A. Firsov, *Nature* **438**, 197 (2005).
9. K. I. Bolotin, K. J. Sikes, Z. Jiang, D. M. Klima, G. Fudenberg, J. Hone, P. Kim, and H. L. Stormer, *Solid State Commun.* **146**, 351 (2008).
10. S. V. Morozov *et al.*, *Phys. Rev. Lett.* **100**, 016602 (2008) 2008.
11. X. Du *et al.*, *Nature Nanotech.* **3**, 491 (2008).
12. R. Murali, Y. Yang, K. Brenner, T. Beck, and J. D. Meind, *Appl. Phys. Lett.* **94**, 243114 (2009).
13. A. A. Balandin *et al.*, *Nano Lett.* **8**, 902 (2008).
14. F. Xia, D. B. Farmer, Y. Lin, and P. Avouris, *Nano Lett.* **10**, 715 (2010).
15. E. McCann and V. I. Falko, *Phys. Rev. Lett.* **96**, 086805 (2006).
16. E. McCann, *Phys. Rev. B* **74**, 161403(R) (2006).
17. T. Ohta *et al.*, *Science* **313**, 951 (2006).
18. S. Park and R. S. Ruoff, *Nature Nanotech.* **4**, 217 (2009).
19. S. Gilje, S. Han, M. Wang, K. L. Wang, and R. B. Kaner, *Nano Lett.* **7**, 3394 (2007).
20. D. A. Dikin *et al.*, *Nature* **448**, 457 (2007).
21. A. N. Obraztsov *et al.*, *Carbon*, **45**, 2017 (2007).
22. Q. Yu *et al.*, *Appl. Phys. Lett.* **93**, 113103 (2008).
23. X. Li *et al.*, *Science* **324**, 1312 (2009).
24. J. Coraux *et al.*, *Nano Lett.* **8**, 565 (2008).
25. A. Reina *et al.*, *Nano Lett.* **9**, 30 (2009).
26. K. S. Kim *et al.*, *Nature* **457**, 706 (2009).
27. F. Schedin *et al.*, *Nature Mater.* **6**, 652 (2007).
28. X. Wang *et al.*, *Nano Lett.* **8**, 323 (2007).
29. G. Eda, G. Fanchini, and M. Chhowalla, *Nature Nanotech.* **3**, 270 (2008).
30. Y. Zhang, Y. Tan, H. L. Stormer, and P. Kim, *Nature* **438**, 201 (2005).
31. K. S. Novoselov, Z. Jiang, Y. Zhang, S. V. Morozov, H. L. Stormer, U. Zeitler, J. C. Maan, G. S. Boebinger, P. Kim, and A. K. Geim, *Science* **315**, 1379 (2007).
32. D. Allor, T. D. Chen, and D. A. McGady, *Phys. Rev. D* **78**, 096009 (2008).
33. A. V. Shytov, M. I. Katsnelson, and L. S. Levitov, *Phys. Rev. Lett.* **99**, 246802 (2007).
34. A. Shytov, D. Abanin, and L. Levitov, *arXiv*:0812.4970.
35. A. F. Young and P. Kim, *Nature Phys.* **5**, 222 (2009).

36. N. Stander, B. Huard, and D. Goldhaber-Gordon, *Phys. Rev. Lett.* **102**, 026807 (2009).

37. J. H. Chen, C. Jang, S. Xiao, M. Ishigami, and M. S. Fuhrer, *Nature Nanotech.* **3**, 207 (2008).

38. X. Du, I. Skachko, F. Duerr, A. Luican, and E. Y. Andrei, *Nature* **462**, 192 (2009).

39. K. I. Bolotin, F. Ghahari, M. D. Shulman, H. L. Stormer, and P. Kim, *Nature* **462**, 196 (2009).

40. B. E. Feldman, J. Martin, and A. Yacoby, *Nat. Phys.* **5**, 889 (2009).

41. J. G. Checkelsky, L. Li, and N. P. Ong, *Phys. Rev. B* **79**, 115434 (2009).

42. A. Fasolino, J. H. Los, and M. I. Katsnelson, *Nat. Mater.* **6**, 858 (2007).

43. E. A. Kim and A. H. Castro Neto, *Europhys. Lett.* **84**, 57007 (2008).

44. Y. Lin and Phaedon Avouris, *Nano Lett.* **8**, 2119 (2008).

45. A. N. Pal and A. Ghosh, *Phys. Rev. Lett.* **102**, 126805 (2009).

46. Y. Lin, J. Appenzeller, J. Knoch, Z. Chen, and P. Avouris, *Nano Lett.* **6**, 930 (2006).

47. A. N. Pal and A. Ghosh, *Appl. Phys. Lett.* **95**, 082105 (2009).

48. A. L. McWhorter, Semiconductor Surface Physics. Philadelphia: University of Pennsylvania Press, p. 207 (1957).

49. F. N. Hooge, *Physica* **83B**, 14 (1976).

50. R. Jayaraman and C. G. Sodini, *IEEE Trans. on Electron Devices* **36**, 1773 (1989).

51. N. W. Ashcroft and N. D. Mermin, Solid State Physics. Philadelphia: Holt, Rinehart, and Winston (1976).

52. S. Adam, E. H. Hwang, V. M. Galitski, and S. Das Sarma, *Proc. Natl. Acad. Sci. U.S.A.* **104**, 18392 (2007).

53. E. H. Hwang, S. Adam, and S. Das Sarma, *Phys. Rev. Lett.* **98**, 186806 (2007).

54. S. Adam and S. Das Sarma, *Phys. Rev. B* **77**, 115436 (2008).

55. A. N. Pal and A. Ghosh, (*To be published*) (2010).

56. A. C. Ferrari *et al.*, *Phys. Rev. Lett.* **97**, 187401 (2006).

57. A. Ghosh and A. K. Raychaudhuri, *Phys. Rev. Lett.* **84**, 4681 (2000); A. Ghosh *et al.*, e-print *arXiv:condmat*/0402130 v1 (2004).

Chapter 14

Spin Transport in Single- and Multi-Layer Graphene

M. Shiraishi,* M. Ohishi, N. Mitoma, T. Takano, K. Muramoto,
R. Nouchi, T. Nozaki, T. Shinjo and Y. Suzuki

*Graduate School of Engineering Science, Osaka Univ.,
Machikaneyama-cho 1-3, Toyonaka 560-8531, Osaka, Japan
*PRESTO-JST, 4-1-8 Honcho, Kawaguchi 332-0012, Saitama, Japan
shiraishi@mp.es.osaka-u.ac.jp

Spin transport in molecular systems has been attracting much attention, because a weak spin-orbit interaction in molecules allows us to expect good spin coherence. Although spin injection and spin transport in molecules were not easily achieved at room temperature, graphene, which is one of the most attractive materials in condensed matter physics since 2004, provided an ideal platform to realize and discuss spin injection and transport at room temperature. We present our study on spin injection into graphene and important findings of unique spin transport properties in graphene.

1. Introduction

After the first success of fabricating multi-layer graphene and its field effect transistors (FETs) in 2004 [1], a tremendous number of studies has been implemented in order to clarify attractive physical features of single-layer and multi-layer graphene (SLG and MLG) [2-9], which induces much interest for graphene electronics.

In 2007, introduction of a spin degree freedom to graphene electronics, namely, establishing a field of graphene spintronics, was successfully achieved by several groups, including our group, individually [10-12], where spins were injected, a pure spin current was generated and the spins were manipulated in SLG and MLG up to room temperature (RT). The reason why people are attracted by spin injection into carbonaceous

molecules is based on facts that the low atomic mass of carbon can induce the weak spin-orbit interaction and that 99% of the carbon isotopes has no nuclear spin and therefore hyperfine interaction between nuclei and electronic spins should be weak.

Our group has vigorously investigated spin transport properties in SLG and MLG in recent several years [10, 13-16]. In this manuscript, we will describe how to generate a pure spin current in graphene and the detail of the non-local spin transport, which enables us possible to exclude spurious signals. Next, we will describe unprecedented robustness of spin polarization in MLG spin valves at room temperature. Surprisingly, the spin polarization of injected spins was *constant* up to a bias voltage of +2.7 V and -0.6 V in positive and negative bias voltage applications at room temperature, which is superior to all spintronics devices. Our finding is induced by suppression of spin scattering due to an ideal interface formation. [13, 14]. In addition, spin transport and gate-induced modulation of a pure spin current in SLG, as theory predicts, will be described [15].

2. Experimental

The starting materials used for preparation of the SLG and MLG spin valves were highly oriented pyrolytic graphite (HOPG, NT-MDT Co.) and polyimide-oriented highly oriented graphite (Super graphite, Kaneka Co.) [17]. Graphene flakes were peeled from these materials using adhesive tape. The flakes were then pushed onto the surface of a SiO_2/Si substrate (SiO_2 thickness = 300 nm). The typical thickness of the MLG that provided observable spin injection signals in a spin valve structure was 2-40 nm. In the case of the SLG spin valves, we have verified that the layer number was one by using Raman spectroscopy. The non-magnetic and ferromagnetic electrodes used were Au/Cr (=40/5 nm) and Co (=50 nm), respectively, and were patterned using an electron beam lithography technique. The width of the Co electrodes, Co1 and Co2, were the same, but Co2 possessed a pad structure in order to weaken the coercive force, and the typical gap width of the Co electrodes was 1.5 μm (see Fig. 1(a)).

All measurements of MR effects were performed at RT. We introduced a non-local scheme [18] in addition to a conventional local
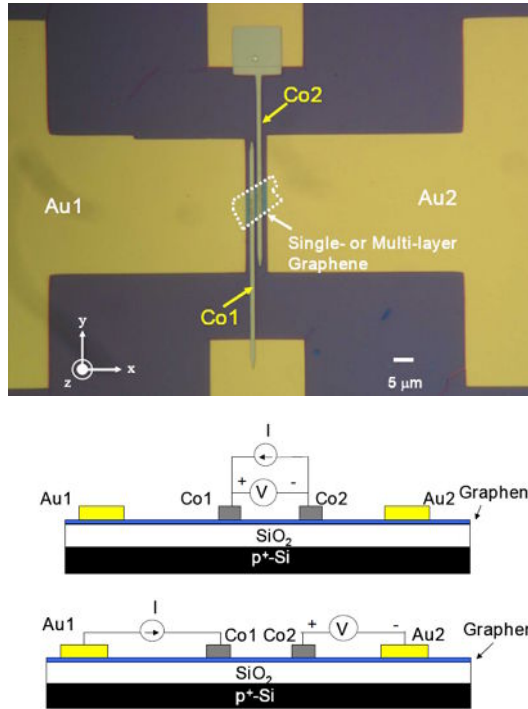
Fig. 1. A microscopic image of a graphene spin valve (top), and a non-local measurement scheme (middle) and a local measurement scheme (bottom) for spin injection into SLG and MLG.

scheme for excluding spurious signals (see Figs. 1(b) and (c)). One can detect a non-local output voltage which is induced by position dependence of electrochemical potential of the generated spin current in the graphene. Here, spins are injected at ferromagnet(FM)/graphene of the top layer of the graphene in the injector side (between Co1 and Au1) as an electric current and accumulated spins diffuse from Co1 to Co2 and Au2 (the detector side). Hence, an output voltage induced by the generated spin current is determined by an amount of accumulated spins, namely, it is strongly affected by the interface spin polarization at Co1/graphene. In a non-local scheme, an electric current I is injected from Co1 into GTF and extracted at Au1. The voltage difference is measured between Co2 and Au2. The

non-local voltage, $V_{\text{non-local}}$, is defined as (V_+- V_-). In a local scheme, an electric current I is injected from Co1 into GTF and extracted at Co2. The voltage difference is measured also between Co1 and Co2. The "local" voltage, V_{local}, is defined as (V_+- V_-). The spin injection was investigated using a four terminal probe system (ST-500, Janis Research Company Inc.) with an electromagnet. The magnetic field was swept from -400 Oe to +400 Oe in steps of 8 Oe. A source-meter (Keithley Instruments Inc., KH2400) and a multi-meter (Keithley Instruments Inc., KH2010) were used to detect spin injection signals. The Hanle effect was investigated using a physical property measurement system (PPMS, Quantum Design Inc.) at RT. The magnetic field was swept from -200 mT to +200 mT in ca. 3 mT steps. The initial magnetization configuration of Co1 and Co2 was set to be either parallel or anti-parallel.

3. Results and Discussion

Figure 2 shows a typical spin injection signal in graphene at RT in a non-local measurement scheme, where an injection electric current was set to be +1 mA, and clear hysteresis of non-local spin voltage is observed. Here, it should be noted that anisotropic MR (AMR) signals, as observed in a local measurement scheme (not shown here, and see ref. [13]) were not observed in this measurement, which unambiguously indicates that the non-local measurement can exclude spurious signals in spin injection measurements, such as AMR signals, and allows us to detect only reliable spin injection signals. When we have changed the injection electric current from +1 mA to -1 mA in an MLG spin valve, linear dependence of the spin voltages was seen as shown in Fig. 3. We have verified that the same linear dependence was also observed even when we introduced the local measurement scheme [13]. When we assume that all contact resistances have same values for simplicity, the non-local output voltage to be expressed as the following generalized form [19],

$$\Delta V_{non\text{-}local} = \frac{2P^2}{(1-P^2)^2}(\frac{R_F}{R_N})R_F \cdot [\sinh(\frac{L}{\lambda_{sf}})]^{-1} \cdot I_{inject} \ , \tag{1}$$
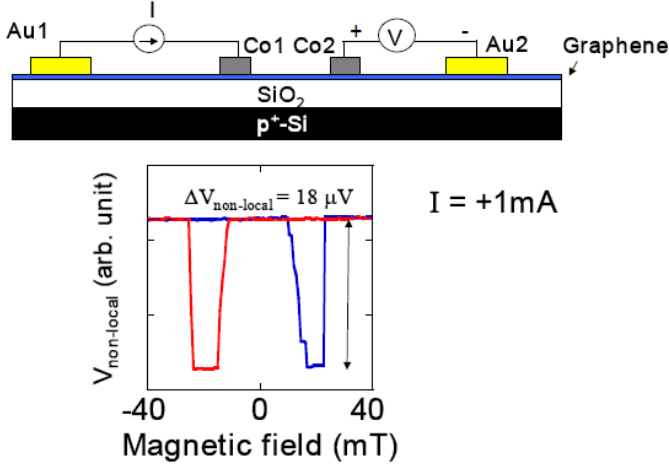
Fig. 2. A typical non-local spin injection signal observed in the graphene spin valves at RT.
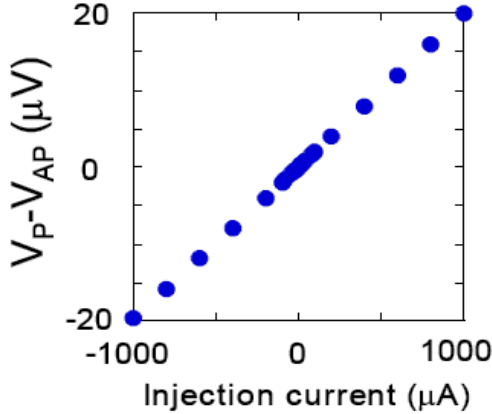
Fig. 3. The observed linear dependence of the spin voltage for the injection electric current in the MLG spin-valves.

where P is the spin polarization, λ_{sf} is the spin flip length, L is the gap length between two FM electrodes, I_{inject} is the injected electric current, R_F and R_N are spin accumulation resistances of FM and NM, respectively, which is defined as (the conductivity) $\times$ (the spin diffusion length)/(the cross-sectional area). From Eq. (1), it is interpreted that the linear dependence is

induced by constant spin polarization, and this finding manifested the robustness of the spin polarization at Co/MLG within ±1 mA. It is widely known that MR ratio in tunnel magnetoresistance (TMR) devices monotonously decreases as bias voltage increases, which is thought to be attributed to decrease of spin polarization of injected spins due to magnon/phonon excitations and the spin signals was *a half* of the maximum at +1 V at RT [18]. Such decrease of spin polarization can be an obstacle for practical applications for MRAM and so on, and much effort has been paid for overcoming the problem. In the case of graphene, such decrease could be also a major problem if spin transistor will be fabricated. Here, the sample resistance was ~200 Ω, in which the resistance of one Co electrode wire and the MLG was measured to be ~50 Ω and ~5 Ω, respectively. This indicates that additional resistance (~50 Ω each) exists at a Co/graphene interface although no tunneling barrier such as Al-O was introduced. As a result, the spin polarization (=MR ratio) of this sample was *constant* up to ~100 mV at RT, which is surprising compared with the results of other spin valves, where no such robustness was observed. In order to determine the maximum voltage where the spin polarization is constant, another MLG device (R_{Au-Co}~109 Ω) was prepared and investigated using the non-local method, where the sample resistance without the Co wire resistance was ~60 Ω. Although the electrode (not the MLG channel) was broken at 20.3 mA, the current dependence of the output voltage exhibited very unique behavior, namely, the output voltage exhibited the linear dependence (robustness of the spin polarization) until 0.5 V; above 0.5 V, it exhibited sub-linear dependence. However, even at ~1.2 V, the spin polarization was still 81% of the initial value (Fig. 4). In addition, further experiments using the other samples exhibited that the robustness was maintained up to +2.7 V under a positive bias voltage application and down to -0.6 V under a negative voltage application (see ref. [13]). More importantly, the robustness was detected even in a SLG spin valves, where the spin polarization of the injected spins was constant up to + 1 V whereas it exhibited deviation from the linear dependence of the spin voltages and no linear dependence in the negatively biased condition [15]. Although the investigation was not carried out in detail, it is notable that the similar asymmetry of spin voltages in positively and negatively biased conditions has been reported by Kawakami and co-workers in SLG when a spin carrier was hole [21]. Further study
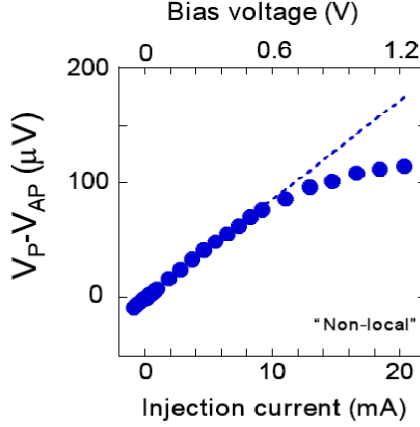
Fig. 4. The observed better robustness.

should be needed, but we believe that the asymmetry is probably ascribed to a difference of spin propagation directions (spin injection from ferromagnet to nonmagnet or spin extraction from nonmagnet to ferromagnet) as observed in CoFe/AlO/Al spin devices [22]. Interestingly, the similar robustness of spin polarization of injected spins in nonmagnetic channels was recently observed in Si spin valves by using a non-local technique [23], and hence the robustness may be an essential nature of group-IV elements (carbon and silicon).

Next, Hanle-type spin precession experiments were implemented in order to verify that the obtained signals are ascribed to spin injection into the MLG. (see Fig. 5). For this purpose, we applied a magnetic field in the *y* direction in order to prepare the Co electrodes in a parallel or anti-parallel magnetization direction, and the field was then removed and a magnetic field, *B*, was scanned in the *z* direction (see Fig. 1). The clear crossing of parallel and anti-parallel signals was observed at +170 and -170 mT, which directly indicates that the observed signals were attributed to the spin injection into the MLG. By using the following equation for spin precession [18],

$$\frac{V_{non\text{-}local}}{I_{inject}} = \frac{P^2}{\sigma_{MLG}A/D} \int_0^\infty \frac{1}{\sqrt{4\pi Dt}} \exp(-\frac{L^2}{4Dt}) \cos(\omega_L t) \exp(-\frac{t}{\tau_{sf}}) dt, \quad (2)$$
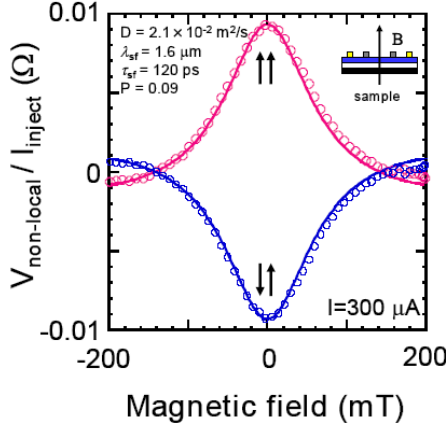
Fig. 5. Modulation of the non-local resistance due to spin precession, as a function of perpendicular magnetic field. The injection current was set at 300 μA. The red (parallel, ↑↑) and blue (anti-parallel, ↓↑) open circles are experimental data, and the red and blue lines are the result of model fitting.
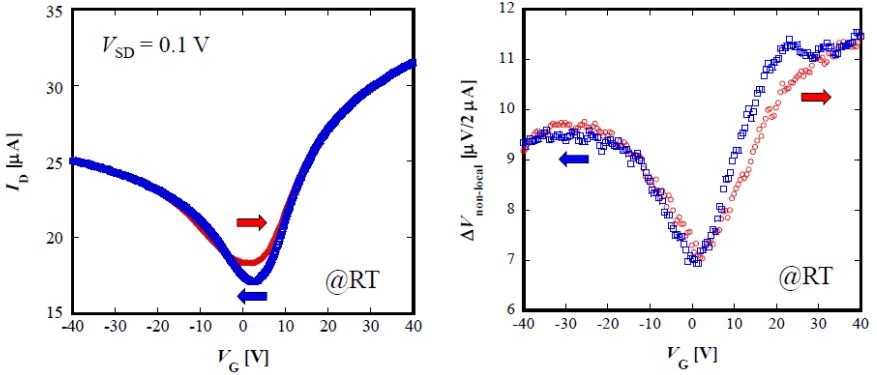
Fig. 6. (Left) A typical FET characteristics of a SLG spin FET at RT. Arrows indicate the directions of the gate-voltage sweep. (Right) Gate-voltage dependence of the corresponding spin voltages in the SLG spin FET. Arrows indicate the directions of the gate-voltage sweep. The spin voltages were detected by using a non-local technique. The signal is the minimum where the conductivity of the SLG is the minimum (the Dirac point), which directly means that the contact is electrically transparent as we have designed.

where t is time, τ_{sf} is the spin coherent time and D is a diffusion constant, the spin diffusion constant D (=2.1×10^{-2} m^2/s), spin flip length λ_{sf} (=1.6 μm), spin coherent time τ_{sf} (=120 ps), and spin polarization P (=0.09) was estimated, although it should be noted that this is an approximate estimation because the Eq. (2) is the only existing expression for the estimation of spin transport properties in the case of the Hanle type spin precession. The observed spin coherence is almost same as that reported in SLG [11], and how to enhance the coherence is the next important milestone.

Finally, a prototypical graphene spin transistor operation using SLG is introduced. So far, there were several reports on gate-voltage-induced modulation of spin voltages in SLG spin valves [11, 12]. According to a theory [19], non-local spin voltage exhibits the following relationships with conductivity of a nonmagnetic channel as the contact between ferro- and non- magnets changes:

for an Ohmic contact,

$$\Delta V_{non-local} = \frac{2P^2}{(1-P^2)^2}(\frac{R_F}{R_N})R_F \cdot [\sinh(\frac{L}{\lambda_{sf}})]^{-1} \cdot I_{inject}, \quad (\sim \sigma_N) \qquad (3)$$

for a tunneling contact

$$\frac{\Delta V}{I} = \Delta R_{non-local} = \frac{1}{2}\frac{P^2 \lambda_{sf}}{\sigma_N A}\exp(-\frac{L}{\lambda_{sf}}). \qquad (4)$$

When we look back a previous study [11], the gate-voltage dependence of the spin voltage in SLG spin valves with Al-O tunneling barriers exhibited an opposite dependence as the theory predicts, namely, the spin voltage was the smallest at the Dirac point where the conductivity of the SLG was the minimum although the Al-O tunneling barrier was inserted between Co and SLG. In the other study, the spin voltage had no obvious gate voltage dependence. In this sense, it can be said that there is much room for investigation of gate-voltage dependence of spin signals in SLG spin valves. We have designed our SLG spin valves as they have no tunneling barriers, and examined whether the spin voltages are proportional or inversely proportional. Figure 6 (Left) shows the FET characteristics of our SLG, and the Dirac point was at the gate voltage of ~5 V. The suppression of the

source-drain current in the negatively bias region, where the carriers were holes, was reported to be attributed to the band mixing between Co and SLG [16]. When we have measured the spin voltages of this SLG spin valves by using a non-local technique with applying the gate voltages, the spin signals were strongly modulated by the gate voltages. As shown in Fig. 6 (Right), the spin signal was the minimum at ~5 V, where the conductivity of the SLG was also the minimum. In addition, the similar suppression of the spin signals as observed in the source-drain current was also observed. Hence, it is concluded that the spin signals can be modulated by the gate voltages as the theory predicts, which has not been reported in previous studies [25].

Acknowledgments

References

[1] K.S. Novoselov et al., Science **306**, 666 (2004).
[2] K.S. Novoselov et al., Nature **438**, 197 (2005).
[3] Y. Zhang et al., Nature **438**, 201 (2005).
[4] K.S. Noboselov et al., Science **315**, 1379 (2007).
[5] K.I. Bolotin et al., Phys. Rev. Lett. **101**, 96802 (2008).
[6] H.B. Heersche et al., Nature **446**, 56 (2007).
[7] J.B. Oostinga et al., Nature Mater. **7**, 151 (2007).
[8] C.N.R. Rao, A.K. Sood, K.S. Subrahmanyam, and A. Govindaraj, Angew. Chem. Int. Ed. **48**, 7752 (2009).
[9] A. Das, S. Pisana, B. Chakraborty, S. Piscanec, S.K. Saha, U.V. Waghmare, K.S. Novoselov, H.R. Krishnamurthy, A.K. Geim, A.C. Ferrari, and A.K. Sood, Nature Nanotech. **3**, 210 (2008).
[10] M. Ohishi, M. Shiraishi, Y. Suzuki et al., Jpn. J. Appl. Phys. **46**, L605 (2007).
[11] N. Tombros et al., Nature **448**, 571 (2007).
[12] S. Cho et al., Appl. Phys. Lett. **91**, 123105 (2007).
[13] M. Shiraishi, Y. Suzuki et al., Adv. Func. Mat. **19**, 3711 (2009).
[14] K. Muramoto, M. Shiraishi, Y. Suzuki et al., Appl. Phys. Express **2**, 123004 (2009).
[15] N. Mitoma, M. Shiraishi, Y. Suzuki et al., in preparation.
[16] R. Nouchi, M. Shiraishi, and Y. Suzuki, Appl. Phys. Lett. **93**, 152104 (2008).

[17] M. Murakami et al., Carbon **30**, 255 (1992).

[18] F.J. Jedema et al., Nature **416**, 713 (2002).

[19] S. Takahashi and S. Maekawa, J. Phys. Soc. Jpn. **77**, 31009 (2008).

[20] S. Yuasa et al., Nature Mat. **3**, 868 (2004).

[21] W. Han, R.K. Kawakami et al., Phys. Rev. Lett. **102**, 137205 (2009).

[22] S.O. Valenzuela et al., Phys. Rev. Lett. **94**, 196601 (2005).

[23] T. Sasaki, M. Shiraishi, Y. Suzuki et al., Appl. Phys. Express **2**, 53003 (2009). *ibid*, Appl. Phys. Lett. **96**, 122101 (2010). *ibid*, IEEE Trans. Mag. in press.

[24] T. Kimura et al., Phys. Rev. B **72**, 014461 (2005).

[25] Note added: When a masking layer (MgO) was inserted between ferromagnet and graphene in order to enhance spin signals, the similar gate voltage dependence has been reported. W. Han, R.K. Kawakami et al., Phys. Rev. Lett. **102**, 137205 (2009).

Chapter 15

Quantum Complexity in Graphene

G. Baskaran

Quantum Science Centre, The Institute of Mathematical Sciences,
C.I.T. Campus, Chennai 600 113, India

Carbon has a unique position among elements in the periodic table. It produces an allotrope, graphene, a mechanically robust two dimensional semimetal. The multifarious properties that graphene exhibits has few parallels among elemental metals. From simplicity, namely carbon atoms connected by pure sp^2 bonds, a wealth of novel quantum properties emerge. In *classical complex systems* such as a spin glass or a finance market, several competing agents or elements are responsible for unanticipated and difficult to predict emergent properties. The complex (sic) structure of quantum mechanics is responsbile for an unanticipated set of emergent properties in graphene. We call this *quantum complexity*. Infact, most quantum systems, phenomena and modern quantum field theory could be viewed as examples of quantum complexity. After giving a brief introduction to the quantum complexity we focus on our own work, which indicates the breadth in the type of quantum phenomena that graphene could support. We review our theoretical suggestions of, (i) spin-1 collective mode in netural graphene, (ii) relativistic type of phenomena in crossed electric and magnetic fields, (iii) room temperature superconductivity in doped graphene and (iv) composite Fermi sea in neutral graphene in uniform magnetic field and (v) 2-channel Kondo effect. Except for the relativistic type of phenomena and Kondo effect, the rest depend in a fundamental way on a weak electron correlations that exist in graphene.

1. Introduction

Graphene has caught a serious attention from the scientific community in the last 6 years or so, because of an outstanding discovery [1; 2], in the form of a simple procedure, that makes preparation and study of single and multilayer graphene feasible in many laboratories all over the

world. A remarkable mechanical robustness of single layer graphene was also revealed. Now, one could prepare, manipulate and study one carbon atom thick layer for several of its properties. The resulting experimental and theoretical efforts [3] have revealed several surprises in simple graphene. Looking back at the fast developments one begins to wonder at the number of quantum phenomena that graphene has revealed, arising from a simple sp^2 bond among only carbon atoms. This is surely a case of an unexpected and welcome *quantum wealth*.

Behind the quantum wealth is a simple sp^2 bonding among carbon atoms and a resulting stable 2 dimensional honey comb lattice structure. Sp^2 hybridization leads to a strong σ bond and leaves one electron per $2p_z$ orbital [4]. Neighboring $2p_z$ orbitals overlap and produce the π and π^* bands. The two bands meet at the K and K' points in the Brillouin zone in the form of a Dirac cone. Further, the Bloch wave functions have special sublattice structure, a chirality property, which influence various quantum dynamical properties of graphene.

This stable 2 dimensional system offers a platform for a rich quantum physics. When we talk about emergent properties in modern times, one is reminded of multicomponent systems with competing interactions among many agents or components. Quantum Condensed matter systems seems to be a play ground for novel and unexpected emergent properties in rather simple situations, even with one or two components. One can cite the example of ^{4}He, which exhibits gas, liquid, superfluid, supersolid, quantized vortices, Josephson phenomena etc. Water molecule H_2O provides hydrogen bonding, proton tunnelling, clathrate hydrates, amorphous ice, 12 phases of ice, water, turbulence etc. One can give similar account for iron and so on. Many of these emergent properties are not due to many competing agents, but due to the peculiar structure of underlying quantum mechanics.

In the present article we introduce a notion of *quantum complexity* through the example of graphene. After a brief discussion of complexity, we will summarise our own results, which indicates the breadth in the type of unexpected quantum phenomena that graphene could support. We review our predictions, (i) spin-1 collective mode in netural graphene, (ii) relativistic type of phenomena in crossed electric and magnetic fields, (iii) room temperature superconductivity in doped graphene (iv) composite Fermi sea in neutral graphene in uniform magnetic field and (v) 2-channel Kondo effect. In the above, except for the relativistic type of phenomena, the rest depend on the electron-electron interaction in the 2 dimensional graphene.

1.1. *Complexity — Classical & quantum*

The science of complexity is a relatively new field. Over decades one has seen that systems involving several agents or components with conflicting interests exhibit certain unique characteristics and surprises. Often a hierarchy of new and unexpected qualitative features emerge [5]. Among the many problems addressed there are many clearly defined, but *hard problems* in the sense of (i) exponentially long time needed to solve the problem and (ii) finding hierarchical structures on the road to final solutions.

An example well known to condensed matter physicist is the problem of spin glass, as illustrated by the Sherrington Kirkpatrick model. Insightful and difficult analysis by Parisi and coworkers have introduced the concept of *replica symmetry breaking* and *unltrametricity structure* in the solution space and several unexpected features. Physical consequences and connection to unexpected mathematics such as p-adic number theory are fascinating. In the spin glass problem, the underlying variable are a simple collection of Ising variables. It is the competing interactions which frustrate any attempts to find the ground state. In models which are constructed to extract generic features of these type of complexity problems, randomness is a key element. It is not necessary, of course, to have several competing agents to get complexity and surprises. In classical mechanics, even in 3 body dynamics of a generic non integrable systems, there is chaos and complexity.

In what follows we define complexity for our purposes as follow: *that which cannot be handled with ease, which does not yield to straight forward analysis by known theoretical methods and where you do not know what to expect next.* Looking back at quantum condensed matter systems that have been studied and understood in the last century, many of them can be called complex. Quantum mechanics underlies the complexity. The basic laws of quantum mechanics and rules for computations, necessary to understand condensed matter systems have been discovered. Quantum mechanics has not failed us so for in understanding the day today material world. Quantitative understanding and predictions we wish to make may be difficult, because of technical difficulties; not because of our ignorance about the laws of nature, as it existed before the invention of quantum mechanics.

Quantum mechanics is complex. Quantum mechanics has revealed novel and *complex quantum worlds* in the last several decades, through simple systems. The structure of quantum mechanics with the possibility of linear

superposition, entanglement, identical particles with fermi or Bose characters, anyons in 2 dimensions, topological order and so on make even simple looking quantum systems much more *unpredictable* and complex than one can comprehend.

Let us discuss a well known case first - the case of cuprate superconductors. Soon after the discovery of superconductivity in $La_{2-x}Ba_xCuO_4$ by Bednorz and Muller new family members of the cuprate family were synthesised and superconducting Tc went up to 163 K (under pressure) in one of the family members. This was a surprise. An old idea of resonating valence bond (RVB) state was revived and found to be relevant for cuprates. RVB theory exposed Mott insulators as seat of high Tc superconductivity. A new electronic mechanism appeared. The superconducting order parameter was found to be unconventional, a d-wave order with nodal quasi particles, with rich consequences. The idea of quantum spin liquid got sharpened and notions like spinon, holon, pseudo fermi surface, dimer models, topological order, topological term in non linear sigma models, dynamically generated RVB gauge fields, Chern-Simons theory etc., were born. Whatever happened during 1986-88 were were exciting and unexpected developments with rich consequences. In cuprates quantum mechanics was at its best in producing a variety of novel phenomena in a Mott insulator template.

^{3}He exemplifies quantum complexity well. Volovik's book, *The Universe in a Helium Droplet* [6] is an elaboration of quantum complexity. A simple monoatomic ^{3}He system, because of its fermionic property and light mass has all the rich consequences that we have discovered in the normal and superfluid phases.

It is amusing that we also encounter complexity in the quantum world, when we go down the length and time scales, within the experimentally accessible regime. Nuclear physics is rich and complex. Elementary particle physics and the standard model description of electromagnetic, weak and strong interaction is complex. It has nearly 19 parameters and a rich variety of unexpected particles and phenomena. Going down further, into frontiers beyond possibilities of experimentation at the present time, we encounter supersymmetry, quantum gravity and superstring theory. Physical realizations apart, they have connected our physics friends to a rich and profoundly complex quantum world and world of mathematics.

The complexity we are talking about are with respect to equilibrium properties or equilibrium states. The world of non equilibrium quantum phenomena is also rich and varied. Thanks to experiments such as femto second spectroscopy, new experiments in meso and nanoscopic systems,

NMR, quantum optics, cold atoms etc., a variety of experimental and theoretical studies exist now: from detailed wave packet dynamics in chemical reactions, to non equilibrium Kondo phenomena in mesoscopic systems to a rich quantum kinetic behaviour in supersolid ^{4}He etc.

1.2. *Novel phenomena in graphene*

One of the first persons to appreciate a novel quantum phenomenon in graphene/graphite was Pauling, back in 1936. He recognized [7] presence of unsaturated π bonds and emphasized resonance of covalent bonds and tried to understand graphite/graphene, before band theory was developed. As we will see later, while Pauling's theory was not entirely correct, there is a key feature, which captures among other things a predicted spin-1 collective mode [8] and possibility of room temperature superconductivity in optimally doped graphene [9]. An important property of graphite, namely Landau diamagnetism was discovered by K S Krishnan and Ganguly [10] in the late 30's. K S Krishnan also discovered the extreme anisotropic conductivity of graphite [11], thereby paving way for study of quasi 2 dimensional and quasi 1 dimensional metals.

Once graphene was separated from graphite by a simple method by Noveselov et al., intense experimental and theoretical activities started in the field of graphene. We will briefly mention the variety of novel phenomena that graphene exhibits and trace its origin to a special quantum mechanical property of carbon atom. Quantum complexity in graphene is illustrated in Fig. 1. Carbon atom has an electronic configuration $1s^22s^22p^2$. There are four valence electrons in the 2s and 2p orbitals. A remarkable property of carbon is its ability to form stable sp^2 and sp^3 bonds and the near equality of bond energies. On the pure sp^2 end it gives rise to graphene and on the sp^3 end it gives diamond. In between, a continuous mixing of sp^2 and sp^3 gives rise to myriad forms (allotropes) of pure carbon - carbon nano tubes, bucky balls, nanotube-graphene hybrids, amorphous carbon, carbon black and so on. In the present article we will focus on graphene.

sp^2 bonding leads to a strong σ bond, which stabilizes a honey comb lattice structure. In turn, a lone electron in the remaining $2p_z$ orbital gets involved in pπ bonding and we get a simple tight binding system on the honey comb lattice. Honey comb lattice and two atoms per unit cell leads to the formation of π and π^* bands that touch each other at the K and K' points in the Brillouin zone in the form of Dirac cones (Fig. 2). The two valleys lead to a valley pseudo spin, a flavor index for the Dirac spinor.

Quantum Complexity in Graphene
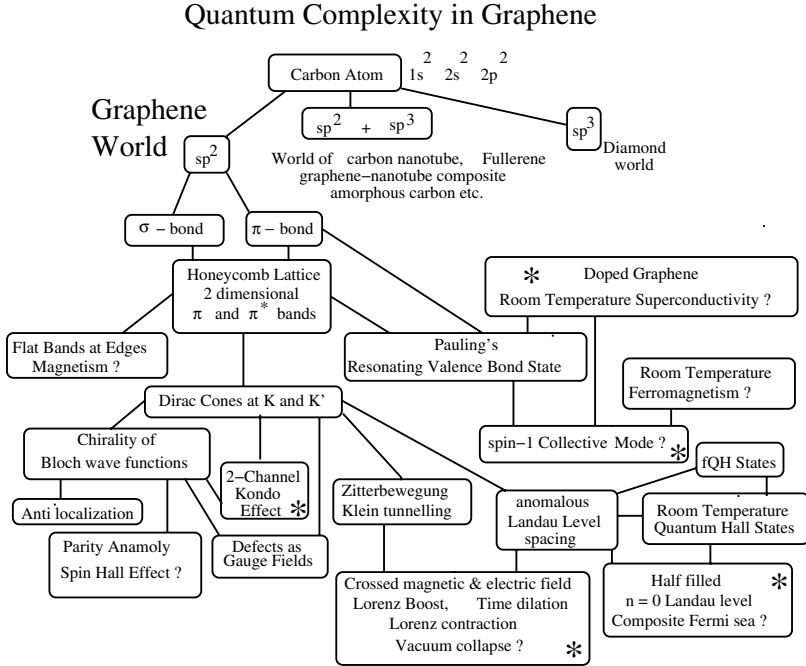
Fig. 1. Some of the important quantum aspects of graphene. Boxes marked with an asterisk indicate theoretical suggestions of ours with collaborators, discussed in this article.

Further, the Bloch states acquires a chirality, in the sense of a momentum dependent phase relation between the amplitudes of the wave functions in the two sublattices. This leads to a special *spinor* like character to the non relativistic electrons wave function. These are at the heart of several phenomena, including Zitterbewegung, Klein tunnelling, antilocalization, parity anomaly and so on. Further, the small spin orbit coupling can make use of the above structure and lead to *spin Hall effect* as predicted by Kane and Mele [12].

Honeycomb lattice offers some special type of topological defects, such as Stone-Walls defect, containing a pentagon and heptagon ring. It has been shown that an isolated pentagon or heptagon defect act like Z_2 gauge fields, as far as electron dynamics is concerned. It has been suggested that even lattice strain acts like an effective magnetic field.

Since graphene is a two dimensional electronic system, it provides opportunity to study quantum Hall phenomena. As far as integer quantum
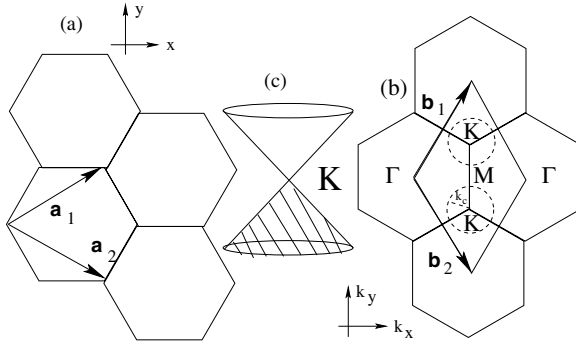
Fig. 2. (a) Honeycomb lattice of carbon atoms in real space; $\mathbf{a}_{1,2} = \frac{a}{2}(\sqrt{3}, \pm 1)$ (b) K-space and the Brillouin Zone; $\mathbf{b}_{1,2} = \frac{2\pi}{a}(\frac{1}{\sqrt{3}}, \pm 1)$ (c) Dirac cone spectrum at a K point.

Hall effect is concerned there is an extra Berry phase in the problem, leading to a general half integer shift in the quantized Hall conductance. Because of the extra degeneracy (flavor index) the nature of fractional and integer quantum Hall effect becomes richer. Recently fQHE and filling $\frac{1}{3}$ and a many body quantum Hall state in neutral graphene have been experimentally observed. Further, the band parameters are such that one gets room temperature quantized Hall effect. There is also a possibility of composite fermi sea that we will see later. If the composite fermi sea starts supporting paired quantum Hall state, we will have the possibility of producing Non Abelian quasi particle, which are very desirable to implement topological quantum computation.

Electromagnetic absorption property by graphene is remarkable. Theory and experiment shows that the absorption coefficient is $\pi\alpha$, where α is the fine structure constant. In other words there is no dependence on material properties such as electron density or lattice parameters, Soft flexural modes trap electrons and holes, leading to charge puddles. There is magnetism at graphene edge [13], spin-1 collective mode at the bulk. Graphene, after appropriate doping is predicted to become a room temperature superconductor. High temperature ferromagnetism has been also reported.

In what follows we will summarise our own predictions for graphene exhibiting the possible richness of graphene. They are manifestations of a simple underlying chemical property namely sp^2 bonding and electron electron interaction, leading to complex consequences as shown in Fig. 1.

2. Spin-1 Collective Mode

Graphene is a broad band semimetal. The band width is of the order of
16 eV. Electron correlation in graphene is weak. This because, in a re-
pulsive Hubbard model description for graphene, on site interaction energy
U $\sim$ 3 to 5 eV, is much smaller than the band width. However graphene
is a lower dimensional, that is, 2 dimensional metal. Are there important
consequences of electron electron interaction in graphene because of 2 di-
mensionality, even though electron correlation is weak? It is well known
that lower the dimension the more important is the effect of electron elec-
tron interactions.

A striking example is benzene, a pπ bonded system, whose quantum
chemical parameters are very similar to graphene. Benzene has a singlet
ground state. The first excited, a spin-1 exciton, is at about 2 eV and the
next excited state is at about 5 eV, a spin singlet exciton. Such a large
splitting arises from exchange and correlation effects, usually ignored in
simple Debye-Huckel or band theory. It is also known that as we go to
larger pπ bonded molecules such as anthracene, pentacene, fullerene etc.,
the singlet triplet splitting survives. A natural question is, what happens to
the spin-1 exciton as we add more and more carbon atoms and reach the end
namely graphene? Does it survive as a separate spin-1 branch excitation in
the entire or part of the Brillouin zone; or completely disappears into the
particle-hole continuum of the semi metal?

Along with Jafari we examined [8] this question. We showed that
graphene possesses a new, unsuspected gapless branch of a spin-1 and
charge neutral collective mode. This branch lies below the electron-
hole continuum (Fig. 3); its energy vanishes linearly with momenta as
$\hbar\omega_s \approx \hbar v_F q(1 - \alpha q^2)$ about three symmetry points (Γ,K K') in the BZ
(Fig. 2).

Since graphene interpolates a metal and insulator, our collective mode
can be viewed both from metallic and insulating stand point. In param-
agnetic metals 'zero sound' is a Fermi surface collective mode [14]. The
'charge' as well as the 'spin' degree of a Fermi sea can undergo independent
oscillations. Because of the long range coulomb interaction. The electron-
electron interactions in normal metals do not usually manage to develop
a low energy spin collective mode branch because of the nature of the
particle-hole spectrum. However, *the particle-hole spectrum of 2d graphite
with a 'window' (Fig. 3) provides a unique opportunity for a spin-1 collective
mode branch to emerge in the entire BZ*. From this point of view our spin-1

collective mode is a *spin-1 zero sound* (SZS) of a 2+1 dimensional *massless Dirac sea*, rather than a *Fermi sea*.

From an insulator point of view our collective mode defines a spin-triplet exciton branch. Triplet excitons are well known in insulators, semiconductors and $p\pi$ bonded planar organic molecules; however, they usually have a finite energy gap.

Our spin-1 collective mode may be also thought of as a manifestation of Pauling's [7] RVB state of graphite: the spin-1 quanta is a delocalized triplet bond in a sea of resonating singlets. The gaplessness makes it a long range RVB rather than Pauling's short range RVB. Later we will present an argument to suggest that at low energies the neutral spin-1 excitation might undergo quantum number fractionization into two spin-$\frac{1}{2}$ spinons.

Existence of our gapless spin-1 collective mode branch should influence the spin part of the magnetic susceptibility, rather than the orbital part, which for graphite is diamagnetic, large and anisotropic. Study of spin susceptibility by ESR, NMR and inelastic neutron scattering are good probes to detect the low energy part of our collective modes over a limited energy up to $\sim 50~meV$. A recent observation of 'large internal fields' in oriented pyrolitic graphite by Kopelevich and collaborators [15], in their ESR studies could be due to our low energy spin-1 collective modes around the Γ point in the BZ. Our mode could be probed over a large energy range, by epithermal neutrons and spin polarized electron energy loss spectroscopy (SPEELS) [16]. In view of a wide energy scale associated with the collective modes, probes such as two magnon Raman scattering, ARPES, STM and spin valves [17] should also be tried.

Importance of electron-electron interaction in graphite [18; 19] and related systems [20; 21; 22] has been realized recently and it has lead to several interesting studies and predictions. 2d cuprates with Dirac cone spectrum has been studied in the context of AFM order in the Mott insulating RVB-flux phase, for spin-1 goldstone modes [23] and d-wave superconducting phases, for spin-1 collective modes [24].

Real graphite is a layered semimetal - stacked layer of graphene. The coupling between graphite layers is van der Waals like. However, a small 'coherent' interlayer hopping has been invoked to explain the presence of small electron and hole tubes and pockets, (with 10^{-4} carriers per carbon atom, i.e., a Fermi energy $\epsilon_F \sim 100 - 200K$), responsible for the semi metallic character of graphite.

We start with a 2-dimensional Hubbard model for graphene, which captures the physics of low energy spin dynamics. The Hamiltonian is:

$$H = -t \sum_{\langle i,j \rangle, \sigma} (c^{\dagger}_{i,\sigma} c_{j,\sigma} + h.c) + U \sum_i n_{i\uparrow} n_{i\downarrow} \qquad (1)$$

Here $t \sim 2.5\ eV$ is the nearest neighbor hopping matrix element. While the bare atomic U is more than $10\ eV$, the effective renormalized U can be of the order of $3 - 4\ eV$. We will keep U as a parameter to be fixed by experiments.

The dispersion relation for the π^* and π bands are:

$$\varepsilon_{\mathbf{k}} = \pm t \sqrt{1 + 4\cos\frac{\sqrt{3}k_x a}{2} \cos\frac{k_y a}{2} + 4\cos^2\frac{k_y a}{2}} \qquad (2)$$

with vanishing gaps at the two K points in the BZ (Fig. 2). The particle-hole continuum of excitations is shown in Fig. 3. The 'Dirac cone single particle spectrum' at the Γ and K points makes the particle hole continuum very different from that of a free Fermi gas, or systems with extended Fermi surface. In contrast to Fig. 4, the particle-hole spectrum of a 2d Fermi liquid, our spectrum has a 'window'. *The 'window' is characteristic of a 1d particle-hole spectrum.* In the Hubbard model two particles with opposite spins at a given site repel with an energy U. This means an attraction between an up spin particle and a down spin hole; or an attraction in the spin triplet channel between a particle and a hole. A spin triplet particle-hole pair could form a bound state, provided there is sufficient phase space for the attractive scattering. We find one spin-1 bound state for every center of mass momentum of the particle-hole pair. In particular an effective 1d character of phase space also makes the collective mode energy vanish linearly with momenta around the three points: Γ and K's.

The collective mode that we are after are obtained as the poles of the particle-hole response function in the spin triplet channel. We will focus on the zero temperature case. The magnetic response function within the RPA (particle-hole ladder summation) is given by:

$$\chi(\mathbf{q}, \omega) = \frac{\chi^0(\mathbf{q}, \omega)}{1 - \upsilon(\mathbf{q})\chi^0(\mathbf{q}, \omega)} \qquad (3)$$

For Hubbard type on site repulsion, $\upsilon(\mathbf{q}) = U$ and the *free particle* susceptibility is :

$$\chi^0(\mathbf{q}, \omega) = \frac{1}{N} \sum_{\mathbf{k}} \frac{f_{\mathbf{k+q}} - f_{\mathbf{k}}}{\omega - (\varepsilon_{\mathbf{k+q}} - \varepsilon_{\mathbf{k}})} \qquad (4)$$
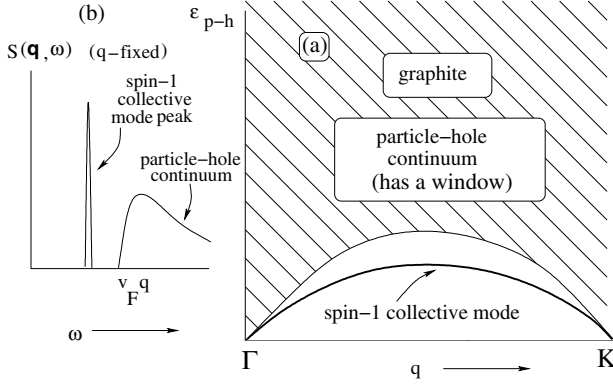
Fig. 3. (a) Particle-hole continuum with a 'window' for graphite. (b) $S(\mathbf{q}, \omega)$ for $q > q_c (\sim \frac{1}{50} \frac{\pi}{a})$.
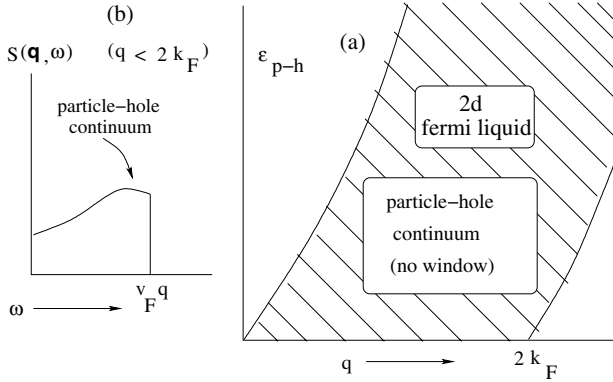
Fig. 4. (a) Particle-hole continuum without a 'window' for a 2d fermi gas. (b) $S(\mathbf{q}, \omega)$ for $q < 2k_F$.

Here f's are the Fermi distribution functions. We have evaluated the RPA response function numerically and found the collective mode branch in the entire BZ, below the particle-hole continuum. However, it is instructive to linearize the electron and hole dispersion for low energies, a Dirac cone approximation [18], and get an analytical handle. We linearize the dispersion around K and K' and replace the BZ by two circles of radii k_c (Fig. 2):

$$\varepsilon_{\mathbf{k}} = \pm v_F \mid \mathbf{k} \mid \quad \text{for} \quad k < k_c \tag{5}$$

where $v_F = \frac{\sqrt{3}}{2}t$ and N is the number of unit cells. In our linearization scheme, in Eq. (4) the summation is over the two circular patches (Fig. 2).

For a finite range of q and ω, $Im\ \chi^0(\omega, \mathbf{q})$ can be evaluated exactly [18]:

$$Im\ \chi^0(\mathbf{q}, \omega) = \frac{1}{16v_F^2} \frac{2\omega^2 - (qv_F)^2}{\sqrt{\omega^2 - (qv_F)^2}} \sim \frac{1}{16\sqrt{2}v_F} \frac{q^{3/2}}{\sqrt{\omega - qv_F}} \quad ,$$

with a square root divergence at the edge of the particle-hole continuum in $(\omega, \mathbf{q})$ space. This expression has the same form as density of states of a particle in $1D$ (with energy measured from $v_F q$). Note that in fact $Im\ \chi^0(q, \omega) = \pi\rho_q(\omega)$, where $\rho_q(\omega)$ is free particle-hole pair DOS for a fixed center of mass momentum q. *That is, the particle-hole pair has a phase space for scattering which is effectively one dimensional.* Thus we have a particle-hole bound state in the spin triplet channel for arbitrarily small U. However, we also have a prefactor $q^{3/2}$, that scales the density of states. This together with the square root divergence of the density of states at the bottom of the particle-hole continuum gives us a bound state for every q as $q \to 0$, with the binding energy vanishing as αq^3, as shown below. The square root divergence has the following phase space interpretation. The constant energy $(\hbar\omega)$ contour of a particle-hole pair of a given total momentum q defines an ellipse in k-space: $\omega = v_F(|\ \mathbf{k} + \mathbf{q}\ | + |\ \mathbf{k}\ |)$. In our convention, the points on the ellipse denote the momentum co-ordinates of the electron of the electron-hole pair. As the energy of the particle-hole pair approaches the bottom of the continuum, i.e., $\epsilon_{p-h} \to v_F q$, the minor axes of the ellipses become smaller and smaller and the elliptic contours degenerate into parallel line segments of effective length $\sim q^{\frac{3}{2}}$. The asymptotic equi-spacing of these line segments leads to an effective one-dimensionality and the resulting square root divergence.

The collective mode in *magnetic* channel is the solution of:

$$1 - U\chi^0(\mathbf{q}, \omega) = 0$$

or equivalently, $Im\ \chi^0(\mathbf{q}, \omega) = 0$ and $Re\ \chi^0(\mathbf{q}, \omega) = \frac{1}{U}$. The asymptotic expression for $Re\ \chi^0(\mathbf{q}, \omega)$ is found to be

$$Re\ \chi^0(\mathbf{q}, \omega) \approx \frac{1}{4\pi^2 v_F}(k_c + \frac{\sqrt{2}}{\sqrt{1-z}} \arctan{(\frac{\sqrt{2}}{\sqrt{1-z}})})$$

where $z \equiv \frac{\omega}{qv_F}$. Using the above expression we obtain the following dispersion relation for the collective mode:

$$\omega = qv_F - \frac{q^3}{32\pi^2 v_F (\frac{1}{U} - \frac{k_c}{4\pi v_F})^2} \equiv qv_F - E_B(q)$$

as $\omega \to q \to 0$. Here $E_B(q)$ is the *binding* energy of the particle-hole pair of momentum q around the Γ point. The binding energy around the K points is roughly half of this.

We mentioned earlier that our collective mode is a 'magnetic zero sound'. While magnetic zero sound are difficult to get in normal metals, graphite manages to get it in the entire BZ because of the window in the particle-hole spectrum (Fig. 3).

Having established the existence of a gapless spin-1 collective mode branch within Hubbard model and the RPA approximation, we will discuss whether the semi-metallic screened interaction in the 3 dimensional stacked layers will affect our result. As mentioned earlier, in tight binding situation like ours, the spin physics is mostly captured by the short range part of the repulsion among the electrons. We have numerically studied the response function for a more realistic intra layer interaction namely the screened coulomb interaction (including interlayer scattering between layers separated by distance d) given by [18]

$$\tilde{v}(\omega, q) = \frac{2\pi e^2}{\epsilon_0 q} \frac{\sinh(qd)}{\sqrt{[\cosh(qd) + \frac{2\pi e^2}{\epsilon_0 q} \sinh(qd)\chi_0(\omega, q)]^2 - 1}}$$

and find that the collective mode survives with small quantitative modifications.

Let us discuss life time effects, that is beyond RPA. A remarkable feature of our collective modes is that it never enters the particle-hole continuum. It does not suffer from Landau damping (resonant decay into particle-hole pair excitations). To this extent our collective modes are sharp and protected; higher order processes will produce the usual life time broadening, particularly at the high energy end. However, in real graphite there are tiny electron and hole pockets in the BZ with a very small Fermi energy ~ 10 to 20 meV. This leads to 'Landau damping' of low energy collective modes around the Γ and K points, but only in a small momentum region $\Delta k \sim 2k_F \sim \frac{1}{50}\frac{\pi}{a}$, where k_F is the mean Fermi momentum of the electron and hole pockets. That is, only a few percent of the collective mode branch in the entire BZ is Landau damped.

A small interlayer hopping between neighboring layers $t_\perp \sim 0.2~eV$ ($<< 2.5~eV$, the in plane hopping matrix element), has been always invoked in the band theory approaches to understand various magneto oscillation experiments and also c-axis transport in graphite. However, a strong renormalization of $t_\perp$ is possible, as anomalously large anisotropic resistivity ratio $\frac{\rho_c}{\rho_{ab}} \sim 10^4$ have been reported in some early experiments on graphite single crystals; a many body renormalization is also partly implied by the existence of our spin-1 collective mode at low energies. As the emergence of the small electron and hole pockets (cylinders) are due to interlayer hopping, interlayer hopping affect the spin-1 collective modes only in a small window of energy 0 and $\sim 0.1~eV$. For the same reason the collective modes do not have much dispersion along the c-axis.

Within our RPA analysis the collective mode frequency becomes negative at the Γ point for $U > U_c \sim 2t$. Because there are two atoms per unit cell, this could be either an antiferromagnetic or ferromagnetic instability. Other studies [22; 25] have indicated an AFM instability for $U > U_c \sim 2t$.

Now we discuss the experimental observability of spin-1 collective mode branch. The collective mode has a wide energy dispersion from 0 to $\sim 2~eV$. The low energy 0 to 0.05 eV part of the collective modes determines the nature of the spin susceptibility (Eq. (3)) of graphite and leaves its signatures in NMR and ESR results. For higher energies we have to use other probes.

Inelastic neutron scattering can be used to study the line shapes and dispersion of our spin-1 collective modes. However, epithermal neutrons in the energy range 0.1 eV to $\sim 1~eV$, rather than the cold and thermal, 0.2 to 50 meV, neutrons is needed in our case, due to the large energy dispersion. The dynamic structure factor $S(\mathbf{q}, \omega)$ as measured by inelastic neutron scattering is obtained by using our calculated RPA expression for our magnetic response function using the relation:

$$(1 - e^{-\beta\omega})~S(\mathbf{q}, \omega) = -\frac{1}{\pi}~Im~\chi(\mathbf{q}, \omega) \qquad (6)$$

Another probe for studying the spin-1 collective mode is the spin polarized electron energy loss spectroscopy (SPEELS); exchange interaction of the probing electron with the π-electrons of graphite can excite the spin-1 collective mode. As the electron current and spin depolarization essentially measures the magnetic response function, our calculation of $\chi(\mathbf{q}, \omega)$ (Eq. (2)) can be profitably used to interpret the experimental results.

The square root divergence of density of states at the bottom edge of the particle-hole continuum tells us that *the low energy spin physics is*

effectively one-dimensional. To that extent, *in a final theory*, we may expect our spin-1 excitation to be a triplet bound state of 'two neutral spin$-\frac{1}{2}$ spinons' rather than 'e^+e^- electron-hole pairs'. Further, as the energy of the spin-1 quantum approaches zero the binding energy also approaches zero and the electron-hole bound state wave function becomes elliptical, with diverging size. We may then view the low energy spin-1 quanta as a 'critically (loosely) bound' two spinon state, very much like the quantum number fractionization of the des Cloizeaux-Pearson spin-1 excitation in the 1d spin-$\frac{1}{2}$ antiferromagnetic Heisenberg model. Our result also suggest a non-linear sigma model and novel $2 + 1$ dimensional bosonization scheme for graphite [26].

We find [27] that our spin-1 collective mode survives in carbon nanotubes in a modified fashion. Preliminary study shows that three dimensional semimetals Bi, HgTe and α-Sn do not have spin-1 collective modes at low energies, because of quadratic dispersion at the zero gap.

3. Relativistic Type Effects

Phenomena unique to relativistic quantum field theories, such as Klein tunnelling and Zitterbewegung, have been predicted [3] to occur in graphene, because of the mathematical similarity of the graphene electron dynamics to dynamics of massless Dirac electrons in $2 + 1$ dimensions, with fermi velocity playing the role of light velocity. Partly keeping the above in mind, along with Lukose and Shankar [28] we investigated the effect of a uniform electric field, applied along the graphene sheet, on its already anomalous Landau level spectrum. We find that, within the low energy approximation near the Fermi surface (Dirac points), the problem can be exactly solved. *We find strikingly new effects of electric field on the Landau levels which is different from the Landau levels of standard 2d electron gas.* What we find can be termed as analogue of Lorenz boost, Lorenz contraction and time dilation that one is familiar in the context of special theory of relativity.

We find that the Landau spectrum gets scaled, for a given k_y quantum number, by an electric field dependent dimensionless parameter($\beta = \frac{E}{v_F B}$). As the value of this parameter is increased, spacings between the Landau levels decreases. This Landau level contraction is consequence of electric field induced quantum mechanical mixing of Landau levels. The entire Landau level structure collapses at a critical value of this parameter. Further, the 'relativistic' character of the spectrum (with Fermi velocity replacing the velocity of light), leads to a novel interpretation of our result in terms of

relativistic boosts and the mixing of electric and magnetic fields in moving frames of reference.

The dispersion relation in the proximity of the Dirac points is linearly proportional to $|\mathbf{k}|$. The low energy modes around these points are described by slowly varying fields fermi fields $\psi_{r\eta\sigma}(\mathbf{R}_i)$ defined as,

$$c_{ir\sigma} = e^{i\mathbf{K}_1 \cdot \mathbf{R}_i} \alpha^z_{rr'} \psi_{r'1\sigma}(\mathbf{R}_i) + e^{i\mathbf{K}_2 \cdot \mathbf{R}_i} \alpha^x_{rr'} \psi_{r'2\sigma}(\mathbf{R}_i) \tag{7}$$

Where α^x, α^y are the Pauli matrices. Here i refers to the unit cell and r = 1,2 refers to the two types of atoms in each unit cell. The effective Hamiltonian for the low energy modes is the Dirac Hamiltonian.

$$H = v_F \int d^2x \sum_{\eta\sigma} \Psi^\dagger_{\eta\sigma} \, \boldsymbol{\alpha} . \mathbf{p} \, \Psi_{\eta\sigma} \tag{8}$$

where $v_F = \frac{\sqrt{3}}{2} \frac{at}{\hbar}$ is the Fermi velocity. $\Psi_{\eta\sigma}$ are two component field operators where $\eta(= 1, 2)$ is the valley index, corresponds to two Dirac points and $\sigma(=\uparrow, \downarrow)$ is the spin index. The spectrum can be obtained by solving the one particle equation to get the linear dispersion, $\epsilon(\mathbf{k}) = \pm \hbar v_F |\mathbf{k}|$. In presence of an external magnetic field perpendicular to the graphene plane the one particle Hamiltonian, $h = v_F \boldsymbol{\alpha}.\boldsymbol{\Pi}$, where $\boldsymbol{\Pi} = \mathbf{p} + e\mathbf{A}$. The energy eigenvalues are

$$\epsilon_{n,k_y} = \text{sgn}(n) \sqrt{2|n|} \frac{\hbar v_F}{l_c} \tag{9}$$

n is the Landau level index, $k_y = \frac{2\pi}{L_y} l$ is the quantum number corresponding to translation symmetry along y-axis, both n and l are integers (we choose Landau gauge $\mathbf{A}(\mathbf{r}) = xB\,\hat{\mathbf{y}}$) and $l_c = \sqrt{\frac{\hbar}{eB}}$ is the magnetic length. Unlike the case of the non-relativistic electron in a magnetic field, where the spectrum has a linear dependence on the magnetic field and the non-negative integer valued Landau level index, the graphene Landau levels have a square root dependence on both magnetic field and Landau level index. The degeneracy of each level is given by the number of magnetic flux quanta passing through the sample. The eigenfunctions are,

$$\psi_{nk_y}(x,y) \propto e^{ik_y y} \begin{pmatrix} \text{sgn}(n)\,\phi_{|n|-1}(\xi) \\ i\,\phi_{|n|}(\xi) \end{pmatrix} \tag{10}$$

where $\phi_n(\xi)$ are the harmonic oscillator eigen-functions and $\xi \equiv \frac{1}{l_c}\left(x + l_c^2 k_y\right)$.
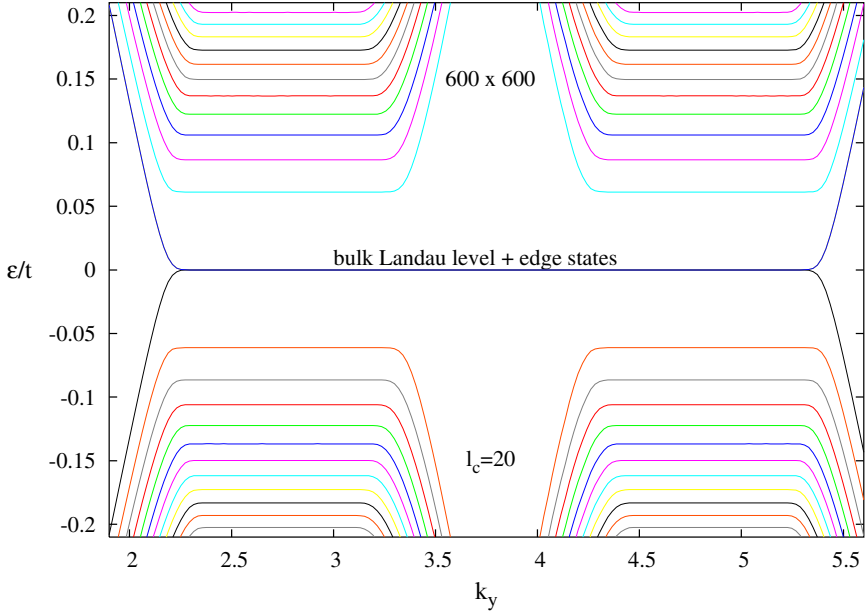
Fig. 5. Energy eigenvalues ϵ_{n,k_y}, for electrons in graphene computed from the tight binding model for a hexagonal lattice subjected to a magnetic field $B = 27.3$ Tesla (or $l_c = 20\,a$ where a is the triangular lattice spacing) for a system size of $600a \times 600a$. The plot shows ϵ_{n,k_y} in the units of t as function of k_y, where k_y is the wavevector in the y direction. Two sets of horizontal lines are Landau levels corresponding to the two valleys and $n = 0$ Landau level and the edge states are degenerate.

We now consider the above system in the presence of an additional constant electric field applied, in a open circuit geometry, along the x-direction. The single particle Hamiltonian is then given by,

$$h = v_F \boldsymbol{\alpha}.\boldsymbol{\Pi} + \mathbf{1}eEx \qquad (11)$$

The Lorentz covariant structure of the Hamiltonian, with v_F playing the role of the speed of light, can be used to solve the problem exactly [29]. It is known from special relativity, if $v_F B > |\mathbf{E}|$, then we can always boost to a frame of reference where the electric field vanishes and the magnetic field is reduced. We can then use the finite magnetic field and zero electric field solution to Dirac equation and boost it to get the exact spectrum in the presence of crossed electric and magnetic field. Here the boost transformation amounts to doing a transformation on the space-time coordinate

system. To implement the above procedure, it is convenient to work with the manifestly covariant time dependent Dirac equation,

$$i\hbar\gamma^{\mu}(\partial_{\mu} + i\frac{e}{\hbar}A_{\mu})\Psi(x^{\mu}) = 0 \tag{12}$$
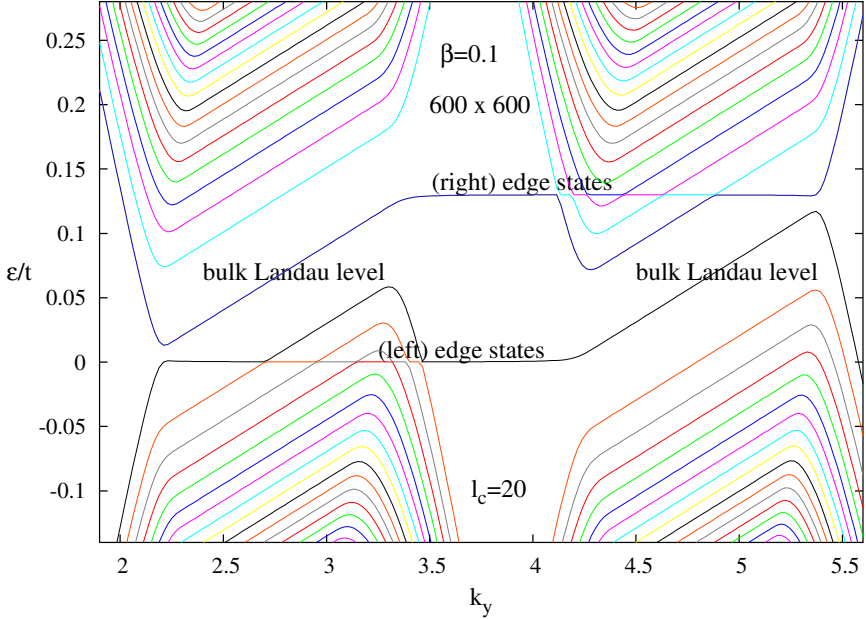
Fig. 6. Energy eigenvalues ϵ_{n,k_y} for electrons computed for the tight binding model for parameters given in Fig. 5 and an external electric field E applied along x-axis, given by the parameter $\beta = \frac{E}{v_F B} = 0.1$. The electric field gives a linear k_y dependence to the bulk Landau levels whereas it gives a constant shift to the edge states. The part of solid line labelled 'bulk Landau level' are $n = 0$ Landau levels and parallel lines above and below them are Landau levels corresponding to positive and negative n respectively. Set of points parallel to k_y labelled 'edge states' are surface states localised at the zig-zag boundary.

Where $x^0 = v_F t$, $x^1 = x$, $x^2 = y$, $\gamma^0 = \alpha^z$, $\gamma^1 = i\alpha^y$, $\gamma^2 = -i\alpha^x$, $\partial_{\mu} = \frac{\partial}{\partial x^{\mu}}$. $A^0 = \phi$, the scalar potential, $A^1 = A_x$, $A^2 = A_y$ and $\Psi(x^{\mu})$ is a two component spinor. We now apply a Lorentz boost in the y-direction (perpendicular to the electric field),

$$\begin{pmatrix} \tilde{x}^0 \\ \tilde{x}^2 \end{pmatrix} = \begin{pmatrix} \cosh\theta \ \sinh\theta \\ \sinh\theta \ \cosh\theta \end{pmatrix} \begin{pmatrix} x^0 \\ x^2 \end{pmatrix} \tag{13}$$

and $\tilde{x}^1 = x^1$. The wave function transforms, $\tilde{\Psi}(\tilde{x}^\mu) = e^{\frac{\theta}{2}\alpha_y}\Psi(x^\mu)$. Applying the above transformations and choosing $\tanh\theta = \frac{E}{v_F B} = \beta$, we can rewrite the Dirac equation in Eq. (12),

$$\left(\gamma^0\tilde{\partial}_0 + \gamma^1\tilde{\partial}_1 + \gamma^2(\tilde{\partial}_2 + \frac{i}{l_c^2}\sqrt{1-\beta^2}\,\tilde{x}^1)\right)\tilde{\Psi}(\tilde{x}^\mu) = 0 \tag{14}$$

In the boosted coordinates, where $|\beta| < 1$, it is a problem of a Dirac electron in a (reduced) magnetic field, $\tilde{B} = B\sqrt{1-\beta^2}$. The time component of the 3-momentum in the boosted frame, $\tilde{\epsilon}_{n,\tilde{k}_y} = \text{sgn}(n)\sqrt{2|n|}\frac{\hbar v_F}{l_c}(1-\beta^2)^{\frac{1}{4}}$ is not the physical energy eigenvalue of our problem. We have to apply the inverse boost transformation to obtain the spectrum and eigen functions of our problem,

$$\epsilon_{n,k_y} = \text{sgn}(n)\sqrt{2|n|}\frac{\hbar v_F}{l_c}(1-\beta^2)^{\frac{3}{4}} - \hbar v_F \beta k_y \tag{15}$$

$$\Psi_{n,k_y}(x,y) \propto e^{ik_y y}e^{-\frac{\theta}{2}\alpha_y}\begin{pmatrix} \text{sgn}(n)\,\phi_{|n|-1}(\xi') \\ i\,\phi_{|n|}(\xi') \end{pmatrix} \tag{16}$$

$$\xi' \equiv \frac{(1-\beta^2)^{\frac{1}{4}}}{l_c}\left(x + l_c^2 k_y + \text{sgn}(n)\frac{\sqrt{2|n|}\,l_c\beta}{(1-\beta^2)^{\frac{1}{4}}}\right) \tag{17}$$

The energy eigenvalues of the standard $2d$ electron gas in crossed magnetic and electric fields are given by $\epsilon_{n,k_y} = (n+\frac{1}{2})\hbar\omega_c - \hbar k_y \frac{E}{B} - \frac{m}{2}(\frac{E}{B})^2$. The main difference between the two besides the $\sqrt{n}$ and $\sqrt{B}$ dependence, is that *the low lying graphene Landau level spacing scales as* $(1-\beta^2)^{\frac{3}{4}}$, whereas the spacing is independent of the electric field in the non-relativistic case. Comparing the eigenfunctions with and without the electric field, we see that the effect of the electric field is to (un)squeeze the oscillator states as well as to mix the particle and hole wave-functions.

Squeezing of the wave function results from change in l_c in an anisotropic fashion. In the standard 2d electron gas, electric field does not cause squeezing of the wave function. We can view the squeezing of wave function as *Lorenz Contraction*. Similarly squeezing of the Landau levels can be viewed as *time dilation*. For example, the energy level difference between n and (n + 1) Landau levels may be viewed as a level dependent cyclotron frequency and a corresponding period for cyclotron motion $T_n = \frac{\hbar}{\epsilon_{n+1}-\epsilon_n}$. In the presence of additional electric field we have the increase in the time period to $\frac{T_n^0}{(1-\beta^2)^{\frac{3}{4}}}$. We view the increase in cyclotron motion period as *time dilation*.

As β approaches unity, we infer that, to keep the gaussian shifts within the linear extent of the system requires larger values of k_y, which takes us beyond the long wavelength approximation. Moreover, we have a collapse of the Landau level spectrum at $\beta = 1$. One may wonder if the collapse we have found is an artifact of the low energy approximation? Interestingly, we find that in our full tight binding calculation the collapse persists, and infact it occurs at a value of β even smaller than unity.

We have performed extensive numerical computations on the tight binding model for graphene with magnetic and electric fields, using lattice sizes ranging from 60×60 to 600×600. The magnetic field enters through the Peierls substitution, $t \rightarrow t\, e^{i\frac{2\pi e}{\hbar}\int \mathbf{A}.d\mathbf{l}}$. $\mathbf{A}(\mathbf{r})$ is chosen in such a way that the contribution to the phase term comes from hopping along one of the three bonds for each carbon atom. This enables us to maintain translation symmetry along the $\hat{\mathbf{e}}_2$ axis of the triangular lattice. The problem then reduces to the 1D Harper equation.

$$\epsilon\phi_{1,n_1} = 2t\cos(\frac{k_2 a + n_1 \varphi}{2})\phi_{2,n_1} + t\phi_{2,n_1+1}$$
$$\epsilon\phi_{2,n_1} = 2t\cos(\frac{k_2 a + n_1 \varphi}{2})\phi_{1,n_1} + t\phi_{1,n_1-1} \qquad (18)$$

Here φ is the magnetic flux passing through each plaquette, k_2 is the wave vector and n_1 is the $\hat{\mathbf{e}}_1$ component of triangular lattice coordinate.

We choose the value of the magnetic field such that $L \gg l_c \gg a$, where L is the linear extent of the system. The condition $l_c \gg a$ ensures that we stay away from the Hofstadter butterfly kind of commensurability effects on the spectrum and $L \gg l_c$ ensures that a large number of cyclotrons orbits fit in the sample. For our numerics, we expressed all energies in units of t and all lengths in units of a.

Figure 5 shows the results of our numerical investigation for zero and Fig. 6 for a finite ($\beta = 0.1$) electric fields. Figure 5 shows the spectrum at low energies and the eigenvalues that are constant w.r.t k_y are the Landau levels. They have $\sqrt{n}$ behaviour and are in excellent agreement with the analytical result and the eigenstates that vary with k_y are the chiral edge states responsible for the quantum Hall current. In our numerics the lattice has zig-zag edges at the two ends along $\hat{\mathbf{e}}_1$.

Figure 7(b), shows $\sqrt{n}$ scaling of Landau levels for a given k_y value. For zero electric field we see an excellent match between analytics and numerics. And for the case of finite electric fields we see a systematic deviation from exact results as we suspected from our exact result. As $\beta \rightarrow 1$, the tight
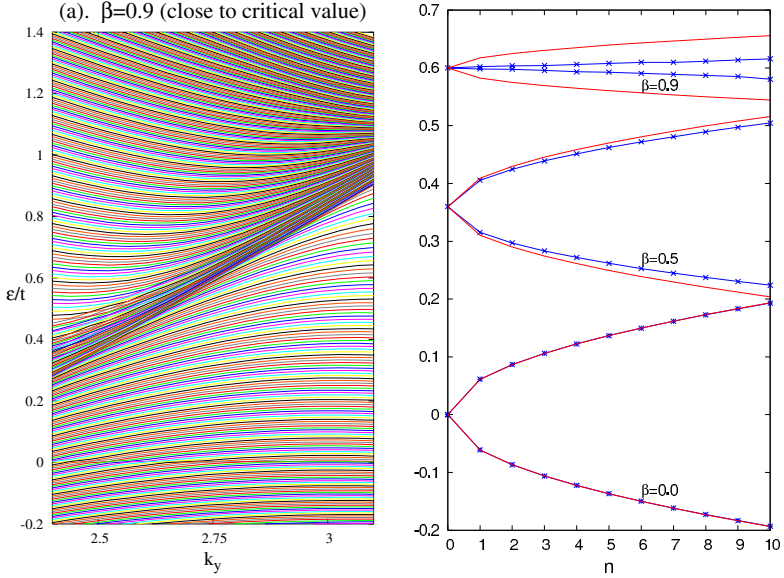
Fig. 7. (a) The energy eigenvalues around the Dirac point plotted as function of k_y for $\beta = 0.9$. The collapse can be clearly seen. (b) The modulus of the eigenvalues $|\epsilon_{n,k_y}|$ for a value of $k_y = 2.785$ computed from the tight binding model for system size $600a \times 600a$, magnetic field $B = 27.3\, Tesla$ or $l_c = 20\, a$, electric field given by parameter $\beta = 0.0, 0.5, 0.9$, plotted as a function of n.

binding results shows a faster collapse. Figure 7(a) shows the collapse has already occurred at $\beta = 0.9$, near one of the Dirac points.

We show below that one of the consequences of the Landau level contraction (15) and the n dependent Gaussian shift (17) is the possibility of a 'dielectric breakdown', which is different from the conventional ones. The single particle spectrum and states we have obtained thus far (for a given E and B) can be used to construct stable many-body quantum Hall ground states. However, the external electric field not only modifies the single particle wave function and spectrum, but can also destabilise the ground state through spontaneous creation of particle-hole pairs; i.e., by a dielectric breakdown. This problem is analogue of relativistic vacuum break down through pair production.

We present a simple formula for dielectric breakdown, without giving full details. It has an unusual dependence on the length scale over which the potential fluctuates and on the Landau level index n. This peculiar feature is absent in standard quantum $2d$ electron systems [31]. Specifically we find

that for slowly varying electric field fluctuations over a length scale ℓ_E and for large Landau level index, the critical voltage for breakdown is given by:

$$V_c \approx \frac{\Delta_n(0, B)}{e} \left(1 \pm \kappa\, n \left(\frac{l_c}{\ell_E} \right)^2 \right) \qquad (19)$$

where κ is a constant of the order of unity, which depends on the strength of the electric field fluctuations and Δ_n is the gap between levels n and $n+1$. This means that if we have an electric field, non-uniform over a nanoscopic scale ($\ell_E \sim l_c$), it will cause local breakdown even before the critical field is reached. Such situations can be created through in plane or out of plane charged impurities or STM tips, in addition to external electric fields. It is interesting that such an anomalous local breakdown is Landau level index n dependent, we expect that the quantum Hall breakdown should be qualitatively different for $n = 0$ and $n \neq 0$ within graphene.

In the light of new spectroscopic experiments [32], we claim that the contraction in Landau level spacing and the collapse can be observed at fields attainable in laboratories. The gap between $n = 0$ and $n = 1$ for $B \sim 1\,\mathrm{Tesla}$ is ~ 35 meV, for $E \sim 3 \times 10^5\,Vm^{-1}$, 10% reduction in the gap is expected. And the collapse of the Landau levels should also be observeable by applying $E \sim 10^6\,Vm^{-1}$. In the context of quantum Hall breakdown, the dependence of critical voltage on ℓ_E as given in Eq. (19) suggests that the breakdown phenomena should be different from what we observe in standard $2d$ quantum Hall system. Moreover graphene's Landau level index dependence on V_c, we expect the breakdown phenomena is going to be different for $n \neq 0$ from that of $n = 0$.

It will be interesting to study graphene from the point of view of the present paper. As quantum Hall phenomena are beginning to be seen in pyrolytic graphite [33] and possibly in carbon eggshells [34], it will be very interesting to study electric field effects in these systems as well, to confirm our predictions.

4. Possibility of Room Temperature Superconductivity in Optimally Doped Graphene

Superconductivity at room temperatures, with its multifarious technological possibilities, is a phenomenon that is yet to be realized in a material system. The search for such systems has lead to the discovery of *high temperature* superconducting materials such as the fascinating cuprates, [35; 36] MgB_2 [37] and most recently, Fe-based pnictides. [38] Undoped graphene

is a semi-metal and does not superconduct at low temperatures. However, on *doping optimally* if graphene supports high T_c superconductivity it will make graphene even more valuable from basic science and technology points of view. In a recent work [9], along with Pathak and Shenoy we built on a seven year old suggestion of us [39] of an electron correlation based mechanism of superconductivity for graphite like systems and demonstrate theoretically the possibility of high temperature superconductivity in *doped* graphene.

We [39] suggested the possibility of high temperature superconductivity in graphene and related systems based on an effective phenomenological Hamiltonian that combined band theory and Pauling's idea of resonating valence bonds (RVB). The model predicted a vanishing T_c for undoped graphene, consistent with experiments. However, for doped graphene superconducting estimates of T_c's were embarrassingly high. Very recently Black-Schaffer and Doniach [40] used our effective Hamiltonian and studied graphitic systems and found that a superconducting state with $d + id$ symmetry to be the lowest energy state in a mean field theory. The mean field theory also predicts a rather high value of the optimal T_c. Other authors have studied possibility of superconductivity based on electron-electron and electron-phonon interactions. [41; 42; 43; 44] While there is an encouraging signal for high T_c superconductivity in our phenomenological model, it is important to establish this possibility by the study of a more basic and realistic model. Since the motivation for our model arose from a repulsive Hubbard model, here we directly analyse this more basic repulsive Hubbard model that describes low energy properties of graphene. We construct variational wavefunctions motivated by RVB physics, and perform extensive Monte Carlo study incorporating crucial correlation effects. *This approach which has proved to be especially successful in understanding the ground state of cuprates, clearly points to a superconducting ground state in doped graphene.* Further support is obtained from a slave rotor analysis which also includes correlation effects. Our estimate of the Kosterlitz-Thouless superconducting T_c is of the order of room temperatures, and we also discuss experimental observability of our prediction of high temperature superconductivity in graphene.

Let us discuss the Hubbard model for graphene. The Hubbard U is about half the $p\pi$ free bandwidth, and this places graphene in an intermediate or weak coupling regime. Based on this one is tempted to conclude that electron correlations are not important. Nonetheless electron correlations are known to be important in finite $p\pi$ bonded planar molecular

systems such as benzene, naphthane, anthracene, caronene etc, all having nearly the same value for quantum chemical parameters t and U. [45] One of the consequences of this is that the first excited spin-0 state lies above the first excited spin-1 state by more than 2 eV. There is a predictable consequence of this large singlet-triplet splitting: graphene can be viewed as an end member of a sequence of planar $p\pi$ bonded system.

As we mentioned earlier, Pauling [7] was the first to recognize dominance of singlet correlation between two neighboring $p\pi$ electrons in the ground state. He argued that doubly occupied or empty $2p_z$ orbitals (polar configurations) are less important because of electron-electron repulsion in the $2p_z$ orbital. Pauling thus ignored polar configurations. Once we ignore polar fluctuations (states with double occupancy) and consider a resonance among the nearest neighbor valence bond configurations we get the well known RVB state. However, such a Hilbert space actually describes a Mott insulating state rather than a metal. Experimentally, undoped graphene is a broad band conductor, albeit with a linearly vanishing density of states at the Fermi energy.

To recover metallicity in Pauling's RVB theory, we combined the broad band feature of $p\pi$ electrons with Pauling's real space singlet (covalent) bonding tendency and suggested [39] a low energy phenomenological model for graphene:

$$\mathcal{H}_{GB} = -\sum_{\langle ij \rangle} t_{ij} c_{i\sigma}^\dagger c_{j\sigma} + h.c. - J \sum_{\langle ij \rangle} b_{ij}^\dagger b_{ij} \qquad (20)$$

where $b_{ij}^\dagger = \frac{1}{\sqrt{2}} \left(c_{i\uparrow}^\dagger c_{j\downarrow}^\dagger - c_{i\downarrow}^\dagger c_{j\uparrow}^\dagger \right)$ creates a spin singlet on the $i-j$ bond. $J \, (>0)$ is a measure of singlet or valence bond correlations emphasized by Pauling, i. e., a nearest neighbour attraction in the spin singlet channel. In the present paper we call it as a 'bond singlet pairing' (BSP) pseudo potential. The parameter J was chosen as the singlet triplet splitting in a 2 site Hubbard model with the same t and U, $J = ((U^2 + 16t^2)^{1/2} - U)/2$. As U becomes larger than the bandwidth this psuedo-potential will become the famous superexchange characteristic of a Mott insulator. As shown in [39], this model predicts that undoped graphene is a "normal" metal. The linearly vanishing density of states at the chemical potential engenders a critical strength J_c for the BSP to obtain a finite mean field superconducting T_c. The parameter J for graphene was less than the critical value, and undoped graphene is not a superconductor despite Pauling's singlet correlations. Doped graphene has a finite density of state at the chemical potential and a superconducting ground state is possible. Black-Schaffer

and Doniach [40] confirmed our findings in a detailed and systematic mean field theory and discovered an important result for the order parameter symmetry. They found that the lowest energy mean field solution corresponds to $d+id$ symmetry, an unconventional order parameter, rather than the extended-s solution. The value of mean field T_c obtained was an order of magnitude larger than room temperature!

Although results of the mean-field theory are encouraging, it is far from certain that the superconducting ground state is stable to quantum fluctuations. In particular, our Hamiltonian does not include U which inhibits local number fluctuations. In the more basic Hubbard model, a superconducting state will suffer further quantum mechanical phase fluctuations since U inhibits local number fluctuations. The key question therefore is does the singlet promotion arising out of the local correlation physics strong enough to resist the destruction of superconductivity arising out of quantum phase fluctuations induced by U?
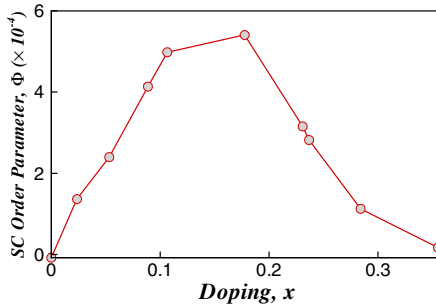
Fig. 8. Strength of superconducting order parameter, as extracted from the Cooper pair correlation function.

To investigate the possibility of superconductivity in doped graphene we construct a variational ground state and optimize it using variational quantum Monte Carlo (VMC). [46] The ground state we construct is motivated by the mean-field theory of our model

$$\mathcal{H}_{GB}^{MF} = \sum_{\mathbf{k}} \left[\varepsilon(\mathbf{k})(a_{\mathbf{k}\sigma}^{\dagger} b_{\mathbf{k}\sigma} + \text{h. c.}) - \mu_f (n_{\mathbf{k}\sigma}^a + n_{\mathbf{k}\sigma}^b) \right]$$
$$- \sum_{\mathbf{k}} \Delta(\mathbf{k})(a_{\mathbf{k}\uparrow}^{\dagger} b_{-\mathbf{k}\downarrow}^{\dagger} - a_{\mathbf{k}\downarrow}^{\dagger} b_{-\mathbf{k}\uparrow}^{\dagger}) + \text{h. c.}$$

where $a_{\mathbf{k}\sigma}, b_{\mathbf{k}\sigma}$ are electron operators on the A and B sublattices, $\mathbf{k}$ runs over the Brillouin zone of the triangular Bravais lattice, $\mathbf{a}_\alpha, \alpha = 1, 2, 3$ are vectors that go from an A site to the three nearest B sublattice sites. The free electronic dispersion is determined by the function $\varepsilon(\mathbf{k}) = -t\sum_\alpha e^{i\mathbf{k}\cdot\mathbf{a}_\alpha}$, and the superconducting gap function $\Delta(\mathbf{k}) = \sum_\alpha \Delta_\alpha e^{i\mathbf{k}\cdot\mathbf{a}_\alpha}$. The $d + id$ symmetry motivated by the meanfield solution [40] provides $\Delta_\alpha = \Delta e^{\frac{i2\pi(\alpha-1)}{3}}$ where Δ is the "gap parameter", μ_f is a "Hartree shift". Starting from this mean field theory, we construct a BCS state $|BCS\rangle_N$ with an appropriate number N of electrons. If we work with a lattice with L sites, this corresponds to a hole doping of $1 - N/L$. Our candidate ground state $|\Psi\rangle$ is now a state with a Gutzwiller-Jastrow factor [47; 48] g

$$|\Psi\rangle = g^{\mathcal{D}}|BCS\rangle_N \tag{21}$$

where $\mathcal{D} = \sum_i(n^a_{i\uparrow}n^a_{i\downarrow} + n^b_{i\uparrow}n^b_{i\downarrow})$ is the operator that counts the number of doubly occupied sites. The wavefunction (21) with partial Gutzwiller projection has three variational parameters: the gap parameter Δ, the Hartree shift μ_f, and the Gutzwiller-Jastrow factor g. The ground state energy $\langle\Psi|\mathcal{H}_H|\Psi\rangle$ is calculated using quantum Monte Carlo method [46], and is optimized with respect to the variational parameters.
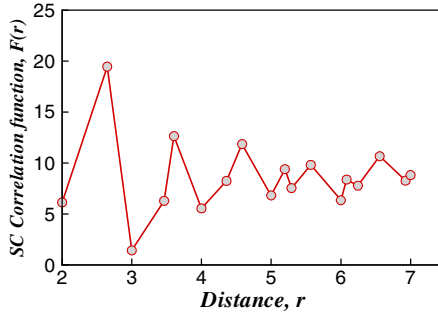
Fig. 9.   Zero temperature coherence length, as extracted from the cooper pair correlation function.

We monitor superconductivity by calculating the following correlation function using the optimized wavefunctions

$$F_{\alpha\beta}(\mathbf{R}_i - \mathbf{R}_j) = \langle b^\dagger_{i\mathbf{a}_\alpha} b_{j\mathbf{a}_\beta}\rangle \tag{22}$$

where $b^\dagger_{i\mathbf{a}_\alpha}$ is the *electron* singlet operator that creates a singlet between the A site in the i-th unit cell and the B site connected to it by the vector

$\mathbf{a}_\alpha$ (this is just $b_{ij}^\dagger$ defined earlier with a minor change of notation). The superconducting order parameter, off-diagonal long range order (ODLRO), is

$$|\Phi|^2 = \lim_{|\mathbf{R}_i - \mathbf{R}_j| \longrightarrow \infty} F(\mathbf{R}_i - \mathbf{R}_j). \qquad (23)$$

where $F(\mathbf{R}_i - \mathbf{R}_j) = \sum_\alpha F_{\alpha\alpha}(\mathbf{R}_i - \mathbf{R}_j)$. All results we show in this paper are performed on lattices with 13^2 unit cells.

The superconducting order parameter $|\Phi|^2$ as a function of doping, calculated for physical parameters corresponding to graphene, obtained using the optimized wavefunction is shown in Fig. 8. Remarkably, a "superconducting dome", reminiscent of cuprates, [49] is obtained and is consistent with the RVB physics. The result indicates that undoped graphene had no long range superconducting order consistent with physical arguments and mean-field theory [40] of the phenomenological GB Hamiltonian. Interestingly, the present calculation suggests an "optimal doping" x of about 0.2 at which the the ODLRO attains a maximum. These calculations strongly suggest a superconducting ground state in doped graphene.

We now further investigate the system near optimal doping in order to estimate T_c. Figure 9 shows a plot of the (singlet)pair correlation function $F(r)$ as function of the separation r. The function has oscillations up to about six to seven lattice spacings and then attains a nearly constant value. From an exponential fit one can infer that the coherence length ξ of the superconductor is about six to seven lattice spacings. A crude estimate of an upper bound of transition temperature can then be obtained by using results from weak coupling BCS theory, using $k_b T_c = \frac{1}{1.764}\frac{\hbar v_F}{\pi \xi}$. *Conservative estimates give us $k_b T_c = \frac{t}{50}$, i.e., T_c is about twice room temperature.* Evidently, this is an upper bound, and an order of magnitude lower than the mean-field theory estimates of Black-Schaffer and Doniach [40]. Further improvement of our estimate of T_c becomes technically difficult. It is interesting to compare these results with those obtained in a Hubbard model on a square lattice that captures cuprate physics. In this latter case, a similar estimate of the coherence length ξ is about two to three lattice spacings [49]; however, the hopping scale is nearly an order of magnitude lower and the estimate of T_c is about $2T_{\text{Room}}$. Again, this provides further support for the possibility of high temperature superconductivity in graphene.

It is important to ask about the possibility of competing orders that could overshadow superconductivity at optimal doping that we have found. Honerkamp [51] has addressed this issue by means of a functional renormalization group study of a general Hamiltonian on the honeycomb lattice. He

finds that in the regime of physical parameter corresponding to graphene, the system appears to flow towards a $d + id$ superconducting state as the temperature is lowered.

Our results shows that there is an adiabatic continuity of strong coupling superconductivity to intermediate coupling in 2d repulsive Hubbard model on the honey comb lattice. *What is remarkable is that superconductivity at low coupling is not exponentially suppressed.* This seems to be unique to 2 dimensions. We have checked this for 2d square lattice repulsive Hubbard model as well, using existing numerical results. What about 3 dimensions? Preliminary analysis shows that the development of near neighbor singlet correlations is much reduced in 3 dimensions. That is, for a given ratio of band width to U, the strength of the induced near neighbor singlet correlations seems to get suppressed as we go from 2 to 3 dimensions, particularly at intermediate or weak couplings. This is also corraborated by the very low Tc one sees in intercalated graphite. Intercalated graphite can be viewed as a set of doped graphene layers. Maximum T_c obtained in these systems is around 16 K. [52; 53] Systems such as CaC_6 has a doping close to the optimal doping of our theoretical result. Infact, if one looks at the doping vs Tc, by collecting various intercalated graphite systems, Tc has a dome like structure, very much like Fig. 8! Why is the T_c so low? A closer inspection suggests to us two possible reasons in CaC_6: (i) an enhanced 3 dimensionality arising through the intercalant orbitals and (ii) competition from intercalant induced charge density wave order.

Superconducting signals with a T_c around 60 K and higher have been reported in the past in pyrolitic graphite containing sulfur. [54; 55] Sulfur doped graphite, however, gives a hope that there is a possibility of high temperature superconductivity. Our present theoretical prediction should encourage experimentalists to study graphite from superconductivity point of view systematically, along the line pioneered by Kopelevich and collaborators. [55] In the past there has been claims (unfortunately not reproducible) of Josephson like signals in graphite and carbon based materials; [56] Again, our result should encourage revival of studies along these lines.

Simple doping of a freely hanging graphene layer by gate control to the desired optimal doping of $10 - 20$ % is not experimentally feasible at the present moment. It will be interesting to discover experimental methods that will allow us to attain these higher doping values. A simple estimate shows that a large cohesion energy arising from the strong σ bond that

stabilizes the honeycomb structure will maintain the structural integrity of graphene. A recent article reviews [57] theoretical study of doping in graphene.

The discovery of time reversal symmetry braking $d+id$ order [40] for the superconducting state, within our RVB mechanism is very interesting. This unconventional order parameter has its own signatures in several physical properties: (i) spontaneous currents in domain walls, (ii) chiral domain wall states (iii) unusual vortex structure and (iv) large magnetic fields arising from the $d = 2$ angular momentum of the cooper pairs, which could be detected μSR measurements. Suggestions for experimental determination of such an order by means of Andreev conductance spectra have been made [58].

There are also several theoretical and experimental issues that needs to be addressed. It is known that graphene realized in experimental systems contains, adsorbed species, inhomogeneities, curvature, ripples etc. [59] Is the superconducting ground state stable to these "perturbations"? In particular our theory gives a substantial ODLRO even for small doping. If disorder effects are indeed suppressing a fragile Kosterlitz-Thouless order in the currently available doping regime in real systems, one could uncover the hidden superconductivity by disorder control or study of cooper pair fluctuation effects. Further analysis is necessary to address these issues.

5. Composite Fermi Sea

Composite fermion is a remarkable discovery [60; 61; 62], made in the context of fractional quantum Hall effect. A bare electron in the lowest Landau level gets attached to an integer number of quantized fluxes. When the number of bound flux quanta is even the composite particle is a fermion and is called a *composite fermion*. This concept helps in unifying an entire gamut of fractional Hall states and also has important consequences. In particular, for the the half filled Landau level, one has an unexpected composite fermi sea as a normal (reference) state. It is natural to look for composite fermi sea in graphene. In particular, neutral graphene in a magnetic field has two Landau levels that are half filled (in the absence of spin polarization). Will these half filled states lead to a composite fermi sea? In a recent theoretical work we provided [63] an affirmative answer.

In comparision to standard 2d electron gas provided by inversion layers and heterostructures, the 2d electron gas in graphene is special. As we saw earlier the Landau spectrum scales as $\sqrt{n}$, the Landau level index. At zero

doping we have two degenerate sets of Landau levels which are half filled, because of particle hole symmetry. Another remarkable feature of graphene is that in the range upto the physically realizable 100 T magnetic field, the Zeeman energy is much smaller compared to the energy level spacing between n = 0 and n = 1 Landau level and the interaction energy scale. Thus Zeeman splitting could be ignored. This results in an approximate global SU(4) symmetry, 2 for valley degeneracy and 2 for spin degeneracy.

Recent experimental [64; 65] and theoretical [69; 68] works suggest a ferromagnetic integer Hall state at n = 0, where an exchange (and to a lesser extent Zeeman) split two (valley) degenerate levels are completely filled (say) with upspin electrons (Fig. 10(A)). There is a puzzle however: even though experiments see a weak Hall plateau beyond about 20 T, diagonal resistance ρ_{xx} is very high and metal like, instead of being zero. It seem to indicate presence of a gapless dissipative state. We proposed a resolution to the puzzle (Fig. 10(B)) by suggesting a composite fermi sea normal state for neutral graphene. Our proposal, if confirmed, has important consequences, as composite fermi seas are one of the strangest form of quantum matter. For example, composite fermi seas are seats of paired Hall states and non Abelian quasi particles. Non Abelian quasi particles are currently being vigorously studied in the context of topological quantum computation [66].

There are many theoretical studies in graphene in the presence of strong external magnetic and electric fields, dealing with both integer and fractional quantum Hall states [67; 68; 70; 69; 71; 72; 73; 74; 75; 76; 77; 78; 79]. A recent experimental study [64] probes nature of low temperature state of the neutral graphene in magnetic fields upto 45 T. Development of a weak Hall plateau at n = 0 is attributed to a ferromagnetic integer quantum Hall state (Fig. 10(A)). However, they find an unexpected, dissipative normal state in neutral graphene. Another work confirms this [65] and also suggests that the dissipative normal state is intrinsic and not a consequence of disorder. Thus a puzzle is the appearance of a very weak quantum Hall plateau and a contrasting (compressible, gapless) metallic and high resistive state; longitudinal resistance is finite and large, $\rho_{xx} > \frac{e^2}{h}$. This work attributes the dissipative state to certain anomalous behaviour of edge states, arising from a theoretically predicted 'spin gap' behaviour [68]. Other, general theoretical study of fractional quantum Hall states in graphene, [80; 81] discuss spin polarized composite fermi sea, but do not address the important experimentally motivated case being discussed in the present paper.

Here we suggest a rather different scenario, that is inspired by the aforementioned experimental results on neutral graphene. We suggest that

A) $n = 0$ Exchange and Zeeman Split Landau Levels

valley 1   valley 2

B)

$k_{F\downarrow}$ $k_{F\downarrow}$

$k_{F\uparrow}$ $k_{F\uparrow}$

valley 1   valley 2
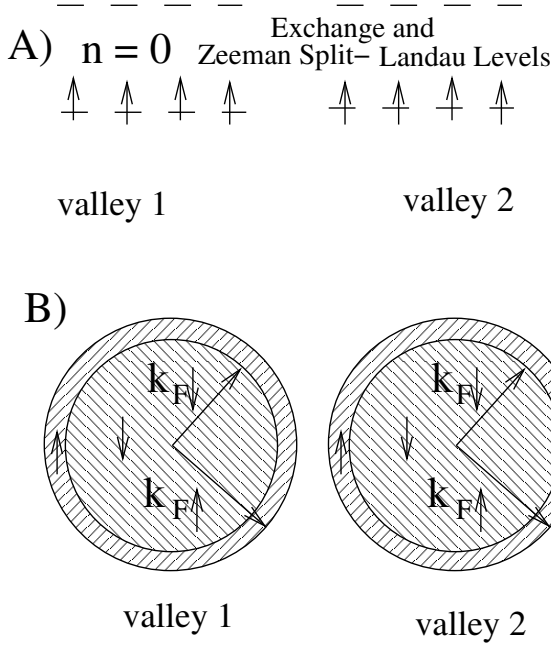
Fig. 10. (A) Exchange and Zeeman split $n = 0$ two valley degenerate Landau levels and completely filled upspin bands. (B) Our proposal of an approximate SU(4) singlet (2 spin × 2 valley) composite fermi sea, at a filling $\nu \approx \frac{1}{2}$ for each component. A small spin polarization ($k_{F\uparrow} \neq k_{F\downarrow}$) arising from Zeeman field is shown.

instead of the expected fully spin polarized integer quantum Hall state at n = 0, we have a SU(4) singlet (2 spin × 2 valley) composite fermi liquid, with each species at $\nu \approx \frac{1}{2}$ filling. We present physical arguments for emergence of a composite fermi sea and a very rough estimate of energy of a variational composite fermi sea wave function.

At the heart of our proposal are the following key physical arguments: a) Two (valley) n = 0 completely filled bands with parallel spins, lack inter band dynamical scattering because of complete Pauli blocking. (We ignore high energy n ≠ 0 Landau levels). Consequently two electrons from different valleys with parallel spins do not have a correlation hole; to that extent coulomb repulsion energy is not minimised. Further, the *overlap charges* of two single particle states p and q, at any lattice site **R**, $\psi_{p,\tau}^{*n=0}(\mathbf{R})\psi_{q,\mu}^{n=0}(\mathbf{R}) = 0$ for n = 0 Landau level states of different valleys τ and μ in graphene. *Thus there is no exchange energy between any two parallel spins belonging to different valleys!*

b) Our composite fermi sea, a global SU(4) singlet (2 spin × 2 valley), on the other hand, is more efficient in building coulomb hole between electrons belonging to different valleys and also different spins (because of the half filled band character and less Pauli blocking), through two body scattering. The process of building correlation hole and avoiding coulomb repulsion will introduce short range SU(4) singlet correlation in the composite fermi sea. To this extent *our proposal is somewhat similar to generic stability of spin liquid or antiferromagnetic state, compared to ferromagnetic state in half filled band of strongly correlated electrons.*

Further, for graphene, correlation and exchange energies are both comparable in magnitude and $\sim \frac{e^2}{\epsilon_0 \ell_B} \approx 130\sqrt{B}K$ (B measured in Tesla); Zeeman energy is negligible for B $\sim$ 30 T. In order to get a good ground state both correlation and exchange energies need to be considered.

We focuss on the n = 0 Landau level of our neutral graphene and assume that the lattice parameter of graphene 'a' is small compared to the magnetic lengthℓ_B; i.e. $\frac{a}{\ell_B} << 1$. Appropriately normalized lattice coordinates of an electron are complex numbers $z_{\sigma\tau}$, where $\sigma =\uparrow,\downarrow$ and $\tau = \pm$ are the spin and valley indeces.

We will make a brief remark about Jain's composite fermion [60; 61; 62] approach. In 2D quantum Hall problems, external magnetic fields generate quantized vortices. Stable many body states are formed, when there is a commensurate relation between total number of vortices and total number of electrons. In most of the stable quantum Hall states an electron gets 'bound' (associated) to a finite number of vortices (flux quanta) to become a quasi particle, in terms of which the complex many body problem becomes essentially non-interacting. When number of bound vortices are even, statistics of the composite object remains a fermion. They are the composite fermions. As these composites have already absorbed the effect of external magnetic field they see an effective magnetic field $B^* < B$, the externally applied field. At the end of some hierarchies (eg. $p \to \infty$, $\frac{p}{2p+1} = \frac{1}{2}$), the effective magnetic field seen by a composite fermion vanishes, leading to a compressible composite fermi liquid state. Composite fermion formation is a profound modification of the bare constituent electron. It also turns out to be an efficient way to build correlation/exchange holes and avoid coulomb repulsion.

Now we will estimate and compare energies of spin polarized (upspin) completely filled n = 0 Landau levels of 2 valleys $\Psi_{\mathrm{G}}^{\uparrow\uparrow}$, with our proposed composite fermi sea state, $\Psi_{\mathrm{G}}^{\mathrm{FS}}$. The explicit form of the spin polarized

state is

$$\Psi_{\text{G}}^{\uparrow\uparrow}[z] = \prod_{i<j,\tau} (z_{i\uparrow\tau} - z_{j\uparrow\tau})e^{-\sum_{i\tau}\frac{|z_{i\uparrow\tau}|^2}{4}} \qquad (24)$$

It is a product of two (antisymmetric) Van der Monde determinant for up spin electrons filling the n = 0 Landau levels of two valleys, $\tau = \pm$. Here $N_e \equiv 2N_\phi$ is the total number of electrons, and $4N_\phi$ is the total number of single particle states in n = 0 Landau level, including spin and orbital degeneracies. And $N_\phi \approx A\frac{eB}{hc}$, where A is the area of the sample.

In quantum Hall effect kinetic energy is frozen and is independent of electron-electron interaction. So one focuses only on two body electrostatic interaction energy. It is customary to write it as an energy gain with reference to electrostatic interaction energy of uniformly smeared electron charges and positive charges of neutralizing background. Energy of interaction of an electron with quantum numbers $\uparrow \tau$, with rest of the electrons is

$$U_{\text{FM}} = \pi \sum_{\tau'} \int \frac{e^2}{\epsilon_0 r}(g_{\tau\tau'}^{\uparrow\uparrow}(r) - 1)r dr \qquad (25)$$

Here $g_{\tau\tau'}^{\sigma\sigma'}(\text{r})$ is the radial distribution function between two electrons having quantum numbers $\sigma\tau$ and $\sigma'\tau'$. For large distances g(r) $\rightarrow$ 1; so there is no energy gain. For short distances, comparable to ℓ_B and less, there is a 'hole' in g(r) and a consequent energy gain by avoiding the strong coulomb repulsions. One of the challenges in quantum Hall effect is to discover the right many body variation wave functions (built from appropriate single particle Landau level states) and get the best g(r). The hole in g(r) in the present ferromagnetic state arises from antisymmetrization of electrons with parallel spins within a given valley. It is an exchange rather than correlation hole.

Within the lowest Landau level approximation $g_{\tau-\tau}^{\uparrow\uparrow}(\text{r}) = 1$; that is, there is no hole! It indicates total absence of correlations between electrons belonging to two different valleys. This is a consequence of complete Pauli blocking of interband two body scattering among two filled bands. Consequently, short distance coulomb repulsion among electrons from two different valleys can not be avoided. Virtual scattering involving high energy n $\neq$ 0 Landau levels will to some extent modify $g_{\tau-\tau}^{\uparrow\uparrow}(\text{r})$, which we ignore as a first approximation.

As mentioned earlier, there is no exchange energy between two parallel spins belonging to different valleys in the n = 0 Landau level, as the

overlap charge density between any two single particle states corresponding
to different valleys are identically zero.

Using Laughlin's plasma analogy, the expression [82] for energy per
electron is found to be

$$U_{\text{FM}} \approx \pi \int \frac{e^2}{\epsilon_0 r}(g_{\tau\tau}^{\uparrow\uparrow}(r) - 1)rdr \approx -0.62\frac{e^2}{\epsilon_0\ell_B} \tag{26}$$

We will argue that we can get a lower energy in our composite fermi sea.
The wave function for the composite fermi sea we are proposing is given by

$$\Psi_{\text{G}}^{\text{FS}}[z] = \hat{P}_{LLL}e^{-\sum_{i<j\sigma\tau\sigma'\tau'} f(|\mathbf{r}_{i\sigma\tau}-\mathbf{r}_{j\sigma'\tau'}|)}$$

$$\prod_{\sigma\tau}\|e^{i\mathbf{k}\cdot\mathbf{r}_{\sigma\tau}}\|\prod_{i<j}(z_{i\sigma\tau} - z_{j\sigma\tau})^2 e^{-\sum_i \frac{|z_{i\sigma\tau}|^2}{4}} \tag{27}$$

There are 4 composite fermi sea of electrons, corresponding to two spin and
two valley indices. Each composite fermi sea has a filling fraction $\nu = \frac{1}{2}$
containing $\frac{N_\phi}{2}$ electrons. There is a common fermi momentum for each
fermi sea given by the expression: $k_F \equiv \sqrt{4\pi\rho}$. Here ρ is electron density.

We have also introduced a two particle short range Jastrow factor
through the function $f(r)$ between any two electrons. This introduces cor-
relation between two electrons having different valley and spin quantum
numbers. Since we have only a half filled Landau level valley exchange
and spin exchange scattering within n = 0 levels are not completely Pauli
blocked and they build short distance holes in the respective g(r), reduce
the coulomb repulsion energy.

Our short range Jastrow correlation for electrons with different quan-
tum numbers is unusual in quantum Hall situation. Long ranged Laughlin-
Jastrow correlation are normally used, as they also take care of antisym-
metry automatically. To keep a gapless fermi sea and at the same time
maintain half filling in each Landau sub band, short range Jastrow func-
tion seems essential in the present case. When we attempt to use Laughlin-
Jastrow factor, it either changes the mean density (expands the Laughlin
drop significantly) or we seem to get incompressible states. Since one im-
plements lowest Landau level projection at the end, in principle our short
range Jastrow factor is allowed. We have no proof that our short range f(r)
maintains the mean density per Landau level to be half.

In the above variational wave function, the projection to n = 0 Landau
level is done by $\hat{P}_{LLL}$. This projector effectively replaces $\bar{z} \to \partial_z$. For
example, $e^{i\mathbf{k}\cdot\mathbf{r}} = e^{\frac{1}{2}i(\bar{k}z+k\bar{z})} \to e^{\frac{1}{2}i(\bar{k}z+k\partial_{\bar{z}})}$ and $f(r_{ij}) \equiv \sum_k \tilde{f}(k)e^{i\mathbf{k}\cdot\mathbf{r}_{ij}} \to$
$\sum_k \tilde{f}(k)e^{\frac{1}{2}i(\bar{k}z_{ij}+k\partial_{\bar{z}_{ij}})}$. Here $k \equiv k_x + ik_y$.

Our composite fermi sea wave function is a global SU(4) singlet (spin × valley). That is, a plane wave state is either filled with four electrons with four possible spin and valley quantum numbers or is completely empty. In view of this it satisfies Fock's cyclic boundary condition. The above SU(4) singlet state is consistent with a two body interaction which is very nearly SU(4) symmetric for graphene in the n = 0 Landau level [72].

As before, interaction energy of an electron with quantum numbers $\sigma\tau$ with rest of the electrons, in the composite fermi state is given by

$$U_{\text{CF}} = \pi \sum_{\sigma'\tau'} \int \frac{e^2}{\epsilon_0 r} (g_{\sigma\sigma'}^{\tau\tau'}(r) - 1) r dr \qquad (28)$$

We will estimate the energy of this state in two approximations made on $|\Psi_G^{\text{FS}}[z]|^2$. As the first approximation we put f(r) = 0. We are left with products of four independent composite fermi sea, each with a filling $\nu = \frac{1}{2}$. The energy of this state has been calculated in the literature [60; 62] for spin polarized $\nu = \frac{1}{2}$ composite fermi state as

$$U_{\text{CF}} \approx -0.46 \frac{e^2}{\epsilon_0 \ell_B} \qquad (29)$$

This energy is about 25 percent higher than the ferromagnetic integer Hall state (Eq. (3)). We will show approximately that inclusion of a short range Jastrow correlation can give more than 25 percent energy gain and make our composite fermi sea stable. Jastrow factor, by construction is capable of generating hole in the radial distribution function $g_{\tau\tau'}^{\sigma\sigma'}(r)$. Physically this possibility arises from possibility of virtual interband scattering between electrons having different $\sigma\tau$ quantum numbers within the n = 0 Landau levels. Fortunately these scattering process are not completely Pauli blocked, because each Landau sub band is only half filled.

Without making a detailed calculation, we can estimate that a 25 percent improvement of energy is possible, by the following rough argument. From two particle scattering point of view, we have both direct and exchange scattering among two electrons with parallel spins. The corresponding matrix elements are comparable, and decay in a Gaussian fashion for localized gaussian orbitals separated beyond magnetic length ℓ_B. For particles with different quantum numbers the exchange term is absent. That is, for our interband scattering, exchange scattering, half of the total processes are absent. Further, the interband scattering can take place to empty single particle states which are only half of the total number of states available (the rest are Pauli blocked). In view of this we approximate the amount

of hole development in g(r) and the corresponding energy gain to be about $\frac{1}{4} = \frac{1}{2} \times \frac{1}{2}$ of energy gain within a given composite fermi sea. Since a given electron can reduce coulomb energy by correlating with three other composite fermi sea, the net energy we gain from the $3 \times \frac{1}{4}$. Putting these numbers we get our estimate of our state as:

$$U_{\text{CF}} \approx -(1 + \frac{3}{4}) \, 0.46 \frac{e^2}{\epsilon_0 \ell_B} \approx -0.8 \frac{e^2}{\epsilon_0 \ell_B} \qquad (30)$$

This energy is lower than that of the fully spin polarized filled Landau level states (Eq. (3)). It is the valley degeneracy which helps us to get a lower energy for the composite fermi sea!

We test our simple argument against a known case, namely stability of the standard n = 1 fully polarized quantum Hall state (no valley degeneracy) with a spin singlet compsite fermi sea. Experimentally it is known (at least for lower odd integer Hall states) that fully polarized quantum Hall state always wins. Interestingly, in our estimate, absence of valley degeneracy reduces the factor $\frac{3}{4}$ to $\frac{1}{4}$ and keeps the spin polarized filled n = 1 state marginally stable.

After the composite fermi sea is formed, the Zeeman energy creates spin polarization in an otherwise spin singlet composite fermi sea. The spin polarization of the composite fermi sea is easily estimated to be $\approx \frac{g\mu_B B}{U_{\text{CF}}}$. We estimate that for graphene for a field of 30 T, spin polarization is less than a few percent.

Very good signatures of composite fermion and fermi sea effects, in standard quantum Hall systems have been experimentally studied [83]. It will be very interesting to perform such studies and look for composite fermi sea in neutral graphene in strong magnetic fields.

Composite fermions are neutral and they carry certain dipole moment [84], as a function of their momenta. The response of the composite fermion fermi surface to external perturbations such as a local defect will be interesting. We will have a Friedel oscillation in dipole density.

Further graphene may offer alternate methods to study composite fermions, because of new access through ARPES, STM etc, which are not possible in standard quantum Hall devices.

So far we have been talking about low temperature normal state. Residual interactions will introduce low temperature pairing instabilities in graphene either in the particle-particle or particle-hole channels. The small spin polarization will interfere with the standard instabilities.

6. Two Channel Kondo Effect

An extremely interesting phenomenon in conventional metal systems is the Kondo effect which occurs in the presence of dilute concentration of localized quantum spins coupled to the spin-degenerate Fermi sea of metal electrons [85]. The impurity spin-electron interaction then results in perfect or partial screening of the impurity spin leading to an apparently divergent resistance, as one approaches zero temperature. It also results in a sharp 'Kondo Resonance' in electron spectral functions. Recent developments in quantum dots and nano devices have given new ways in which various theoretical results in Kondo physics, which are not easily testable otherwise, can be tested and confirmed experimentally [86]. Most of the early studies in Kondo effect were carried on for conventional metallic systems with constant density of states (DOS) at the Fermi surface [87]. Some studies on Kondo effect in flux phases [88], nodal quasiparticles in d-wave superconductors [89], Luttinger liquids [90], and hexagonal Kondo lattice [91], for which the DOS of the associated Fermions vanishes as some power law at the Fermi surface, have also been undertaken. However, although effect of non-magnetic impurities has been studied [94], there has been no theoretical study till date on the nature of Kondo effect in graphene.

In a recent work along with Sengupta we presented [92] a large N analysis [93] for a generic local moment coupled to Dirac electrons in graphene to show that Kondo effect in graphene is unconventional and can be tuned by gate voltage. We demonstrated the presence of a finite critical Kondo coupling strength in neutral graphene. We pointed out that local moments in graphene can lead to non Fermi-liquid ground state via multi channel Kondo effect. We also suggested possible experimental realization of such Kondo scatterers in graphene.

The crucial requirement for occurrence of Kondo effect is that the embedded impurities should retain their magnetic moment in the presence of conduction of electrons of graphene. We expect that large band width and small linearly vanishing density of states at the fermi level in graphene should make survival of impurity magnetic moment easier than in the conventional 3D metallic matrix. A qualitative estimate of the resultant Kondo coupling can be easily made considering hybridization of electrons in π band in graphene with d orbitals of transition metals. Typical hopping matrix elements for electrons in π band is $t \sim 2$ eV and effective Hubbard U in transition metals is 8 eV. So the Kondo exchange $J \sim 4t^2/U$, estimated via standard Schrieffer-Wolf transformation, can be as large as 2 eV which is

close to one of the largest $J \simeq 2.5$ eV for Mn in Zn. In the rest of this work, we shall therefore use the Kondo Hamiltonian [95] as our staring point.

Our analysis begins with the Hamiltonian for free Dirac electrons in graphene and consider interaction with a single magnetic impurity at the origin. We first find that we need a critical Kondo coupling J_c to get Kondo screening for neutral graphene. This is because of linear vanishing of density of states at the fermi level. By applying a gate voltage we can change the chemical potential and make the density of states finite at the fermi level. This is the tunability offered by graphene.

After a detailed analysis we obtain the expression for $J_c(q,T)$, the critical value in the large N limit as,

$$J_c(q,T) = J_c(0) \left[1 - 2q \ln\left(1/q^2\right) \ln\left(k_B T/\Lambda\right)\right]^{-1} \qquad (31)$$

where the temperature $k_B T$ is the infrared cutoff, $J_c(0) = (\pi \hbar v_F k_c^2)^2/\Lambda = \pi^2 \Lambda$ is the critical coupling in the absence of the gate voltage and q = $\frac{eV}{\Lambda}$. We have omitted all subleading non-divergent terms which are not important for our purpose. For $V = 0 = q$, we thus have, analogous to the Kondo effect in flux phase systems [88], a finite critical Kondo coupling $J_c(0) = \pi^2 \Lambda \simeq 20$ eV which is a consequence of vanishing density of states at the Fermi energy for Dirac electrons in graphene. Of course, the mean-field theory overestimates J_c. A quantitatively accurate estimate of J_c requires a more sophisticated analysis which we have not attempted here.

The presence of a gate voltage leads to a Fermi surface and consequently $J_c(q,T) \to 0$ as $T \to 0$. For a given experimental coupling $J < J_c(0)$ and temperature T, one can tune the gate voltage to enter a Kondo phase. The temperature $T^*(q)$ below which the system enters the Kondo phase for a physical coupling J can be obtained using $J_c(q, T^*) = J$ which yields

$$k_B T^* = \Lambda \exp\left[(1 - J_c(0)/J)/(2q \ln[1/q^2])\right] \qquad (32)$$

For a typical $J \simeq 2$ eV and voltage $eV \simeq 0.5$ eV, $T^* \simeq 35$K [96]. We stress that even with overestimated J_c, physically reasonable J leads to experimentally achievable T^* for a wide range of experimentally tunable gate voltages.

We now discuss the possible ground state in the Kondo phase qualitatively. In the absence of the gate voltage a finite J_c implies that the ground state will be non-Fermi liquid as also noted in Ref. [88] for flux phase systems. In view of the large J_c estimated above, it might be hard to realize such a state in undoped graphene. However, in the presence of the gate voltage, if the impurity atom generates a spin half moment and the

Kondo coupling is independent of the valley(flavor) index, we shall have a realization of two-channel Kondo effect in graphene owing to the valley degeneracy of the Dirac electrons. This would again lead to overscreening and thus a non Fermi-liquid like ground state [87]. The study of details of such a ground state necessitates an analysis beyond our large N mean-field theory. To our knowledge, such an analysis has not been undertaken for Kondo systems with angular momentum mixing. In this work, we shall be content with pointing out the possibility of such a multichannel Kondo effect in graphene and leave a more detailed analysis as an open problem for future work.

Next, we discuss experimental observability of the Kondo phenomena in graphene. The main problem in this respect is creation of local moment in graphene. There are several routes to solving this problem. (i) Substitution of a carbon atom by a transition metal atom. This might in principle frustrate the strong sp^2 bonding and thus locally disturb the integrity of graphene atomic net. However, nature has found imaginative ways of incorporating transition metal atoms in p-π bonded planar molecular systems such as porphyrin [97]. Similar transition metal atom incorporation in extended graphene, with the help of suitable bridging atoms, might be possible. (ii) One can try chemisorption of transition metal atoms such as Fe on graphene surface through sp-d hybridization in a similar way as in intercalated graphite [98]. (iii) It might be possible to chemically bond molecules or free radicals with magnetic moment on graphene surface as recently done with cobalt pthalocyanene (CoPc) molecule on AU(111) surface [99]. This might result in a strong coupling between graphene and impurity atom leading to high Kondo temperatures as seen for CoPc on AU(111) surface ($T_K \simeq 280K$). (iv) Recently ferromagnetic cobalt atom clusters with sub nano-meter size, deposited on carbon nanotube, have exhibited Kondo resonance [100]. Similar clusters deposition in graphene might be a good candidate for realization of Kondo systems in graphene. (v) From quantum chemistry arguments, a carbon vacancy, or substitution of a carbon atom by a boron or nitrogen might lead to a spin-half local moment formation. In particular, it has been shown that generation of local defects by proton irradiation can create local moments in graphite [101]. Similar irradiation technique may also work for graphene.

For spin-1 local moments and in the presence of sufficiently large voltage and low temperature, one can have a conventional Kondo effect in graphene. The Kondo temperature for this can be easily estimated using $k_B T_K \sim D\exp(-1/\rho J)$ where the band cutoff $D \simeq 10$ eV, $J \simeq 2-3$ eV and DOS per

site in graphene $\rho \simeq 1/20$ per eV. This yields $T_K \simeq 6-150$K. The estimated value of T_K has rather large variation due to exponential dependence on J. However, we note that Kondo effect due to Cobalt nano-particle in graphitic systems such as carbon nanotube leads to a high $T_K \approx 50K$ which means that a large J may not be uncommon in these systems.

Finally, we note that recent experiments have shown a striking conductance changes in carbon nanotubes and graphene, to the extent of being able to detect single paramagnetic spin-half NO_2 molecule [102]. This has been ascribed to conductance increase arising from hole doping (one electron transfer from graphene to NO_2). Although Kondo effect can also lead to conductance changes, in view of the fact that a similar effect has been also seen for diamagnetic NH_3 molecules, the physics in these experiments is likely to be that of charge transfer and not local moment formation.

7. Summary

In this article we have tried to view the richness of quantum phenomena exhibited by graphene as a quantum complexity. A closer look reveals that at every stage or level some details related to the quantum property play an important role in leading to the next level of surprise. The structure of quantum mechanics allows for wonderful possibilities. The point of view presented in this article might help us to appreciate the origin of quantum wealth and be prepared to expect similar phenomena in other corners in quantum science.

Acknowledgment

References

1. K.S. Novoselov et al., Science **306**, 666 (2004).
2. K.S. Novoselov et al., Proc. Natl. Acad. Sci. USA **102**, 10451 (2005).
3. A.H. Castro Neto et al., Reviews of Modern Physics **81**, 109 (2009).
4. M.S. Dresselhaus and G. Dresselhaus, Adv. Phys. **30**, 139 (81); R. Saito, G. Dresselhaus and M.S. Dresselhaus, *Physical Properties of Carbon Nanotubes,* Imperial College Press, London (1998).
5. P.W. Andeson, Science **177**, 393 (1972).

6. G.E. Volovik, The Universe in a Helium Droplet, *Oxford University Press, Oxford 2003.*

7. L. Pauling, The Nature of the Chemical Bond, (Cornell Univ Press, NY) 1963.

8. G. Baskaran and S.A. Jafari, Phys. Rev. Lett. **89**, 016402 (2002); S.A. Jafari and G. Baskaran, Eur. Phys. J. **B 43**, 175 (2005); see also an important comment and our reply: N.M. Peres, M.A. Arajo and A.H. Neto, Phys. Rev. Lett. **92**, 199701 (2004); G. Baskaran and S.A. Jafari, Phys. Rev. Lett. **92**, 199702 (2004).

9. S. Pathak, V. Shenoy and G. Baskaran, Phys. Rev. B **81**, 085431 (2010).

10. K.S. Krishnan and N. Ganguli, Nature **144**, 667 (1939).

11. K.S. Krishnan and N. Ganguli, Nature **144**, 667 (1939).

12. C.L. Kane and E.J. Mele, Phys. Rev. Lett. **95**, 226801 (2005).

13. Sudipta Dutta, S. Lakshmi and Swapan K. Pati, Phys. Rev. **B 77**, 073412 (2008).

14. The Many-Body Problem, David Pines (W.A. Benjamin, NY) 1962.

15. M.S. Sercheli et al., Solid State Communications **121**, 579 (2002). Y. Kopelevich et al., J. Low Temp. Phys. **119**, 691 (00).

16. M. Plihal, D.L. Mills and J. Kirschner, Phys. Rev. Lett. **82**, 2579 (99).

17. R. Jansen et al., Phys. Rev. Lett. **85**, 3277 (00).

18. J. González, F. Guinea and M.A.H. Vozmediano, Nucl. Phys. B **424**, 595 (1994); Phys. Rev. Lett. **77**, 3859 (96); Phys. Rev. B **63**, 134421 (2001).

19. D.V. Khveshchenko, Physical Review Letters **87**, 246802 (2001).

20. Yu.A. Krotov, D.H. Lee and S.G. Louie, Phys. Rev. Lett. **78**, 4245 (97).

21. L. Balents and M.P.A. Fisher, Phys. Rev. **B 55**, R11973 (97).

22. K. Harigaya, J. Phys: Condens. Matt. **13**, 1295 (01); K. Harigaya and T. Enoki, Chemical Physics Letters **351**, 128 (2002).

23. T.C. Hsu, Phys. Rev. **B41**, 11379 (90); Chang-Ming Ho et al., Phys. Rev. Let. **86**, 1626 (01).

24. see for example, J. Brinckmann and P.A. Lee, Phys. Rev. Lett. **82**, 2915 (99).

25. S. Sorella and E. Tosatti, Euro. Phys. Lett. **19**, 699 (92); N. Furukawa, J. Phys. Soc. Jpn. **70**, 1483 (2001).

26. G. Baskaran and S.A. Jafari (unpublished).

27. G. Baskaran and R Ganesh (unpublished).

28. L. Vinu, R. Shankar and G. Baskaran, Phys. Rev. Lett. **98**, 116802 (2007).

29. A.H. MacDonald, Phys. Rev. B **28**, 2235 (1983).

30. Y. Niimi et al., Phys. Rev. B **73**, 085421 (2006); L. Brey and H.A. Fertig, Phys. Rev. B **73**, 195408 (2006); Phys. Rev. B **73**, 235411 (2006); K. Sasaki, S. Murakami and R. Saito, J. Phys. Soc. Jpn. **75**, 074713 (2006); A. Abanin, P.A. Lee and L.S. Levitov, Phys. Rev. Lett. **96**, 176803 (2006); D.N. Sheng, L. Sheng and Z.Y. Weng, Phys. Rev. B **73**, 233406 (2006); V. M. Pereira et al., Phys. Rev. Lett. **96**, 036801 (2006).

31. G. Ebart et al., J. Phys. C **16**, 5441 (1983); V. Tsemekhman et al., Phys. Rev. B **55**, R10201.

32. M.L. Sadowski et al., Phys. Rev. Lett. **97**, 266405 (2006).

33. H. Kempa, P. Esquinazi and Y. Kopelevich, Solid State Communications **138**, 118 (2006).
34. Timir Datta et al., cond-mat/0503166.
35. J. Bednorz and K. Mueller, Possible high T_c superconductivity in the Ba-La-Cu-O system. *Z. Phys. B* **64**, 189 (1986).
36. P.W. Anderson, Science **235**, 1196 (1987).
37. J. Nagamatsu et al., Nature **410**, 63 (2001).
38. Y. Kamihara et al., J. Am. Chem. Soc. **130**, 3296–3297 (2008).
39. G. Baskaran, Phys. Rev. B **65**, 212505 (2002).
40. A. Black-Schaffer and S. Doniach, Phys. Rev. B **75**, 134512 (2007).
41. B. Uchoa and A.H.C. Neto, Phys. Rev. Lett. **98**, 146801 (2007).
42. T.C. Choy and B.A. McKinnon, Phys. Rev. B **52**, 14539–14543 (1995).
43. N. Furukawa, J. Phys. Soc. Jpn. **70**, 1483 (2001).
44. S. Onari et al., Phys. Rev. B **68**, 024525 (2003).
45. D. Baeriswyl and E. Jackelman, The Hubbard Model: Its Physics and Mathematical Physics (ed. Baeriswyl, D.), 393 (Plenum, New York, 1995).
46. D. Ceperley, G. Chester and M. Kalos, Phys. Rev. B **16**, 3081 (1977).
47. M.C. Gutzwiller, Phys. Rev. **137**, A1726–1735 (1965).
48. H. Shiba, Two-Dimensional Strongly Correlated Electron Systems, Zi-zhao Gan and Zhao-bin Su, Ed., chap. Some aspects of strongly correlated electronic systems – variational Monte Carlo studies (Gordon and Breach Science Publishers, 1989).
49. A. Paramekanti, M. Randeria and N. Trivedi, Phys. Rev. B **70**, 054504 (2004).
50. S. Florens and A. Georges, Phys. Rev. B **70**, 035114 (2004).
51. C. Honerkamp, Phys. Rev. Lett. **100**, 146404 (2008).
52. T.M. Klapwijk, Nat. Phys. **1**, 17 (2005).
53. T.E. Weller et al., Nat. Phys. **1**, 39 (2005).
54. R.R. da Silva, J.J.S. Torres and Y. Kopelevich, Phys. Rev. Lett. **87**, 147001 (2001).
55. Y. Kopelevich and P. Esquinazi, J. Low Temp. Phys. **146**, 629 (2007).
56. S. Lebedev, Cond-mat/0802.4197, and references therein.
57. Arun K. Manna and Swapan K. Pati, World Scientific, Doping of Graphene: A Computational Study (Book chapter, to appear, 2010).
58. Y. Jiang et al., Phys. Rev. B **77**, 235420 (2008).
59. A. Fasolino, J. Los and M. Katsnelson, Nat. Mat. **6**, 858 (2007).
60. J.K. Jain, Phys. Rev. Lett. **63**, 199 (1989); Phys. Rev. **B 41**, 7653 (1990); Science **266**, 1199 (1994).
61. J.K. Jain, Composite Fermion (Cambridge University Press, Cambridge) 2007.
62. B.I. Halperin, P.A. Lee and N. Read, Phys. Rev. **B 47**, 7312 (1993); E.H. Rezayi and N. Read, Phys. Rev. Lett. **72**, 900 (1994).
63. G. Baskaran, arXiv:cond-mat/0702420.
64. Y. Zhang et al., Phys. Rev. Lett. **96**, 136806 (2006).
65. D.A. Abanin et al., Phys. Rev. Lett. **98**, 196806 (2007).

66. S.D. Sarma, M. Freedman and C. Nayak, Physics Today 4, 123 (2006); Chetan Nayak et al., Rev. Mod. Phys. **80**, 1083 (2008).
67. V.P. Gusynin and S.G. Sharapov, Phys. Rev. Lett. **95**, 146801 (2005); C.L. Kane and E.J. Mele, Phys. Rev. Lett. **95**, 146802 (2005); A.H. Castro Neto, F. Guinea and N.M.R. Peres, Phys. Rev. B **73**, 205408 (2006).
68. D.A. Abanin, P.A. Lee and L.S. Levitov, Phys. Rev. Lett. **96**, 176803 (2006); Phys. Rev. Lett. **98**, 156801 (2007).
69. K. Nomura and A.H. MacDonald, Phys. Rev. Lett. **96**, 256602 (2006); K. Yang, Kun; Das Sarma and A.H. MacDonald, Phys. Rev. **B 74**, 075423 (2006).
70. H.A. Fertig and L. Brey, Phys. Rev. Lett. **97**, 116805 (2006); A. Iyengar et al., Phys. Rev. B **75**, 125430 (2007).
71. J. Alicea and M.P.A. Fisher, Phys. Rev. B **74**, 075422 (2006).
72. M.O. Goerbig, R. Moessner and B. Doucot, Phys. Rev. B **74**, 161407 (2006).
73. V.M. Apalkov and T. Chakraborty, Phys. Rev. Lett. **97**, 126801 (2006).
74. I.F. Herbut, Phys. Rev. Lett. **97**, 146401 (2006).
75. V.P. Gusynin, V.A. Miransky and I.A. Shovkovy, Phys. Rev. Lett. **73**, 3499 (1994).
76. D.V. Khveshchenko, Phys. Rev. Lett. **87**, 206401 (2001); ibid. **87**, 246802 (2001).
77. V.P. Gusynin, V.A. Miransky, S.G. Sharapov and I.A. Shovkovy, Phys. Rev. B **74**, 195429 (2006).
78. J.-N. Fuchs and P. Lederer, Phys. Rev. Lett. **98**, 016803 (2007).
79. Vinu Lukose, R. Shankar and G. Baskaran, Phys. Rev. Lett. **98**, 116802 (2007).
80. C. Toke et al., Phys. Rev. B **74**, 235417 (2006); C. Toke and J. Jain, Phys. Rev. B **75**, 245440 (2007).
81. D.V. Khveshchenko, Phys. Rev. B **75**, 153405 (2007).
82. R.B. Laughlin, Phys. Rev. Lett. **50**, 1395 (1983).
83. W. Kang, H.L. Stormer, L.N. Pfeiffer, K. Baldwin and K.W. West, Phys. Rev. Lett. **71** (1993); R.L. Willett, R.R. Ruel, K.W. West and L.N. Pfeiffer. Phys. Rev. Lett. **71** (1993); V.J. Goldman, B. Su and J.K. Jain, Phys. Rev. Lett. **72** (1994).
84. N. Read, Semicond. Sci. Technol. **9**, 1859 (1994); Surf. Sci. **361/362**, 7 (1996); G. Baskaran, Physica **B 212**, 320 (1995).
85. See for example A.C. Hewson *The Kondo Problem to Heavy Fermions*, Cambridge University Press (1993).
86. M. Pustilnik and L. Glazman, J. Phys.: Condens. Matter **16**, R 513 (2004).
87. For a review see I. Affleck, Acta Phys. Polon. **B26**, 1869 (1995); available in the arXiv as, cond-mat/9512099.
88. C.R. Cassanello and E. Fradkin, Phys. Rev. B **53**, 15079 (1996); D. Withoff and E. Fradkin, Phys. Rev. Lett. **64**, 1835 (1990); K. Insergent, Phys. Rev. B **54**, 11396 (1996).
89. A. Polkovnikov, S. Sachdev and M. Vojta, Phys. Rev. Lett. **86**, 296 (2001).
90. A. Furusaki and N. Nagaosa, Phys. Rev. Lett. **72**, 892 (1994).
91. S. Saremi and P.A. Lee, Phys. Rev. B **75**, 165110 (2007).

92. K. Sengupta and G. Baskaran, Phys. Rev. B **77**, 045417 (2007).
93. N. Read and C.J. Newns, J. Phys. C **16**, 3273 (1983).
94. C. Bena and S. Kivelson, Phys. Rev. B **72**, 125432 (2005); T.O. Wehling et al., Phys. Rev. B **75**, 125425 (2007).
95. J. Kondo, Prog. Theor. Phys. **32**, 37 (1964).
96. Note that J in our analysis is an effective coupling valid below the scale Λ *i.e.* $J > J_{\text{bare}}$. This might further enhance T^*.
97. Porphyrin Hand Book, Eds. K.M. Kadish, K.M. Smith and R. Guilard (Academic Press, New York) 1999.
98. M.E. Vol'pin and Yu.N. Novikov, Pure and Appl. Chem., vol. **60**, No. 8, 1133 (1988).
99. A. Zhao et al., Science **309**, 1542 (2005).
100. T.W. Odom et al., Science **290**, 1459 (2000).
101. P.O. Lehtinen et al., Phys. Rev. Lett. **93**, 187202 (2004).
102. T.O. Wehling et al., Nano Lett. 8; 173–177 (2008); S. Adam, S. Das Sarma and A.K. Geim, Phys. Rev. B **76**, 195421 (2007).
103. M. Hentschel and F. Guinea, Phys. Rev. B **76**, 115407 (2007).